# Shell middens - Unlocking hidden archaeological information using Raman spectroscopy

Andre Luiz de Lima Ponzoni

Doctor of Philosophy

University of York

Physics

September 2017

# Abstract

The study of shell middens and archaeological marine shells is important to investigate palaeoenvironments and human development. Analytical methods, such as isotope analyses, used for these reconstructions can only be trustworthy if the shells have not been drastically changed by the effect of diagenesis or by human intervention, *eg.*, heating of the shells. These changes are difficult to quantify by the current methods, which are either limited or destructive. In this thesis, a quantitative method for the assessment of diagenesis and the evidence of heating in sea shells has been proposed with Raman spectroscopy (RS), which is based on the inelastic scattering of light, whereby a small difference in the incoming and outgoing light energy provides highly sensitive spectroscopic information. The quantitative analysis of the Raman spectrum involved peak fitting procedures to obtain the peak position, amplitude and full width half maximum (FWHM) parameters, which were then compared between modern and ancient *Conomurex fasciatus* and *Nucella* sp. shells to obtain markers of diagenesis. Modern *Conomurex fasciatus* shells were heated at different temperatures and time conditions with the quantitative Raman parameters compared across different heat-treatments that were later compared to burnt archaeological *Conomurex fasciatus* fragments obtained from the same shell midden. The results have proven that quantitative RS is responsive to diagenetic alterations and heating of sea shells with the most sensitive markers obtained for the FWHM of the $L_1$, $L_2$ and $\nu_1$ peaks, which indicated an increase in the calcium carbonate crystallinity caused by the degradation of the organic macromolecules that supported the strained mineral lattice. An additional Raman marker of heating in sea shells was the peak intensity ratio $L_1/\nu_1$, which was also used to estimate the aragonite to calcite transition temperature; therefore, demonstrating that RS is sensitive to indicate diagenesis in sea shells.

# *Dedication*

To Raquel and Francobollo who joined me on this long journey

# Contents

# List of Figures

# List of Tables

# Acknowledgements

I would like to thank firstly both my supervisors, Dr Yvette Hancock and Prof Geoff Bailey for accepting me as their PhD student, since the project proposal, back in mid 2013 when it was submitted. They contributed not only with their knowledge but also applied their own resources to this project, buying consumables and others.

Secondly, I would like to thank the many friends I have made in the university at the Archaeology Department. They helped me in many different ways and made me better understand the archaeology world. This list includes Dr Andre Carlo Colonese, Dr Beatrice Demarchi, Dr Eva Laurie, Matthew Von Tersch and Dr Niklas Hausmann.

To CAPES for the financial support, the Brazilian funding agency that sponsored my master's degree many years ago, and now funded my PhD. This work would be impossible without their support.

To my wife Raquel who incentivised, supported and helped this PhD in many different ways.

Last but not least, to many other friends I have made in York, outside the university or not related to my PhD, in all these years. I am not listing one by one because then I would probably forget a few names, but thanks to all friends from the boardgames group and also from the scuba diving group.

# Declaration

This thesis is the result of my own investigations, except where otherwise stated. Other sources are acknowledged by explicit references. This work has not previously been presented for an award at this, or any other, University. I hereby give consent for my thesis, if accepted, to be made available for photocopying and for inter-library loan, and for the title and summary to be made available to outside organisations. Some of the material presented within this thesis forms part of the following papers/manuscripts:

N. Hausmann, A. C. Colonese, **A. de Lima Ponzoni**, Y. Hancock, M. Meredith-Williams, M. J. Leng and G. N. Bailey. Isotopic composition of *Conomurex fasciatus* shells as an environmental proxy for the Red Sea. *Quaternary International*, 427:115–127, 2017 – Joint work. Author carried out the Raman analysis.

**A. de Lima Ponzoni**, B. Demarchi, N. Hausmann, G. N. Bailey and Y. Hancock. Biogenic aragonite to calcite transition – a quantitative study using Raman spectroscopy, (in prep) – Chapter 4.

# Chapter 1

# Introduction

## 1.1 Raman spectroscopy

### 1.1.1 The Raman effect

The Raman effect was discovered by Chandrasekhara Venkata Raman in 1928, who noted that a fraction of a beam of coloured light entering a liquid was scattered with different colours. He tested 60 different types of substances, demonstrating that the nature of the scattered light depended on the type of sample [1]. In these first experiments, Raman used only the sunlight from a heliostat that had been concentrated with a telescope objective [1]. Since then, many components have improved Raman spectroscopy (RS), such as the use of monochromatic lasers to irradiate the sample and very precise sensors to detect the smallest change in the frequency of the light [2].

The Raman effect is explained by the interaction between matter and light. The interaction of light with a molecule polarises the electron cloud by distorting it around the nuclei, generating the short-lived virtual states [3]. Thus, the Raman scattering occurs for vibrations that cause a change in the polarisability of the electron cloud around the nuclei [2,3]. Figure 1.1 shows the electric field from the laser perturbing the charges of the

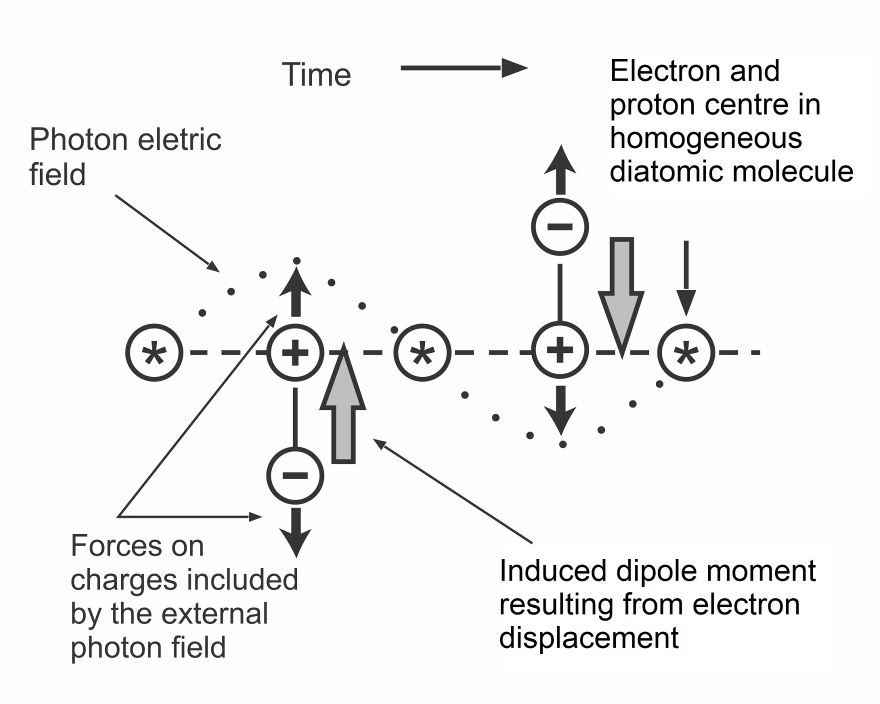

**Figure 1.1:** Displacement of the electric charges in the molecule by an external electric field, inducing a dipole moment that oscillates at the photon frequency, as per [4], page 16.

molecule and creating a dipole moment [4]. As the electric field is not static and varies with time at photon frequency, the polarisability varies slightly from the molecular vibrational frequency [4]. Therefore, to describe this effect, it is necessary to first introduce concepts about the electromagnetic radiation.

The fundamental properties of the wave description of electromagnetic radiation are the wavelength ($\lambda$), speed of the light ($c$) and frequency ($\nu$). The relationship between these properties are shown in Equation 1.1.

$$\lambda = \frac{c}{\nu} \tag{1.1}$$

However, for vibrational spectroscopies, it is common to measure wavenumbers ($\bar{\nu}$) instead of measuring the frequency or wavelength of the light [2–4], where

$$\bar{\nu} = \frac{1}{\lambda} \tag{1.2}$$

and with $\bar{\nu}$ measured in centimetres (cm$^{-1}$). For a green laser ($\lambda = 532$ nm $= 532 \times 10^{-7}$ cm), it will be as follows:

$$532 \text{ nm} \approx 18,797 \text{ cm}^{-1} \implies 1 \text{ nm} \approx 35.3 \text{ cm}^{-1}.$$

The electric field strength of a laser beam at a given time $t$ is written as

$$E = E_0 \cos(2\pi\nu_L t), \tag{1.3}$$

where $E_0$ is the electric field amplitude and $\nu_L$ is the frequency of the incident laser beam [2]. This electric field, when interacting with a molecule, will induce an electric dipole moment $P$, where

$$P = \alpha E \tag{1.4}$$

and $\alpha$ is a proportionality constant called polarisability [2–4]. Thus, combining Equations 1.3 and 1.4, the electric dipole moment $P$ can be written as

$$P = \alpha E_0 \cos(2\pi\nu_L t). \tag{1.5}$$

Considering that a diatomic molecule interacts with the laser, if the molecule is vibrating with a frequency $\nu_m$, the atomic displacement $q$ from equilibrium is

$$q = q_0 \cos(2\pi\nu_m t) \tag{1.6}$$

where $q_0$ is the maximum vibrational amplitude of the molecule [2].

The polarisability $\alpha$ varies with the vibrational motions of the molecule; therefore, for small amplitude of vibration, $\alpha$ can be approximated to a linear function of $q$, thus

$$\alpha = \alpha_0 + \left(\frac{\partial\alpha}{\partial q}\right)_0 q_0 \ + \ldots \tag{1.7}$$

where $\alpha_0$ is the polarisability at the equilibrium position and $(\partial\alpha/\partial q)_0$ is the rate of change of $\alpha$ in respect to the change in $q$ at the equilibrium [2].

Finally, by combining Equations 1.5, 1.6 and 1.7, the induced dipole moment can be written as

$$P = \alpha_0 E_0 \cos(2\pi\nu_L t) + \left(\frac{\partial\alpha}{\partial q}\right)_0 q_0 E_0 \cos(2\pi\nu_L t)\cos(2\pi\nu_m t), \tag{1.8}$$

which after the use of the trigonometric formula for the product of two cosines, becomes

$$P = \alpha_0 E_0 \cos(2\pi\nu_L t) + \frac{1}{2}\left(\frac{\partial\alpha}{\partial q}\right)_0 q_0 E_0 \left[\cos\{2\pi(\nu_L + \nu_m)t\} + \cos\{2\pi(\nu_L - \nu_m)t\}\right]. \tag{1.9}$$

In Equation 1.9, the first term represents the Rayleigh scattering, which is the elastic scattering of an oscillating dipole radiating light with the same incident frequency $\nu_L$ [2, 4]. The other two terms represent the Raman scattering, which is an inelastic light scattering [2,4]. The second term, characterised by the frequency shift $\nu_L + \nu_m$, represents the anti-Stokes scattering, which is blue-shifted with respect from the incident laser beam frequency. The Stokes scattering, represented by the frequency shift $\nu_L - \nu_m$, is the third term in Equation 1.9 and occurs when the scattered radiation is red-shifted from the incident laser beam frequency [2,4]. For a vibration to be Raman-active, the rate of change of the polarisability with the vibration must be different from zero, *i.e.*, $(\partial\alpha/\partial q)_0 \neq 0$ [2–4].

From Bohr's frequency condition, the difference in the energy between two quantised states ($\Delta E$) is proportional to the frequency ($\nu$) and given by

$$\Delta E = h\nu, \tag{1.10}$$

where $h$ is the Planck's constant ($6.63 \times 10^{-34}$ m$^2$kg/s) [2–4].

By combining Equations 1.1, 1.2 and 1.10; and the associated wavenumbers of the laser $\bar{\nu}_L$ and molecule vibration $\bar{\nu}_m$, the energy transition, caused by the Raman effect is given by

$$\Delta E = h\ c\ (\bar{\nu}_L \pm \bar{\nu}_m) \tag{1.11}$$

where $(\bar{\nu}_L \pm \bar{\nu}_m)$ corresponds to the Raman shifts *i.e.*, the Stokes and anti-Stokes scattering.

$\bar{\nu}_m$ is positive in the case of anti-Stokes scattering, negative in the case of Stokes scattering and zero for the Rayleigh scattering [4].

Figure 1.2 is a schematic illustration showing the energy levels and the spectrum generated by the Stokes, anti-Stokes and Rayleigh scattering from a fictitious material. When the electric field from an electromagnetic radiation (laser beam) interacts with a molecule, a photon is momentarily absorbed and the molecule is raised to a virtual energy state. A photon is then scattered when the molecule relaxes and returns to a lower vibrational state [2,4]. The virtual energy state is not a quantum state of the molecule and it is considered as a short-lived distortion of the electron-cloud caused by the oscillating electric field of the incident laser beam [5]. In the Rayleigh scattering the transition takes place from the ground state, with the scattered photon having the same frequency of the incident photon [2, 4]. For the Rayleigh scattering the Raman shift is zero. The two Raman scatterings depend whether the scattered photon has higher or lower energy compared to the incident laser beam photon. Molecules initially at the ground state give rise to Stokes scattering, while molecules initially at a vibrational excited state will give rise to the anti-Stokes scattering [2, 4]. Since both Stokes and anti-Stokes lines represent the same molecular vibrations, Raman spectrometers normally record only one scattering mode.

The intensity of the Raman scattering ($I_R$) depends on the frequency ($\nu_L$) and intensity ($I_L$) of the exciting laser, the number of scattering molecules in a given state ($N$) and on the rate of change of the polarisability of the molecules with the vibration ($\partial\alpha/\partial q$) [4,5]; being, therefore, expressed by

$$I_R \propto \nu_L^4 I_L N \left(\frac{\partial\alpha}{\partial q}\right)^2 . \tag{1.12}$$

The Maxwell-Boltzmann distribution law states that the population ratio between the

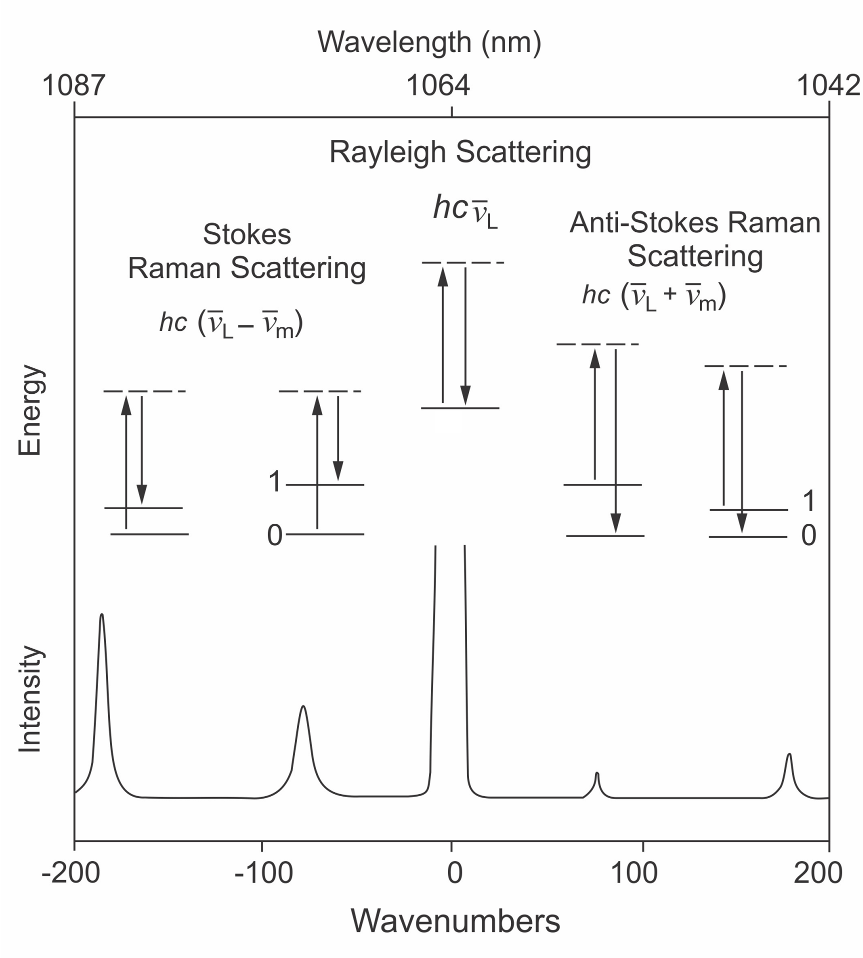

**Figure 1.2:** Example schematic illustration of showing the Raman Stokes and anti-Stokes lines for a fictitious material as per [4], page 16. The dotted lines represent the virtual energy states, while the numbers 0 and 1 represent the ground state and first vibrational excited state, respectively.

first excited state ($P_1$) and ground level ($P_0$) is

$$\frac{P_1}{P_0} = e^{-\Delta E/kT} \tag{1.13}$$

where $\Delta E$ is the energy difference between two quantise states, $k$ is the Boltzmann constant ($1.38 \times 10^{-23}$ J/K) and $T$ is the absolute temperature [2,3,6]. Therefore, at room temperature, there are more molecules at the ground state, the Stokes scattering peaks are stronger than the anti-Stokes peaks [4], as shown in the illustration of Figure 1.2. Thus, an intensity ratio between the Stokes and anti-Stokes scattering can be expressed by

$$\frac{I_R(\nu_L + \nu_m)}{I_R(\nu_L - \nu_m)} = \frac{(\nu_L + \nu_m)^4}{(\nu_L - \nu_m)^4} e^{-h\nu_m/kT}, \tag{1.14}$$

where $\nu_L$ is the incident laser frequency, $\nu_m$ is the molecular vibrational frequency, $k$ is the Boltzmann constant and $T$ the absolute temperature [3,6].

Although Raman and infrared are vibrational spectroscopies, the way light interacts with the molecule is different. In infrared spectroscopy, when the frequency of the incident radiation matches that of a vibration, a molecule is raised to a vibrational excited state [3]. Thus, a loss in the frequency of the incident radiation is detected. The greatest absorption in infrared is caused by a change in the dipole, and this will be most intense for asymmetric vibrations [2,3]. On the other hand, symmetric vibrations cause the largest change in polarisability; thus, giving rise to intense Raman scattering. This basic selection rule explains why some vibrations are Raman active and infrared inactive and vice-versa.

### 1.1.2 General applications of Raman spectroscopy

Raman spectroscopy is a very versatile technique that can be employed in the analysis of solids, liquids and gases. When carefully applied, it is a non-destructive technique and it has been used in a broad range of applications, from materials sciences to art and archaeology.

Since the discovery of the Raman effect, RS has been mostly used in materials science research and employed in studies of a broad range of materials, such as Kevlar, plastic explosives or even spider silk fibres [7]. A key example use of RS has been for standard characterisation of carbon systems [8, 9]. RS can be used to determine the structure of carbon and then classify it as disordered, amorphous or diamond-like [8, 10–12]. In the case of graphene, RS is well suited to discriminate graphite from graphene due to changes in the shape, position and relative intensity of Raman bands with the number of graphene layers [9]. Another application in materials sciences is in the area of mineralogy, where RS has been used for the identification of minerals and gems [13–15], and gemstone treatments, such as the filling of fissures with oil or epoxy resins for enhancing the gem's clarity [15, 16] or the use of high temperature and high pressure treatments to alter the colour of diamonds [16, 17].

RS has also been used in forensic sciences, applied in the identification of pigments and dyes in inks and paints [18], identification of drugs [19] and in the analyses of evidence consisting in blood, body fluid [20] or transferred fibres [21]. Lately, there has been an increasing use of RS in biology, pharmaceutical and medical sciences due to its molecular-scale fingerprinting capacity. Examples are the study of biochemical changes during malaria infection [22], identification of pathogens of urinary tract infection [23] and the investigation of drug delivery systems [24]. RS is also foreseen as a potential diagnostic tool for cancer due to its sensitivity to structures of biological molecules and ability in discriminating cancerous from non-cancerous tissues [25–28].

In art, RS has been used in the identification of the binding media, varnishes and natural and synthetic pigments used in paintings [29, 30], as well as in the deterioration assessment of stained-glass windows from the thirteenth century [31]. In archaeology, the compositional characterisation of ceramics and potteries, and the materials used in their decoration, has been done with the use of RS [32–36]. RS has also been used for characterising archaeological and fossilised osseous materials, such as ivories, teeth and bone [37–39]. Diagenetic alteration in bones can be assessed with RS by changes in the position and full width half maximum (FWHM) of the phosphate peak present in the hydroxyapatite spectrum [39–41]. RS has been also applied to archaeological and fossilised shells; such an example is the identification of the biogenic carbonates from different shell taxa used on Early Bronze Age beads [42]. A deeper review of the applications of RS on biogenic calcium carbonates and for diagenesis assessment is presented in Subsections 1.2.2 and 1.3.1.

## 1.2 Sea shells

### 1.2.1 Shell structure

In the animal kingdom, molluscs are the second largest phylum, with representatives distributed across all habitable continents and found on land, in fresh water and in the sea [43, 44]. Examples of the phylum are squids, octopi, slugs and snails [43]. Within the molluscan phylum, the largest class is the gastropoda, followed by clams, also known as bivalvia [43].

There are more than 100,000 living molluscs species that secrete a shell [45], which is a calcium carbonate exoskeleton that keeps the animal safe from predators [46]. Figure 1.3 identifies the main parts of a gastropod shell, characterised by a spiral growth pattern ending in the aperture. The adult size of a gastropod varies with species, ranging from 1 mm to 1 m [43].

The shell is comprised of a mineral phase made of calcium carbonate, accounting for 95 to 99% of the its weight with the remaining being an organic matrix composed of

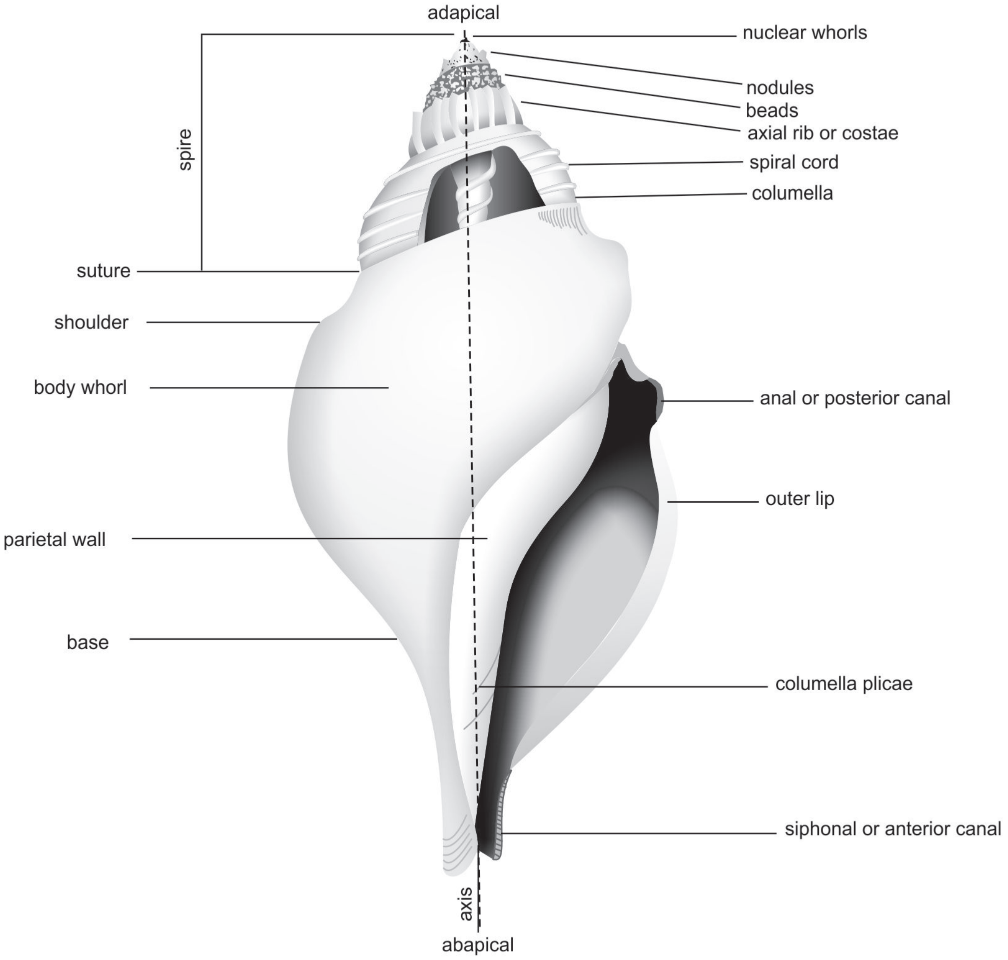

**Figure 1.3:** Terms and shapes of a gastropod shell as per Claassen [46].

glycoproteins [45,47]. Within the polymorphs of calcium carbonate, aragonite and calcite are commonly found in marine shells [43,48], whereas vaterite, is common in fresh water molluscs [49]. Additionally, amorphous calcium carbonate has been observed in several pearls and mussels [50].

The process of biomineralisation is a complex phenomenon involving an organic matrix and an isolated compartment from the external environment – the extrapallial space [45, 48,51]. This space exists between the periostracum and the epithelial cells of the mantle, which is the organ directly responsible for the shell formation [48]. The organic matrix is a framework built by the organism where ions are introduced and induced to crystallise and grow [51, 52]. The major components of the organic matrix are the polysaccharide $\beta$-chitin, silk protein and glycoproteins, rich in aspartic acid [48,52,53]. Biomineralisation is often studied in respect to the shell nacre, which is comprised of thick aragonite layers, separated by interlamellar layers of organic matrix [45, 48, 52].

The mineralisation process has originally been considered as a spontaneous process where biogenic crystals would be formed by the crystallisation of a supersaturated fluid [45, 46]. This fluid, also referred to as the extrapallial fluid, is saturated in carbonate ions extracted from sea water [45]. The specialised cells of the mantle would secrete the calcifying matrix, which interacts with the mineral ions and, together, self-assemble to generate crystallites exhibiting well defined morphologies [45, 48]. However, this spontaneous process does not explain how the self-assemblage is controlled.

Addadi *et al.* (2006) discuss that the organic matrix controls the biomineralisation, with the acidic proteins acting as sites of crystal nucleation and with the chitin and silk protein compartments dictating the crystal orientation [48]. They propose that an amorphous calcium carbonate phase forms in vesicles within specialised cells of the mantle. These vesicles are delivered into the mineralisation sites where the aragonite crystals are then nucleated and later propagated, through mineral bridges or holes in the organic matrix [48]. Some of the macromolecules may be incorporated within the mineral phase during its formation [48]. Jacob *et al.* (2008) have shown that in bivalves the crystallisation and orientation of the carbonate crystals started before the full completion of the interlamellar organic matrix sheets [52].

*In vitro* studies have shown that aspartic acid-rich macromolecules actively induce the polymorph nucleation, controlling the size, shape and organisation of the crystallites [54]. Although the regulation of aragonite and calcite polymorphs is strongly related to the species this biomineral control can be influenced by the water temperature of the animal's environment [46] and by the presence of extraneous ions, such as magnesium [55, 56].

Shells are composed by layers forming their microstructure; these layers can be resolved through scanning electron microscopy (SEM) and vary in thickness, number and in the way they are combined [46]. Due to the diversity of shell species and the combinations of microstructural patterns, there is a variety in the nomenclature used to describe the shell layers [47]. In a general and simplified way, as reviewed by de Paula and Silveira (2009), shells are usually described as containing the following three microstructures: an external prismatic layer, made either of calcite or aragonite; a middle crossed-lamellar layer, containing obliquely crossed crystals; and an innermost layer known as the aragonitic nacre [53]. Other arrangements such as the homogenous structure formed of layers of fine aragonitic or calcitic particles with less than 5 $\mu$m in diameter, or the presence spherulitic structures are also observed in bivalves and gastropodes [53]. In addition, some shells also have an external organic and impervious layer called *periostracum* [43, 46]; however, this is rarely found in archaeological shells [46]. Crossed-lamellar layers are most widespread in grastropoda and bivalvia [53, 57].

### 1.2.2 Calcium carbonate allotropes

Aragonite and calcite, the most common biominerals produced by molluscs, are calcium carbonate crystals that share the same chemical composition with different atomic arrangements, thus having distinct crystal geometries. A crystal is the repetition of unit cells defined by the length of its axes (a, b and c) and their angles ($\alpha$, $\beta$ and $\gamma$) [58], as shown in Figure 1.4. According with these properties, seven crystal systems are allowed [58]. Aragonite belongs to the orthorhombic system [59–62] and calcite to the trigonal system [63–65], as illustrated in Figure 1.4. The trigonal structure of calcite can also be described as hexagonal by the combination of three trigonal unit cells (Figure 1.4). The aragonite orthorhombic symmetry is transformed into triclinic (Figure 1.4) due to deformation caused by impurity atoms, such as Sr or Fe, or point defects [66, 67]. The Sr ions are known to substitute Ca without a change in the crystal structure; however, the inclusion of Fe ions causes a significant lattice distortion in the $CaCO_3$ unit cell because of the great difference in ionic radii [67]. For geological aragonite, as long as the concentration of impurities is lower than 0.06 at%, the aragonite has the orthorhombic symmetry [67].

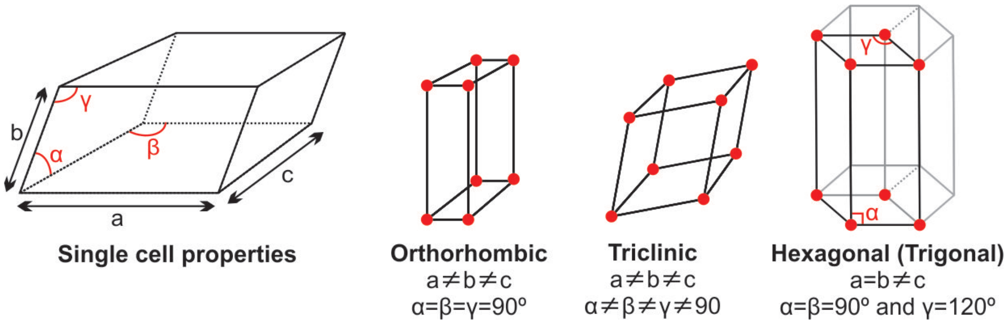

**Figure 1.4:** Properties of the single unit cell. A unit cell is defined by the length (a, b and c) and angles of the axes ($\alpha$, $\beta$ and $\gamma$). The orthorhombic, triclinic and trigonal are three of the seven possible crystal systems according to different single unit cell properties. Aragonite has orthorhombic symmetry; however, it can be transformed into triclinic due to deformations caused by impurity atoms. Calcite belongs to the trigonal system and can also be described as hexagonal by the combination of three trigonal unit cells.

In synthetic carbonates, impurities not only affect the crystal symmetry, but also influence the crystal growth rate during crystallisation, inhibit phase formation and crystallinity [68]. The trigonal structure of calcite allows the presence of divalent cations as Mn, Mg, Fe, Zn, Co and Ni, while aragonite may have larger cations, such as Sr, Pb and Ba [69]. In general, due to their atomic radii, Ca is replaced by Mg in calcites and by Sr in aragonites [70]. High concentrations of S have also been found in calcitic shells with the use of energy dispersive X-Ray spectroscopy (EDX) technique combined with SEM; however, S is not found interstitially or substituting Ca, being its major source from amino acids and polysaccharides [71]. In the case of biogenic carbonates, the shell species, mollusc body part, sea temperature and salinity, geological environment, calcite-to-aragonite ratio, diagenesis process and the effect of time are factors that influence the presence of impurity atoms, thus affecting the elemental composition of these carbonates [70, 72].

Although aragonite belongs to the orthorhombic system and calcite to the trigonal, the crystalline structure of both polymorphs alternates layers of calcium and carbonate ions (Figure 1.5) [62, 65, 66]. The length of the unit cell axes of aragonite and calcite have been determined by X-ray diffraction measurements (XRD), resulting in a = 4.962 Å, b = 7.969 Å and c = 5.743 Å for geological aragonite [67] and in a = 4.989 Å and c = 17.064 Å for geological calcite [63, 64].

When compared to geological and synthetic carbonates, biogenic aragonite and calcite show anisotropic structural lattice distortions, which are correlated to the presence of the organic macromolecules that support the strained mineral lattice [73–76]. In aragonite these lattice distortions were positive for the a- and c-axes, while negative for the b-axis [73]. Systematically larger a and c unit cell parameters were also found for biogenic calcite when compared to non-biogenic [74]. Therefore, it can be said that biogenic carbonates are less crystalline than the geological or synthetic samples.

Annealing studies conducted on biogenic calcium carbonates have shown that such distortion is reduced with heating; consequently, the lattice parameters are reverted to those of geological samples, which results in an increase of the biogenic samples' crystallinity [73, 74, 76, 77]. The relaxation of the mineral lattice is explained by the degradation of the organic macromolecules that were incorporated within the mineral crystals during the biomineralisation process [73, 74, 76, 77]. For aragonite, an annealing of 30 min at temperatures ranging from 50 to 350°C can relieve such lattice distortions, retrieving geological lattice parameters without triggering a conversion to calcite [73]. Similar lattice

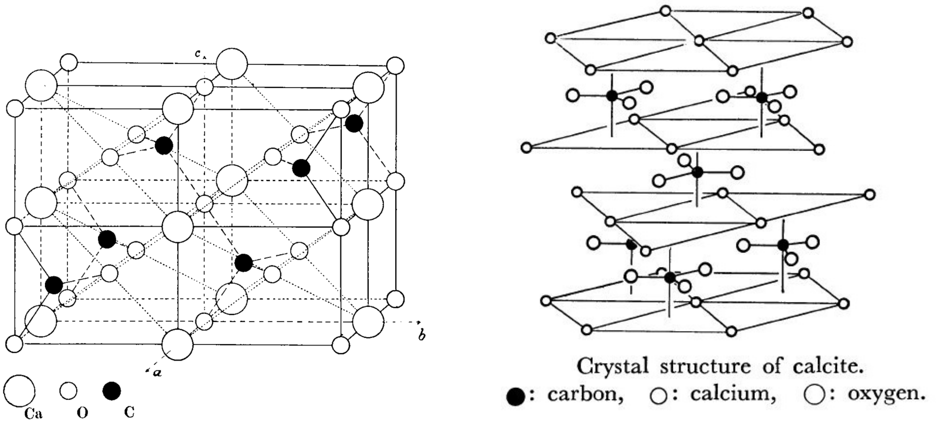

(a) (b)

**Figure 1.5:** Calcium carbonate structures. a) Crystalline structure of aragonite showing its orthorhombic configuration, as per [62] and b) the trigonal crystalline structure of calcite, as per [65].

relaxation has also been observed for calcites under heat-treatments over 200°C [74]. An increase in the crystallinity of biogenic calcium carbonates is also observed during the recrystallisation of biogenic aragonite to calcite, or through the dissolution of disordered phases of calcite [78, 79].

Calcite is the most thermodynamic stable phase of calcium carbonate at ambient temperature and pressure, followed by aragonite, vaterite and amorphous calcium carbonate [49, 50, 80–82]. Experiments for determining the calcite-aragonite equilibrium at temperature and pressure have shown that pure synthetic aragonite is unstable relative to calcite at a temperature of 25°C and one bar, which is stabilised by the presence of trace elements; however, aragonite is more stable for increasing pressures at constant temperature [81]. XRD studies on the aragonite-calcite transformation in fossil snail shells have shown that on Earth-surface conditions, pressure is not a factor influencing this conversion and that temperature influences the transition only in a long time scale, with the presence of trace Mg inhibiting such conversion [83].

Biogenic calcium carbonates are less thermally stable than geological or synthetic carbonates, as demonstrated by the lower aragonite to calcite phase transition temperature of biogenic aragonite [84]. In geological and synthetic aragonite the aragonite-calcite phase transition occurs at temperatures ranging from 450°C to 480°C [84–87]. For biogenic aragonite the transition temperature depends on the species, ranging from 280°C [84, 86] to 400°C [88]. However, a broad range for the conversion temperature may also be observed within the same species *e.g.*, for the *Pinctada maxima* oyster the transition temperature ranges from 300°C to 400°C [88]. In shells, the aragonite-calcite transition has been observed, for example, from 330°C to 350°C for the *Saxidomus purpuratus, Hyriopsis schlegeli, Corbicula japonica, Pinctada martensii* species [84]. At much higher temperatures occurs the transition of calcite to calcium oxide (CaO), which starts at ∼700°C in biogenic calcites, with a complete decarbonation at ∼800°C [84, 89]. Complete decarbonation of geological calcite was measured at ∼815°C, which was indicated by the release of $CO_2$ and a strong weight loss in differential thermal analysis (DTA) and thermogravimetric (TG) analysis [90].

The similar crystal structures of aragonite and calcite results into similar Raman spectroscopy signatures. As discussed in Section 1.1, the Raman spectra depends on the vibrational energy and polarisability of the molecules, and in the case of aragonite and calcite it will mainly depend on the vibrational modes of the carbonates. Figure 1.6 illustrates the Raman active modes of vibration for the carbonate ions, with their occurring Raman band ranges, in wavenumbers, as per Bischoff *et al.* (1985) [91].

For calcite, five fundamental vibration modes are active, of which two are lattice modes and three are internal modes [92,93]. The vibrations observed with RS for the lattice mode are the translational ($L_1$) and rotational ($L_2$) modes (Figure 1.6). The rotational mode is also commonly referred to as librational mode [91, 93, 94]. As per the internal modes, the three observed vibrations are the symmetric ($\nu_1$) and antisymmetric ($\nu_3$) stretches, and

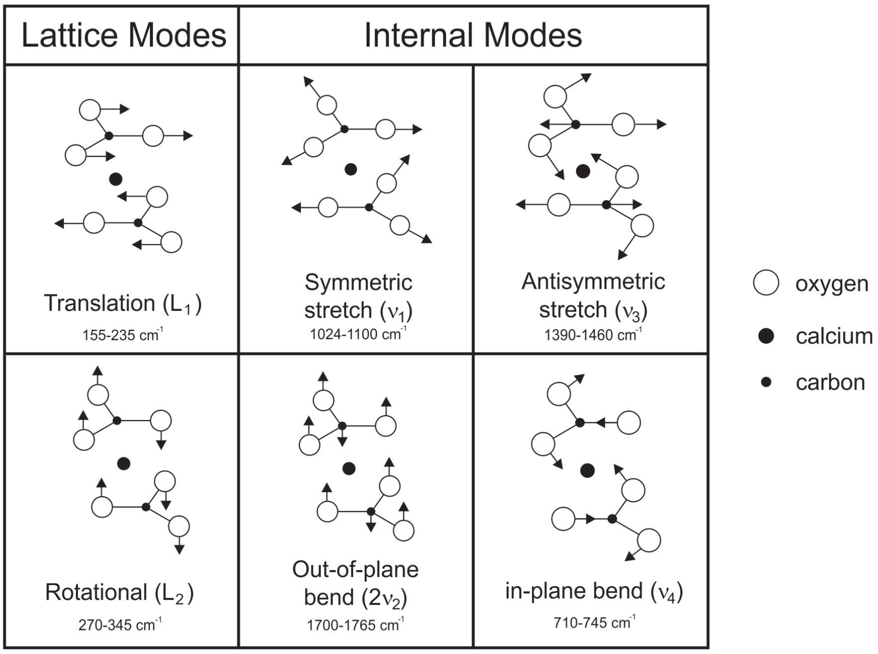

**Figure 1.6:** Raman vibrational modes for carbonate ions, with their Raman band ranges, in wavenumbers, as per [91].

the in-plane ($\nu_4$) bend (Figure 1.6). An overtone of the $2\nu_2$ infra-red active mode is also allowed in the Raman spectra of calcite [91, 92]. For aragonite, 30 fundamental vibration modes are expected to be active [65, 92]; however, Urmos *et al.* (1991) only observed 14 of them, attributing the difference mainly to the low intensity of such peaks [92]. The aragonite allowed vibrations that can be easily observed with RS, due to their intensities, are the translational ($L_1$) and rotational ($L_2$) lattice vibrations; the in-plane bend ($\nu_4$), which is characterised by a doublet peak; and the symmetric stretch ($\nu_1$) (Figure 1.6) [92]. Table 1.1 summarises the peak assignments and peak position range found in literature for the major peaks observed in the Raman spectra of biogenic aragonite and calcite from gastropods [94–97], bivalves [52, 96–98], corals [91, 92, 99] and pearls [92].

**Table 1.1:** Literature peak assignments for biogenic aragonite and calcite gastropods, bivalves, corals and pearls. The range is defined by the smallest and highest values found for the peak positions in the provided references.

| Polymorph | Code | Peak range ($cm^{-1}$) | Assignment | References |
|---|---|---|---|---|
| Aragonite | $L_1$ | 125–154 | Translational lattice mode | [92, 94–99] |
| | $L_2$ | 203–208 | Rotational (librational) lattice mode | [92, 94–99] |
| | $\nu_4$ | 700–705<br>704–711 | In plane antisymmetric bend | [52, 92, 95–99]<br>[92, 94–98] |
| | $\nu_1$ | 1080–1086 | Symmetric stretch | [52, 92, 94–99] |
| Calcite | $L_1$ | 145–159 | Translational lattice mode | [91, 92, 94, 96, 97, 99] |
| | $L_2$ | 270–285 | Rotational (librational) lattice mode | [91, 92, 94, 96, 97, 99] |
| | $\nu_4$ | 710–716 | In plane antisymmetric bend | [91, 92, 94, 96, 97, 99] |
| | $\nu_1$ | 1084–1089 | Symmetric stretch | [91, 92, 94, 97, 99] |
| | $\nu_3$ | 1434–1527 | Anti-symmetric stretch | [91, 92] |
| | $2\nu_2$ | 1750 | Out of plane bend - overtone | [91, 92] |

RS is commonly used to characterise the mineral composition of shells due to its sensitivity for distinguishing the calcium carbonate phase polymorphs and amorphous calcium carbonate (ACC) [50, 52, 95–98, 100]. One example is the use of RS to show that the periostracum-prismatic layer interface in bivalve shells is analogous to the interface between innermost organic lamella and the prismatic layer in pearls. This was achieved due to the presence of amorphous calcium carbonate in both interfaces, which was revealed by spectra comparison and investigation of the peak position of the $\nu_1$ band at ~1085 cm$^{-1}$ [98].

RS has been used to investigate the process of biomineralisation in pearls, corals and bivalves. Jacob *et al.* (2008) noted that laser irradiation could induce the unstable ACC to crystallise into aragonite in bivalve shells, and into vaterite in pearls [52]. This showed that the granular structures directly at the growth front are not crystallised and that crystallisation and orientation of the $CaCO_3$ nano-crystals started, in bivalves, before the interlamellar organic sheets were formed [52]. Although their conclusions were based in the shape and position of the $\nu_1$ and $\nu_4$ bands, these were drawn from qualitative analyses of the Raman spectra without the use of quantitative measurements of peak positions and FWHM. In corals, skeletogenic and biomineralisation were studied by Clode *et al.* (2011), who noted that coral skeletons had no evidence of calcite or amorphous precursor phases, concluding that skeletons of new coral recruits shared the same aragonitic mineralogy as those of their mature counterparts [99]. Similarly, these conclusions were obtained from a qualitative analyses of the Raman spectra, with peak positions inferred from the spectra without the use of peak fitting procedures.

Composite maps can be constructed with RS and used to identify calcitic and aragonitc layers in shells, and also to map the distribution of pigments. A good use of peak fitting routines allied to spatially resolved RS performed on the gastropod shell *Nerita undata* identified calcite and two different crystallographic orientations of aragonite by mapping the area of two lattice peaks: the translational mode at $\sim$152 cm$^{-1}$ and the librational mode at $\sim$206 cm$^{-1}$ [94]. Nehrke and Nouet (2006) used these data to describe shell deposition [94]; however, in their work, these changes in orientation were only visually and qualitatively compared.

Fluorescence intensity distribution maps of the organic components have also been used to verify the ability of RS to identify growth patterns in bivalves [101]. Shell growth increments observed with RS were identical to those obtained by established Mutvei staining and fluorescence microscopy methods [101]. Advantages of RS over these methods include the fact that it requires no sample pre-treatment and it allows high spatial resolution to the order of several hundred nanometers.

Heating causes a thermal crystal expansion, which has been observed with XRD in calcites heated from the room temperature up to 900°C [102]. For geological calcite and aragonite, when analysed with RS, this change in the crystal volume, and therefore in the bond length, caused by the heating, reflects in broadening of peaks and shifts in their positions [87,103]. Both lattice mode and internal mode peaks are temperature dependent; however, RS applied to geological aragonite has shown that the lattice modes are more sensitive to increasing temperature, reflecting the progressive rotational disordering that precedes the aragonite-calcite phase transition [87]. RS evaluation of the influence of increasing pressures from the room pressure up to 30 GPa, at ambient temperature, show no pressure-induced aragonite-calcite transition; however, shifts in the peak positions of the $2\nu_2$ Raman mode of calcite and in the $\nu_4$ modes of aragonite were observed with the increasing pressures and explained by the incompressibility of the $CO_3$ groups and by structural changes upon high-pressure compression [87].

Parker *et al.* (2010) used RS to characterise the aragonite-calcite phase transition in bio- and synthetic carbonates during heating [104]. The biogenic aragonite used in their experiments was extracted from the nacre of mussel shells (*Mytilus edulis*). They estimated the relative concentration of the carbonate polymorphs using a method described by Edwards *et al.* (2005), which consists in comparing the peak intensities of the $L_2$ lattice mode of aragonite at $\sim$205 cm$^{-1}$ and calcite at $\sim$280 cm$^{-1}$ [105]. Edwards *et al.* noted that both peaks have similar intensity in a sample comprising of 50% calcite and 50% aragonite, thus concluding that the intensity of both peaks could be used to estimate these polymorphs proportions. Although Parker *et al.* estimated the relative polymorphs proportions during heat-treaments, this was only performed for the synthetic samples and no further investigation of the peak positions and widths with RS was done. The bio-carbonates were studied only at room temperature and after being annealed at 550 °C for 12h, for which the aragonite and calcite spectra were respectively obtained. For the synthetic samples, heat-treated for 1h at 390 °C, 400 °C, 410 °C and 550 °C, they showed that during the phase transition the intermediate Raman spectra displayed distinct features for the aragonite and calcite, confirming that the two polymorphs existed as distinct phases in the same sample [104].

The above examples described the broad range of applications of RS on biogenic carbonates, from studies of the biomineralisation to investigations of the phase transition during heat-treatments. Due to its sensitivity RS can be used not only to determine and map the mineral structure of shells but also to estimate their relative proportions in samples. However, to maximise the RS applications, it is necessary that quantitative rather than qualitative analyses are performed. The next sections describe the research in shell middens and the analytical methods applied to it. They also address the factors affecting these methods and how RS could be used in that context.

## 1.3 Shell Middens

Shell middens are important archaeological records pertaining to human activity. In general the term *midden* is used to indicate the accumulation of shells as result of food being discarded [44, 106]. Studies on shell middens started around the 1850s when the human origin and age of mounds of mussels and oyster shells in Denmark were questioned. The Danish scientist J. J. A. Worsaae pioneered studies investigating them, and the discovery of artefacts within the shells led to these accumulations being called as *kitchen middens* [44, 106]. However, although shell middens can contain animal bones, pottery, stone artefacts, plant remains and human remains in the immense quantity of sea shells [106,107], they can be associated to a diverse range of past human activities [44]. Many large mounds were either deliberately constructed or natural accumulations of shells were augmented by a subsequent human occupation [44]. Some of the Brazilian *Sambaquis* (from the Tupi word literally meaning mound of shells) reached up to 70 metres in height and 500 metres in length [108]. The Brazilian shell middens were used not only for discarding shells but also for ritual purposes, with artefacts, food offerings and heaths being identified within the shell mound [108]. Therefore, the neutral term 'shell matrix site' is also currently in use [44], and further, due to their use for different human activities, shell middens are not directly analogous to fossil or sub-fossil deposits [109].

The identification of different sites have shown how unique a shell midden can be. They are scattered around the world, with mounds identified in the Atlantic Europe, Arabian and Red Seas, Channel Islands of California, Florida, Georgia, Argentina, Brazil and in the tropical island Asia-Pacific region [44, 107, 110]. Shell middens can be found close to coastal zones, lacustrine and river environments due to the significant importance of aquatic environments and their resources for hunter-gathering groups [106, 107]. Shell middens vary in size, composition, age and accumulation period, with middens spanning the past 200ka [106, 107, 111].

Due to the calcium carbonate present in shells, shell middens are characterised by alkaline conditions, thus making up an environment favourable to the preservation of organic and plant remains that provide records to study the interaction between humans and the environment [106, 109]. Shell middens provide means of studying aquatic resource exploitation and human dispersion [112–114], social complexity and group diversification [106–108, 115], and palaeoenvironment reconstructions [95, 109, 116, 117]. Research on shell middens has opposed the convention that hunter-gatherers formed small and stable societies. Conversely, it has shown that the littoral food resources could support large population densities, which reduced their mobility, favouring the development of complex hunter-gatherer societies [106]. Examples of these are the studies on Brazilian shell middens [108] and on the shell middens of the Pacific Coast of North America [118].

Analytical approaches applied to archaeological sites contribute towards enhancing the ability to reconstruct the human past [119]. The methodologies and protocols often used are radiocarbon and amino acid racemization dating, isotopic analyses and sclerochronology and sclerochemistry analyses [44, 119]. An example of the use of analytical techniques is the determination of the age of shell mounds for estimating the accumulation rate of shells. Hausmann and Meredith-Willians (2016), using radiocarbon dating and oxygen isotope analyses, estimated that approximately 400 shells per day were accumulated in the JW1727 shell midden of the Farasan Islands over a seven-month period [120].

The complex task of determining the age of a shell midden can be achieved by radiocarbon dating or amino acid racemization. However, both techniques have problems and limitations. Radiocarbon dating cannot be used for dating periods longer than $\sim$45,000 years [121]. Diagenetic process affect radiocarbon dating due to the carbon exchange with enclosing deposits or ground waters, which usually happens when biogenic aragonite recrystallises into calcite [44]. Thus, it is important to identify these recrystallised shells. The amino acid racemization dating is also limited by the environment conditions, specifically high temperatures, which affect the rate of change of the L-form amino acids into D-form after the mollusc death [44]. The use of intracrystalline amino acids, which behave as closed systems avoids this issue [122, 123]; however, as Demarchi *et al.* (2015) showed for the bivalve *Glycymeris*, such closed systems are not present in all molluscs [124]. In summary, both techniques are affected by diagenetic alterations, thus the importance of assessing the samples towards such modifications.

Indications of sea-temperature changes can be found within the mineralogy of some marine invertebrates. Isotopic analyses are used for palaeoclimatic and environmental studies, being the stable carbon ($\delta^{13}$C) and oxygen ($\delta^{18}$O) the most often used isotopes [109] The oxygen isotope ratio ($^{18}$O/$^{16}$O) at the sea surface is function of temperature [125, 126]. Molluscs secrete calcium carbonate out of the isotopic equilibrium with the ambient water [96], resulting in a difference that is strictly a function of the temperature [127]. Thus, isotopic ratios can be calibrated and linked with the temperature of the water when the shell was made [96, 127]. In a similar way, the carbon isotope ratio ($^{13}C/^{12}C$) can be linked with other variables including salinity of the water, amount of dissolved inorganic carbon and physiological processes [128, 129].

Sclerochronology studies the physical organisation of the accretionary hard tissues of organisms, such as shells, while sclerochemistry applies isotope or elemental analyses to these sclerochronological growth patterns [44]. Shells grow at the outer lip by expanding it and keeping its overall shape the same. This process is not constant and temporarily ceases marking the presence of growth lines that represent the previous positions of the aperture rim [43]. These growth increments record the environmental conditions experienced by the mollusc during its life [44]. For example, when a mollusc is harvested it stops growing and the $\delta^{18}O$ signature of the final shell increment give an approximated period of the year for its death [130], thus indicating seasonality and reconstructing subsistence strategies and foraging habits [109].

Apart from determining the time of shell harvest, oxygen and carbon isotopes can also be used to identify shell source areas, investigate mammalian diets, as well as for palaeoenvironmental reconstructions [46, 117, 131]. Isotopic analyses coupled to sclerochronology were applied to the bivalve *Anomalocardia flexuosa* obtained from Holocene shell mounds to reconstruct the lagoonal environment of the shell species showing that it was marked by lower salinity variations, in comparison to present day [116]. Hausmann *et al.* (2017), using both sclerochronology and oxygen isotopic analyses, tested the *Conomurex fasciatus* shell, which is the most common mollusc in the shell middens of the Farasan Islands, as an environmental proxy for the Red Sea, demonstrating their suitability for palaeoclimate reconstructions [95].

Factors affecting the isotopic analyses can be extrinsic, such as the environment, temperature and carbonate source; or intrinsic, which are often associated with the animal physiology [44]. Post-depositional changes caused by leaching and groundwater fluctuations within archaeological sites compromise the isotopic analyses due to alterations in the shell mineralogy [130]. Diagenesis is among the extrinsic factors affecting the analytical methodologies and approaches used for reconstructing human past. In order to maximise the reliability of archaeological interpretations, diagenesis has to be taken into account and the integrity of the shells has to be assessed. Archaeological specimens should be investigated not only to inform about the past, but also to provide information on what happened to them after being accumulated. The next subsection focuses on how diagenesis affects shells and the methods used so far to assess their integrity.

### 1.3.1 Diagenesis of shells

Taphonomy encompasses the processes an organism has been subjected from its death until its recovery [132]. Diagenesis is the final part of the taphonomy process and refers to any modification of the organism, or its parts, with the surrounding sediment, ending up in complete disintegration and dissolution of the organism or its lithification [132]. In shells, diagenesis is used to explain any modification suffered by the biomineral after its deposition [133], such as fragmentation, abrasion, encrustation, perforation, heating, dissolution and chemical conversion [46].

From the above modifications, the dissolution, chemical conversion and heating hamper the accuracy of analytical methods due to alterations in the shell mineralogy, and thus compromise environmental, climatic and dietary reconstructions [109, 133–135]. During dissolution, the shell initially loses its colouration and lustre then, as dissolution progresses, it becomes thinner, particularly at the edges [46]. The rate at which calcium carbonate is dissolved in a terrestrial setting depends on the acidity of the ground water and the duration of exposure to acids, which among others are carbonic acid, calcium bicarbonate, ammonium nitrate, sulphuric acid and nitric acid [46].

The chemical conversion is related to the spontaneous inversion of the unstable aragonite to calcite, this happens even at temperatures at or below 30 °C [46]. Apart from this recrystallisation process, the stability of biominerals is also increased through dissolution of the unstable aragonite phase or by the growth of new authigenic phases [79].

Heating can lead to an aragonite to calcite transition, thus removing the heavy $O^{18}$ atoms by the lighter $O^{16}$ from the atmosphere [136]. Shells that have undergone heating, independently if the purpose was of cooking or of altering the colour of the shell for ornaments, have their mineralogy altered, and in extreme conditions, recrystallise into calcite [46, 134, 136, 137]. However, as demonstrated by Milano *et al.* (2016) the isotopic ratios may change with heating even without the conversion of aragonite into calcite [134]. Therefore, the preservation and integrity of the biomineral in the samples has to be assessed and measured.

One approach to investigate diagenesis of biocarbonates is through the analysis of minor elements. This is done by comparing the atom percentage of Mg and Sr relative to Ca between ancient and modern shells, by using analytical methods such as atomic absorption spectroscopy or EDX. Atom substitution of Ca by Mg in the case of calcite, or Sr if aragonite, can occur in shells during diagenetic alterations [70, 138, 139]. Thus, the Mg/Ca or the Sr/Ca concentration ratios can be used as an indication of diagenesis. Ragland *et al.* (1979) studied the contents of Mg, Sr, Mn, Fe, Na and K, with atomic absorption spectroscopy, in 230 unrecrystallised mollusc shells, comprising bivalves and gastropods, ranging from late Cretaceous to Holocene [139]. They noted consistent differences between fossil and Holocene shells with respect to concentrations of all of these elements, attributing these changes to diagenetic alterations. However, due to the variation of these minor elements with many factors, such as the shell species, water chemistry and mineralogy [70], there is no consensus on how these ratios should change.

Another approach on assessing diagenesis of biocarbonates is by the analysis of the shell's mineralogy and the conversion of the original biogenic aragonite into calcite by XRD, electron microscopy and spectroscopic methods [46, 70, 133, 138, 140]. Bjorn and Weiner (1981) used SEM and XRD to investigate the integrity of nacre aragonite from ammonite samples that were considered preserved, moderately preserved or poorly preserved by visual inspection [138]. By investigating the mineralogy of these samples they noted that visual inspections did not correlate well with the percentage of calcite found in the samples by XRD; for example, the poorly preserved samples were expected to be fully converted into calcite, however, their results showed a concentration of only 2% of calcite in their composition. By doing elemental analysis they also noted an increase in the Mg concentration in the diagenetically altered samples; thus, proposing that both calcite/aragonite ratios and Mg concentration were the most sensitive parameters to post-depositional modifications [138].

Changes induced by diagenesis in the microstructure, nanostructure and chemical composition of fossil and modern *Concholepas* shells were investigate by Guzman *et al.* (2009) [133]. This shell species is formed by layers of calcite and aragonite, for which atomic force microscopy (AFM) and SEM investigations revealed alterations in the structure of the aragonitic layer [133]. In their work, elemental investigations through EDX were also conducted showing that the fossil shells were enriched with S and K at different levels, which could reflect either differences on their biogenic composition or in their fossilisation process.

It is important to highlight, however, that a proxy to assess diagenesis based on the presence of calcite can only be applied to shells that are composed of aragonite. In the case of calcitic samples their preservation is be assessed by analyses of its crystallography and crystallinity. Calcitic fossil craniid brachiopods analysed with SEM and with electron backscattered diffraction have shown different conservations for the calcite crystallography of samples from the Late Ordovician and Late Cretaceous [141]. These analyses showed that diagenesis was independent of geological time, with the Late Ordovician samples being more preserved.

A pitfall of electron microscopy based methods is that they often require the coating of the sample, and therefore cannot be considered non-destructive techniques, thus revealing the relevance of spectroscopic methods. The analyses of the calcite in foraminifera with Fourrier transformed infrared spectroscopy (FTIR) revealed that an increase in the sample crystallinity was caused by the dissolution of small disordered phases of the carbonate due to diagenesis [79]. Since the improvement of lasers and detectors, RS has been widely applied in the analyses of post-depositional modifications. One example is the work of Urmos *et al.* (1991), who used RS to characterise biogenic carbonates from corals and pearls and noted an increase in the peak widths of lattice mode peaks in biogenic calcite when compared to synthetic calcite bands [92]. They concluded that this increase was caused by positional disorder of the carbonate ion from the substitution of $Mg^{2+}$ for $Ca^{2+}$ in calcite, which could affect the biomineral relative stability while undergoing diagenesis. Bischoff *et al.* (1985), investigating synthetic and biogenic calcites, determined that the increase in FWHM of the lattice mode and also $\nu_1$ peaks was correlated with an increasing concentration of Mg [91]. Similar observations were also made for increasing Mg concentrations in synthetic vaterite [49]. However, this correlation has been often used to infer the mineral composition of shells as being either low- or high-magnesian calcite without a careful measurement of the FWHM of such peaks via quantitative analyses and peak fitting procedures [96, 97].

Many of the published works about RS on biogenic carbonates do not clarify the amount of spectra needed for such characterisation and, in general, only a dozen spectra is collected. In a work using RS to investigate the mineralogy of modern *Glycymeris* shells for further comparison with their fossil counterparts, only 11 points were sampled in two cross sections, where five spectra were obtained in each point [124]. However, to produce statistically relevant results, a large sampling is needed due to the heterogeneity of biological samples, as demonstrated by my contribution to Hausmann *et al.* (2017) [95]. In our characterisation of the *Conomurex fasciatus* shell, 760 spectra were randomly obtained in the modern shells and 500 in the archaeological specimens; from the data obtained in the archaeological samples 0.4% showed an admixture of both aragonite and calcite spectra. Therefore, considering that the sampling size of each measurement was ∼1 micron, we concluded that the biogenic aragonite in the samples was well-preserved against diagenesis mechanisms leading to an aragonite-calcite transformation.

Initially, it was understood that because of diagenetic alterations, sugars and proteins could not be preserved in fossil skeletons [140]. Nowadays, it is known that these macromolecules can be preserved intracrystalline in shells, demonstrated by the possibility of using amino acid racemization for sample dating [122,123]. However, diagenesis continues to affect the shell's organic matrix that once destroyed is replaced by inorganic materials [138,140]. Glycoproteins from this organic matrix are hydrolysed during diagenesis, hence initiating an early biogenic aragonite recrystallisation [78]. Therefore, diagenesis can also be confirmed by assessing a shell's organic matrix, as did Guzman *et al.* (2009) in their studies of the *Concholepas* shells using FTIR, revealing that the calcitic shell layer contained more of the organic matrix than the aragonitic layer [133].

RS is also able to identify the vibrations from the organic shell matrix. These are the C-H vibrations situated between 2847 and 2960 $\mathrm{cm}^{-1}$ which have weaker relative intensities in part due to the significant small proportion of the organic matrix in comparison to the total mineral content and also, in part due to the different inherent Raman cross-section of each material [78, 94]. Perrin and Smith (2007) hypothesised that a decrease in the intensity of such peaks could indicate an early diagenesis of the samples, and that this was explained by the hydrolysis of glycoproteins, thus being decomposed in a series of multiple vibrations, hence decreasing the signal of individual Raman bands [78]. Despite that, their results might have been compromised by the presence of amorphous carbon in some of the spectra, which was formed by the deterioration of skeletal organic compounds due to the strong laser beam power at the sample (∼30 – 50 mW) [78].

As explained before, heating affects amino acid racemization and also alters the mineralogy of shells, hampering isotopic analyses. Shells could be exposed to high temperatures accidentally in hearths in the shell middens or with the purpose of cooking, implicating the interpretation of a site containing burnt shell fragments [142]. Another possibility is that heating was used to modify the appearance of shells so they could be used as ornaments. Lange *et al.* (2008) used RS to qualitatively investigate if darkened *Cyclope neritea* archaeological shells had been heated, since they normally show an ivory colouration [137]. Their RS results showed that white shells were mainly composed of aragonite, while black shells had calcite and amorphous carbon bands. They concluded that only reducing conditions would allow for the carbonised material to stain the shells because the amorphous carbon released when organic products are burnt would escape in the form of carbon dioxide if the shells were heated in an open fire place, which forms an oxidising atmosphere.

Milano *et al.* (2016) explored the effects of cooking/heating on isotopic analysis. In their work they used RS to investigate the aragonite-calcite transition during heat treatments ranging from 100 °C to 700 °C for 20 min and 60 min [134]. Their qualitative inspection of the Raman spectra indicated that the transformation started at 300 °C and finished at 500 °C. Thus, although cooking at this temperature range did not drastically change the shell appearance, it altered its mineralogy. They noted that isotopic ratios were compromised even before the full aragonite to calcite conversion [134]. However, their identification of the heating evidence in shells was purely based in the inspection of the Raman spectra for the mineral signatures of aragonite, calcite or a mixture of both phases; added to this is the fact that only two spectra were obtained from the inner and outer shell layers in each time point.

When a shell is heated its colour will not always be altered. Thus, it is necessary to investigate temperature and temporal dependencies of the aragonite-calcite phase transition in order to accurately identify heated shells. The extreme case of the phase transition may not happen if a shell was heated at lower temperatures or for shorter amounts of time, but this may compromise isotopic informations. Since molluscan shells are important for reconstructing past climates and investigating human development, it is essential to recognise the alterations caused by natural and cultural processes. However, not enough attention has been devoted into developing non-destructive approaches for the identification of diagenesis. Nonetheless, when a non-destructive technique is used, such as RS, it is mainly done qualitatively, without quantitative data analyses being applied, which can put at risk the reliability of the archaeological interpretations drawn.

## 1.4 Research objectives and thesis outline

This research, involving interdisciplinary physics and archaeology, focuses on the study of modern, fossil and archaeological shells using quantitative Raman spectroscopy. Since RS can be used as a non-destructive technique, it can be applied even to the most rare artefacts using little or no sample preparation.

The main goal in this research is to unlock hidden time and temperature sensitive information from sea shells. Therefore, the research aims to identify Raman features that can be used in determining and assessing diagenesis, and in the recognition of heated/cooked shells. Many of the published works with RS, as reviewed in the previous section, focus on identifying diagenesis and taphonomic changes purely by investigating the shell's mineralogy with qualitative analyses of the Raman spectra [96, 97, 124, 134]. Thus, the intention of this thesis is to develop means for quantitative analyses of shells using RS, establishing markers correlated to the shell crystallinity and also to the temperature, in order to quantify percentage conversion of aragonite into calcite, and the aragonite to calcite transition point in heated shells. For such intent, the Raman spectra of shells were deeply analysed, with peak fitting results such as peak position, amplitude and width compared across samples.

Modern and archaeological shell specimens of *Conomurex fasciatus* were studied. This small gastropod is the dominant shell species in shell mounds of the Farasan Islands, which form a group of more than one hundred islands with varied sizes, located in the Red Sea (Figure 1.7 a and b) [143]. The Farasan Islands, which were a military area with low population density and lack of modern developments, contain an almost pristine distribution of archaeological material distributed over more than 3000 shell middens, forming the largest concentration of mounds in the Arabian Peninsula [143]. Several different shell species were found during the excavation of the Khur Maadi Bay middens, however, an insignificant quantity when compared with the *Conomurex fasciatus* species [143]. The *Conomurex fasciatus* shells studied in this thesis are from the KM1057 Khur Maadi Bay shell midden (Figure 1.7 c and d), dated with an age range of 5046 − 5515 calibrated years before present (cal BP) [143].

Shell species from other archaeological sites were also studied, a modern specimen of *Nucella lapillus* from Devon - UK, and a fossilised *Nucela* sp. shell from the Easington

Raised Beach site were included in the RS analyses.

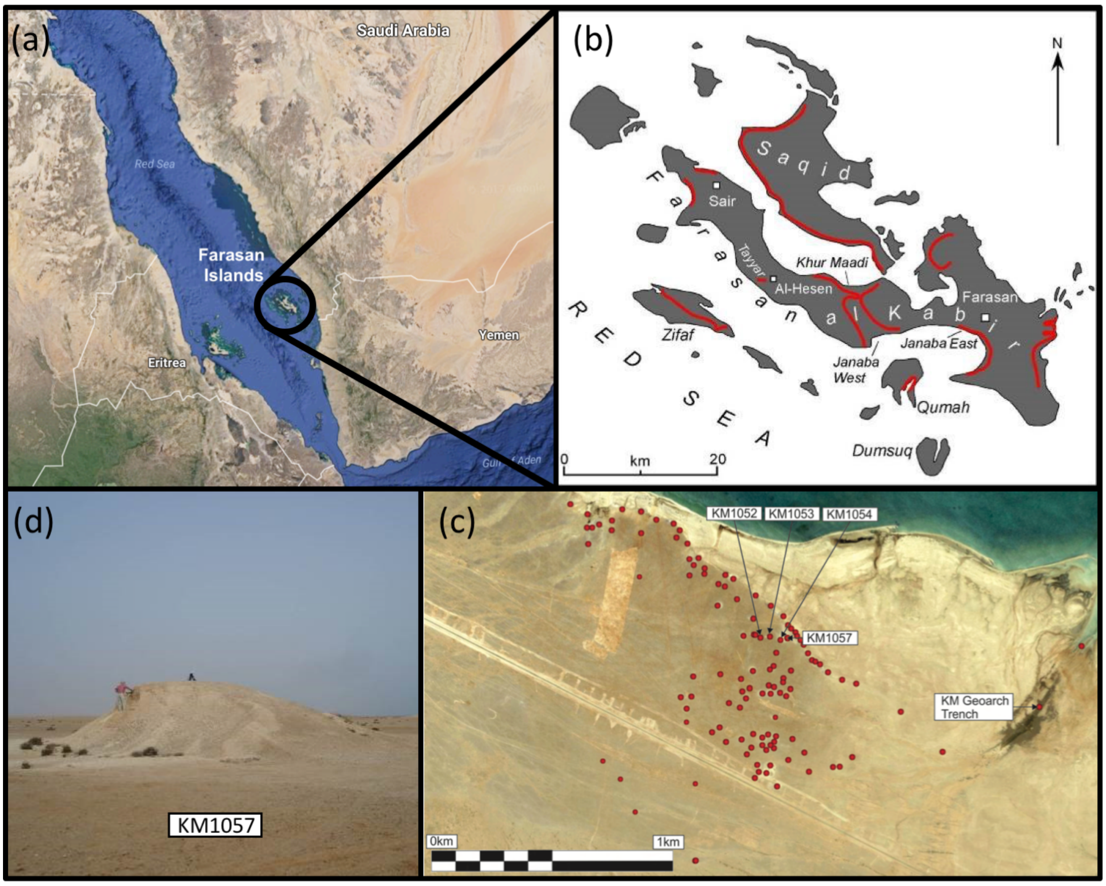

**Figure 1.7:** Maps of the Farasan Islands and Khur Maadi Bay shell middens. (a) Satellite image of the Farasan Islands obtained from Google Earth images. (b) Farasan Islands map; the red lines show the distribution of shell middens across the shoreline. The map was drawn by Prof G. N. Bailey and Dr M. G. M. Williams. (c) Shell middens of the Khur Maadi Bay. The distribution of mounds was superimposed on a Google Earth image by Dr M. G. M. Williams. (d) View of the KM1057 shell midden in the Khur Maadi Bay. Photo by M. G. M. Williams, March 2008.

This thesis has one methods chapter, three results chapters and a final conclusions chapter. Specific details about the samples and how they were prepared and treated under different conditions can be found in Chapter 2, along with details of the analytical techniques used. This methods chapter also describes details about the Raman equipment used and how the data analyses of the Raman spectra were performed with the use of peak fitting procedures. It also explains the development of a convergence test of the standard error used to determine the minimum amount of Raman spectra needed to describe each sample.

In Chapter 3, the biogenic shell carbonates were characterised with RS. The two ancient shell species, *Conomurex fasciatus* and *Nucella* sp., were compared with their modern counterparts aiming to identify Raman markers based on quantitative spectral properties such as relative peak intensities and FWHM that could be used to study the shell mineralogy and in the assessment of the diagenesis process. Additionally, the chapter also shows the results of the *Conomurex fasciatus* shell microstructure and elemental composition obtained with SEM and EDX respectively.

The fourth chapter describes the results obtained after heat treatments performed in powdered modern *Conomurex fasciatus* shells. The samples were thermally treated in many different conditions and quantitative Raman spectral properties such as relative peak intensities and FWHM were compared. A calcium carbonate polymorph percentage was estimated from the Raman spectra and used to determine the aragonite to calcite transition point. In this chapter SEM and EDX analyses were also used to inspect the shell microstructure and elemental composition during heating. Finally, the Raman results of the heated modern *Conomurex fasciatus* shells were compared to burnt fragments of this shell species also found in the KM1057 shell midden. This comparison aimed to validate the results obtained with heat-treatments of the modern shells and also to verify if the method could determine for how long and at which temperature the fragments had been heated.

The fifth results chapter compares archaeological *Conomurex fasciatus* shells collected at different layers of the KM1057 shell midden, which was divided into 12 layers. This experiment aimed to verify if shells from top, middle and bottom layers would have been differently affected by diagenesis. Again, quantitative RS was performed by the analyses of peak intensity ratios and FWHM. Finally, these archaeological shells from different layers were also compared to the modern *Conomurex fasciatus* specimens. The thesis is then concluded with a final conclusions chapter, where future possibilities for this research are explored.

# Chapter 2

# Methods

This chapter describes the methods used for all the experiments performed in this thesis. Specifically it describes the origin of the sea shell specimens, the sample preparation for the experiments, which were done in sliced and powdered shells, and the thermal treatments performed. The chapter also describes details about the Raman equipment and the choice of settings used for data collection. It explains how the quantitative values, such as peak position, intensity and full width at half maximum were obtained from the peak fittings and further analysed.

## 2.1 Samples

This thesis comprises the analysis of sea shells of different ages and from different places in the world. It aims to investigate diagenesis and human intervention on shells using RS. Two shell species were studied, *Conomurex fasciatus* and the *Nucella* sp., which were cleaned and treated in different ways, as described in the next subsections. All samples used in this work are summarised in Table 2.1.

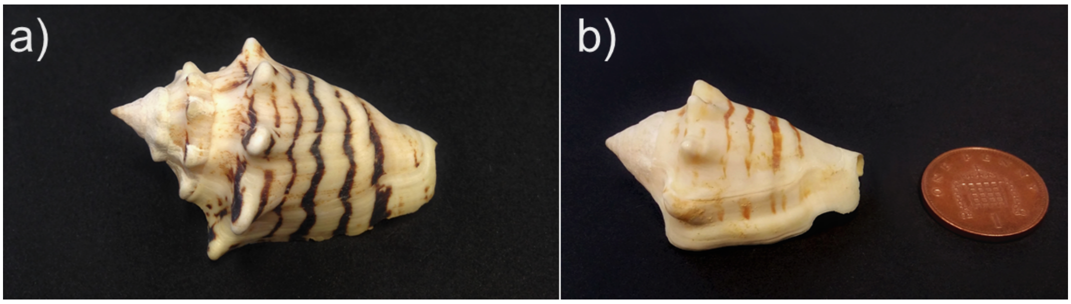

**Figure 2.1:** *Conomurex fasciatus* shells species from the Red Sea. The left image (a) shows a modern specimen while the right image (b) shows an archaeological specimen from KM1057 shell midden, from layer 6.

### 2.1.1 Conomurex fasciatus specimens

*Conomurex fasciatus* is a small gastropod found in the Red Sea [143] and all the specimens provided for this research were collected in the Farasan Islands (Saudi Arabia). Despite being collected in the same area by the same group, the specimens were donated by different collaborators that cleaned their shells in different ways, as described next.

Two pictures of the *Conomurex fasciatus* species can be seen in the Figure 2.1. The left image (Figure 2.1a) shows a modern specimen while the image on the right (Figure 2.1b) is from an archaeological shell. A reference for the size is missing in the picture of the modern specimen, but its length is approximately 4 cm. The length of the archaeological shell is approximately 4.5 cm.

Seven archaeological shells were provided by Prof. Geoffrey Bailey and Dr. Eva Laurie from the Department of Archaeology at University of York. The specimens are from the KM1057 shell midden in the Khur Maadi Bay with a radiocarbon date range of 5046–5515 cal BP [143]. These shells are from different layers in the shell midden, comprising two shells from layer three, three shells from layer six and two shells from layer ten. They were only cleaned by myself using tap water and a soft toothbrush, being dried at room temperature.

One of the three shells collected from layer six (Figure 2.1b) was used in the experiments of Chapter 3, where it was compared to its modern counterpart. The six remaining archaeological shells were used in Chapter 5, where shells from different layers were compared, and their pictures are shown in that chapter.

One modern *Conomurex fasciatus* was provided by Dr. Eva Laurie. This specimen is shown in Figure 2.1a and it was cleaned by herself using only tap water. The shell was left under water to macerate, to loosen the flesh without affecting the shell. The water was changed daily until all the flesh had been removed. This process can take a few weeks to be completed. Unfortunately the day the specimen was collected and the length of the cleaning process were not recorded.

Three whole modern specimens were donated by Dr Niklas Hausmann from the same group. The modern shells were collected alive on 18/02/2013, precisely at the coordinates: 16.683680 N, 42.103829 E. These shells were cleaned by himself using chemicals, removing the flesh by immersion in a solution of 5% of NaClO for 24h. Afterwards they were rinsed with pure water. No pictures were taken from these samples; however, they were very similar in size and colour to the specimen from Figure 2.1a. These shells were used in Chapters 4 and 5 with codes S1, S2 and S3.

Two burnt sea shell fragments from layers three and ten of the KM1057 shell midden were also donated by Prof. Geoffrey Bailey and Dr. Eva Laurie. They are shown in Figure 2.2. These charred fragments are approximately 1 cm wide and their masses are 0.33 g (layer three) and 0.26 g (layer ten), both belonging to the *Conomurex fasciatus* species. Burnt samples are rare and only a few grams of this material were found in the entire shell midden.

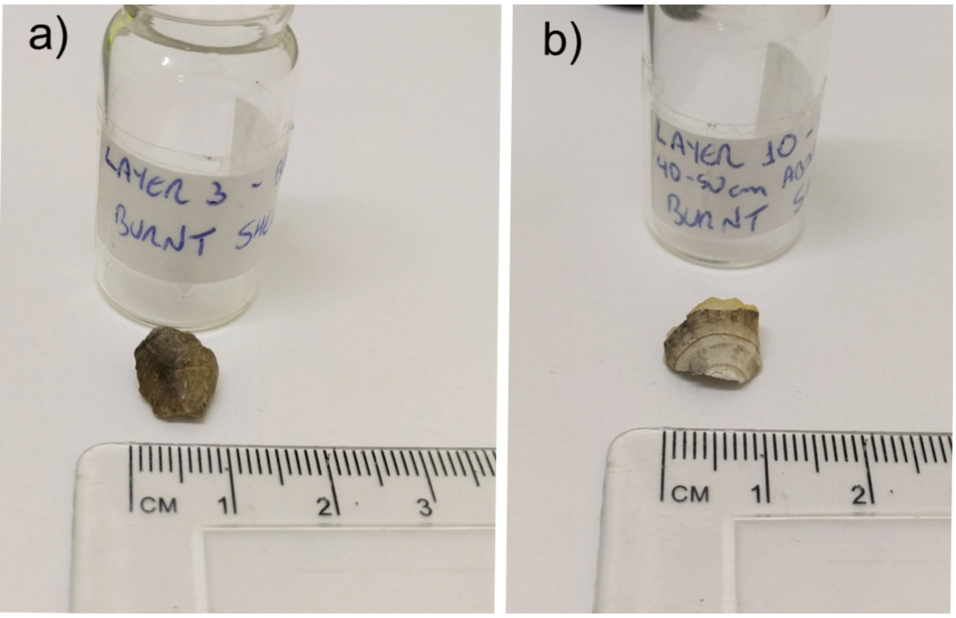

**Figure 2.2:** Burnt fragments belonging to the *Conomurex fasciatus* species from the KM1057 shell midden. The specimen shown in the left picture (a) was collected in layer 3, while the specimen shown in the right picture (b) was collected in layer 10.

### 2.1.2 Nucella specimens

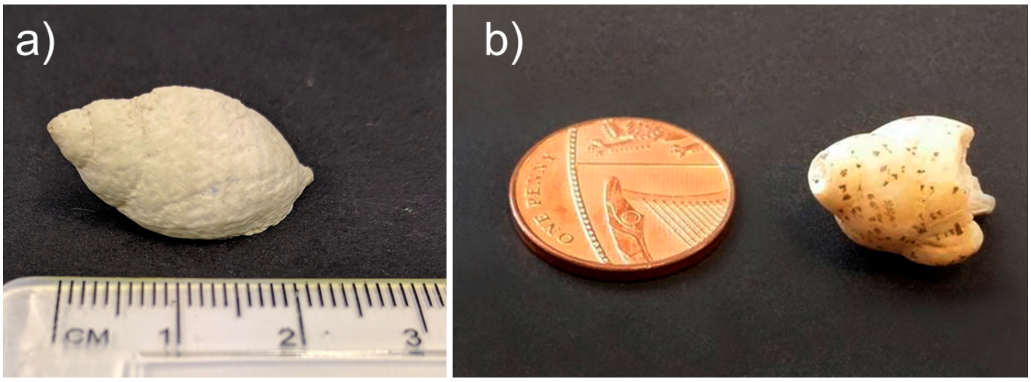

**Figure 2.3:** The picture on the left (a) shows a modern *Nucella lapillus* collected in Devon-UK. The picture on the right (b) shows a fossilised *Nucella* sp. shell, from Easington Raised Beach, with an approximate length of 1.3 cm.

One modern *Nucella lapillus* shell was collected dead on the beach in Devon-UK by Dr. Sebastian Payne, previously from English Heritage. The shell was cleaned by himself by soaking in fresh water. Date of collection and precise location were not recorded. This shell is shown in Figure 2.3a.

One fossilised shell, shown in Figure 2.3b, was provided by Dr. Beatrice Demarchi until recently at the BioArCh group in the Department of Archaeology at University of York. This specimen is from the Easington Raised Beach site. Due to its deteriorated condition, it was not possible to identify the shell subspecies from its appearance, therefore it was nominated only as *Nucella* sp. The age of this sample is 250,000 ± 30,000 years BP, determined by optically stimulated luminescence [144].

### 2.1.3 Summary of samples

All the samples used in this thesis are summarised in Table 2.1. This table is sub-divided according to the thesis chapters, listing all samples used in each experiment. For the samples used in Chapter 3, no code was created as the four shells can be discriminated by species and age. The column 'Condition' refers to how the shell was prepared for the analyses, informing their current condition. More details about their preparation are given in the next sections of this chapter.

One important detail to be noted, is that Table 2.1 only shows the main samples. For example, the samples used in Chapter 4 were split into sub-samples to be thermally treated at different conditions. In the same chapter the archaeological burnt fragments were also sub-divided. In this case, the sub-samples are not listed in Table 2.1, and more details are provided further.

**Table 2.1:** Summary of samples used in the thesis. The list is organised according to the thesis chapters, containing all the samples used for that experiment, detailing the shell species, age and location from were they were obtained.

Samples used in Chapter 3

| **Code** | **Species** | **Age** | **Location / Site** | **Condition** | **Cleaning** |
|---|---|---|---|---|---|
| | *Conomurex fasciatus* | Archaeo. | Farasan Islands, Red Sea / KM1057 shell midden, layer 6 | Sectioned into 5 slices | Fresh water only |
| | *Conomurex fasciatus* | Modern | Farasan Islands, Red Sea | Sectioned into 5 slices | Fresh water only |
| | *Nucella* sp. | Fossil | Durham UK / Easington Raised Beach | Sectioned into 3 slices | Not cleaned |
| | *Nucella lapillus* | Modern | Devon UK | Sectioned into 3 slices | Fresh water only |

Samples used in Chapter 4

| **Code** | **Species** | **Age** | **Location / Site** | **Condition** | **Cleaning** |
|---|---|---|---|---|---|
| S1 | *Conomurex fasciatus* | Modern | Farasan Islands, Red Sea | Powdered | Chemicals |
| S2 | *Conomurex fasciatus* | Modern | Farasan Islands, Red Sea | Powdered | Chemicals |
| S3 | *Conomurex fasciatus* | Modern | Farasan Islands, Red Sea | Powdered | Chemicals |
| BL3 | *Conomurex fasciatus* | Archaeo. | Farasan Island, Red Sea / KM1057 shell midden, layer 3 | Burnt fragment | Sliced |
| BL10 | *Conomurex fasciatus* | Archaeo. | Farasan Island, Red Sea / KM1057 shell midden, layer 10 | Burnt fragment | Sliced |

Samples used in Chapter 5

| **Code** | **Species** | **Age** | **Location / Site** | **Condition** | **Cleaning** |
|---|---|---|---|---|---|
| S1 | *Conomurex fasciatus* | Modern | Farasan Islands, Red Sea | Powdered | Chemicals |
| S2 | *Conomurex fasciatus* | Modern | Farasan Islands, Red Sea | Powdered | Chemicals |

*Continued on next page*

Table 2.1 – *Continued from previous page*

| | | | | | |
|---|---|---|---|---|---|
| S3 | *Conomurex fasciatus* | Modern | Farasan Islands, Red Sea | Powdered | Chemicals |
| L3S1 | *Conomurex fasciatus* | Archaeo. | Farasan Islands, Red Sea / KM1057 shell midden, layer 3 | Powdered | Fresh water only |
| L3S2 | *Conomurex fasciatus* | Archaeo. | Farasan Islands, Red Sea / KM1057 shell midden, layer 3 | Powdered | Fresh water only |
| L6S1 | *Conomurex fasciatus* | Archaeo. | Farasan Islands, Red Sea / KM1057 shell midden, layer 6 | Powdered | Fresh water only |
| L6S2 | *Conomurex fasciatus* | Archaeo. | Farasan Islands, Red Sea / KM1057 shell midden, layer 6 | Powdered | Fresh water only |
| L10S1 | *Conomurex fasciatus* | Archaeo. | Farasan Islands, Red Sea / KM1057 shell midden, layer 10 | Powdered | Fresh water only |
| L10S2 | *Conomurex fasciatus* | Archaeo. | Farasan Islands, Red Sea / KM1057 shell midden, layer 10 | Powdered | Fresh water only |

## 2.2 Raman Spectroscopy

### 2.2.1 Equipment and settings

A Horiba XploRA micro-Raman was used in this research (Figure 2.4a). The XploRA is equipped with green, red and infra-red lasers. The Raman radiation is a very weak phenomenon, being proportional to the frequency of the radiation source [2,145], thus the use of the green laser (532 nm) was preferred to increase the Raman signal. Unfortunately as a consequence, it also increases the fluorescence levels [145]. However, there are ways of reducing the background generated on each spectrum and these methods are discussed throughout this chapter.

The Raman capability is on top of the microscope comprising a 180° backscattering configuration. This means that the incident laser light and the scattered light follow the same path being delivered and collected by the objective lens [3,5], as shown in Figure 2.4. Different objective lenses may be used for data collection; however, their choice changes the laser spot size at the sample. The spot size diameter ($d_l$) depends on the numerical aperture ($NA$) of the lens and the wavelength ($\lambda$) of the source [146], such that

$$d_l = \frac{1.22\lambda}{NA}. \tag{2.1}$$

On biogenic materials, randomly distributed impurities over the sample are normally the greatest source of fluorescence [147, 148]. Using the smallest laser spot size available helps to minimise this effect, as the information from the biogenic system is collected from

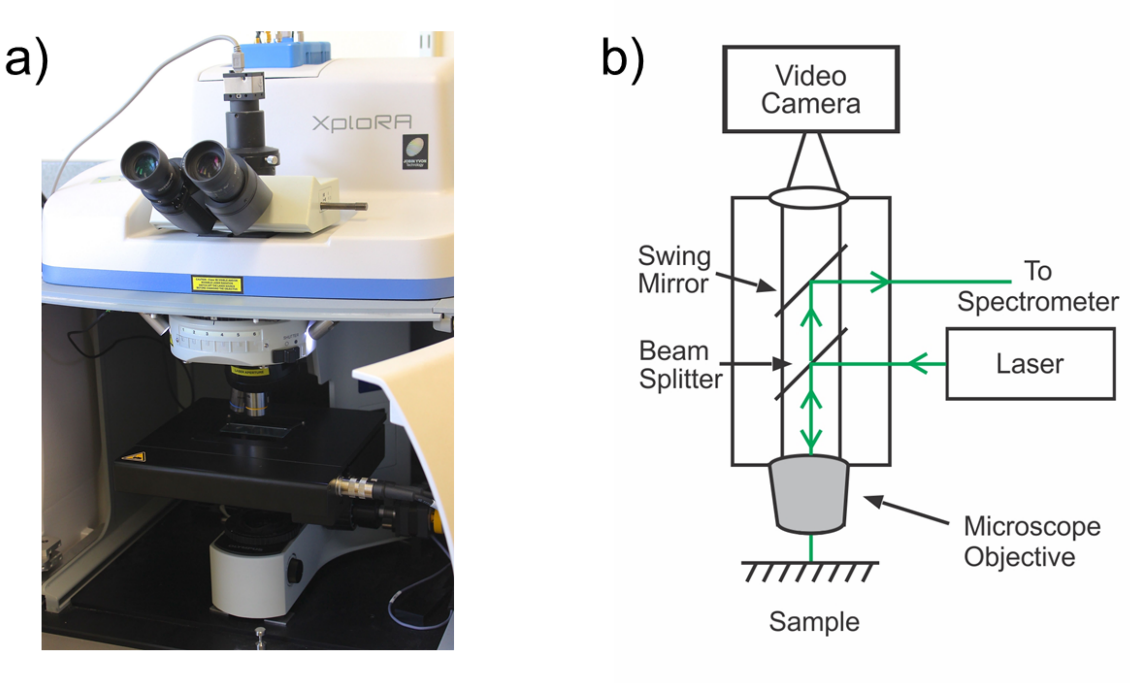

**Figure 2.4:** On the left (a) the Horiba XploRA micro-Raman from Department of Physics at University of York. On the right (b) a schematic of a 180 backscattering geometry used in the Raman microscope, as per [5].

**Table 2.2:** Available objective lenses and their properties.

| Objectives | Numerical Aperture | Working distance (mm) | Spot size[1] ($\mu$m) | Brand |
|---|---|---|---|---|
| 10x | 0.25 | 10.6 | 2.6 | Olympus |
| 50x | 0.75 | 0.38 | 0.9 | Olympus |
| 100x | 0.90 | 0.21 | 0.7 | Olympus |
| 100x LWD | 0.75 | 4.70 | 0.9 | Leica |

[1] Calculated from Equation 2.1 for the green laser (532 nm).

a smaller sampling area.

The working distance of a lens is simply the vertical distance between the sample and the lens when focused. Normally for standard lenses this distance is smaller than one millimetre, which is not a problem for flat samples. However, sea shells have irregular surfaces and the lens normally touches the shell before reaching the focusing point. Thus, the ideal lens and choice of laser for performing Raman analyses of sea shells should provide the smallest laser spot size (thereby reducing the spectral background) and have the longest working distance available. Table 2.2 shows the lenses available for this research along with their properties for Raman spectroscopy using the green (532 nm) laser. In comparing these properties, the 100x long working distance (LWD) lens was selected allowing for a working distance of 4.70 mm and small spot size of 0.9 $\mu$m.

The 532 nm green laser available in Raman equipment is a Neodymium-YAG (yttrium-aluminium-garnet) solid state laser, which has a stated maximum output power of ~10 mW. To control the laser power at the sample and prevent sample damage, neutral density filters are used. The available filters are 0.1%, 1%, 10%, 25%, 50% and 100% (no filter). The most fragile part of the sea shells is their organic structure, comprising carotenoids and impurities that can be easily burnt. To ensure non-destructive Raman measurement a 50% filter was chosen to analyse the sea shells in this research, allowing no more than 5 mW of laser power at the sample.

Figure 2.5a illustrates the path taken by the light from the laser to the CCD via the various optical components of the Raman microscope. The laser incident on the sample is represented by the green line. The light blue line represents the Rayleigh scattering light combined with the Raman scattered light. An edge filter blocks the Rayleigh scattered light allowing for only the Raman scattered light to progress forward, as represented by the purple line. It is important to highlight that edge filters block a range of wavelengths that would compromise the start of the spectrum [3, 145]. For the Horiba XploRA the first 50 wavenumbers are compromised.

The Horiba XploRA has an adjustable hole (or pinhole) located in the image plan of the microscope, allowing confocal Raman spectroscopy to be performed. The confocal setting blocks the light from other planes situated above or below the focal plane [145]. The smaller the size of the confocal hole, the smaller the amount of scattered light that reaches the detector, due to spatial filtering. Figure 2.5b shows the scheme for a confocal microscope as per [145], where only the light from the focal plane is allowed to pass through the confocal hole. This technique results in a high image contrast and also helps blocking fluorescence by controlling the sampling depth [145]. The culmination of which results in a clearer Raman spectrum. The available choices for confocal hole settings on the Horiba XploRA are 100, 300 or 500 $\mu$m. In this work, the smallest confocal hole of 100 $\mu$m was used.

Before reaching the charged-couple device (CCD), the Raman scattered light passes a slit and diffraction grating, as shown on Figure 2.5a. These two optical apparatus are the coupling between the microscope and the sensor [145], which controls the spectral resolution [5, 145, 149]. The spectral resolution is the ability to clearly distinguish individual peaks and to separate convolved peaks [5, 150].

The slit controls the divergence angle of the light that reaches the diffraction grating.

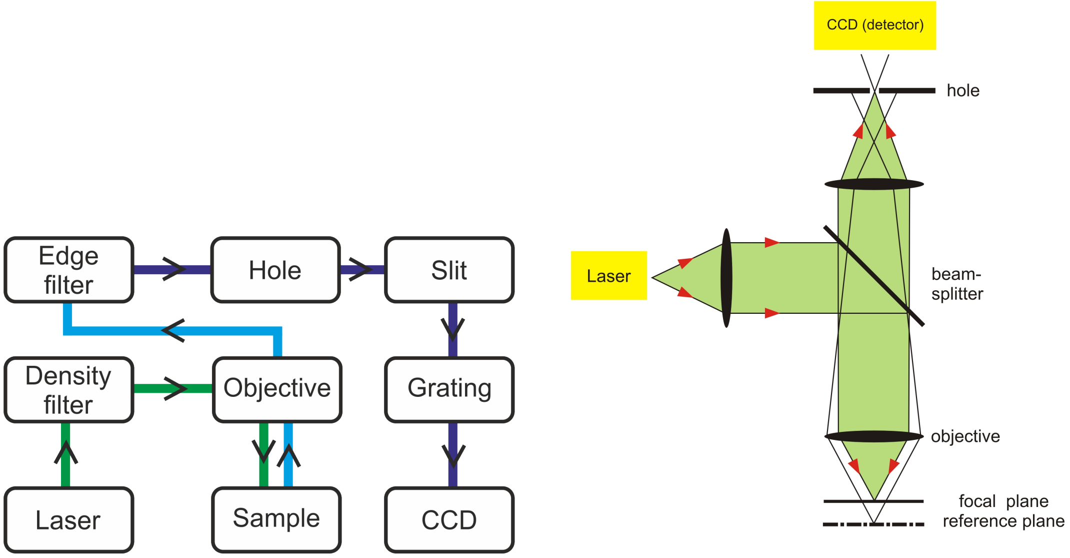

(a)

(b)

**Figure 2.5:** (a) The main equipment components for Raman spectroscopy showing the incident and scattered light paths. (b) Confocal microscope setup as per [145].

A higher divergence angle obtained by a narrower slit can result in signal loss, while a small divergence from a wide slit may only partially illuminate the diffraction grating, therefore lowering the resolution [145]. There are three available choices for the slit size on the Horiba XploRA: 50, 100 and 200 $\mu$m. Although the smaller slit increases the spectral resolution, it reduces the signal intensity. Therefore, to ensure maximum signal on the experiments, the largest slit size of 200$\mu$m was selected.

The diffraction grating disperses light of different wavelengths into different angles [145]. Higher groove densities on the diffraction grating result in bigger dispersion achieving better spectral resolution, however at the cost of reducing the wavelength coverage [145, 151]. The diffraction grating densities available on the Horiba XploRA are 600, 1200, 1800 and 2400 grooves/mm. The choice from 600 to 1800 grooves/mm allows analyses covering a range up to 4000 wavenumbers. The grating also affects the amount of time it takes to collect a single spectrum, which decreases for smaller diffraction grating densities. For maximum spectral resolution the 2400 grooves/mm grating was used allowing for analyses up to 3200 wavenumbers.

Data collection was performed using the Horiba Labspec software versions 5 and 6. Apart from the choice of the objective, all of the settings explained so far (such as the laser wavelength, grating choice, slit size, etc.) are controlled via software. Labspec has several options and settings for data acquisition, with two of these settings explained here: the number of accumulations and the acquisition time. For the Raman data collection, the spectrum is divided into windows, where the size of each window depends on the diffraction grating selected. For example, with a diffraction grating that has 2400 grooves/mm, the maximum size of each spectral window is $\sim$ 750 wavenumbers. Thus, five windows are necessary to complete the full spectral range from 0 to 3200 wavenumbers. The acquisition time defines the length of time that the scattered light is collected from the sample per spectral window. The number of accumulations defines how many times the spectrum is collected and then averaged per spectral window. By increasing the number of accumulations, the software is able to significantly reduce the noise, and also eliminates cosmic rays, which interact with the CCD creating false peaks.

Due to their mineral phase, sea shells have a strong Raman signal intensity after only one second of acquisition. Therefore, all spectra collected in this work were obtained after one second exposition, repeated 32 times. Using these settings, about four minutes were required to collect a full spectrum range, during which the laser keeps irradiating the sample. Table 2.3 summarises the acquisition settings for the shell analyses.

The Horiba XPloRA is also equipped with an automated X-Y-Z stage controlled by Labspec software, which allows the instrument to build spatially-resolved Raman maps from the sample. On a Raman map, the user can set an area on the sample to be mapped, which can be covered by square, rectangular, circular or polygonal maps. It is also possible

**Table 2.3:** Summary of the Raman acquisition settings. With these settings, the amount of time necessary for collecting a single spectrum is approximately four minutes.

| | | | |
|---|---|---|---|
| **Laser:** | 532 nm | **Acquisition time:** | 1 sec |
| **Objective:** | 100x LWD | **Accumulations:** | 32x |
| **Filter:** | 50% | **Grating:** | 2400 grooves/mm |
| **Hole:** | 100 $\mu$m | **Spectral range:** | 0-3200 cm$^{-1}$ |
| **Slit:** | 200 $\mu$m | | |

to set the density of Raman sampling points in order to build the map. According to the stage manufacturer, the smallest step size is 0.01 $\mu$m and the stage accuracy is ±3 $\mu$m.

The Horiba XploRA also has an auto focusing feature that can be used either for Raman maps or point acquisitions. The Labspec software uses the intensity of any predefined peak to make fine adjustments to the focus by changing the Z-coordinate of the stage. The user defines a range for moving the stage on Z direction, and how many times the focus should be tested in the selected range. This feature, although useful, can considerably increase the amount of time spent to acquire each spectrum and may not be recommended for samples that require high acquisition time.

### 2.2.2 Whole shell analyses

Whole sea shells can be large, making Raman analysis using the Horiba XploRA not possible due to it having a limited vertical space between the objective and the stage. The use of a LWD lens makes this gap even smaller. To circumvent this issue, the shells used in this study (*Conomurex fasciatus* and *Nucella* sp.) were sectioned using a Buehler precision saw, model Isomet 1000 (Figure 2.6). As these are gastropod shells, they were then sliced perpendicular to their length, with the number of slices produced varying with the size of the whole shell. Figure 2.7 shows two shells of different length sliced in this way: (a) the archaeological *Conomurex fasciatus* on the left and (b) the fossil *Nucella sp.* on the right.

**Figure 2.6:** Buehler precision saw (model Isomet 1000) from Department of Archaeology at University of York. The saw was used for sectioning the sea shells in this study.

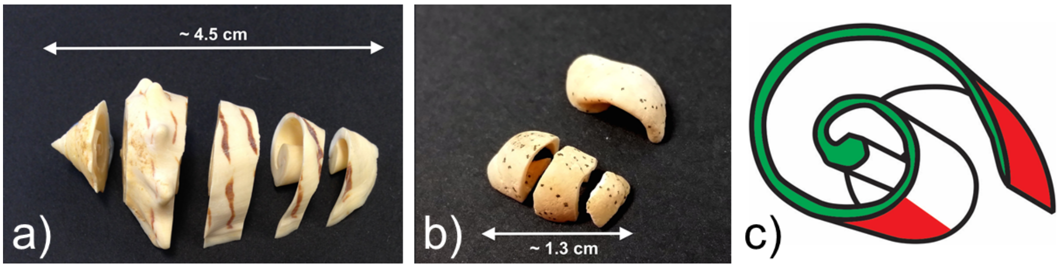

**Figure 2.7:** Sectioned shells: (a) the archaeological *Conomurex fasciatus* shell which was sectioned into five slices. (b) The fossil *Nucella* sp. shell, sectioned into three slices. The modern shells from both of the shell species were sectioned in the same way. (c) Sampling areas for the shells used in this study showing the cross-section of a gastropod shell and regions where the spectra were obtained. The external region is marked in red, and the internal region is marked in green.

The sectioning of the shells also makes it possible to collect information from their inner parts, rather than just from their external surfaces. Figure 2.7c illustrates the cross-section of a gastropod shell, showing in red the external region and in green the internal region, where Raman data were collected. The data obtained from these sectioned shells were grouped according to the region of sampling, to generate representative results for the external and internal shell regions. Regardless of the region sampled, it is important to highlight that point data acquisition was always performed at random positions on the slices.

### 2.2.3 Powdered shell analyses

Due to the irregular surfaces of the shells, it proved difficult to keep them fixed during Raman acquisition on the external surfaces. Glues or tapes could also not be used due to the risk of contamination of the shells. Therefore, to circumvent these issues, powdered shell samples were also extensively used in this research. Powdered shell samples could be easily deposited on top of a microscope slide, split into portions if necessary, and have random spectral collection from any part on the sample.

Shells were ground using a mortar and pestle until a fine powder was obtained. To avoid contamination from previous materials, a brand new pestle and mortar was used. Once ground, the shell samples were stored in glass vials.

The sample preparation for Raman acquisition was simple, with a small amount of powder being pressed between two microscope slides in order to obtain a flat surface. The great advantage of working with powdered samples, is the possibility of performing Raman maps instead of single point acquisitions. In this case, the Raman maps were not performed to obtain a spectral image of the samples, but rather to automate the process of data collection.

As mentioned previously, the acquisition time used for shells was one second. Because of the short acquisition time, it is possible to use the auto focusing feature on the Horiba XploRA, which adjusts the focus for each point of the Raman map. This feature increases the duration of the map by a few hours, depending on the map settings and on how flat the powdered sample was.

All of the spectra from the powdered shell samples were collected using square Raman maps. As a shared instrument, the size of each Raman map performed depended on the availability of the Raman microscope. Also, big areas tend to be less flat than smaller areas, thus increasing the time spent on the auto focusing feature, and as consequence, reducing the amount of spectra collected per hour. Therefore, the mapped area was always between 1 and 3 mm square. The density of acquisition points varied for the same reason and ranged from 5x5 (25 spectra), up to 12x12 (144 spectra).

One disadvantage of using a mapping tool is that even when the auto focus is used, poor quality spectra might be obtained. Normally for manually point acquisitions, these spectra are simply ignored and deleted, but on a Raman map the software is not discriminatory. Thus, for all samples more spectra were collected than needed, in order to remove from the dataset poor quality spectrum, which were normally unfocused due to the sample topography.

### 2.2.4 Burnt fragment analyses

As archaeological burnt fragments are very rare, the specimens from layers three and ten from the KM1057 shell midden were also sectioned. They were split into thirds in order to analyse them under different experimental conditions. As the shell fragments are really small, as shown in Figures 2.2a and 2.2b, they were sectioned using a different saw. The sectioning took place at the Thin Section Lab in the School of Earth and Environment at University of Leeds. The two shell fragments were cut by the technician Harri Wyn Williams who kindly volunteered to help this research. The saw used was a ML Beach Faceters Trim Saw, shown in Figure 2.8, which is equipped with a 4 inch continuous rim diamond blade.

One third of each shell fragment was kept in its original condition. The two third segments left from each shell fragment were cleaned with ultrasonic bath followed by gentle brushing under tap water and then dried at room temperature. One of these fragments was then ground after cleaning, with the grinding performed using the same methods described in the ‘Powder shell analysis’ (section 2.2.3).

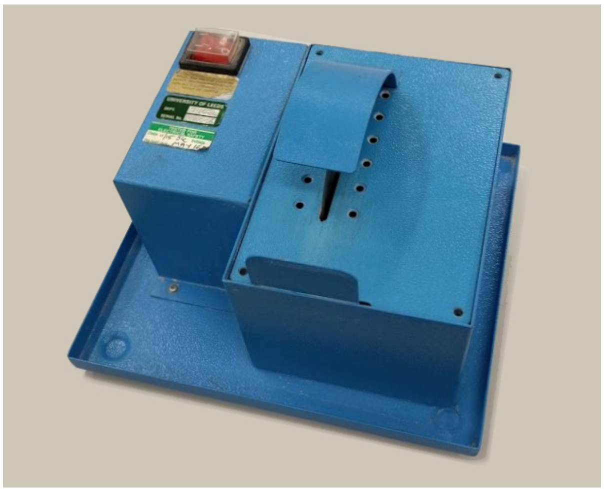

**Figure 2.8:** ML Beach Faceters Trim Saw from the Thin Section Lab at the University of Leeds.

In summary, each one of the burnt shell fragments shown in Figures 2.2a and 2.2b were fractioned into three parts with the first part kept in its original condition, the second part cleaned, and the third part cleaned and then powdered.

Random point acquisitions were used to collect Raman spectra only at the external surface of the original, and cleaned, burnt shell fragments. For the powdered samples, the Raman spectra were obtained using Raman maps, as described in Section 2.2.3.

### 2.2.5 Data analyses and curve fitting

The Labspec software from Horiba has the option to save the spectra in text format, therefore allowing it to be exported to any other software. Each line of the Raman data text file contains a single spectral point corresponding to the wavenumber and intensity. All data analyses were carried out using the Igor Pro software, Version 6.32, which can easily import the text files and perform multi-peak fittings, a feature used frequently in this research.

For quantitative RS analyses, the three main properties from the spectral peaks are measured: the peak position on the X-axis (wavenumber position), its amplitude or intensity, and its FWHM. Igor Pro allows the user to obtain these peak properties by controlling all the necessary parameters for the fitting, such as the spectral region to be fitted, the number and type of peaks with their initial estimates (positions, widths and intensities), and the baseline curve. The software will find the best spectral fit by adapting these initial estimates in order to obtain the smallest difference between the original and the theoretical (or fitted) curves. This difference between curves is measured by the $\chi^2$ value, which is given by:

$$\chi^2 = \sum_i \frac{(y - y_i)^2}{\sigma_i}, \tag{2.2}$$

where y is the theoretical value for a given point, $y_i$ is the original data value for the point and $\sigma_i$ is an estimate of the standard deviation for the original data [152]. In other words, the $\chi^2$ value measures the accuracy of the peak fitting.

An example of peak-fitting is demonstrated in Figure 2.9 showing the lattice mode in the aragonite spectrum fitted using five Gaussian peaks. The selected spectral range is between 100 and 240 cm$^{-1}$. The red line shows the original spectral data, and the blue line is the fitted theoretical curve. A linear baseline correction is performed in order to obtain the peak intensity by defining as zero intensity the line connecting the beginning and the end of the fitted spectral range. The baseline is represented by the green line in Figure 2.9. Once the software has reached the smallest $\chi^2$ value for the defined settings, it will return the quantitative properties of each peak.

Aragonite and calcite, as explained in Section 1.2.2 of Chapter 1, have similar Raman signatures, however the main differences between them are the number of peaks in two regions. Specifically, aragonite has a doublet in the $\nu_4$ region ($\sim$ 700 cm$^{-1}$), whilst calcite shows a single peak. In the lattice mode between $\sim$ 100 and $\sim$ 300 cm$^{-1}$, calcite has two well separated peaks, whilst aragonite has more than five convoluted peaks in this region.

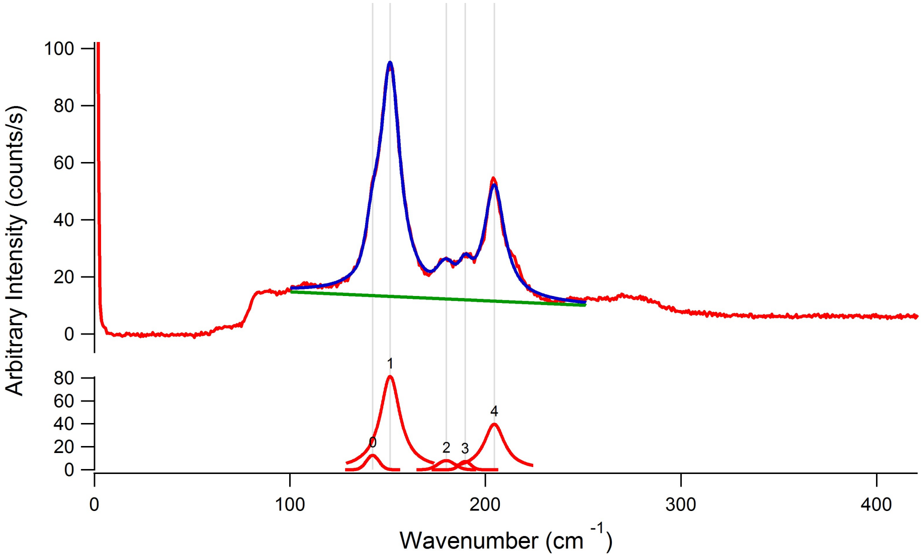

**Figure 2.9:** Curve fitting on Igor Pro. The graph shows the fitting (blue line) of the lattice mode of aragonite (red line), with five peaks and a baseline correction in the fitted range (green line).

These differences require the use of special settings for each case.

The aragonite Raman spectrum was divided into four regions comprising the six peaks studied in this work (Table 2.4). The $\nu_1$ and $L_2$ regions were both fitted with a single Gaussian peak in these ranges. The $\nu_4$ and $L_1$ regions have convolved peaks, thus each region was fitted with two Gaussian peaks. The calcite Raman spectrum was also divided into four regions, although these regions do not have any convolved peaks. Therefore, all regions were fitted with single Gaussian peaks. In fitting both the aragonite and calcite Raman spectra, only a linear baseline correction was applied. The peak positions shown in Table 2.4 are approximated values, and the fitted spectral range is also shown. Both quantities are measured in wavenumbers.

Igor Pro also has a programming interface allowing the user to write procedures to perform data analysis or data processing using the imported data. For example, if the user needs to perform the same modification to 100 spectra loaded into the software, it is possible to create a procedure for automating this change. In this respect, procedures were

**Table 2.4:** Settings for fitting aragonite and calcite Raman spectra. The peak position column shows approximated values in wavenumbers (cm$^{-1}$). The range is also measured in wavenumbers (cm$^{-1}$).

**Aragonite peak fitting settings using Igor Pro**

| Region | Peak positions | Range | Peak type | Baseline |
|---|---|---|---|---|
| $\nu_1$ | 1082 | 1060-1100 | Gaussian | Linear |
| $\nu_4$ | 705<br>701 | 690-720 | Gaussian | Linear |
| $L_2$ | 205 | 195-220 | Gaussian | Linear |
| $L_1$ | 151<br>141 | 125-172 | Gaussian | Linear |

**Calcite peak fitting settings using Igor Pro**

| Region | Peak positions | Range | Peak type | Baseline |
|---|---|---|---|---|
| $\nu_1$ | 1082 | 1060-1100 | Gaussian | Linear |
| $\nu_4$ | 712 | 690-720 | Gaussian | Linear |
| $L_2$ | 280 | 260-300 | Gaussian | Linear |
| $L_1$ | 154 | 125-172 | Gaussian | Linear |

developed to perform peak fitting, where the same peaks had to be fitted under exactly the same conditions across different spectra. These batch fittings procedures were developed so that the quantitative results could be quickly obtained given the large amount of Raman data that were collected on each shell sample.

Thus, when it is mentioned that a certain sample had $N$ spectra collected, then this means that each single spectrum was individually fitted, generating long tables containing the quantitative properties of each fitted peak. Table 2.5 shows a simple example output with two peaks analysed, demonstrating how this information is saved. Equation 2.3 exemplifies, for the first average of the table, how it was calculated:

$$AVG_1 = \sum_{i=1}^{N} \frac{P_{i1}}{N}. \tag{2.3}$$

**Table 2.5:** Typical representation for a quantitative results table. The averages were calculated for the fitted positions and the FWHM results, using the standard error of the mean as the uncertainty and the coefficient of variation the as measure of the dispersion. The peak intensity was only assessed through intensity ratios.

| **SAMPLE NAME** | | | | | | | |
|---|---|---|---|---|---|---|---|
| **Spectrum** | **Peak 1** | | | **Peak 2** | | | **Intensity ratio** |
| | **Position** | **Intensity** | **FWHM** | **Position** | **Intensity** | **FWHM** | |
| Spec-1 | $P_{11}$ | $I_{11}$ | $F_{11}$ | $P_{12}$ | $I_{12}$ | $F_{12}$ | $I_{11}/I_{12}$ |
| Spec-2 | $P_{21}$ | $I_{21}$ | $F_{21}$ | $P_{22}$ | $I_{22}$ | $F_{22}$ | $I_{21}/I_{22}$ |
| Spec-3 | $P_{31}$ | $I_{31}$ | $F_{31}$ | $P_{32}$ | $I_{32}$ | $F_{32}$ | $I_{31}/I_{32}$ |
| ⋮ | ⋮ | ⋮ | ⋮ | ⋮ | ⋮ | ⋮ | ⋮ |
| Spec-N | $P_{N1}$ | $I_{N1}$ | $F_{N1}$ | $P_{N2}$ | $I_{N2}$ | $F_{N2}$ | $I_{N1}/I_{N2}$ |
| **Mean** | $AVG_1$ | | $AVG_2$ | $AVG_3$ | | $AVG_4$ | $AVG_5$ |
| **SDEV** | $SDEV_1$ | | $SDEV_2$ | $SDEV_3$ | | $SDEV_4$ | $SDEV_5$ |
| **SE** | $SE_1$ | | $SE_2$ | $SE_3$ | | $SE_4$ | $SE_5$ |
| **CV** | $CV_1$ | | $CV_2$ | $CV_3$ | | $CV_4$ | $CV_5$ |

From the averages, the following statistical quantities were obtained: the standard deviation (SDEV), the standard error of the mean (SE) and the coefficient of variation (CV). Equations 2.4, 2.5 and 2.6 show how these statistical quantities were calculated using the first average ($AVG_1$) as an example:

$$SDEV_1 = \sqrt{\frac{\sum (P_{i1} - AVG_1)^2}{(N-1)}} \tag{2.4}$$

$$SE_1 = \frac{SDEV_1}{\sqrt{N}} \tag{2.5}$$

$$CV_1 = \frac{100(SDEV_1)}{AVG_1} \tag{2.6}$$

The intensity of each peak was assessed by calculating the two-peak intensity ratio, as shown in the last column of Table 2.5. Thus, no statistical quantities were calculated for the intensity columns.

Lastly, another useful tool that Igor Pro has and was frequently used in this thesis, is the function for averaging graphs. Once all Raman spectra from a certain sample is loaded into the software, this function creates a final graph, which is the average of them. This function was applied to all samples, only to obtain a representative spectrum for all data collected.

### 2.2.6 Convergence Tests

Due to biological materials being heterogeneous, spectral differences are therefore expected in the Raman signatures obtained from different positions of the sample. To examine this heterogeneity, statistical analysis was used to determine the minimum amount of random sampling on each sample that would represent the whole sea shell.

Convergence tests analyse how the SE decreases with the amount of data averaged, therefore showing how many spectra are necessary for the SE to stabilise. This test requires a high amount of fitted data and can be applied to any peak using any quantitative property.

Figure 2.10 shows an example of a convergence test applied to the FWHM of the main calcium carbonate peak ($\nu_1$), which is a measure of the sample's cristallinity. This simple example has only eight points, which means that eight FWHM averages were calculated. Each FWHM average was obtained with an increasing amount of fitted data. For example, the first point corresponds to five averaged FWHM values, the second point to 10 averaged FWHM values and so on. The last point in the convergence graph corresponds to the total amount of data available, in this case 80 FWHM values. It is important that the FWHM values generating the mean are randomly selected. The Y-axis of the graph corresponds to the SE of each respective average. For this example test, the result suggests that the SE converges to a minimum value from the average obtained from 25 spectra onwards.

All convergence tests performed in this research used the $\nu_1$ peak, which was fitted

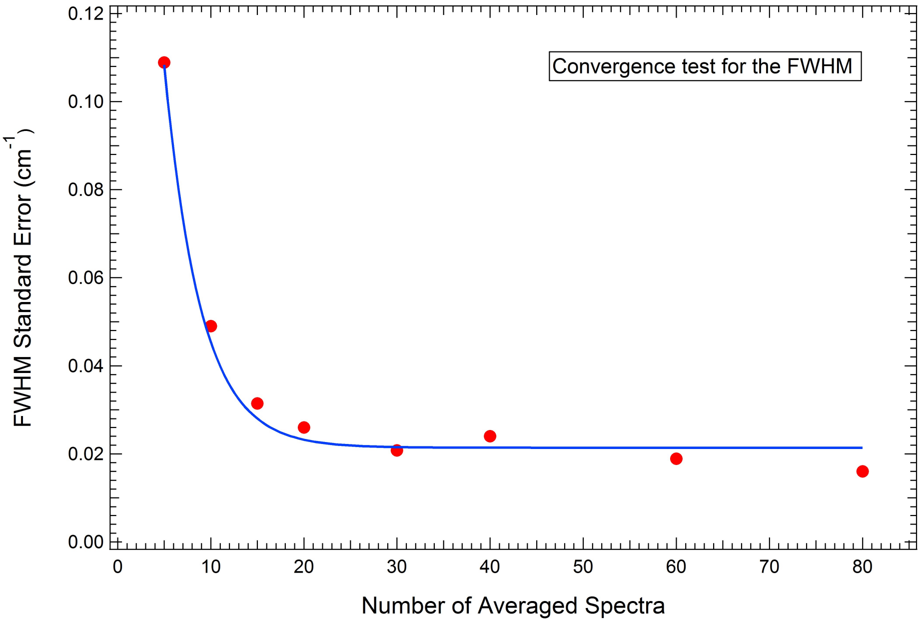

**Figure 2.10:** Example of a convergence test for the FWHM of the main calcium carbonate peak ($\nu_1$). For the X-axis, each point represents the number of FWHM values averaged, while the Y-axis corresponds to the SE of each respective average. The blue curve is used only for visual guidance.

using the settings discussed in Section 2.2.5. The $\nu_1$ peak is present in both aragonite and calcite Raman spectra. Since the FWHM property was studied in all of the experiments performed in this research, it was therefore chosen as the quantitative value against which the averages used for the convergence tests were performed.

As the convergence test requires a large amount of spectra and only analyses the FWHM for the $\nu_1$ peak, the spectral range was sometimes reduced to allow more efficient data collection. For these cases, the acquisition range was limited to the $\nu_1$ peak region, from 1060 to 1100 cm$^{-1}$, resulting in a reduced collection time of $\sim$ 35 seconds.

## 2.3 Heat treatment

Thermal treatments were applied only to the powdered shells, as it is possible to split the powdered samples into any required number of sub-samples that could then be treated

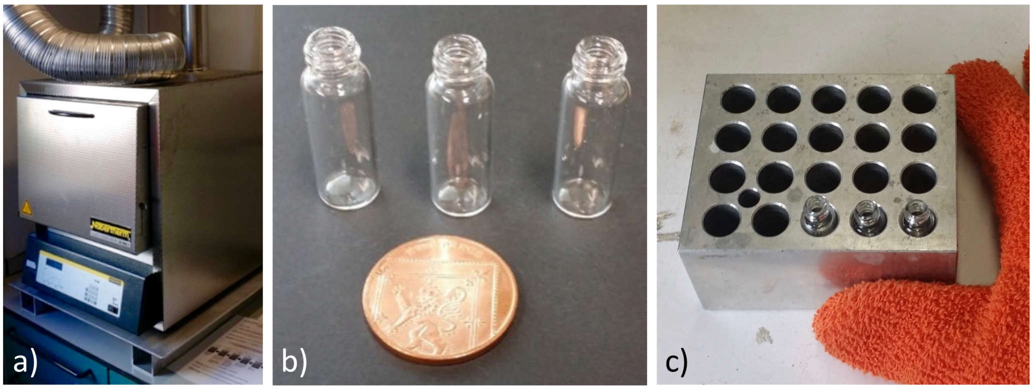

**Figure 2.11:** Thermal treatments experiments using a (a) Nabertherm furnace (model B180), (b) 2 ml borosilicate glass vials and an (c) aluminium block as the sample holder.

**Table 2.6:** Heat treatments performed on the powdered modern *Conomurex fasciatus* shells. The time and temperature uncertainties are ±3s and ±3°C, respectively.

| Samples | Treatment temperature | Treatment times |
|---|---|---|
| S1; S2; S3 | 100°C | 4h; 8h |
| | 180°C | 4h; 8h |
| | 250°C | 4h; 8h |
| | 325°C | 4h; 8h |
| | 400°C | 3min, 7min, 15min, 30min, 1h, 2h, 4h, 8h |
| | 500°C | 3min, 7min, 15min, 30min, 1h, 2h, 4h, 8h |

under different heating conditions. The heating treatments only involved the three modern *Conomurex fasciatus* shells (S1, S2 and S3), as defined in Table 2.1. For each heat treatment condition, the three modern shells were used as biological replicates.

The heat treatments were performed in a Nabertherm furnace model B180 (Figure 2.11a), which has an uncertainty of ±3°C. The powdered samples were treated inside sterilised borosilicate glass vials of 2 ml of size (Figure 2.11b). In order to insert and remove the three replicate vials precisely at the same time, an aluminium block was used as a sample holder (Figure 2.11c).

The heat treatments were performed at constant temperatures for different amounts of time (Table 2.6). The aim of the heat treatment was to study the aragonite-calcite transition. Since no transition was obtained for temperatures below 400°C after eight hours, the shorter treatments were not included for these temperatures. The samples were inserted inside the furnace after the desired temperature had stabilised. After achieving the desired amount of time, the samples were then immediately removed from the furnace and cooled down at room temperature.

The thermally treated powdered shell samples had their Raman spectra collected using Raman maps as per Section 2.2.3, 'powdered shell analyses'.

### 2.3.1 Laser Heating Test

As the laser may heat the shell samples, a simple test was performed in order to check if the laser could change the Raman quantitative parameters, *i.e.*, whether non-destructive Raman sampling was being performed.

To perform this test a single random position in the shell powder was chosen and two spectra were collected, one before and one after laser photobleaching of the sample. The spectra were obtained using the same Raman settings used in the experiments (Table 2.3). The photobleaching was performed with the density filter disabled, therefore allowing 100% laser power at the sample for 210 seconds, which is the approximate time needed to collect a single Raman spectrum, over the full spectral range.

The spectra obtained before and after the photobleaching experiment were compared and checked for changes in the measured quantitative parameters from the spectra. This test was applied to bulk unheated and heat-treated shell samples, being repeated at different positions, five times per each sample tested.

## 2.4 Scanning Electron Microscopy and Energy Dispersive X-Ray Analyses

Scanning Electron Microscopy and Energy Dispersive X-Ray spectroscopy were performed on *Conomurex fasciatus* shells, as complementary techniques on the shell fragments and powders in order to obtain the elemental compositions of each sample.

The analyses were performed at the Nanocentre in the Physics Department at the University of York. The electron microscope used was a FEI Sirion XL30 SFEG. The X-Ray detector used was a Thermo Scientific Ultra Dry Silicon Drift. EDX analyses and the SEM imaging software were provided by Thermo Scientific Noran System Six.

The powdered and fragment samples were first coated with a Pt/Pd alloy at a thickness of ~6 nm. This preparation avoids charging the samples with the electron beam, therefore resulting in better image quality. The coater that was used was a Ted Pella Inc. High Resolution Coater, model 208HR with planetary stage.

Between 10 to 14 micrographs were saved at random positions for each shell sample, using different magnifications and with EDX maps generated. The electron accelerating voltage varied from 5 to 15kV.

For the EDX quantitative analyses, the Proza (Phi-Rho-Z) correction method was used with the coating elements excluded from the results. The atomic percentages from each map were averaged obtaining a single average result for each element found in the analysed samples.

# Chapter 3

# Raman spectroscopy for comparing modern versus ancient shells

Diagenesis is a natural process that changes the carbonate skeletons over time. This process can compromise the isotopic information used for paleoenvironmental interpretations. In this chapter, quantitative Raman spectroscopy was applied to two different shell species: *Conomurex fasciatus* and *Nucella* sp., comparing the modern shells with their ancient counterparts. The aim was to characterise both modern and ancient shells looking for Raman spectroscopic markers that could be associated with the diagenesis process. Quantitative Raman spectroscopy parameters, such as peak intensity ratios and FWHM, obtained from peak fitting procedures were analysed. Scanning electron microscopy was used for investigating the *Conomurex fasciatus* shell microstructure and EDX was applied to obtain its elemental composition.

## 3.1 Convergence Test

Convergence tests were performed to determine the minimum number of spectra necessary to statistically represent each shell specimen. These tests were made according to the methods described in Section 2.2.6 of Chapter 2. Each convergence test measured the decay of the standard error of the mean associated with the FWHM of the main calcium carbonate peak ($\nu_1$ peak at 1082 cm$^{-1}$) as a function of the increase in the number of randomly averaged spectra.

These tests were performed on ancient and modern shells of the *Conomurex fasciatus* and *Nucella* species. The convergence test was applied to all shell slices from the studied samples (Figure 2.7 of Chapter 2). This generated two sets of results for each slice: one for the internal and other for the external region of each respective shell slice. Due to differences in the size between the two shell species, they were cut into a different number of slices, as described in Subsection 2.2.2 of Chapter 2. Therefore, each *Conomurex fasciatus* shell generated 10 results (from five slices), while each *Nucella* sp. shell generated 6 results (from three slices).

Table 3.1 summarises the convergence tests results obtained for the four specimens. It also shows the converged number of spectra for each shell slice. Each result was obtained from the corresponding convergence graph, which depicted how the SE corresponding to the $\nu_1$ peak FWHM decreased with the number of random spectra averaged. Since there are 32 graphs in total, they are not shown in this chapter and are all included in Appendix A, displayed from Figure A.1 to Figure A.32.

The convergence tests aimed to determine the minimum amount of spectra needed per slice to represent each shell specimen. Thus, the converged number of spectra obtained for each slice was then averaged. This resulted into two final mean values for each shell, one representing the external region and the other representing the internal region. These

**Table 3.1:** Convergence test results for the modern versus ancient shells comparison. The converged number of spectra for which the smallest SE is achieved for the FWHM are shown for each slice for both internal and external regions of the analysed shell specimens. The convergence graphs that generated these results are shown in Appendix A. The row called 'Value set' represents the minimum number of spectra to be collected in each slice of the respective shells.

| ***Conomurex fasciatus*** | | | | |
|---|---|---|---|---|
| | **Archaeological** | | **Modern** | |
| | External | Internal | External | Internal |
| Slice 1 | 22 | 25 | 65 | 50 |
| Slice 2 | 28 | 30 | 50 | 25 |
| Slice 3 | 30 | 30 | 25 | 40 |
| Slice 4 | 18 | 28 | 50 | 20 |
| Slice 5 | 25 | 30 | 32 | 40 |
| **Mean** | 24.6 | 28.6 | 44.4 | 35 |
| **Value set** | 30 | 30 | 45 | 45 |

| ***Nucella sp.*** | | | | |
|---|---|---|---|---|
| | **Fossil** | | **Modern** | |
| | External | Internal | External | Internal |
| Slice 1 | 28 | 32 | 28 | 24 |
| Slice 2 | 28 | 28 | 28 | 28 |
| Slice 3 | 24 | 28 | 32 | 28 |
| **Mean** | 26.7 | 29.3 | 29.3 | 26.7 |
| **Value set** | 30 | 30 | 30 | 30 |

results are displayed in the row 'Mean' of Table 3.1. It can be seen that the mean values of the converged number of spectra obtained for the internal and external regions of each shell are different. Therefore, the highest mean value of the converged number of spectra obtained for a region, either that being internal or external, was rounded up and adopted for that shell. This is represented by the 'Value set' row of Table 3.1. Therefore, for the *Conomurex fasciatus* species, 30 spectra per slice were defined as the minimum amount for the archaeological shell while 45 spectra per slice were defined for the modern. For the *Nucella* sp. 30 spectra per slice were set as the minimum quantity for both cases.

It is important to highlight that the 'Value set' row on Table 3.1 represents the number of spectra to be collected in each slice of the respective shell, and not the final amount of data. Thus, for the *Conomurex fasciatus* species, 150 spectra were collected in each internal and external regions of the archaeological shell (30 spectra per slice), while a total of 225 spectra were obtained in each region of the modern specimen (45 spectra per slice). For the fossil and modern *Nucella* sp. shells, 90 spectra were collected in each region.

## 3.2 Averaged Raman spectra and peak assignments

Once the previously determined amount of data was obtained for each shell slice, all the spectra collected for each shell was averaged together. These were separated only according to the internal and external shell regions of data collection, thus generating two averaged spectra for each shell specimen. These averaged spectra are displayed here only for the peak assignment purposes, all quantitative data analyses were carried out by fitting each individual spectrum, as described in the data analyses and curve fitting Section 2.2.5 of Chapter 2.

All individual spectra obtained for the *Conomurex fasciatus* and *Nucella* sp. shells were peak fitted and their peak positions and assignments corresponded, according to the literature, respectively to aragonite and calcite [91, 92, 104]. The presence of carotenoids and phenylalanine was noted only for the modern *Conomurex fasciatus* and these are discussed further on this section. The peak positions shown in Table 3.2, along with their respective literature assignments, correspond to the average of the positions obtained from the fitting of all individual spectra. The uncertainty of the measured peak position is SE of the mean.

Figures 3.1 and 3.2 show, respectively, the averaged spectra obtained for the archaeological and modern *Conomurex fasciatus*. The averaged spectra of the fossil *Nucella* sp. is displayed in Figure 3.3, while the averaged spectra of its modern sample is shown in

**Table 3.2:** Measured Raman peak positions and literature assignments. The peak positions correspond to the average of the positions obtained from the fitting of all individual spectra. Thus, their associated peak position uncertainty is the SE of the mean.

| Polymorph | Code | Measured position (cm$^{-1}$) | Literature peak assignments |
|---|---|---|---|
| Aragonite | $L_1$ | 141.30 ± 0.05<br>151.30 ± 0.04 | Translational lattice mode [92, 94, 96–99] |
| | $L_2$ | 204.80 ± 0.04 | Librational lattice mode [92, 94, 96–99] |
| | $\nu_4$ | 700.50 ± 0.03<br>704.90 ± 0.03 | In plane antisymmetric bend [52, 92, 94, 96–99] |
| | $\nu_1$ | 1081.80 ± 0.03 | Symmetric stretch [52, 92, 94, 96–99] |
| Calcite | $L_1$ | 153.70 ± 0.08 | Translational lattice mode [91, 92, 94, 96, 97, 99] |
| | $L_2$ | 280.00 ± 0.06 | Librational lattice mode [91, 92, 94, 96, 97, 99] |
| | $\nu_4$ | 711.90 ± 0.03 | In-plane antisymmetric bend [91, 92, 94, 96, 97, 99] |
| | $\nu_1$ | 1082.50 ± 0.02 | Symmetric stretch [91, 92, 94, 97, 99] |
| | $\nu_3$ | 1433.2 ± 0.1 | Anti-symmetric stretch [91, 92] |
| | $2\nu_2$ | 1746.0 ± 0.1 | Out of plane bend - overtone [91, 92] |
| Carotenoid | $C\nu_2$ | 1121.3 ± 0.3 | C–C stretching [153–156] |
| | $C\nu_1$ | 1509.2 ± 0.4 | C=C stretching [153–156] |
| Phenylalanine | $P$ | 999.6 ± 0.4<br>1028.2 ± 0.5 | Phenylalanine ring breathing [157] |

Figure 3.4. In all these figures, the external region is represented by the red spectrum and the internal region by the green spectrum.

All spectra collected for the *Conomurex fasciatus* species corresponded to aragonite, while for the *Nucella* sp. specimens they represented the spectral signature of calcite. As published before in literature, the *Conomurex fasciatus* shell is entirely made of aragonite [95] and the presence of calcite would be an indication of diagenesis [70, 95, 138, 140].

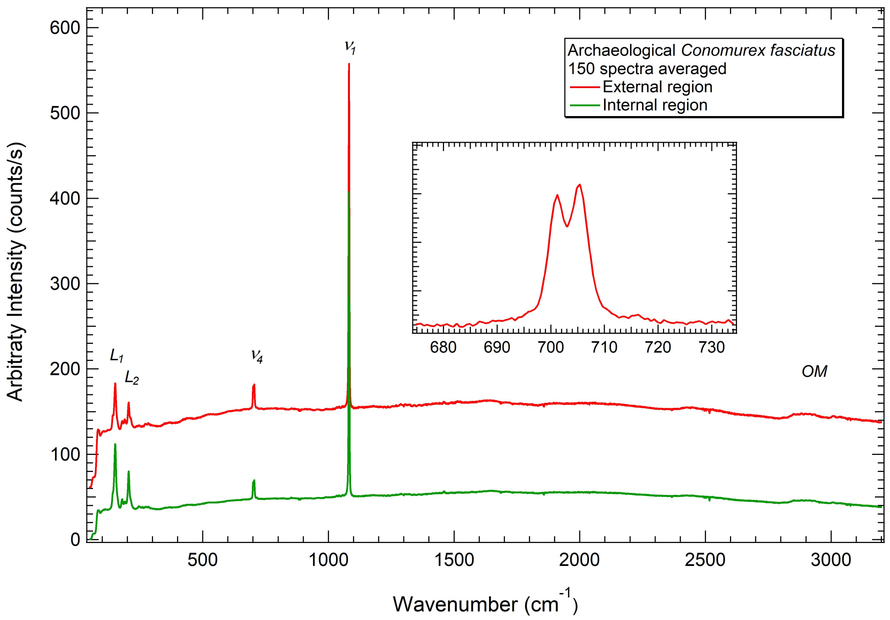

**Figure 3.1:** Archaeological *Conomurex fasciatus* averaged spectra. Both external (red line) and internal (green line) shell region spectra correspond to aragonite. The assignments and positions of the identified calcium carbonate peaks ($L_1$, $L_2$, $\nu_4$ and $\nu_1$) are shown in Table 3.2. $OM$ corresponds to the vibrations of the organic shell matrix. The insert shows a detail of the $\nu_4$ peak in aragonite.

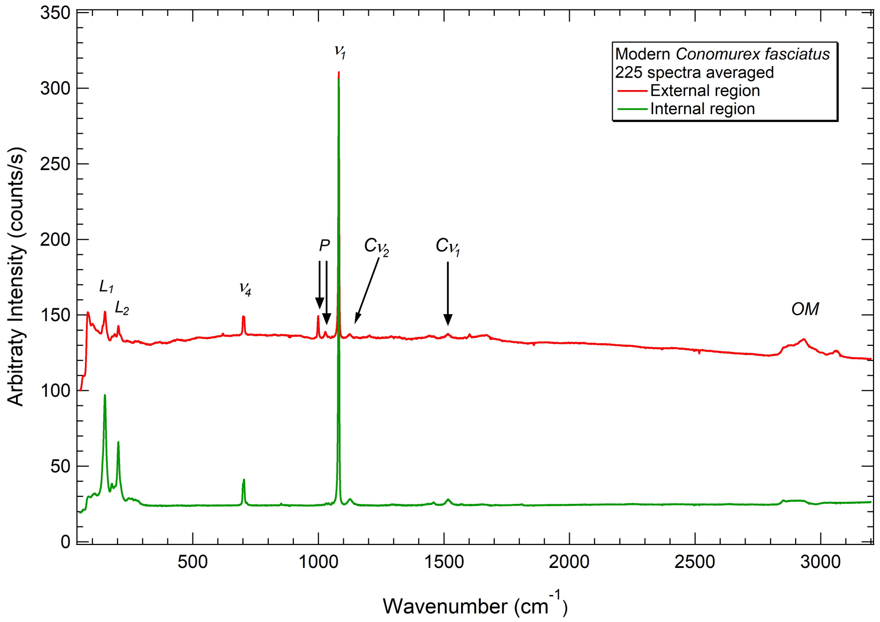

**Figure 3.2:** Modern *Conomurex fasciatus* averaged spectra. Both external (red line) and internal (green line) shell region spectra correspond to aragonite. Calcium carbonate ($L_1$, $L_2$, $\nu_4$ and $\nu_1$), carotenoid ($C\nu_1$ and $C\nu_2$) and phenylalanine ($P$) peaks are identified. Their peak positions and assignments are shown in Table 3.2. $OM$ corresponds to the vibrations of the organic shell matrix.

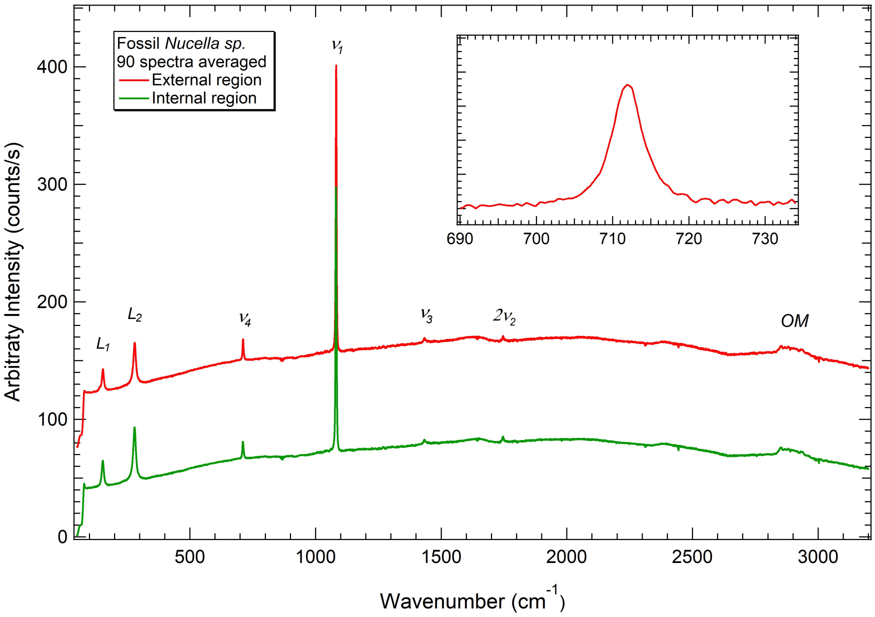

**Figure 3.3:** Fossil *Nucella* sp. averaged spectra. Both external (red line) and internal (green line) shell region spectra correspond to calcite. The assignments and positions of the identified calcium carbonate peaks ($L_1$, $L_2$, $\nu_4$, $\nu_1$, $\nu_3$ and $2\nu_2$) are shown in Table 3.2. $OM$ corresponds to the vibrations of the organic shell matrix. The insert shows a detail of the $\nu_4$ peak in calcite.

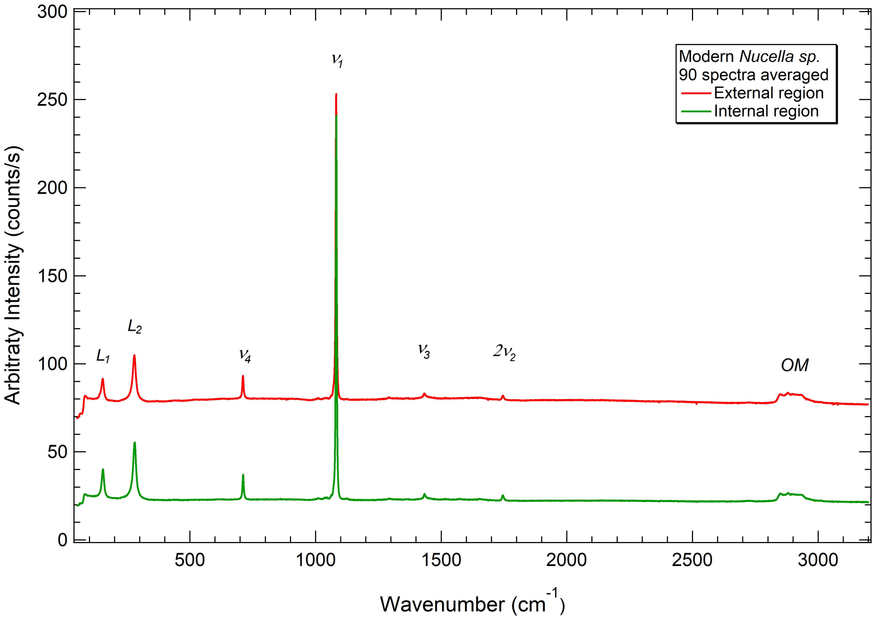

**Figure 3.4:** Modern *Nucella* sp. averaged spectra. Both external (red line) and internal (green line) shell region spectra correspond to calcite. The assignments and positions of the identified calcium carbonate peaks ($L_1$, $L_2$, $\nu_4$, $\nu_1$, $\nu_3$ and $2\nu_2$) are shown in Table 3.2. $OM$ corresponds to the vibrations of the organic shell matrix.

As seen from the spectra collected in these shells, the Raman signature of aragonite (Figures 3.1 and 3.2) and calcite (Figures 3.3 and 3.4) although similar, has some very distinct characteristics that easily discriminate one from another. These differences are found in the band between 100 and 300 cm$^{-1}$ and in the peaks around 700 cm$^{-1}$.

In the band between 100 and 300 cm$^{-1}$ lies the translational ($L_1$) and librational ($L_2$) lattice modes [92, 104]. The $L_1$ mode corresponds, in aragonite to two peaks that were observed at 141.30 cm$^{-1}$ and 151.30 cm$^{-1}$ (Figures 3.1 and 3.2); as for calcite just one peak is observed and it was measured at 153.70 cm$^{-1}$ (Figures 3.3 and 3.4). The librational mode $L_2$ was measured at 204.80 cm$^{-1}$ for aragonite and at 280.00 cm$^{-1}$ for calcite (Figures 3.1 to 3.4).

The peaks around 700 cm$^{-1}$ are the internal in-plane antisymmetric bend (marked with $\nu_4$ in the Figures 3.1, 3.2, 3.3 and 3.4) [92, 104]. This band involves a doublet measured at 700.50 cm$^{-1}$ and 704.90 cm$^{-1}$ in the case of aragonite and a single peak observed at 711.90 cm$^{-1}$ for calcite (Figures 3.1 and 3.3). The strongest Raman band lies at ∼1082 cm$^{-1}$ ($\nu_1$) for both aragonite and calcite (Figures 3.1, 3.2, 3.3 and 3.4) and it is related to the symmetric stretching of the carbonate ion [92].

For calcite the band between 1400 cm$^{-1}$ and 1800 cm$^{-1}$ has other two rather small peaks: the $\nu_3$ measured at 1433.2 cm$^{-1}$, which is related to the antisymmetric stretch [91], and the $2\nu_2$ observed at 1746.0 cm$^{-1}$, which is an overtone of the infra-red active only mode $\nu_2$ [91, 158]. These peaks can be seen in Figures 3.3 and 3.4.

The calcium carbonate peaks studied in this research are the translational and librational modes ($L_1$ and $L_2$), along with the in-plane antisymmetric bend ($\nu_4$) and the symmetric stretch ($\nu_1$). These were marked with $L_1$, $L_2$, $\nu_4$ and $\nu_1$ in the Figures 3.1, 3.2, 3.3 and 3.4. However, throughout this chapter they are identified by their peak positions, as two peaks are observed for the $L_1$ and $\nu_4$ vibrations for aragonite, whereas only one peak is observed for calcite.

Carotenoids were observed in both internal and external regions of modern *Canomurex fasciatus* shell and are marked with $C\nu_1$ and $C\nu_2$ in the spectra displayed in Figure 3.2. Carotenoids are a strong natural colourant, widespread in nature that can be found in many animals and vegetables [159]. They are polyene chains with multiple conjugated carbon-carbon single and double bonds [153]. The two strong bands in their Raman signature, $\nu_1$ (between 1400-1600 cm$^{-1}$) and $\nu_2$ (between 1100-1200 cm$^{-1}$), are related, respectively, to double and single carbon-carbon stretching vibrations [153–156]. The position of the carotenoid $\nu_1$ peak is known to depend on the length of the carbon chain [156, 159], but within the large number of different carotenoids, the Raman spectra of the natural carotenoids do not differ much from the $\beta$-carotene [154].

Organic residue, probably from the cleaning process, was found by RS on the external surface of the modern *Conomurex fasciatus* shell. This shell was cleaned by our collaborators only with fresh water, without any other chemicals being used. Thus, the presence of organic biomolecules were found together with the aragonitic signature. This organic residue caused the fluorescent background that is not present in the internal shell region, as observed in Figure 3.2. Two peaks assigned to vibrations of phenylalanine are indicated with $P$ in the figure; their positions are at 999.6 cm$^{-1}$ and 1028.2 cm$^{-1}$ and are in accordance with the literature [157]. Although phenylalanine is an amino-acid present in the organic matrix of shells [94], the organic matrix is only detected by RS in the high-wavenumber region above 2800 cm$^{-1}$ [101]. The organic matrix peaks were marked with $OM$ in Figures 3.1, 3.2, 3.3 and 3.4. Another piece of evidence for the presence of these external organic molecules is the intense CH vibrations, observed from 2800 to 3100 cm$^{-1}$ that are originated from the external organic biomolecules overlapping with the low intense peaks from the organic shell matrix.

## 3.3 Modern versus ancient shell comparison

For the comparison of modern versus ancient shells, as indicated by the convergence tests, 300 spectra were collected, including external and internal regions of the shells, for the archaeological *Conomurex fasciatus*, 450 spectra for the modern *Conomurex fasciatus* and 180 spectra for each fossil and modern *Nucella* sp. shell. As these data are extensive, the complete tables containing the fitting coefficients of each individual spectrum as described in Table 2.5 from Subsection 2.2.5, of Chapter 2 are not included here. However, summarised versions of these tables, called here statistical tables, containing only the final average for each peak are shown in Appendix A.2 and contain all the quantitative data split by shell species, age and shell region of spectra collection (internal or external). The averaged information for all analysed peaks, such as the final mean value, the SE and the CV are found in the statistical tables for the FWHM and peak intensity ratio analyses. These eight tables (Table A.1 to A.8) are shown in Appendix A.2.

Figures 3.5 and 3.6 compare the FWHM obtained from the statistical tables between the modern and ancient shells for the *Conomurex fasciatus* and *Nucella* sp., respectively. Each figure compares the final FWHM mean for the (a) external and (b) internal regions of the respective shells. The error bars represent the SE of the mean associated with the FWHM.

As seen from these two figures, modern shells have large FWHM mean values for most peaks in both external and internal regions. The only exception to this trend was the 141 $\text{cm}^{-1}$ peak measured at the external region for the *Conomurex fasciatus* shell. The aragonite lattice mode peak at 141 $\text{cm}^{-1}$ has a weak intensity Raman signal and it is neighboured by a more intense peak at 151 $\text{cm}^{-1}$, a combination that makes it difficult for curve fitting. This feature can be seen in Figures 3.1 and 3.2, and it is highlighted in Figure 2.9. The peak at 141 $\text{cm}^{-1}$ can also be easily overcome by the fluorescent background or

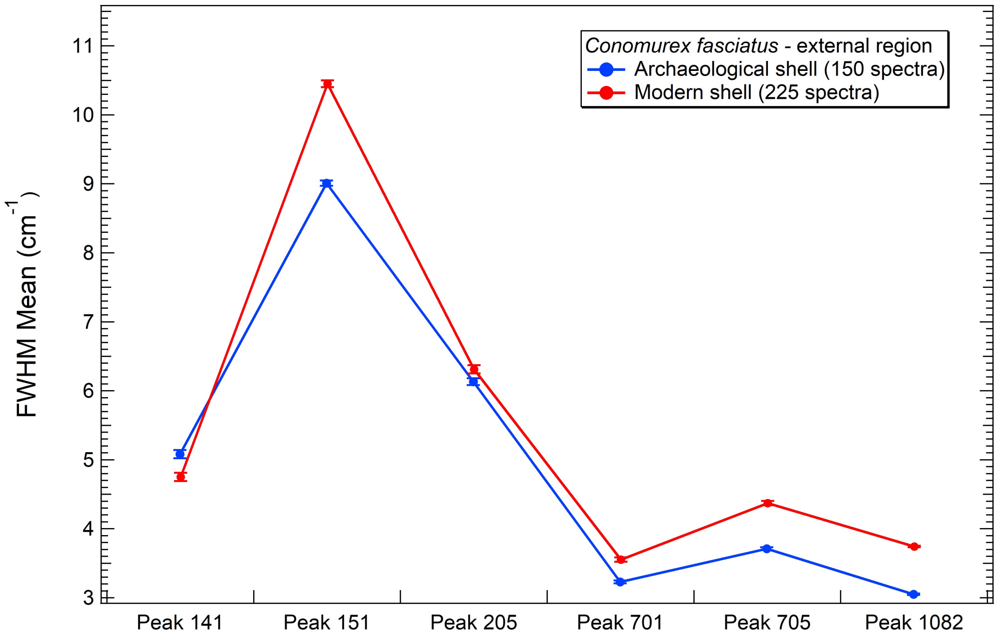

**(a)**

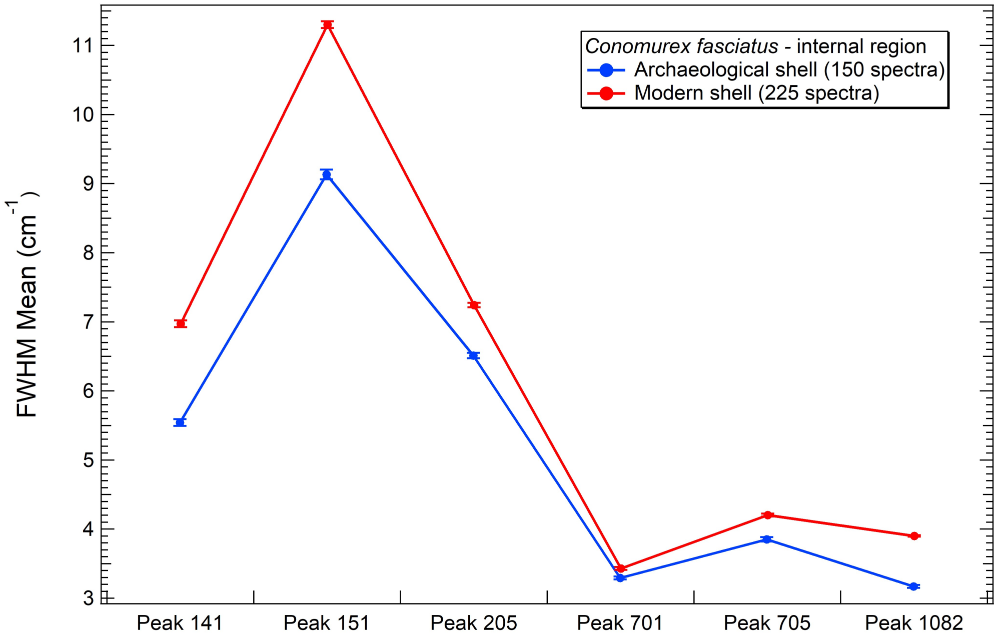

**(b)**

**Figure 3.5:** Modern versus ancient shell FWHM mean comparisons for the *Conomurex fasciatus*. The FWHM mean values from the six peaks studied are shown for the (a) external and (b) internal regions of the shell. The error bars represent the SE of the mean over all obtained spectra.

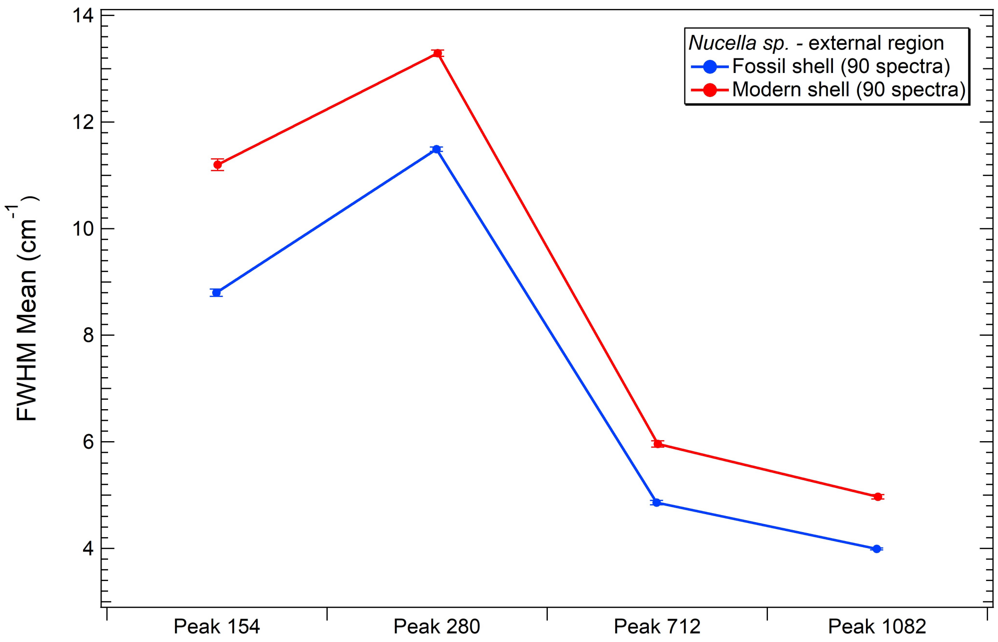

**(a)**

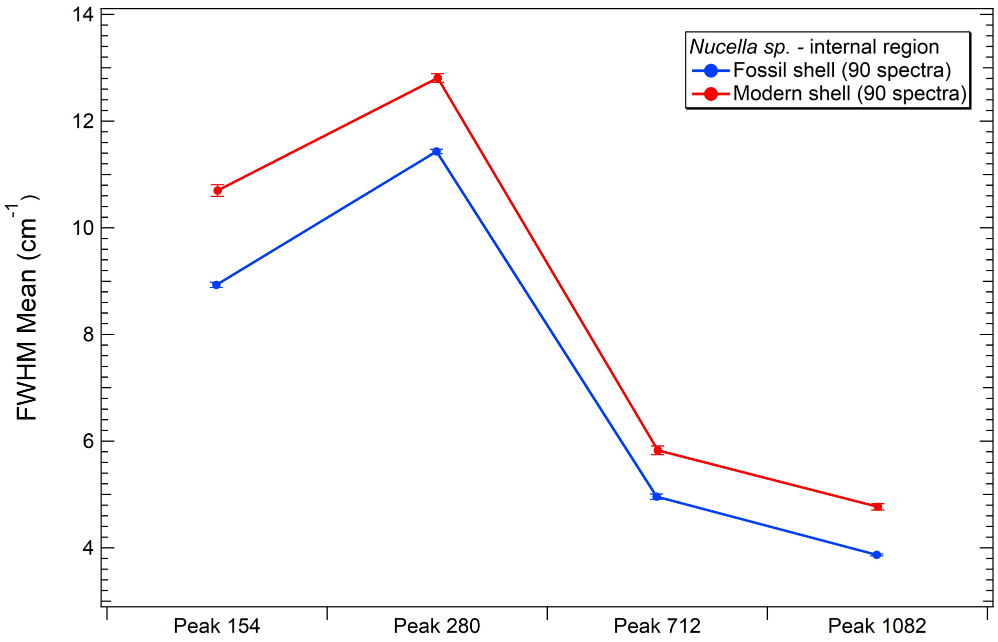

**(b)**

**Figure 3.6:** Modern versus ancient shell FWHM mean comparisons for the *Nucella* sp. The FWHM mean values from the four peaks studied are shown for the (a) external and (b) internal regions of the shell. The error bars represent the SE of the mean over all obtained spectra

even by noise in the cases where the quality of the spectrum is poor. Also this peak may be fully convoluted with the peak at 151 cm$^{-1}$. These problems increased the statistical dispersion for the peak at 141 cm$^{-1}$, being higher than any other peak for this shell, as demonstrated by its coefficient of variation in Tables 3.3 and 3.4.

For the *Conomurex fasciatus* species, the biggest separation between the FWHM of the modern and archaeological shells was found for the peak at 151 cm$^{-1}$, in both internal and external shell regions; however, a separation of their FWHM was also achieved for the peaks at 705 cm$^{-1}$ and 1082 cm$^{-1}$ (Figure 3.5). The FWHM of all peaks from modern and fossil *Nucella* sp. shells were separated, for both external and internal shell regions, as seen in Figure 3.6. Likewise for the *Conomurex fasciatus*, the largest difference in the FWHM values was observed for the lattice mode peaks, *i.e.* at 154 cm$^{-1}$ and 280 cm$^{-1}$ (Figure 3.6).

Tables 3.3 and 3.4 quantify the FWHM difference for each peak between modern and ancient shells, for the external and internal shell regions of both studied species. These tables summarise the results from the graphs shown in Figures 3.5 and 3.6. In the tables, the peaks are sorted by the absolute FWHM difference found, placing the highest value first. The CV column is the statistical dispersion of the population that generated the FWHM mean for each respective peak. The CV result only informs the highest value found, which may belong to the modern or the ancient shell.

The FWHM is correlated with the crystallinity of the material, such that the thinner the spectral band, the higher the crystallinity of the material [50]. Therefore, the ancient shells had their crystallinity increased through the diagenesis process. The same trend has been noticed for archaeological bioapatites, in bones and teeth, where an increase in the crystallinity has been linked to changes in the crystal structure caused by the loss of collagen (organic compound) [39, 160–162]. On biocarbonates, the destruction of the

**Table 3.3:** FWHM difference between the modern and the ancient shell for the external shell region. The table is sorted by the absolute FWHM difference. The CV column informs the highest statistical dispersion found for the population that generated the FWHM mean.

| Shell species | Peak position ($cm^{-1}$) | FWHM difference ($cm^{-1}$) | CV (%) |
|---|---|---|---|
| *Conomurex fasciatus* | Peak 151 | 1.50 ± 0.09 | 7 |
| | Peak 705 | 0.70 ± 0.05 | 11 |
| | Peak 1082 | 0.60 ± 0.02 | 6 |
| | Peak 701 | 0.40 ± 0.05 | 13 |
| | Peak 205 | 0.2 ± 0.1 | 15 |
| | Peak 141 | -0.3 ± 0.1 | 18 |
| *Nucella* sp. | Peak 154 | 2.2 ± 0.2 | 9 |
| | Peak 280 | 1.8 ± 0.1 | 5 |
| | Peak 712 | 1.1 ± 0.1 | 9 |
| | Peak 1082 | 1.00 ± 0.06 | 9 |

**Table 3.4:** FWHM difference between the modern and the ancient shell for the internal shell region. The table is sorted by the absolute FWHM difference. The CV column informs the highest statistical dispersion found for the population that generated the FWHM mean

| Shell species | Peak position ($cm^{-1}$) | FWHM difference ($cm^{-1}$) | CV (%) |
|---|---|---|---|
| *Conomurex fasciatus* | Peak 151 | 2.2 ± 0.1 | 10 |
| | Peak 141 | 1.5 ± 0.1 | 12 |
| | Peak 1082 | 0.70 ± 0.03 | 8 |
| | Peak 205 | 0.70 ± 0.07 | 8 |
| | Peak 705 | 0.30 ± 0.05 | 9 |
| | Peak 701 | 0.10 ± 0.04 | 8 |
| *Nucella* sp. | Peak 154 | 2.1 ± 0.1 | 10 |
| | Peak 280 | 1.4 ± 0.1 | 6 |
| | Peak 1082 | 0.90 ± 0.08 | 12 |
| | Peak 712 | 0.8 ± 0.1 | 12 |

organic components, or their replacement by inorganic materials, takes place during diagenetic alterations [138, 140]. This decay of the organic matrix has also been observed for Pleistocene brachiopod shells [163]. Perrin and Smith (2007) studied the organic skeletal matrix of aragonitic corals with RS and linked a reduction in the intensity of the C–H bands (2850 – 2960 $cm^{-1}$) with the diagenesis process [78]. They correlated this decay of the Raman peaks' intensities to the hydrolysis of glycoproteins, which caused the C–H bands to decompose into a series of multiple vibrations, hence decreasing the signal of individual bands [78]. In their work, they also suggested that, in corals, the hydrolysis of the organic matrices could also initiate the recrystallisation of biogenic aragonite into calcite [78]. In foraminiferan calcite, studies conducted with FTIR, revealed that the dissolution of small disordered phases of the carbonate contributed to bulk increases in crystallinity [79]. Therefore, these compositional changes led to an increase of the crystallinity that can be used to quantify the diagenetic alterations in the ancient shells.

The peak intensity ratio analyses, unlike the FWHM analyses, does not show a clear trend between the modern and ancient shells for the internal and external regions. Figures 3.7 and 3.8 illustrate the peak intensity ratio comparison for the *Conomurex fasciatus* and *Nucella* sp., respectively, for the (a) external and (b) internal regions. The error bars are represented by the propagated SE of the mean corresponding to the obtained peak intensities.

As seen for the *Conomurex fasciatus* (Figure 3.7), the trends in the peak intensity ratios are not consistent, such that the red and blue lines, which represent the modern and archaeological shells, respectively, cross and do not display a trend that can be applied for both internal and external shell regions. A discrepancy in the intensity ratio value was also noticed when the same ratio is compared between the internal and external regions, as seen in Figure 3.7. To facilitate this comparison both graphs are shown on

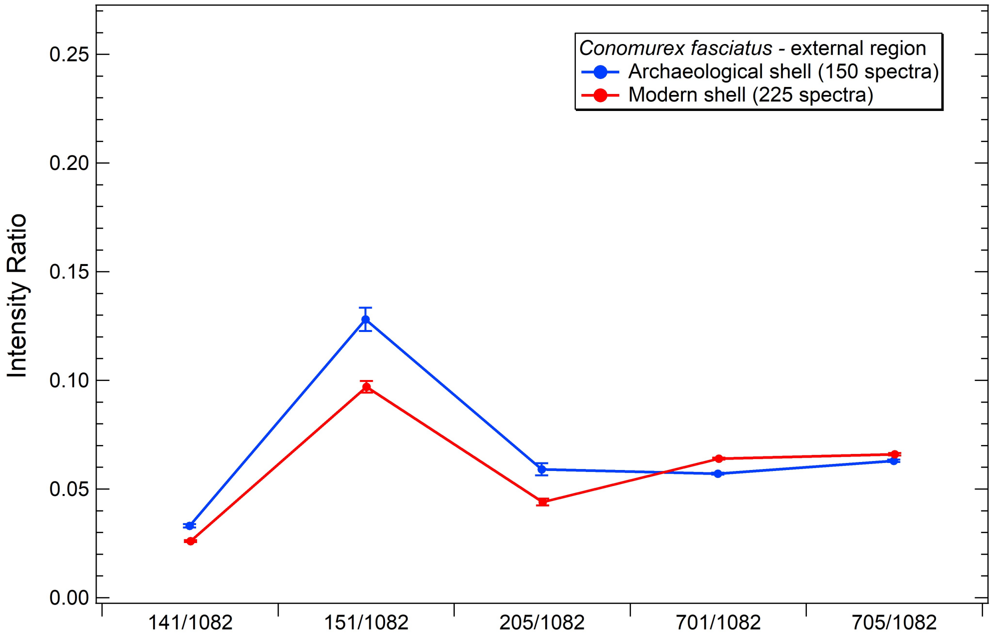

**(a)**

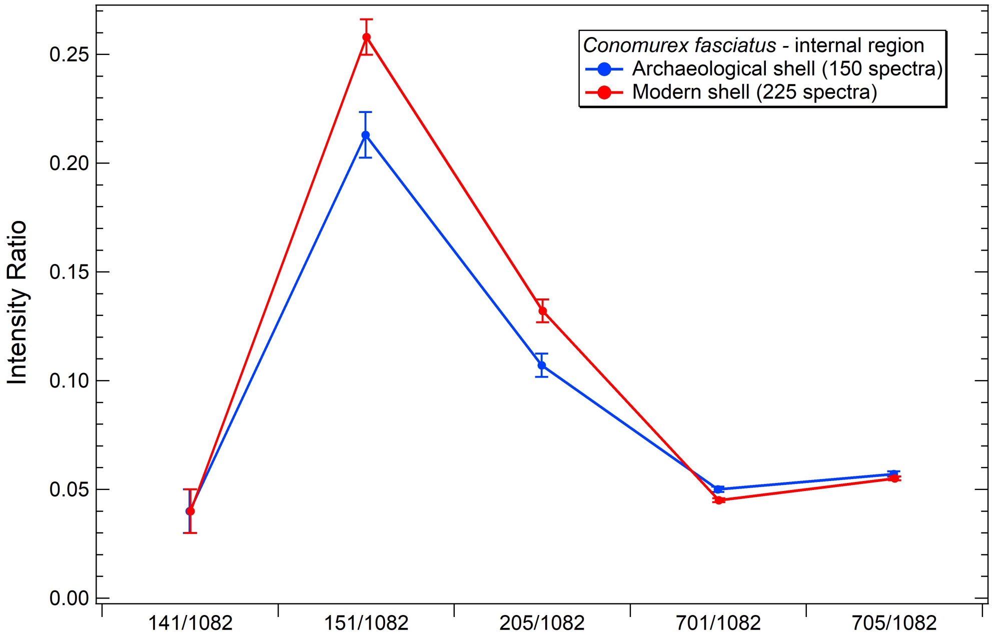

**(b)**

**Figure 3.7:** Modern versus ancient shell peak intensity ratio mean comparisons for *Conomurex fasciatus*. The peak intensity ratios from the six peaks studied are shown for the (a) external and (b) internal regions of the shell. The error bars are the SE of the mean, over all obtained spectra, determined from the propagated peak intensity errors.

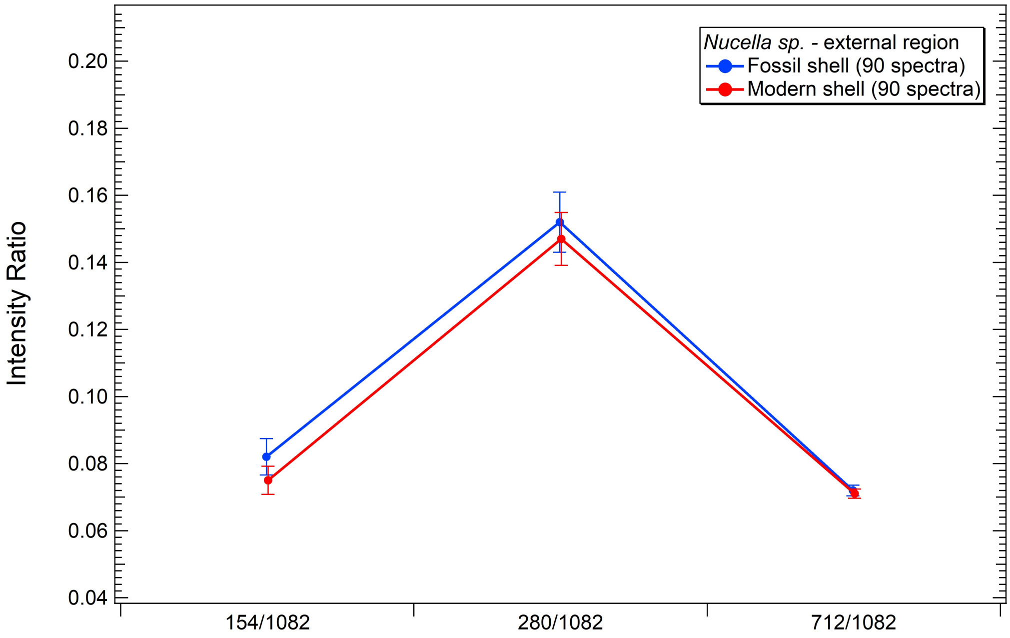

**(a)**

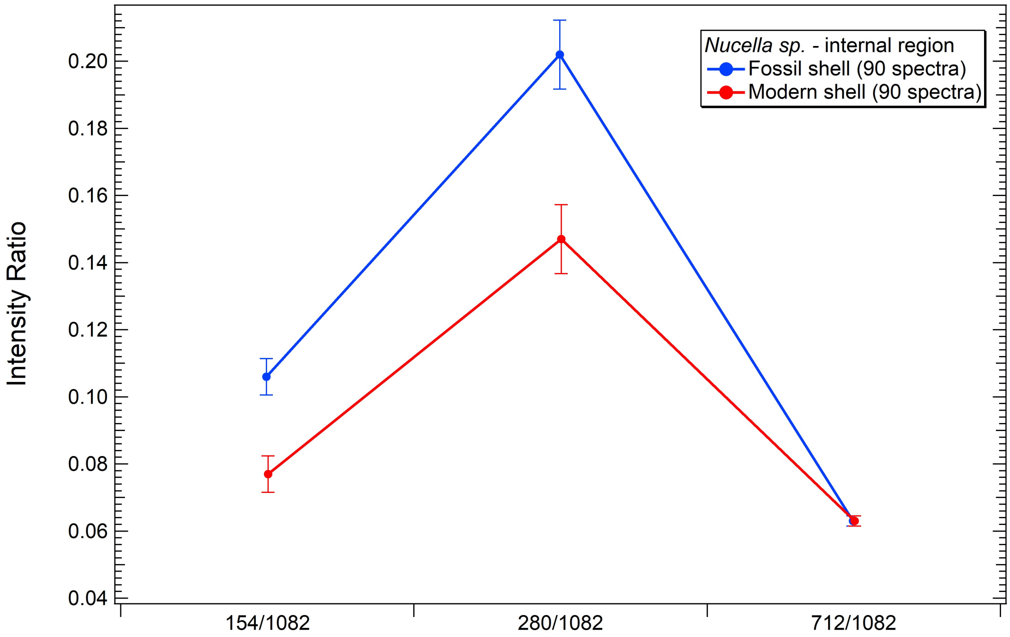

**(b)**

**Figure 3.8:** Modern versus ancient shell peak intensity ratio mean comparisons for *Nucella* sp. The peak intensity ratios from the four peaks studied are shown for the (a) external and (b) internal regions of the shell. The error bars are the SE of the mean, over all obtained spectra, determined from the propagated peak intensity errors.

the same scale. It can be seen that the external 151/1082 and 205/1082 intensity ratios are dwarfed in comparison to the internal region ratios. Finally, for certain ratios, such as 141/1082, 701/1082 and 705/1082, the modern and ancient shells are not separated, or their separation is not expressive enough, as demonstrated by Figure 3.7.

For the *Nucella* sp. (Figure 3.8), the external and internal graphs show the same trend observed for the *Conomurex fasciatus* shells; however, the external region (Figure 3.8a) did not show a statistically significant separation between fossil and modern shells. The internal region (Figure 3.8b) is more sensitive to these differences, and apart from ratio 712/1082, all other ratios fully discriminated both shells. For both shells, the intensity ratios that were able to identify some separation between modern and ancient shell were those involving peaks from the lattice mode, such as the 151/1082 and 205/1082 for the *Conomurex fasciatus*, and 280/1082 and 154/1082 for the *Nucella* species. The magnitude of the lattice peaks, which arise from translational and rotational motions of the $CO_3$ groups, is determined by inter-ionic forces [103]. Thus, the peak intensity ratios reflect the changes in the inter-ionic forces between modern and ancient samples.

The diagenesis constitutes alterations after the spatial configuration is no longer altered by currents, organisms or desiccations, and until a primary metastable phase has been eliminated [164]. This means that the mineral will undergo changes that will engender a mineral stability. In biominerals the stability can be increased through the dissolution of unstable phases, recrystallisation of the unstable phases and/or growth of new authigenic phases [79]. Therefore, diagenesis is a difficult process to assess and, according to N. Guzman *et al.* (2009), there has been little progress in understanding diagenesis over the past 50 years [133]. Initially, it was common that only visual inspection of the shells was used to assess diagenesis. This included the identification of weathering processes, overgrowth of secondary calcite and the state of preservation of aragonite [138]. This visual classification method was soon proven inefficient when compared to other approaches, such as the analysis of the shell's elemental composition, the assessment of the organic matrices or the percentage concentration of calcite [138].

Measuring the diagenesis process through analyses of the mineralogy of shells consists in observing changes in the original mineralogy by the recrystallisation of aragonite into calcite by X-ray diffraction, electron microscopy or spectroscopic methods [70, 138, 140]. However, this approach can only be used to assess aragonitic shells. Nonetheless, it has to be clear that other processes may occur before the extreme case of the mineralogical transformation of aragonite to calcite [133].

In this section, modern and ancient shells of two different species were analysed. For both cases, their quantitative RS was able to detect differences between ancient and modern shells. However, unlike what was observed for the FWHM comparisons, the peak intensity ratios are not consistent in all of the cases analysed, which included the two shell species and their internal and external regions. These observations show that the FWHM obtained from the RS results are a more reliable variable for assessing the diagenesis process. Thus, this quantitative Raman parameter can be used to assess diagenesis on aragonitic shells and to complement other methods used for diagenesis evaluation.

## 3.4 SEM results

Scanning electron microscopy combined with energy dispersive x-ray was applied to the modern and archaeological *Conomurex fasciatus* shells to obtain their elemental composition. From both specimens, a small fragment near the shoulder of the shell was removed from the middle slice (Figure 2.7), which was also used for the RS analyses, and was coated with 6 nm of Pt/Pd alloy to prevent charging the samples with the electron beam. The accelerating voltage was 15 kV, with EDX analyses performed at random positions on the sample, and at magnifications ranging from 140x up to 4200x. Measurements were made from the internal and external regions of the fragment (see Section 2.4 for further details of the method).

SEM can be used to resolve the shell microstructure. Figure 3.9 shows two SEM micrographs from an archaeological *Conomurex fasciatus* specimen at two different magnifications (139x and 280x), taken from the internal shell region. The images suggest that the species has a crossed-lamellar structure, which is one of the most common structures found in the Gastropoda class [53, 165, 166]. The crossed-lamellar structure is described in literature as made of crossed layers of aragonite at variable angles, most commonly intersecting between 45 and 60 degrees, although the crossing is also possible at right angles [53, 57]. Such crossed layers can be clearly seen in the previous images.

Figure 3.10 shows three SEM micrographs from the internal region of a modern *Conomurex fasciatus* specimen. As seen in Figure 3.10a, there is a clear separation in the shell microstructure, marked with a dotted line rectangle. Both areas from inside and outside the rectangle have crossed-lamellar features, however orientated at different angles. Higher magnification of these two areas are presented in Figures 3.10b and 3.10c, which show, respectively, the inside and outside areas of the dotted line rectangle. These images highlight the different orientation observed for the crossed-lamelar layer. Similar observations in the orientation of the crossed-lamellar layer have been reported for other gastropod shells such as *Cypraea leviathan*, [57] *Phalium granulatum* [57] and *Strombus gigas* [57, 166].

The previous figures (Figure 3.9 and 3.10) also show the presence of aragonite in the *Conomurex fasciatus* shells. This calcium carbonate polymorph is characterised by a needle-like morphology that is clearly depicted by SEM [57, 166, 167], and is evident in the high magnification micrograph shown in Figure 3.10c.

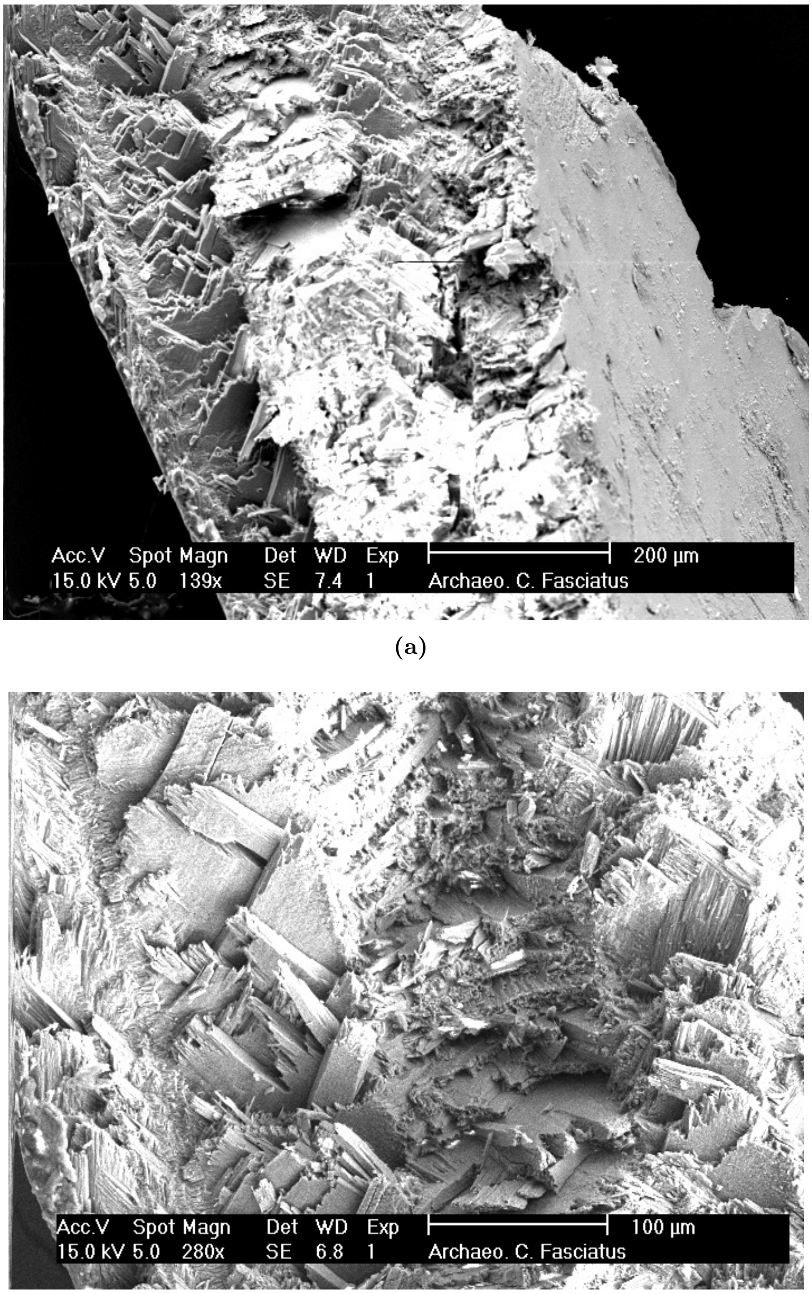

**(a)**

**(b)**

**Figure 3.9:** SEM micrographs for an archaeological *Conomurex fasciatus* shell fragment, at (a) 139x and (b) 280x magnification. Both micrographs show the internal shell region suggesting that the shell has a crossed-lamellar structure.

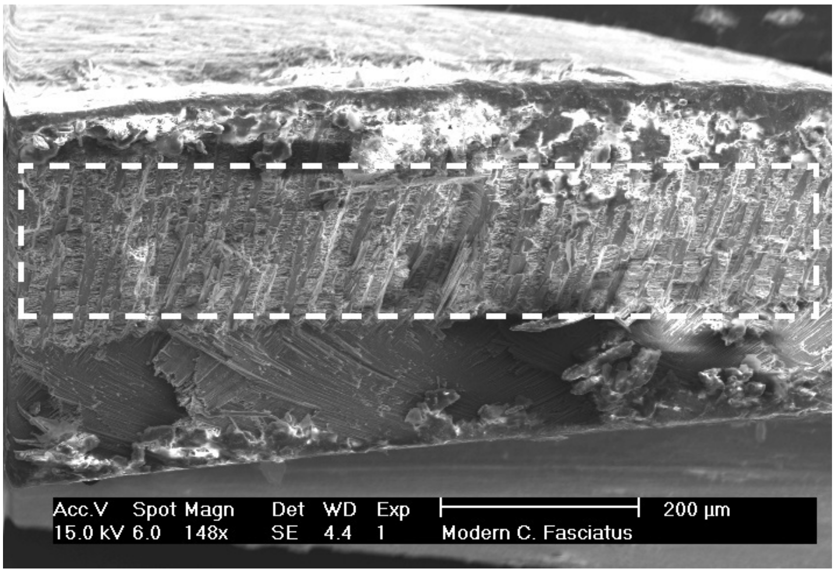

**(a)**

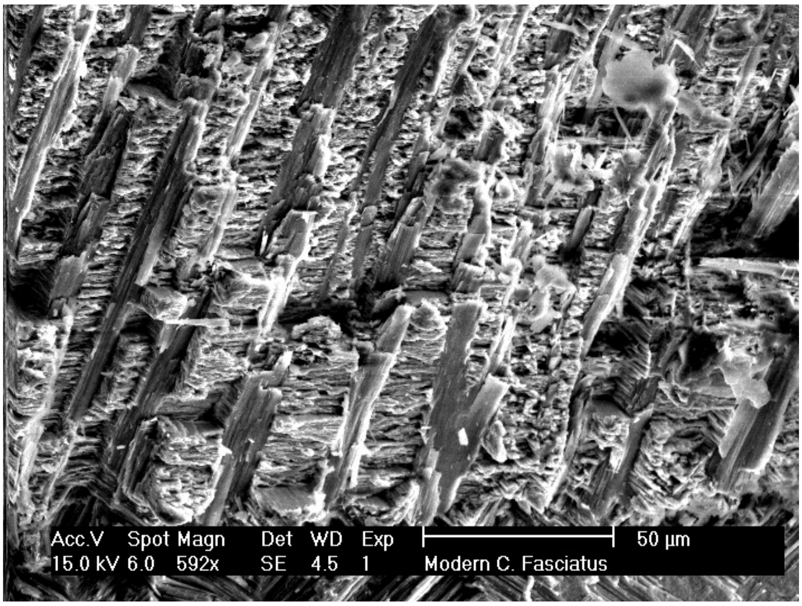

**(b)**

**Figure 3.10:** SEM micrographs for a modern *Conomurex fasciatus* shell fragment. The figure (a) shows a clear separation in the shell microstructure (marked with a dotted line rectangle). Both inside and outside areas of the rectangle have crossed-lamellar features orientated at different angles. Higher magnification of the inside and outside rectangle areas are also shown, respectively in figures (b) and (c). – *continued on the next page.*

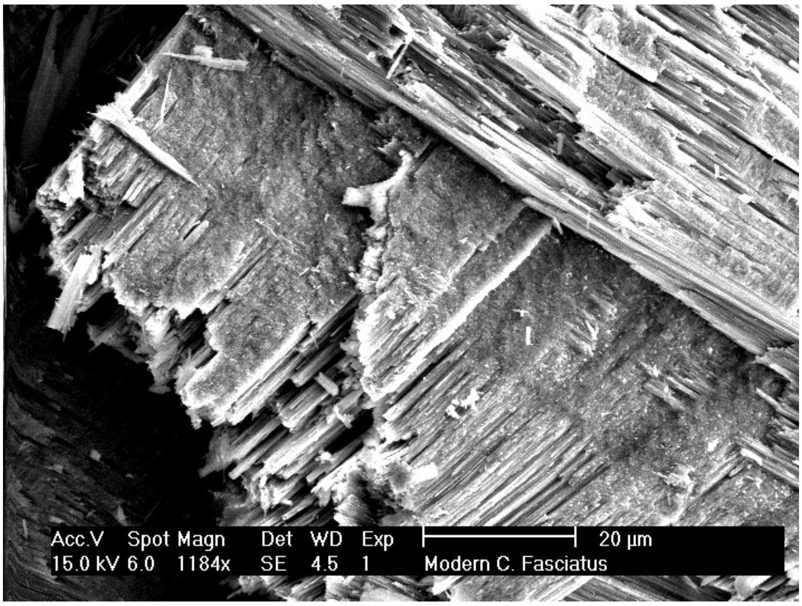

**(c)**

**Figure 3.10:** *Continued from previous page.*

The SEM quantitative analyses via EDX were performed at random positions and at different magnifications in each case; therefore, the results reflect only the analysed portions of the shells. For the archaeological shell, nine EDX analyses were performed at the external region, and eleven on the internal region. For the modern specimen, twelve and thirteen EDX spectra were taken at the external and internal regions, respectively. The quantitative results were then averaged together to compare both the internal and external regions of the modern and archaeological shells.

Figure 3.11 compares the EDX quantitative results for the major elements (Ca, C and O) found for the *Conomurex fasciatus* specimens. The atom percentage of each element is compared between modern and archaeological shell specimens. The Figure 3.11a informs the composition results for the internal shell region while Figure 3.11b presents the same for the external region.

The calcium carbonate molecule ($CaCO_3$) has one carbon atom, one calcium atom and three oxygen atoms. Thus, in an ideal case without impurities, the same proportion would be expected for the atom percentages obtained with the EDX analyses. That is approximately what the EDX has found for the internal regions of both modern and archaeological shells (Figure 3.11a), where the atom percentage for C and Ca is ∼20%, whilst ∼60% for O, with a maximum SE of 4.7%.

However, for the external region of the modern shell, a considerable amount of carbon was found, thus dropping the percentage values for the calcium and oxygen, and caused a separation between the modern and archaeological lines in Figure 3.11b. This result agrees with the Raman analyses on the external region of the modern shell, where extra peaks from organic biomolecules were found in the majority of the spectra collected, as consequence of the cleaning method of this shell. These organic biomolecules would then increase the amount of carbon found in the external part of the shell, thus reflecting the 66% ± 2% atom percentage found.

Claassen and Sigmann (1993), using atomic absorption spectroscopy (AAS), indicated that shells containing more than 40% of calcium in their composition had been subjected to diagenetic alterations [72]. This has not been the case for the analysed archaeological shells, since for both internal and external shell regions, the maximum percentage of calcium found was of 20% ± 2% (Figures 3.11 a and b).

The results of the quantitative analyses for the minor elements are shown in Figure 3.12, with (a) representing the internal and (b) the external regions of the shell. Magnesium, sulphur, potassium, sodium, zirconium and silicon were the elements found above the detection limits. Zirconium and sodium were present at higher percentages in all analysed samples. High concentrations of Na have also been observed in aragonitic modern gastropodes [57] and in fossil shells [139]. Apart from zirconium, all other elements have already been identified in calcitic and aragonitic corals [69], gastropodes and bivalves [57, 72, 77, 133, 139].

The calcite structure allows a wide compositional variation, including divalent cations such as Mn, Fe, Mg, Zn, Co and Ni; while aragonite include large cations like Sr, Pb and Ba [69]. However, the elemental composition may vary with shell species, calcite-to-aragonite ratio, geological environment, temperature, salinity, mollusc body part, diagenesis and time [70, 72]. As a general rule, Mg tends to replace the Ca on calcitic shells, while for aragonite Ca is normally replaced with Sr [70].

Atom percentage ratios of Mg/Ca and Sr/Ca, are used to evaluate diagenetic changes [70,138,139]. Therefore, the comparison of the chemistry of ancient shell skeletons to their modern counterparts would allow an evaluation of the chemical changes that occurred [70]. A decrease in the Mg/Ca ratios could indicate dissolution of the disordered phase that had been stablised with high Mg/Ca ratios (modern) [79]. In general the Mg concentration is observed to decrease for ancient shells [70, 139].

Although Sr was not observed in the *Conomurex fasciatus* shells analysed, which precludes the calculation of a Sr/Ca ratio, it can be seen that the concentration of Mg increased for the archaeological shell, on both external and internal shell regions (Figure 3.12). Such a finding however is in accordance with the results of Guzman *et al.* (2009) who observed, using EDX, an increase in Mg when comparing Pleistocene to modern shells, and a decrease in Mg when Holocene shells were compared to modern counterparts [133]. They correlated these variations for Holocene and Pleistocene shells to differences in the original compositions or differences in the fossilisation process.

Buchard and Weiner (1981), using AAS, although noted a depletion of Sr, also observed an increase of Mg in diagenetically modified ammonites [138]. They have demonstrated that the Mg/Ca concentration ratio, combined with the proportion of calcite in aragonitic samples were the most useful inorganic parameters for tracing diagenetic alterations. In the same work, they also showed that a diagenetic classification based only on the visual appearance of the shells is insufficient, finding no correlation between shell appearance and elemental composition [138].

There is no consensus on how much the Mg and Sr concentrations should change over time and this is because the minor element content varies according to the taxa, and also due to variations of the microstructure, mineralogy and chemical contents within a single layer of the shell structure [140]. From Figure 3.12, it can be seen that there is not a regular pattern for the elemental atom percentage between external and internal shell regions; thus, making the diagenesis assessment difficult. Therefore, diagenesis cannot be checked only within a site, but needs to be checked within a single shell or even within a single layer of a shell [133].

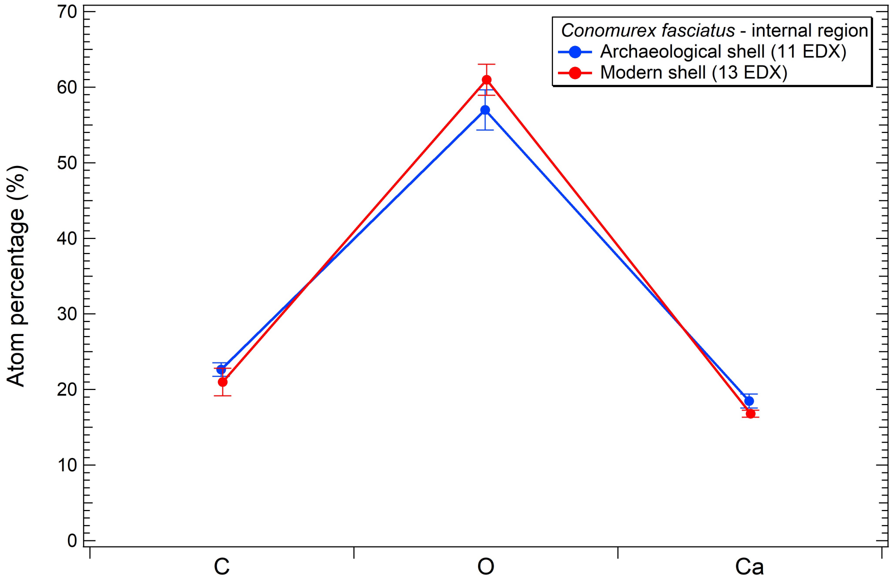

(a)

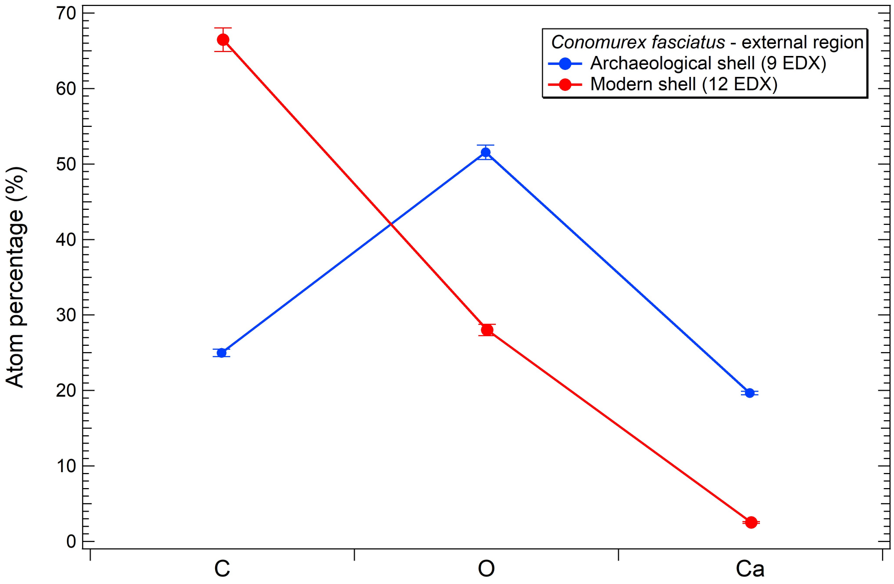

(b)

**Figure 3.11:** Quantitative EDX results for carbon, calcium and oxygen in the *Conomurex fasciatus* shell fragment obtained from the (a) internal and (b) external shell regions. The atomic percentages represent the average of all EDX performed, with error bars representing the SE. In (b), the increased percentage of C for the external region of the modern shell results from organic biomolecule residues as consequence of the cleaning process.

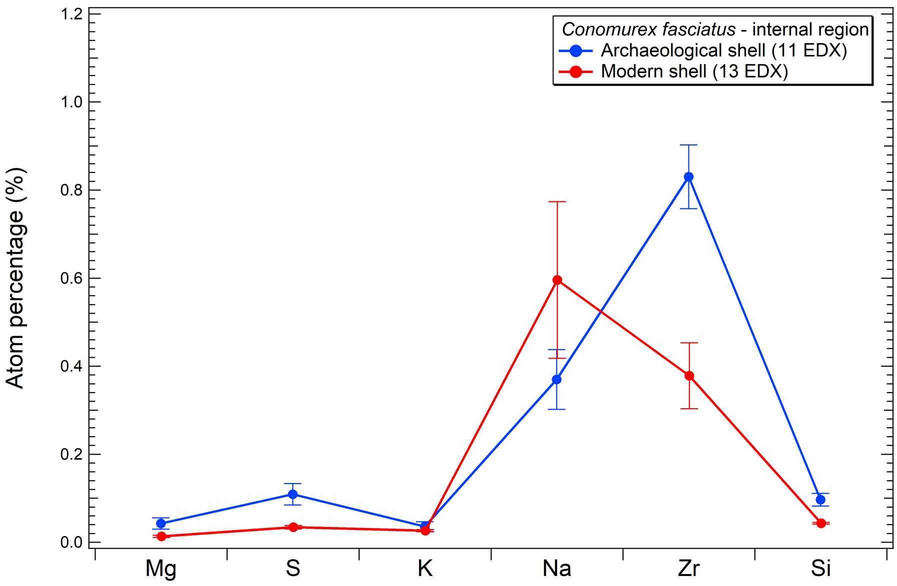

**(a)**

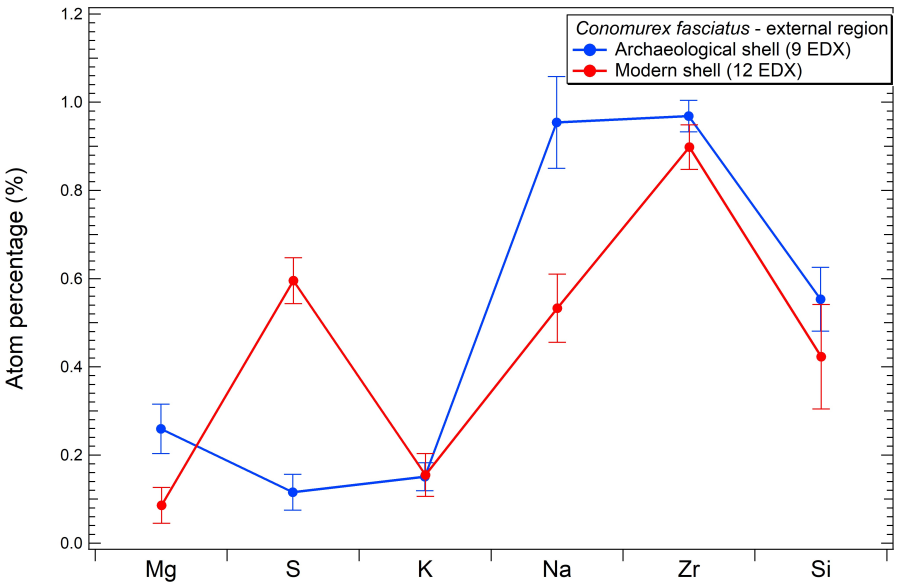

**(b)**

**Figure 3.12:** Quantitative EDX results for minor elements in the *Conomurex fasciatus* shell fragments obtained from the (a) internal and (b) external shell regions. The atomic percentages represent the average of all EDX performed, with error bars representing the SE.

## 3.5 Conclusions

Diagenesis has been a difficult process to assess, mainly for visually well preserved specimens. It can be measured through the assessment of the original shell mineralogy and the recrystallisation of aragonite into calcite. Although this approach can only be applied to aragonitic shells, other processes may still occur before the extreme mineralogical phase transformation of aragonite to calcite.

The aim of this chapter was to verify whether RS could be used as a complementary technique for assessing diagenetic changes on both aragonitic and calcitic shells. Thus, two different shell species were analysed and compared to their modern counterparts: *Conomurex fasciatus* and *Nucella* sp. species.

Initially, convergence tests determined the minimum amount of spectra necessary to statistically represent each shell specimen. Therefore, 150 spectra were collected in each internal and external regions of the archaeological *Conomurex fasciatus* shell (30 spectra per slice), while a total of 225 spectra were obtained in each region of the modern specimen (45 spectra per slice). As per the fossil and modern *Nucella* sp. shells, 90 spectra were collected in each region.

From the obtained Raman spectra, the *Conomurex fasciatus* species were characterised as composed of aragonite, whereas the *Nucella* sp. specimens were represented by calcite, with peak positions of both calcium carbonate polymorphs corresponding to the literature. Natural colourants, known as carotenoids were observed in both internal and external regions of modern *Conomurex fasciatus*. Peaks assigned to vibrations of phenylalanine were observed in the external surface of the modern *Conomurex fasciatus* shell, characterising remaining organic residues from the cleaning process, once only fresh water was used.

FWHM and peak intensity ratios of Raman bands were investigated as markers for diagenetic alterations. Although the peak intensity ratio results were not consistent for both internal and external regions of modern and ancient shells, ratios involving peaks from the lattice mode were able to separate modern from ancient shells. Such ratios are the 151/1082 and 205/1082 for the *Conomurex fasciatus*, and 280/1082 and 154/1082 for the *Nucella sp.*

The FWHM of the Raman bands was noted to be a better and more sensitive marker for diagenetic changes. For both species analysed the FWHM decreased, on both regions of sampling (internal and external) for the ancient shells. If the statistical dispersion on the samples, the difficulty of fitting low intensity peaks and the absolute difference on the FWHM is taken into account, the best FWHM markers are the main calcium carbonate peak ($\nu_1$) at 1082 cm$^{-1}$ and the lattice mode peak ($L_1$) at 151 cm$^{-1}$ if aragonite or at 154 cm$^{-1}$ if calcite.

Since the FWHM is correlated with the material's crystallinity, this decrease in the FWHM for the ancient shells indicates that they had become more crystalline over time. Such increase in crystallinity has already been noticed on archaeological bioapatites and linked to changes in the crystal structure caused by the loss of their organic compound, which take place during diagenetic alterations. During the diagenesis of biominerals, a mineral stability is obtained by the dissolution and recrystallisation of unstable phases or the growth of new phases. Thus, these compositional changes lead to an increase of the crystallinity that can be measured by RS and used to quantify the diagenetic alterations in the ancient calcitic or aragonitic shells.

SEM was used to depict the microstructure of the *Conomurex fasciatus* shells, suggesting that the species has a crossed-lamellar structure with different angled orientations. It also showed the presence of aragonite, characterised by its needle-like morphology.

EDX quantitative analyses of the major elements (Ca, C and O) present in the *Conomurex fasciatus* specimens, revealed no alterations in the Ca atom percentage, with a maximum of 20% ± 2% measured. Shells that contain more than 40% of calcium in their composition are considered diagenetically altered. A considerable amount of carbon (66% ± 2% atom percentage) was found in the external region of the modern shell, thus corresponding to the organic residue also observed with RS.

Minor compositional elements, such as magnesium, sulphur, potassium, sodium, zirconium and silicon were found on both internal and external shell regions. With the exception of zirconium, all other elements have already been described in corals and shells. No regular pattern for the elemental atom percentage between external and internal shell regions was noted; thus, making the diagenesis assessment difficult. Sr was not measured in the *Conomurex fasciatus* shells analysed and an increase of Mg was observed on both internal and external regions of the archaeological specimen. Such an increase has already been noted in Pleistocene shells and diagenetically modified ammonites. However, there is no consensus in the literature on how much the Sr and Mg concentrations should change over time, once this minor element content varies with the taxa, microstructure and mineralogy.

The findings of this chapter reveal that the crystallinity of the calcium carbonate can be a good and consistent parameter for assessing diagenesis. The crystallinity is easily measured with RS and can be straightforwardly compared between modern and ancient samples. Although the results are promising, more studies with shells of different ages, species, preservation states and geographic locations are necessary to validate this method.

# Chapter 4

# Quantitative study of biogenic aragonite to calcite transition

Ancient shells are often used in palaeoenvironmental reconstructions, where heavy isotopes of oxygen and carbon are linked to the sea temperature and its salinity. However, heating hampers these analyses once the isotopes are removed from the sample during the aragonite to calcite phase transition. Thus, since archaeological shells may have endured unintentional heating, or even intentional heating with the purpose of cooking, it is important to understand how the temperature affects them. In this chapter, quantitative RS was used to study the aragonite to calcite transition in *Conomurex fasciatus* modern shells as a first step to detecting heating evidence in archaeological sea shells. Modern specimens were powdered and to simulate cooking these were heat-treated at constant temperatures from 100°C up to 500°C for periods of time ranging from 3 min up to 8h. Percent composition change from aragonite to calcite were estimated from the Raman spectra by comparing the intensity of the aragonite and calcite lattice mode $L_2$ peak (~205 cm$^{-1}$ for aragonite and ~280 cm$^{-1}$ for calcite). The $L_1$ and $\nu_1$ peaks were studied to investigate their sensitivity to the heat treatments by analysing their FWHM and peak intensity ratios. SEM and EDX complemented the analyses carried out in the modern powdered shells. Burnt archaeological *Conomurex fasciatus* fragments were analysed with RS and their results were compared to those obtained from the modern shells, attempting to use RS as a tool to detect evidence of heating in shells and estimate the temperature at which it has occurred.

## 4.1 Convergence test on powdered samples

In order to identify the minimum quantity of spectra necessary to characterise the powdered samples, a convergence test of the SE associated with the FWHM of the main calcium carbonate peak ($\nu_1$) was used. This test was explained in Section 2.2.6 and the methods to obtain the powdered shells were detailed in Section 2.2.3 of Chapter 2. The convergence test was applied to one of the three shell replicates used in the heating experiments: the S1 sample, unheated. As shown in Figure 4.1, the stabilisation of the SE, corresponding to the FWHM, occurred with $\sim$200 random spectra averaged. Therefore, for each of the three powdered replicates (S1, S2 and S3) used in this chapter, 200 spectra were collected for each unheated and thermally treated sub-sample, which then were individually fitted. For the laser heating test a different quantity of spectra was collected, this being further explained in Section 4.3.

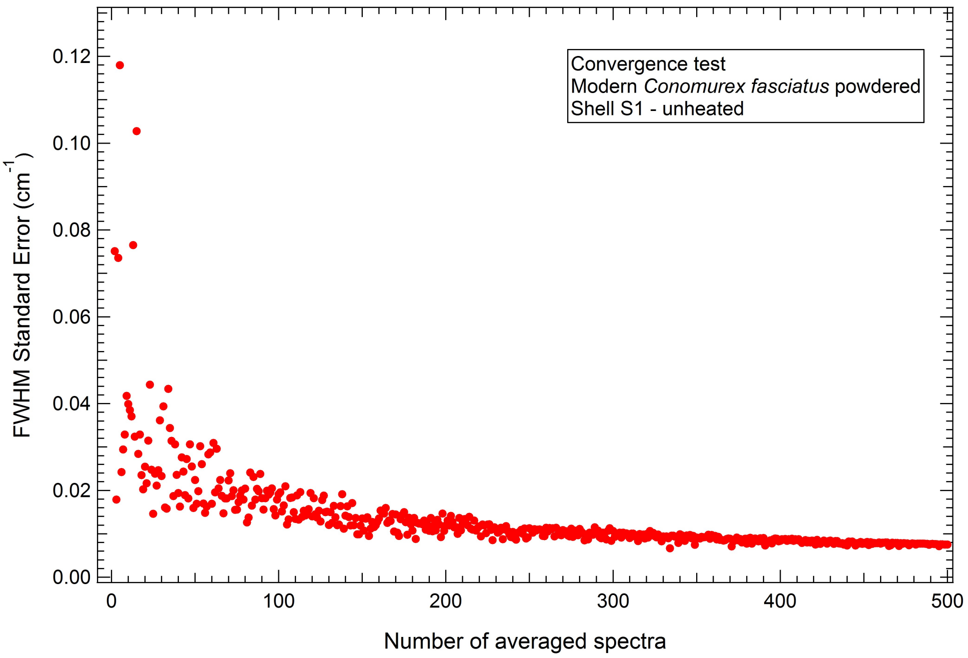

**Figure 4.1:** Convergence test for the unheated powdered shell S1, showing how the standard error associated with the FWHM of the main calcium carbonate peak ($\nu_1$) decreases with the amount of spectra averaged. This result was used to guide the quantity of spectra needed from each powdered sub-sample to decrease the uncertainty associated with the quantitative measurements.

## 4.2 Spectral range

This chapter focuses on studying the quantitative parameters of two Raman peaks from the calcium carbonate signature: the lattice mode $L_1$ and the main $\nu_1$ peak, respectively positioned around ~152 cm$^{-1}$ and ~1082 cm$^{-1}$. These are the only peaks shared in common by the aragonite and calcite Raman spectra.

The Figure 4.2 shows, as an example, the full spectral range of the averaged spectra obtained for the modern *Conomurex fasciatus* unheated samples S1, S2 and S3. The only peaks present in the spectra, above 2000 cm$^{-1}$ are overtones of the carotenoid vibrations (marked in the figure with *). Since there is no other mineralogical information above 2000 cm$^{-1}$, all graphs presented in this chapter are only displayed up to this wavenumber. The peak assignments are detailed further in this chapter, in Section 4.4.

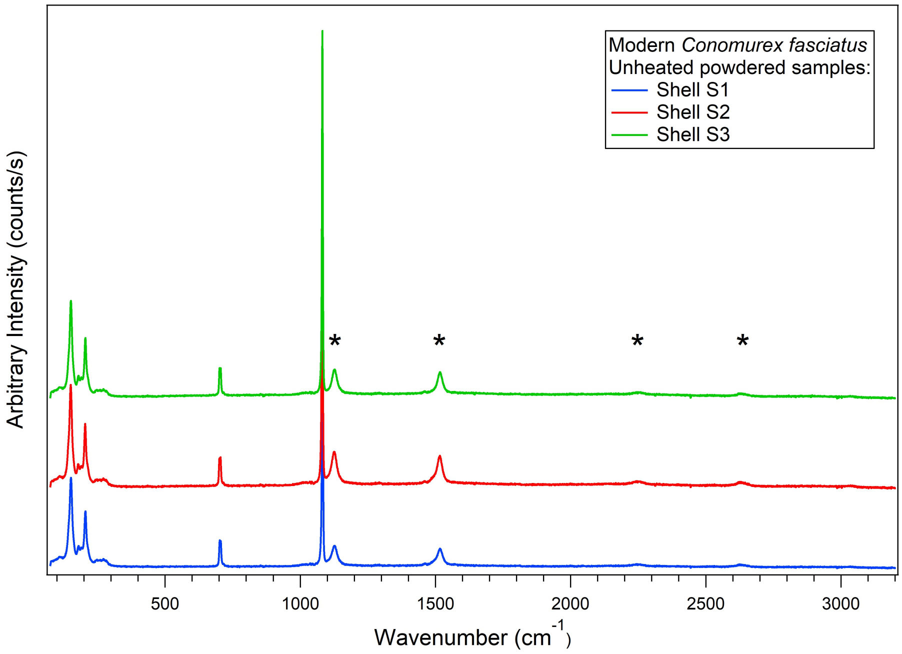

**Figure 4.2:** Full range spectra for the unheated modern *Conomurex fasciatus* powdered samples S1, S2 and S3. Each spectrum comprises an average of 200 spectra. Peaks marked with * are from carotenoids, while all other peaks represent the spectral signature of aragonite.

## 4.3 Laser heating test

It is known that several pearls and mussels have amorphous calcium carbonate in their composition [50]; however, due to its thermodynamically unstable nature, the laser radiation from RS can heat the sample and change the crystallisation into aragonite [52]. Because aragonite is thermodynamically less stable than calcite [80], and with the purpose of checking if the laser irradiation could change the spectral parameters, a laser heating test was conducted, photobleaching the samples for the total amount of time used in a normal spectrum acquisition, which is 210 seconds. However, for this test 100% laser power was used, which is twice the laser power used in this work; thus, stressing the samples to an extreme situation.

To perform the test, a single random position in the shell powder was chosen and spectra were collected before and after photobleaching the sample, as detailed in Section

2.3.1 of Chapter 2. Quantitative Raman parameters, such as peak position and FWHM of the $L_1$ and $\nu_1$ peaks were then compared for these two situations. This test was performed on the modern *Conomurex fasciatus* powdered sample S3, being repeated at different positions, five times for each of the following sub-samples thermally treated at different conditions: unheated, heated at 500°C for 15 min, and heated at 500°C for 30 min. The results suggest that photobleaching was not able to significantly change the peak position and FWHM of peaks $L_1$ and $\nu_1$, as demonstrated by the averaged values of these quantitative parameters in Table 4.1.

Other parameters such as the peak intensity ratio $L_1/\nu_1$ and the percentage of aragonite and calcite were also investigated. The latter polymorph proportion was estimated from the obtained Raman spectra using the method established by H. Edwards *et al.* (2005) for mineral calcium carbonates, which consisted in comparing the peak intensities of the $L_2$ lattice mode of aragonite at ~205 cm$^{-1}$ and calcite at ~280 cm$^{-1}$ [105]. In their work, they investigated the sensitivity of RS towards the discrimination of calcite and aragonite present in the same sample by analysing prepared mixtures containing different proportions of the two polymorphs. They noted that in a sample comprising 50% calcite and 50% aragonite, both the $L_2$ peaks at ~205 cm$^{-1}$ and ~280 cm$^{-1}$ had similar intensities. Thus, H. Edwards *et al.* concluded that the relative intensity of these two peaks could be used to estimate calcite and aragonite proportions in the same sample. This method was used in this thesis to estimate the percentage of calcite and aragonite by the following equations

$$\%Calcite = \frac{100 \times I_{280}}{I_{205} + I_{280}}, \tag{4.1}$$

$$\%Aragonite = \frac{100 \times I_{205}}{I_{205} + I_{280}}. \tag{4.2}$$

Therefore, the polymorph percentages for each of the three sub-samples, before and after the laser irradiation, were estimated by Equations 4.1 and 4.2. Table 4.2 shows the results for the peak intensity ratio $L_1/\nu_1$ and polymorph percentage. It can be seen that neither the peak intensity ratio nor the polymorph percentages have changed for the three sub-samples tested, before and after the laser irradiation.

**Table 4.1:** Laser heating test results for the peak position and FWHM, before and after photobleaching the modern *Conomurex fasciatus* powdered samples. This test was performed on sample S3, which was thermally treated at different conditions. The results of each condition correspond to the average over five measurements with the uncertainties being the SE. The results suggest that no significant changes were caused by the laser photobleaching.

| Sample S3 | Peak | Before irradiating<br>Position ($cm^{-1}$) | Before irradiating<br>FWHM ($cm^{-1}$) | After irradiating<br>Position ($cm^{-1}$) | After irradiating<br>FWHM ($cm^{-1}$) |
|---|---|---|---|---|---|
| Unheated | $L_1$ | $151.77 \pm 0.08$ | $11.8 \pm 0.3$ | $151.68 \pm 0.05$ | $11.8 \pm 0.2$ |
| | $\nu_1$ | $1081.80 \pm 0.08$ | $3.81 \pm 0.07$ | $1081.74 \pm 0.07$ | $3.82 \pm 0.06$ |
| 500°C - 15 min | $L_1$ | $152.2 \pm 0.1$ | $8.57 \pm 0.04$ | $152.3 \pm 0.2$ | $8.48 \pm 0.05$ |
| | $\nu_1$ | $1081.84 \pm 0.09$ | $3.1 \pm 0.1$ | $1081.80 \pm 0.09$ | $3.10 \pm 0.09$ |
| 500°C - 30 min | $L_1$ | $153.40 \pm 0.07$ | $8.0 \pm 0.2$ | $153.43 \pm 0.06$ | $8.0 \pm 0.2$ |
| | $\nu_1$ | $1082.27 \pm 0.04$ | $3.17 \pm 0.04$ | $1082.25 \pm 0.04$ | $3.17 \pm 0.04$ |

**Table 4.2:** Laser heating test results for the peak intensity ratio and calcium carbonate polymorph percentages, before and after photobleaching the modern *Conomurex fasciatus* powdered samples. This test was performed on sample S3, which was thermally treated at different conditions. The results of each condition correspond to the average over five measurements with the uncertainties being the SE. The results suggest that no significant changes were caused by the laser photobleaching.

| Sample S3 | Before irradiating<br>Intensity ratio ($L_1/\nu_1$) | Before irradiating<br>Aragonite (%) | Before irradiating<br>Calcite (%) | After irradiating<br>Intensity ratio ($L_1/\nu_1$) | After irradiating<br>Aragonite (%) | After irradiating<br>Calcite (%) |
|---|---|---|---|---|---|---|
| Unheated | $0.16 \pm 0.01$ | 100 | 0 | $0.17 \pm 0.01$ | 100 | 0 |
| 500°C - 15 min | $0.16 \pm 0.02$ | $82 \pm 7$ | $18 \pm 7$ | $0.17 \pm 0.02$ | $83 \pm 7$ | $17 \pm 7$ |
| 500°C - 30 min | $0.09 \pm 0.01$ | $3 \pm 2$ | $97 \pm 2$ | $0.09 \pm 0.01$ | $3 \pm 2$ | $97 \pm 2$ |

## 4.4 Aragonite to calcite transition

Archaeologists often use ancient sea shells for paleoenvironmental reconstruction [46,117], e.g. linking the oxygen isotope ratio ($O^{18}/O^{16}$) from the shells to the temperature of the sea water [125]. If the sea shells are archaeological, they could have been prone to heating processes [46], such as cooking, unintentional heating when discarded in fireplaces or even heating with the purpose to change the shell's colour so they could be used as ornaments [168]. It is also known that heating aragonite puts the original isotopic information at risk, because it removes the heavy isotopes from the sample during the phase transition to calcite [135,136], thus leading archaeologists to erroneous temperatures. Recently, S. Milano *et al.* (2016) showed that isotopic ratios can change with heating even if the aragonite to calcite transition has not taken place [134]. Because of these issues, it is therefore important to study the effect of heating in archaeological sea shells, with the aim of this experiment to better understand the aragonite to calcite transition in heated shells using quantitative Raman spectroscopy.

The heat treatment involved exposing powdered *Conomurex fasciatus* shells to constant temperatures from 100°C up to 500°C, for different amounts of time (3min, 7min, 15min, 30min, 1h, 2h, 4h and 8h). For more details on the heat-treatments see Section 2.3 of Chapter 2. Figure 4.3 shows the averaged Raman spectra for the S1 samples that were thermally treated for four (Figure 4.3a) and eight hours (Figure 4.3b) at 100°C 180°C, 250°C and 325°C. The aragonite to calcite transition was not observed and only the spectral signature of aragonite was noted in all of these cases. The averaged Raman spectra obtained for the biological replicate samples, S2 and S3, are shown in Appendix B from Figure B.1 to B.4.

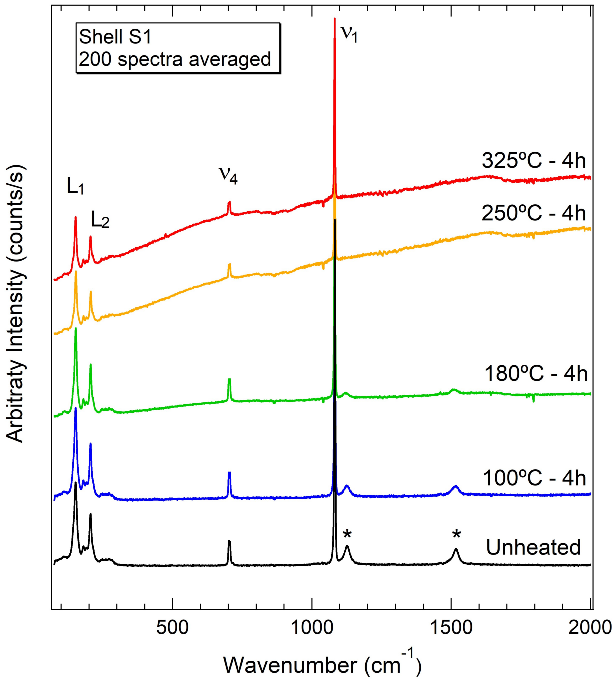

(a)

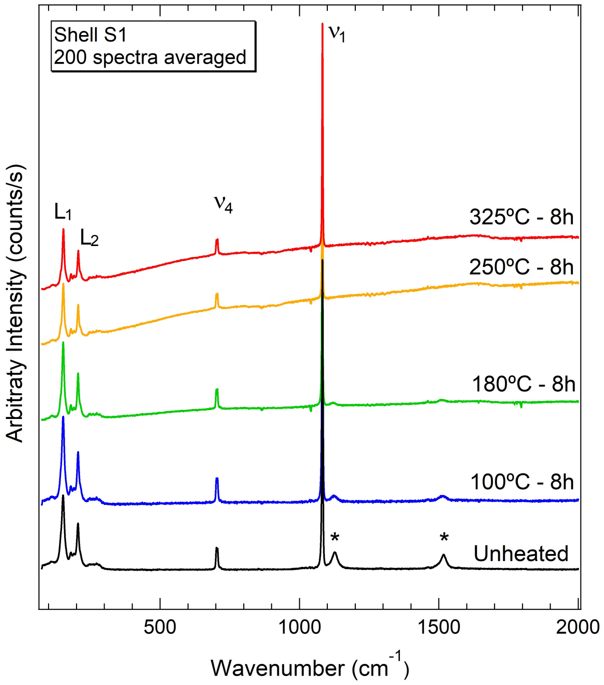

(b)

**Figure 4.3:** Raman spectra for the modern *Conomurex fasciatus* powdered sample S1 heat-treated for (a) 4 hours and (b) 8 hours at 100°C, 180°C, 250°C and 325°C. Spectra were offset and each of them corresponds to the average of 200 spectra. No aragonite to calcite transition is observed. Unheated results are shown for comparison. The carotenoid peaks are marked with (*). The positions and assignments for the other peaks are shown in Table 4.3.

The aragonite-calcite transition was noted for the samples heat treated at 400°C and 500°C, as shown in Figures 4.4 and 4.5 for the S1 shell. Similar results were also obtained for the biological replicates, S2 and S3, and are presented in Appendix B (Figures B.5 to B.8). In these graphs, each spectrum comprises the average of the 200 spectra collected for each respective time-point. A complete transition to calcite is observed after 2h for the samples heated at 400°C (Figure 4.4) and after 1h when heated at 500°C (Figure 4.5). A mixture of the spectral signatures of both aragonite and calcite is observed at the time-point of 1h when heated at 400°C (Figure 4.4) and at the time-points of 15min and 30min for the heat treatment at 500°C (Figure 4.5).

The peak positions and assignments for the unheated aragonite and converted calcite are shown in Table 4.3. The peak positions shown in this table were obtained from peak fitting procedures performed in each individual spectra collected for the unheated aragonite and converted calcite heat-treated at 500°C for eight hours. These sub-samples were chosen because at these conditions they are only composed of aragonite (unheated sub-sample) or calcite (500°C for 8h sub-sample). These peak positions were then averaged across all spectra obtained for the three samples (S1, S2 and S3), with the peak position uncertainties being the standard error of the mean. The translational ($L_1$) and librational ($L_2$) lattice modes are observed in the bands between 100 and 300 cm$^{-1}$ [92, 104], which were, respectively, measured at 151.50 ± 0.03 cm$^{-1}$ and 205.20 ± 0.03 cm$^{-1}$ for aragonite, and at 154.40 ± 0.05 cm$^{-1}$ and at 280.40 ± 0.03 cm$^{-1}$ for calcite. The internal in-plane antisymmetric bend ($\nu_4$) involves a doublet in the case of aragonite and a single peak for calcite [92, 104] (Figures 4.4 and 4.5). The aragonite doublet was measured at 701.60 ± 0.04 cm$^{-1}$ and at 705.90 ± 0.03 cm$^{-1}$, while the single peak for calcite was observed at 713.40 ± 0.03 cm$^{-1}$. The strongest Raman band corresponds to the symmetric stretching of the carbonate ion [92], and it was measured at 1082.10 ± 0.03 cm$^{-1}$ and at 1083.90 ±

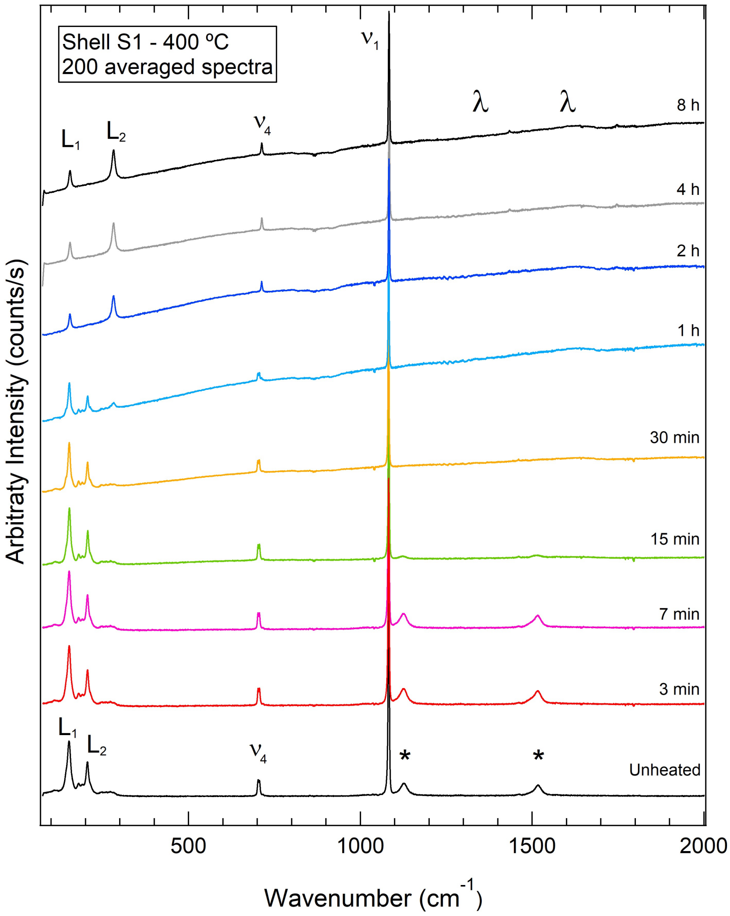

**Figure 4.4:** Raman spectra of the aragonite to calcite transition at 400°C for the modern *Conomurex fasciatus* powdered sample S1. Each spectrum corresponds to the average of 200 spectra collected from each sub-sample heated for different times. The aragonite to calcite transition is noted after 1h, where initially a mixture of the spectral signatures of aragonite and calcite is observed. The unheated results are shown for comparison. The peaks associated with carotenoids and amorphous carbon are marked with (*) and ($\lambda$), respectively. The positions and assignments for the other peaks are shown in Table 4.3.

0.04 cm$^{-1}$, respectively for aragonite and converted calcite.

Figures 4.3, 4.4 and 4.5 also show the peaks associated with carotenoids (marked with *), which are a strong natural colourant widespread in nature and found in many animals and vegetables [159]. Carotenoids are polyene chains with multiple conjugated carbon-carbon single and double bonds [153]. The two strong bands in their Raman signature, $\nu_1$ (between 1400-1600 cm$^{-1}$) and $\nu_2$ (between 1100-1200 cm$^{-1}$) are related, respectively, to

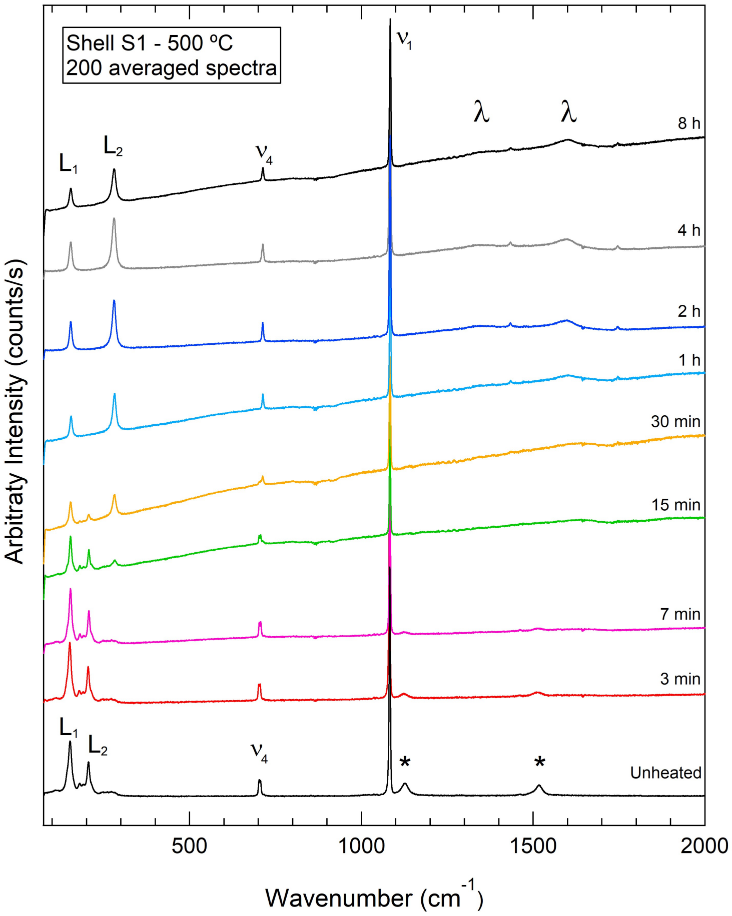

**Figure 4.5:** Raman spectra of the aragonite to calcite transition at 500°C for the modern *Conomurex fasciatus* powdered sample S1. Each spectrum corresponds to the average of 200 spectra collected from each sub-sample heated for different times. The aragonite to calcite transition is noted after 15min, where initially a mixture of the spectral signatures of aragonite and calcite is observed. The unheated results are shown for comparison. The peaks associated with carotenoids and amorphous carbon are marked with (*) and ($\lambda$), respectively. The positions and assignments for the other peaks are shown in Table 4.3.

double and single carbon-carbon stretching vibrations [153–156]. The position of the $\nu_1$ peak depends on the length of the carbon chain [154, 156, 159].

When sea shells are heated, the organic matter can be converted to amorphous carbon [137], which has no crystalline structure and can contain any mixture of diamondlike, graphitelike and hydrocarbons [8, 10]. Amorphous carbon can originate from the decomposition of the carotenoids and impurities during heating. The Raman spectrum for disor-

**Table 4.3:** Peak positions and assignments for biological aragonite and converted calcite. The peak positions are the average across all spectra obtained for the analysed bio-replicate samples (S1, S2 and S3) for the unheated aragonite and converted calcite heat treated at 500°C for eight hours. The uncertainties are the standard error of the mean.

| Polymorph | Code | Measured position ($cm^{-1}$) | Literature peak assignments |
|---|---|---|---|
| Aragonite | $L_1$ | 151.50 ± 0.03 | Translational lattice mode [92, 94, 96–99] |
| | $L_2$ | 205.20 ± 0.03 | Librational lattice mode [92, 94, 96–99] |
| | $\nu_4$ | 701.60 ± 0.04<br>705.90 ± 0.03 | In plane antisymmetric bend [52, 92, 94, 96–99] |
| | $\nu_1$ | 1082.10 ± 0.03 | Symmetric stretch [52, 92, 94, 96–99] |
| Converted calcite | $L_1$ | 154.40 ± 0.05 | Translational lattice mode [91, 92, 94, 96, 97, 99] |
| | $L_2$ | 280.40 ± 0.03 | Librational lattice mode [91, 92, 94, 96, 97, 99] |
| | $\nu_4$ | 713.40 ± 0.03 | In plane antisymmetric bend [91, 92, 94, 96, 97, 99] |
| | $\nu_1$ | 1083.90 ± 0.04 | Symmetric stretch [91, 92, 94, 97, 99] |

dered carbon has two strong bands: the D band around 1400 $\mathrm{cm}^{-1}$ and the G band around 1600 $\mathrm{cm}^{-1}$ [10], which were studied by many authors on synthetic samples [8, 10–12].

Amorphous carbon bands are marked with $\lambda$ in Figures 4.4 and 4.5, showing the D and G bands. Evidence of amorphous carbon is seen in the sub-samples heat-treated for one hour onwards (Figures 4.4 and 4.5). In the same figures the carotenoid peaks are seen fading over time for a set temperature. The carbon present in the crystal structure of mineral content of the shell does not contribute to the appearance of the amorphous carbon as the transition from calcite to calcium oxide (CaO) happens at a much higher temperature. This transformation was verified to start around ~700°C in ark clam shells; however, calcite was completely decarbonised only at ~800°C [89]. S. W. Lee *et al.* remark that they verified the calcite to CaO transformation above 600°C for oyster shell; however, no specific values or results were presented in their publication [169]. The smallest transition temperature to calcium oxide for biogenic samples, obtained by S. Yoshioka and Y. Kitano (1985), who worked with many different species of sea shells and corals, is

816°C [84].

The estimated percentages of aragonite and calcite, for the three analysed samples, are shown in Figure 4.6, where the error bars are SE associated to the average of 200 spectra for each time-point. These percentages were, as previously explained in Section 4.3, estimated from the spectra using the method established by H. Edwards *et al.* (2005), which compares the relative intensities of the aragonite and calcite $L_2$ peak (librational lattice mode) by Equations 4.1 and 4.2 [105]. For the phase transition of aragonite to calcite, as expected, a majority of aragonite was observed in the quicker time-points while a predominance of calcite was found for the longer time-points (Figure 4.6).

From Figure 4.6, it can be seen that the calcite signature appeared between 1h and 2h of heating for 400°C (Figure 4.6a) and between 15 min and 30 min for 500°C (Figure 4.6b). About 20% of the aragonite was converted into calcite after the sample had been heat treated for 1h at 400°C, with a full conversion happening after 2h (Figure 4.6a). At 500°C, about 10% of the aragonite was converted to calcite in the initial 15min of heating, followed by a conversion of around 80% after 30min of heat treatment (Figure 4.6b). Thus, it is noted that full polymorph transition happened more rapidly at 500°C. The error bars in Figure 4.6 are larger during the phase transition due to a higher statistical dispersion of polymorph percentages at these time-points, expected for a structural transition.

The translational lattice mode ($L_1$) and the $CO_3^{-2}$ symmetric stretch ($\nu_1$) peaks at $\sim$153 cm$^{-1}$ and $\sim$1082 cm$^{-1}$, respectively, were carefully inspected as they are common in both aragonite and calcite phases; therefore, both peaks are present in all spectra collected. The peak intensity ratio ($L_1/\nu_1$) was found to be a marker for the phase transition, as shown in Figures 4.7 and 4.8. Figure 4.7 illustrates how this peak intensity ratio behaves with the time of the samples in furnace at 400°C (Figure 4.7a) and 500°C (Figure 4.7b). The large drop, in the intensity ratio values, shows when the transition to calcite started,

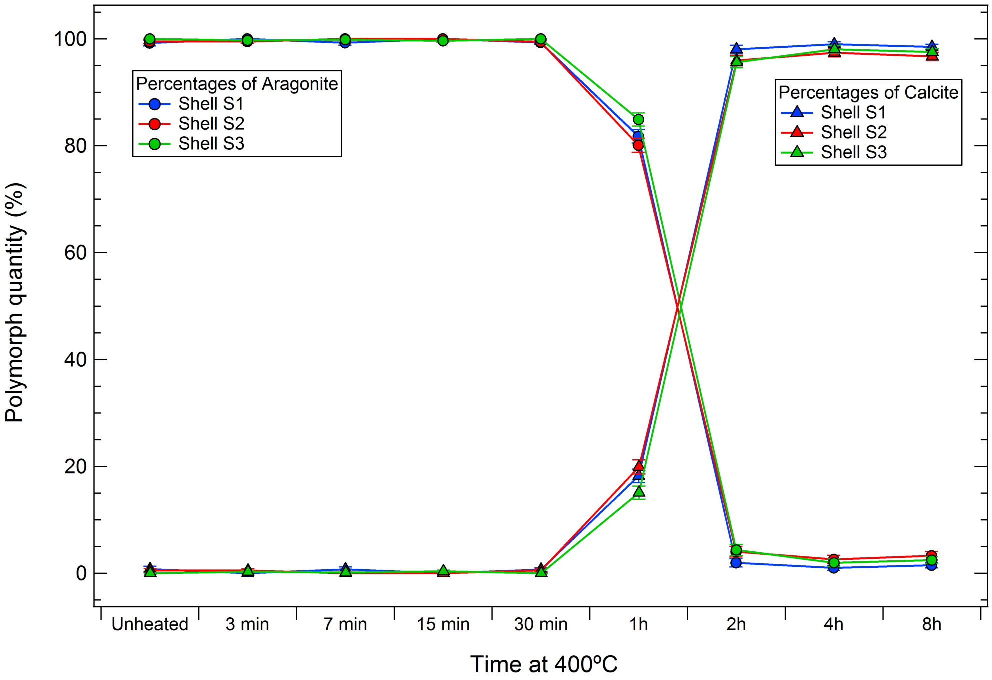

**(a)**

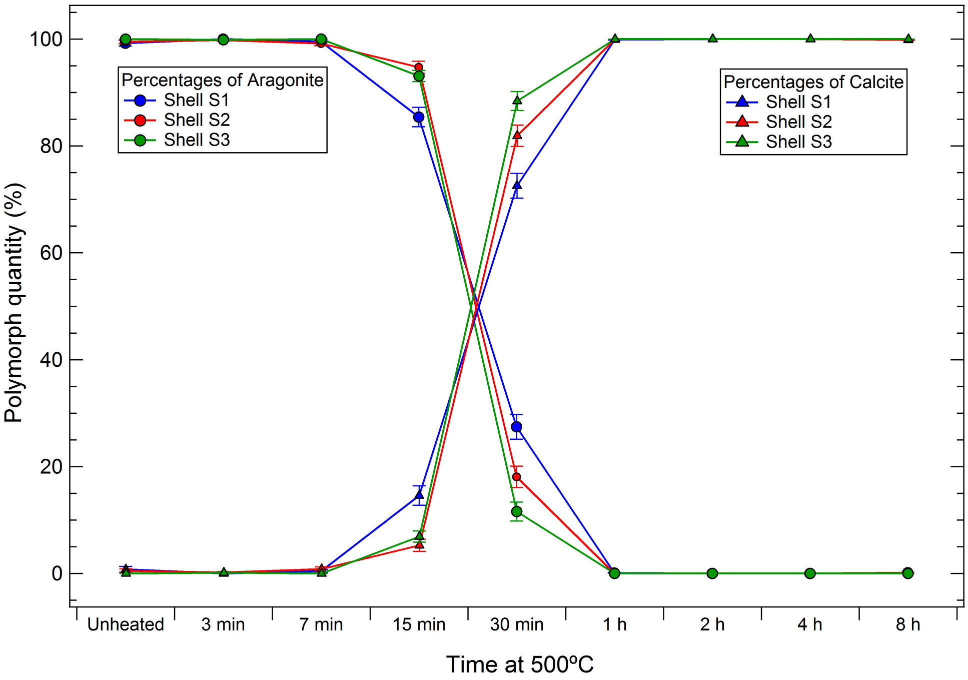

**(b)**

**Figure 4.6:** Aragonite to calcite phase transition of the modern *Conomurex fasciatus* powdered samples (S1, S2 and S3) for heat-treatments at (a) 400°C and (b) 500°C. The graphs show the estimated percentage of aragonite and calcite obtained at each time point by comparing the relative intensities of the librational lattice mode peak ($L_2$) from their Raman spectra (Equations 4.1 and 4.1). The error bars are the SE associated to the average of 200 spectra for each time-point.

*i.e.* after 1h at 400 °C and after 15 min at 500 °C. These results match the percentage information curve exhibited in Figure 4.6. The lattice modes of geological calcite and aragonite are greatly affected by variations of temperature, while the internal oscillations of the $CO_3^{-2}$ group are not affected to the same extent [87, 103]. Thus, since the peak intensity ratio $L_1/\nu_1$ is calculated between lattice and internal vibrational modes, the results observed in Figure 4.7 could be mostly driven by variations of the $L_1$ peak. As the $L_1/\nu_1$ peak intensity ratio is sensitive to the calcium carbonate phase, it can be used as a complement to the method established by H. Edwards *et al.* (2005) [105], for estimating the polymorph percentages.

Most published works have studied the aragonite to calcite transition by heating the sample at a fixed rate. In these studies, the transition of geological and synthetic aragonite occurred at higher temperatures ranging from 450°C to 480°C [84–87]. As per biogenic aragonite, the transition temperature is dependent on the species. Some of the lowest values of the transition temperature were recorded for corals and ranged from 280°C to 360°C [84,86]. The oyster species *Pinctada maxima* had an aragonite to calcite conversion happening in the broad range of 300°C to 400°C [88]. As per shells, S. Yoshioka and Y. Kitano (1985) noticed a phase transition at 350°C for the *Saxidomus purpuratus, Hyriopsis schlegeli, Corbicula japonica*, and at 330°C for the *Pinctada martensii* [84]. These lower phase transition temperatures observed in the literature show that biogenic aragonite is less thermally stable than geological or synthetic aragonites [84]. In this thesis, the study focused on the variation of the heating time for a set temperature. Thus, the ratios obtained for all samples heat treated for four and eight hours were plotted against the temperature (Figure 4.8), revealing that for the *Conomurex fasciatus* shells the conversion started at temperatures greater than 325°C and ending at a maximum temperature of 400°C.

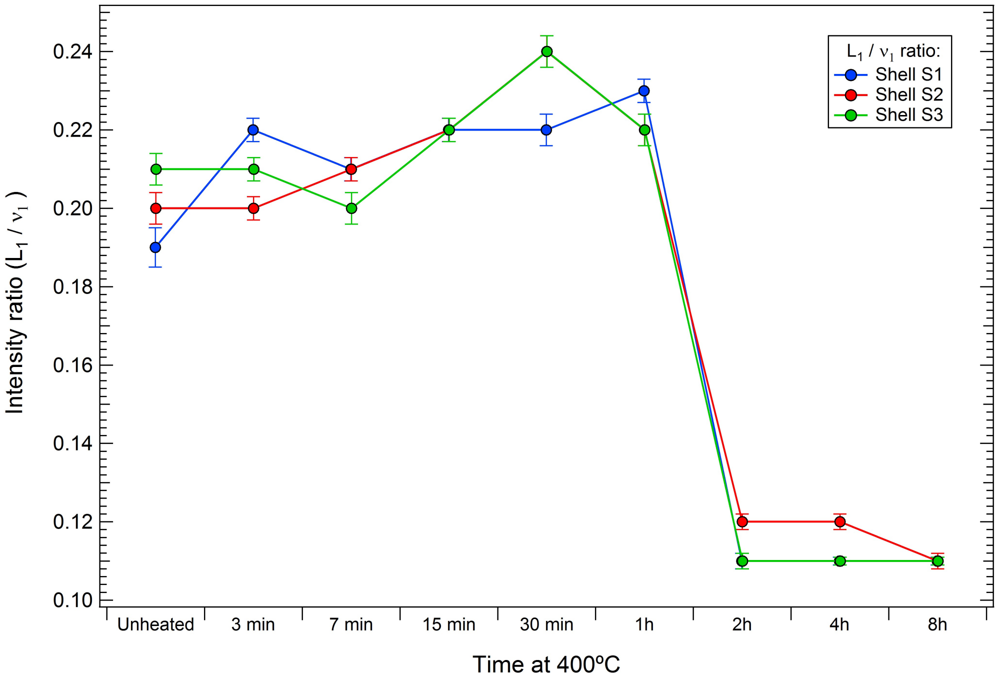

(a)

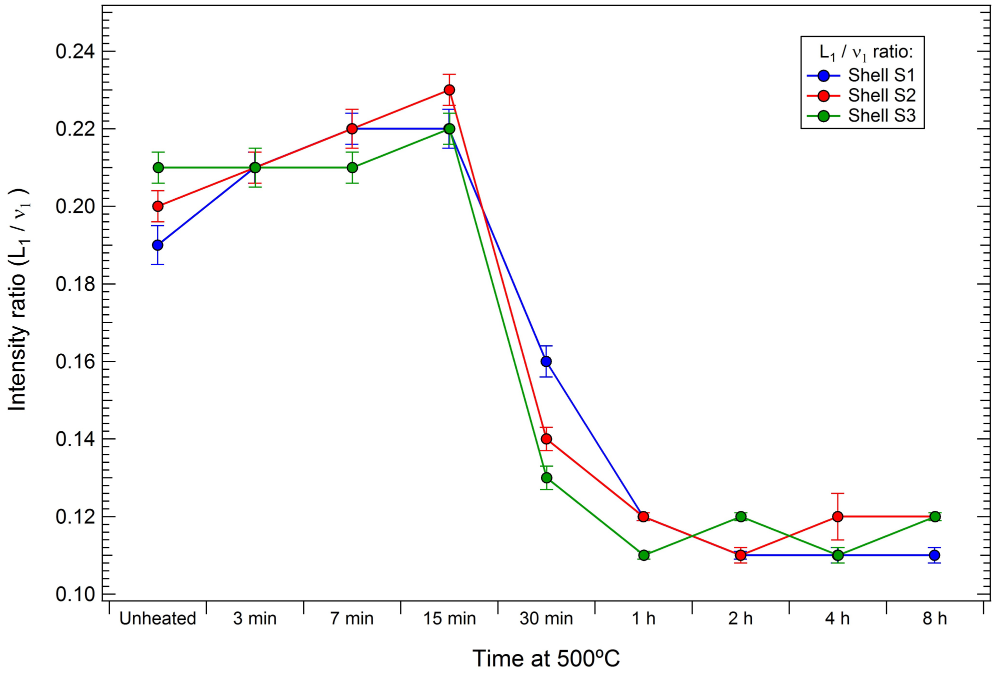

(b)

**Figure 4.7:** Intensity ratio of the $L_1$ (∼153 $cm^{-1}$) and $\nu_1$ (∼1082 $cm^{-1}$) peaks during the aragonite to calcite phase transition of the modern *Conomurex fasciatus* powdered samples (S1, S2 and S3) for heat treatments at (a) 400°C and (b) 500°C. The large drop in the peak intensity ratio values represents the start of the aragonite-calcite transition, *i.e.* after 1h at 400 °C and after 15 min at 500 °C. The error bars are the SE for the peak intensity ratios associated to the average of 200 spectra for each time-point.

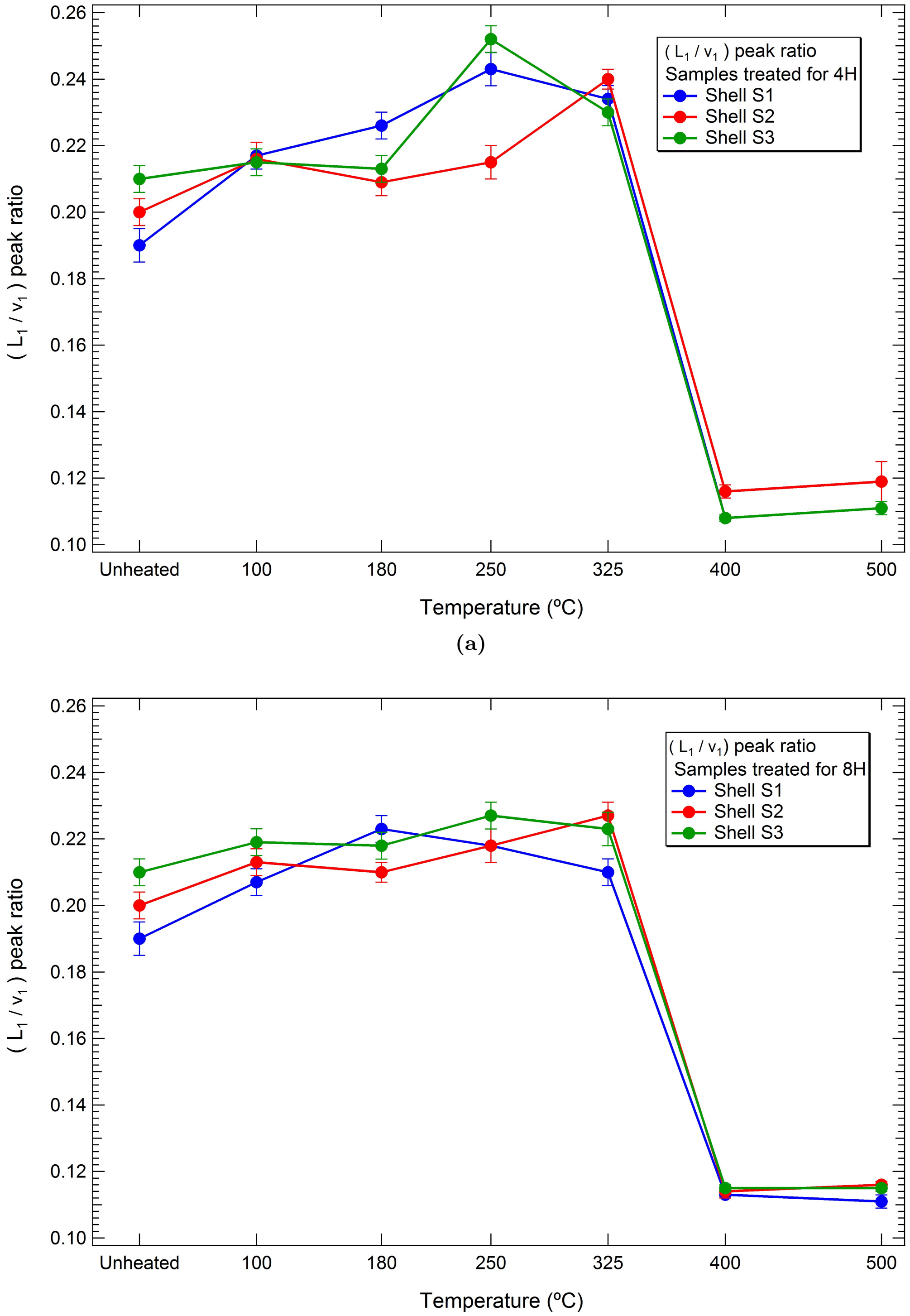

(a)

(b)

**Figure 4.8:** Intensity ratio of the $L_1$ ($\sim$153 cm$^{-1}$) and $\nu_1$ ($\sim$1082 cm$^{-1}$) peaks as function of temperature for the modern *Conomurex fasciatus* powdered samples (S1, S2 and S3) heat-treated for (a) four and (b) eight hours. For temperatures up to 325°C, the shells were mainly composed of aragonite, which was then converted to calcite above that temperature. The error bars are the SE for the peak intensity ratios associated to the average of 200 spectra for each time-point.

When a palaeoenvironmental reconstruction is being made, it is necessary to investigate if recrystallisation of the shell mineralogy has occurred. The aragonite-calcite transformation changes the oxygen isotopic ratios, thus leading to the determination of erroneous paleotemperatures [125, 136]. This is due to the replacement of the $O^{18}$ atoms by the lighter $O^{16}$ from the atmosphere [136]. Until very recently, archaeologists were only interested in knowing if the structure had changed, which would alter the isotopic composition. However, S. Milano *et al.* (2016) noted that while a heating at 300°C for 20 min and 60 min did not cause the full aragonite-calcite conversion, it did cause an overestimation of the paleotemperatures [134]. As Figures 4.6 and 4.7 show, the samples had to be heated for around 15 min to trigger the transition at 500°C, while at 400°C it took about 1 hour. Therefore, the aragonite-calcite conversion cannot be the only parameter taken into account to detect heating evidence in archaeological sea shells, as they could have been heated for an amount of time shorter than that necessary to trigger the transition. Thus, if recrystallisation has not occurred, it is important to provide alternative methods that can identify heat-treatments of shells. To investigate this, the crystallinity of calcium carbonate was also studied to determine if there were detectable changes related to heat-treatment prior to the aragonite to calcite phase transition.

In RS measurements, the crystallinity of a material is measured by the FWHM of the spectral bands. The thinner the spectral band, the higher the crystallinity of the material, and vice-versa [50]. Figures 4.9 and 4.10 illustrate how the FWHM of the $L_1$ and $\nu_1$ peaks varied with the time of heating in furnace at 400°C (Figures 4.9a and 4.10a) and 500°C (Figures 4.9b and 4.10b). A decrease in the FWHM of both the $L_1$ and $\nu_1$ peaks is observed after seven minutes for the samples heat treated at 400°C and after three minutes for the samples heat-treated at 500°C. In both cases, these changes happened before the phase transition.

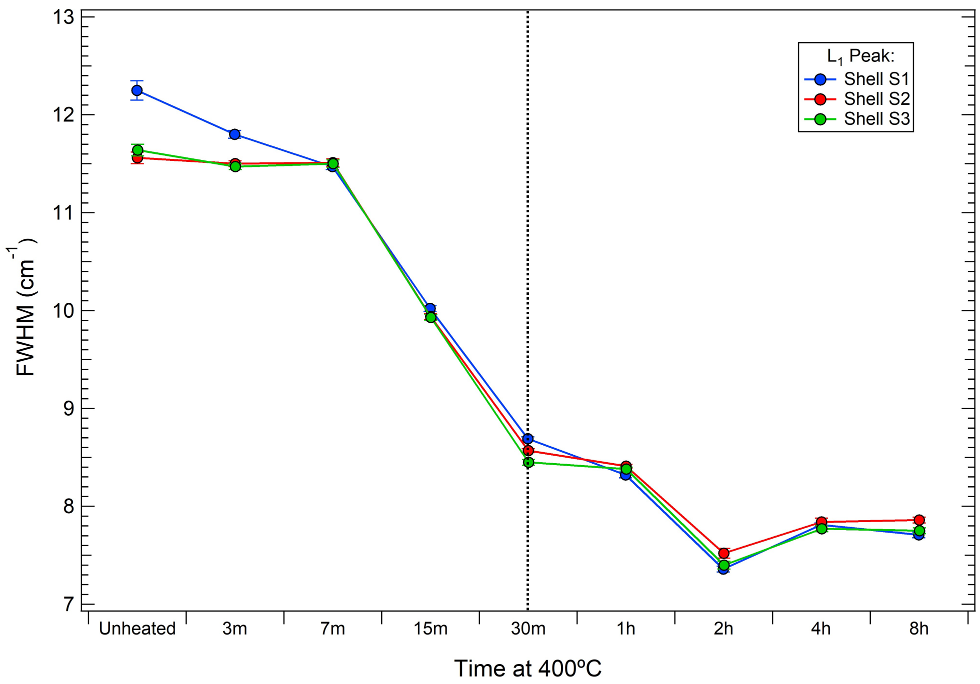

(a)

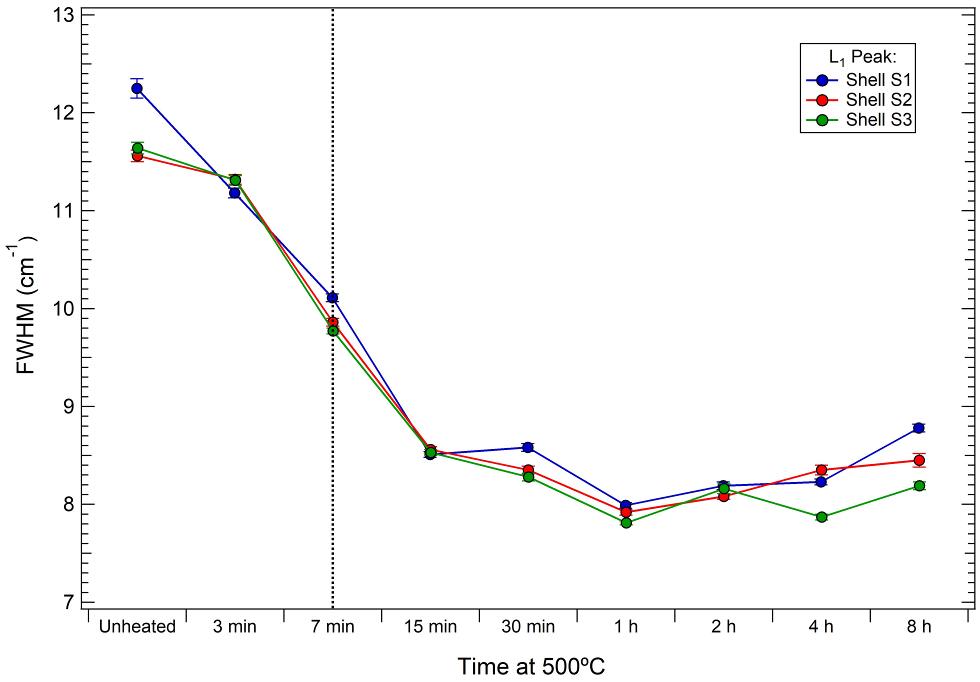

(b)

**Figure 4.9:** FWHM of the $L_1$ (~153 cm$^{-1}$) peak with increasing time in furnace at (a) 400°C and (b) 500°C for the modern *Conomurex fasciatus* powdered samples (S1, S2 and S3). The vertical line marks the start of the aragonite to calcite transition. From the maximum to the minimum values achieved, the FWHM dropped ~36% in (a) and ~32% in (b). A decrease in the FWHM indicates an increase in the sample crystallinity. The error bars are the SE associated to the average of 200 spectra for each time-point.

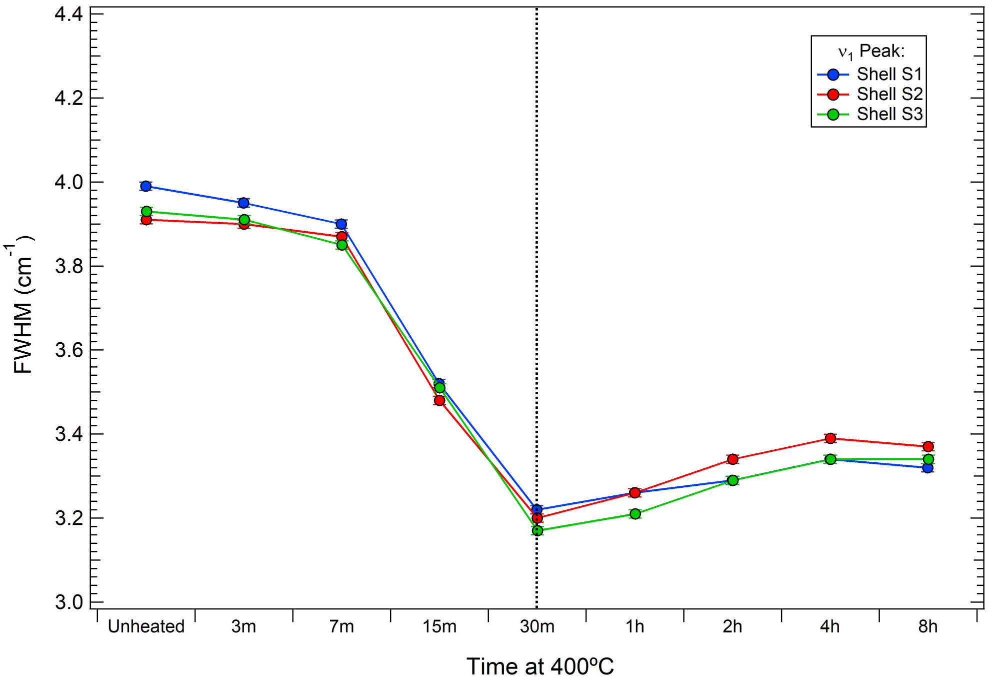

**(a)**

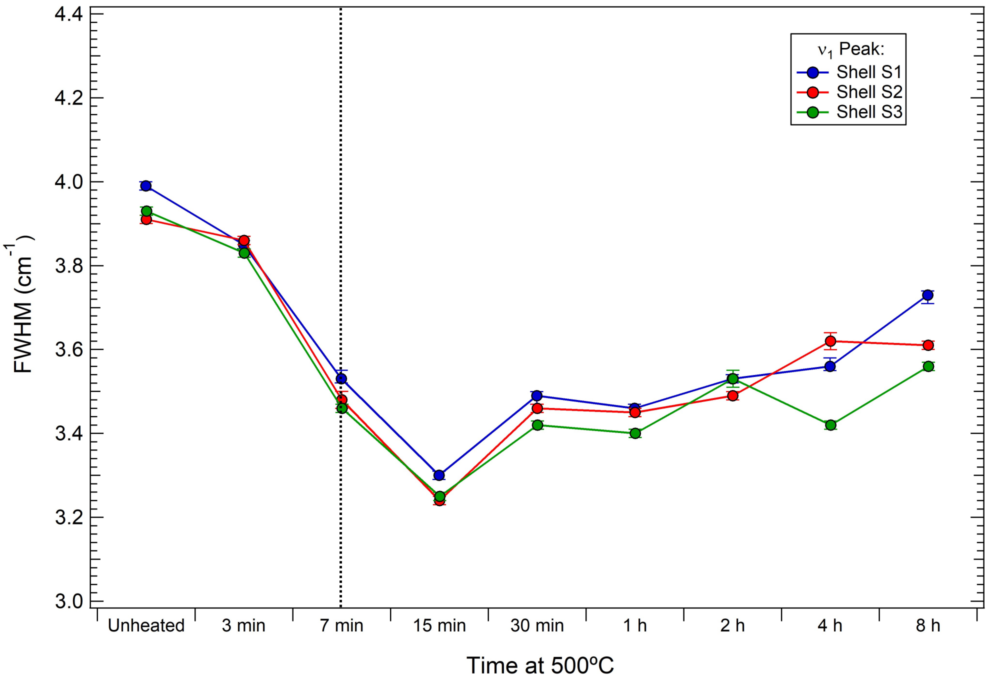

**(b)**

**Figure 4.10:** FWHM of the $\nu_1$ ($\sim$1082 cm$^{-1}$) peak with increasing time in furnace at (a)400°C and (b)500°C for the modern *Conomurex fasciatus* powdered samples (S1, S2 and S3). The vertical line marks the start of the aragonite to calcite transition. From the maximum to the minimum values achieved, the FWHM dropped ∼18% in (a) and ∼15% in (b). A decrease in the FWHM value indicates an increase in the sample crystallinity. The error bars are the SE associated to the average of 200 spectra for each time-point.

Biogenic aragonite and calcite have anisotropic structural lattice distortions when compared to geological or synthetic compounds [73–75]. These lattice distortions have been verified in 12 different types of shells comprising bivalves, gastropods and cephalopods and were similar for all of them [76]. B. Pokroy *et al.* (2007) noted that in biogenic aragonite, an increase in its crystallinity is obtained even for short periods of annealing (30min to 1h) at temperatures from 50 to 350°C, which relieves the lattice distortions reverting the lattice parameters close to the values of geological aragonite [73]. They also used mass spectrometry analyses to show that $CO_2$ discharge in biogenic aragonite starts at 70°C, reaching a peak at 250°C, while in geological samples this discharge only happened at much higher temperatures of 500 - 600° and its only source would be the $CaCO_3$ to CaO decomposition [76]. Thus, they assumed that this low temperature discharge of $CO_2$ would be related to the degradation of the shell's organic matrix. These observations led them to conclude that the lattice distortions observed in the biogenic aragonites were correlated to the organic macromolecules that support the strained mineral lattice and degrade under heat-treatment, leading to a mineral lattice relaxation and a size reduction of the crystal blocks [73, 76]. Thus, the decrease in the FWHM and therefore, increase in the crystallinity of the heat-treated *Conomurex fasciatus* samples (Figures 4.9 and 4.10) originates from the degradation of the organic macromolecules in the shell structure.

The increase in the crystallinity of the heat-treated *Conomurex fasciatus* samples is more evident for the lattice mode peak $L_1$, which decreased, from the maximum to the minimum measured values, $\sim$36% at 400°C and $\sim$32% at 500°C (Figure 4.9). The $\nu_1$ peak (symmetric stretch of the $CO_3^{-2}$ ion) decreased $\sim$18% and $\sim$15%, respectively for the heat treatments performed at 400°C and 500°C (Figure 4.10). This trend agrees with RS observations that the lattice modes of geological aragonite are more sensitive to increasing temperatures and that they reflect progressive rotational disordering preceding the aragonite to calcite transition [87]. This trend was observed for the geological carbonates as shifts in peak positions and changes in the FWHM during heat-treatments performed up to 800°C in the case of calcite, and up to 450°C in the case of aragonite [87]. The internal modes are also temperature dependent, but with a smaller contribution, reflecting a greater expansion of the C-O bond length with temperature [87].

After the aragonite-calcite transition, thermal expansion leads to the next transition, from calcite to calcium oxide, which has been reported to take place over 600°C in biogenic samples [84,89,169]; thus, happening at a much higher temperature than those used in this work. Thus, to understand the nature of an increase in the FWHM after the aragonite to calcite transition (Figures 4.9 and 4.10), the graphs for this quantitative parameter were also plotted as a function of the temperature, grouping all the samples treated for four and eight hours. These comparisons are shown in Figures 4.11 and 4.12. As seen in both figures, the FWHM of both $L_1$ and $\nu_1$ peaks decrease with temperature reaching its smallest value at 400°C and 325°C, respectively. Once this minimum point had been reached, the FWHM starts to increase for both peaks. S. A. Markgraf and R. J. Reeder (1985) used XRD to study the crystal structure of the calcite noting a thermal expansion of the crystal when heated from the room temperature to 900°C [102]. Often these changes in the crystal volume or bond length are linked, in RS, to shifts in the peak positions [87]. Such simple volume thermal expansion was also attributed to a FWHM increasing of the lattice peaks in geological calcite heated up to ∼800°C [87]. In a work using Raman spectroscopy, P. K. Narayanasway (1947) analysed the spectrum of calcite at different temperatures (up to 425°C), reporting a broadening of the two lattice mode and $\nu_1$ peaks with increasing temperatures [103]. Thus, the increase in the FWHM values after the aragonite-calcite transition is probably related to the thermal expansion of the calcite crystal prior to the next phase transition to CaO.

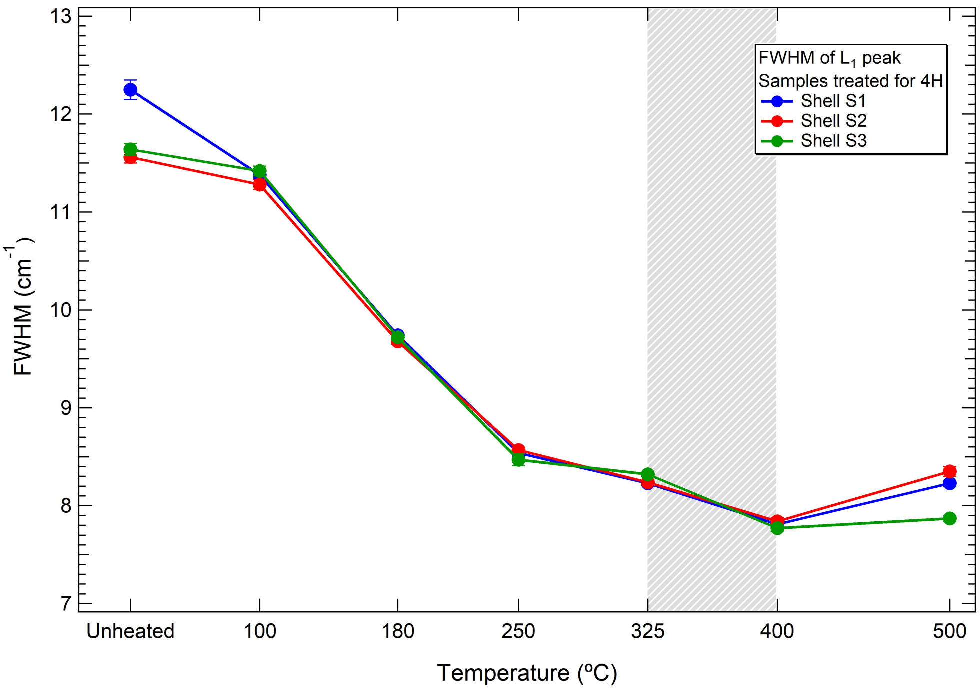

(a)

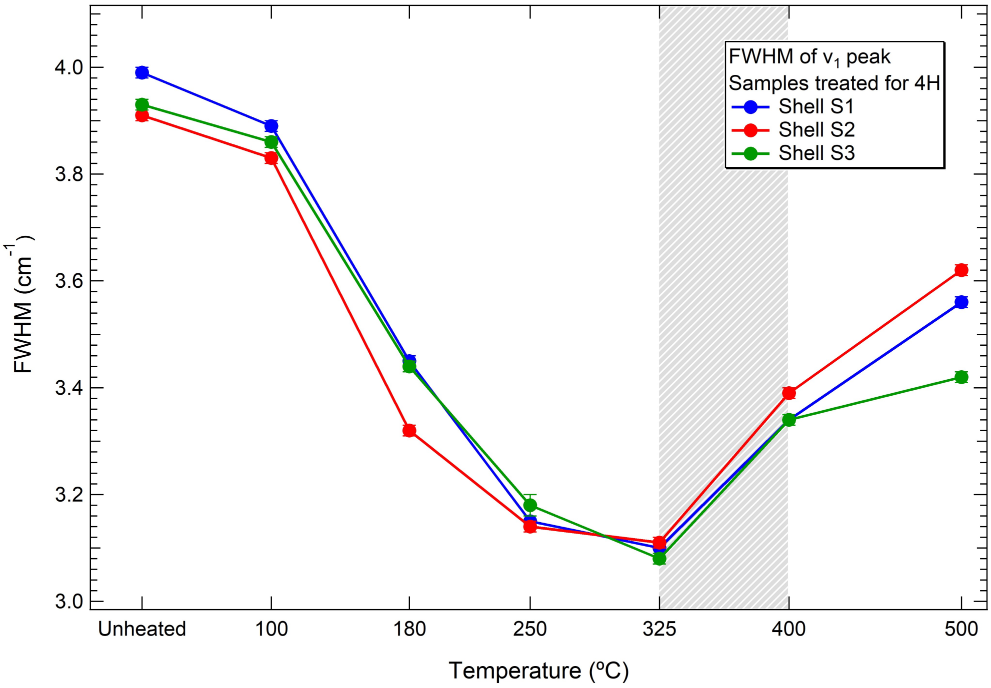

(b)

**Figure 4.11:** FWHM of the (a) $L_1$ ($\sim$153 cm$^{-1}$) peak and (b) $\nu_1$ ($\sim$1082 cm$^{-1}$) peaks as function of temperature for the modern *Conomurex fasciatus* powdered samples (S1, S2 and S3) heat-treated for 4h. The shaded area marks the temperature range for which the aragonite to calcite transition takes place. After the transition, the FWHM of both peaks starts to increase.

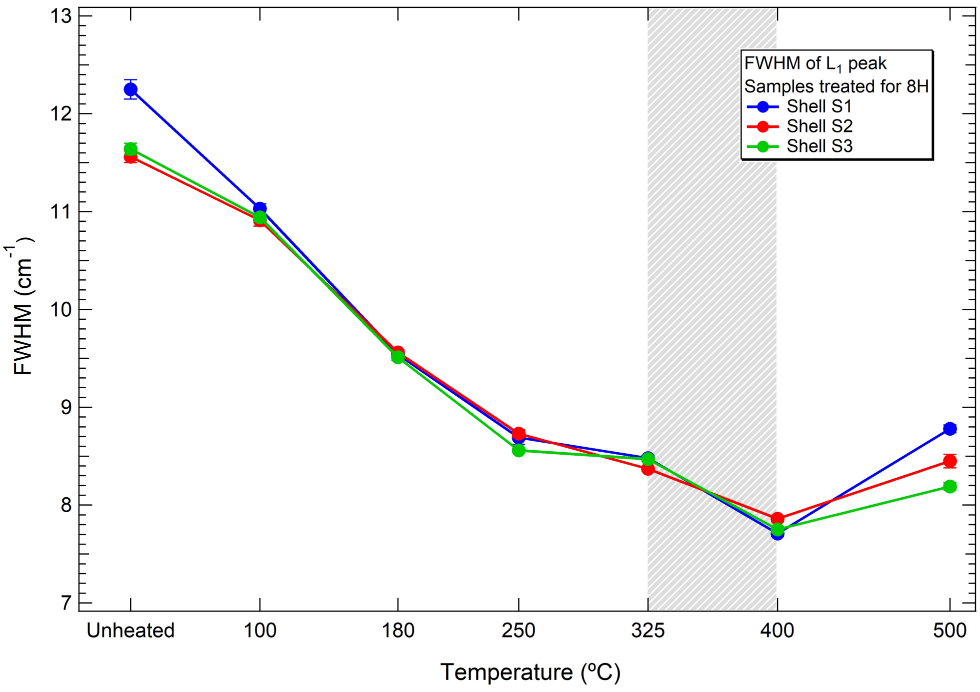

(a)

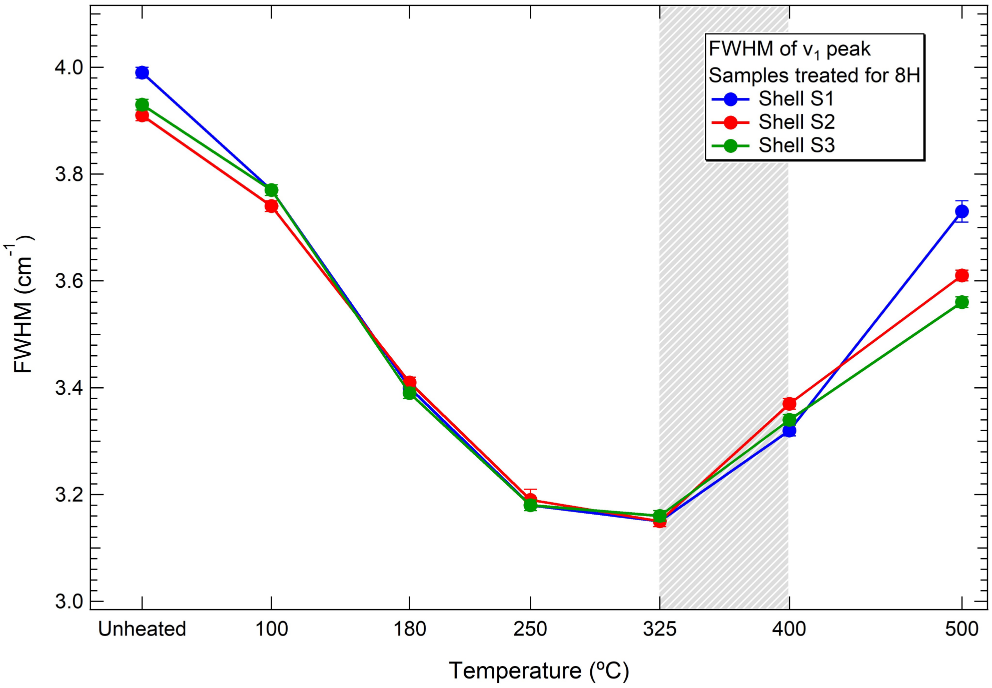

(b)

**Figure 4.12:** FWHM of the (a) $L_1$ (~153 cm$^{-1}$) peak and (b) $\nu_1$ (~1082 cm$^{-1}$) peaks as function of temperature for the modern *Conomurex fasciatus* powdered samples (S1, S2 and S3) heat-treated for 8h. The shaded area marks the temperature range for which the aragonite to calcite transition takes place. After the transition, the FWHM of both peaks starts to increase.

## 4.5 SEM of heat treated shells

SEM was used to inspect the modern *Conomurex fasciatus* powdered sample S1 as unheated and thermally treated at 500°C for 30min and 8h. EDX was also performed on each of the previous conditions plus the time-point of 15min at 500°C. The EDX was used for compositional analysis, focusing on determining if the presence of minor elements varied with the heating times. For more details about the SEM and EDX experiments, please refer to Section 2.4 of Chapter 2.

Figure 4.13 compares the SEM micrographs for the unheated and heated modern *Conomurex fasciatus* powdered sample S1. Aragonite has a very distinct needle-like structure shape, whereas calcite is represented by rhombohedral structures [69, 167, 170]. Figure 4.13(a) shows the needle-like structure of aragonite found in the unheated powdered S1 shell. Figure 4.13b shows the micrograph of powdered S1 shell heat treated at 500°C during 30 min, where the coexistence of both phases is observed. Finally, Figure 4.13(c) shows the characteristic rhombohedral structure of calcite, which was converted from aragonite after a heat treatment of eight hours at 500°C. The conversion from aragonite to calcite was confirmed by RS (Figure 4.6).

Table 4.4 shows the average atom percentage of major elements (Ca, C and O) found in each analysed sample, corresponding to the proportion for the calcium carbonate molecule ($CaCO_3$). The degradation of the organic molecules is believed to be the responsible for the increase in the sample's crystallinity [73, 77]. The measured carbon atom percentage remained fairly constant for all analysed heat treatments. This indicates that the EDX results may correspond only to carbon from the carbonate in the mineral shell matrix instead of carbon present in the organic shell matrix.

The presence of impurities, such as Fe, Zn, Pb or Mn, are known to influence the growth rate of crystals during crystallisation, inhibit phase formation and change the

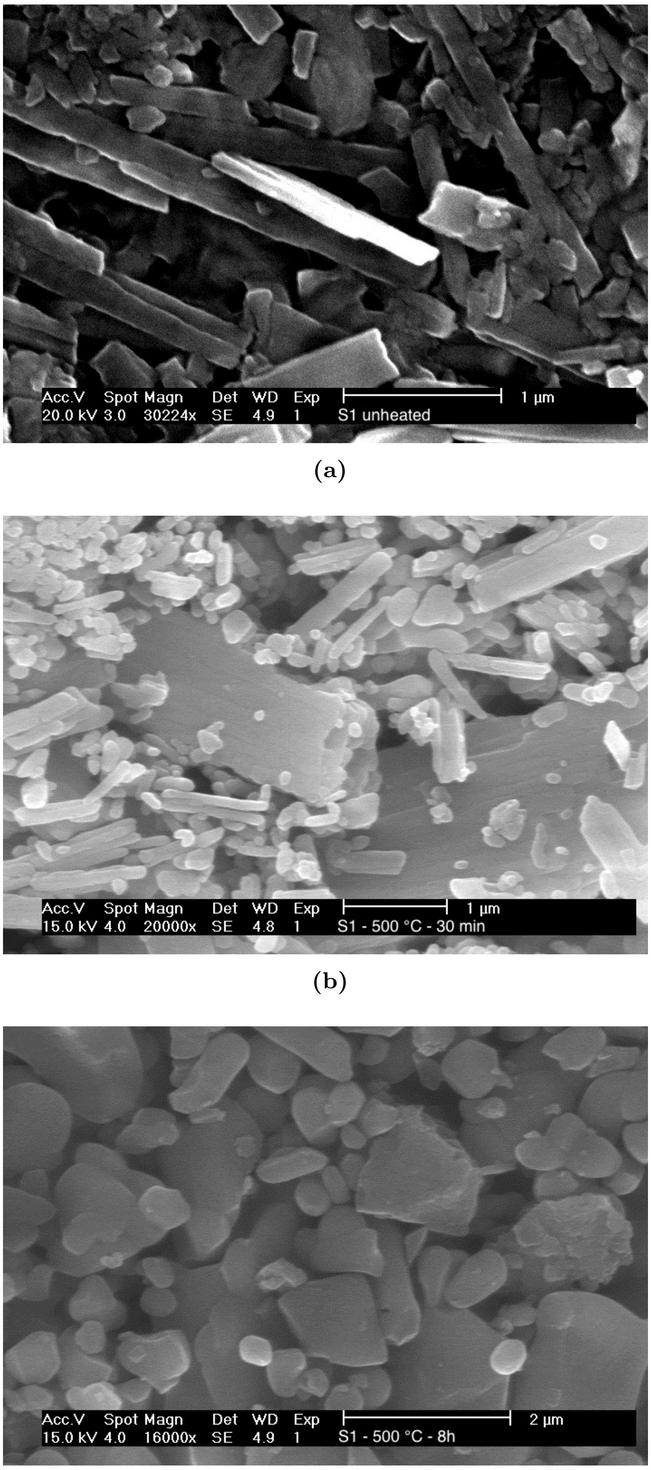

**(a)**

**(b)**

**(c)**

**Figure 4.13:** SEM micrographs for the modern *Conomurex fasciatus* powdered sample S1 at different heat treatments: (a) unheated, showing the needle-like aragonite structure, (b) treated at 500°C for 30 minutes, showing the presence of both aragonite and calcite phases and (c) treated at 500°C for 8h, showing the characteristically rhombohedral calcite crystals.

**Table 4.4:** Quantitative EDX results for major elements in the modern *Conomurex fasciatus* powdered sample S1. The atom percent values were averaged over the number of EDX taken in each sample, with the uncertainties being the SE.

| S1 sample | EDX taken | Averaged atom percentages | | |
|---|---|---|---|---|
| | | Ca | C | O |
| Unheated | 11 | 22±2 | 14±1 | 62±1 |
| 15 min at 500°C | 11 | 22±1 | 17±1 | 61±1 |
| 30 min at 500°C | 12 | 20.0±0.3 | 13.6±0.1 | 64.8±0.3 |
| 8 h at 500°C | 13 | 20.2±0.2 | 13.9±0.4 | 64.5±0.2 |

crystallinity in synthetic carbonates [68]. Table 4.5 shows the average atom percentage of minor elements found in each sample. Sulphur, zirconium, silicon and sodium were present in all samples regardless of the heating time, whereas magnesium was only detected in the sample that was heated for 15min at 500°C. It is commonly known that calcitic shells, as a rule, contain high concentrations of sulphur and magnesium [71]. However, the presence of sulphur in the analysed samples results from the aragonite phase prior to its conversion to calcite. Although the EDX analyses were repeated several times, it has to be clear that the analysed areas are small, ranging only of a few microns, and do not reflect the whole powdered samples. This then explains why magnesium was only detected in one sample, regardless of it being detected in the modern *Conomurex fasciatus* sample analysed in Chapter 3. Additionally, the elemental composition can also varies with shell species, geological environment, temperature and salinity of the sea, mollusc body part, amongst others [70, 72].

From Table 4.5, no trend is observed in the impurity percentage values with heating times. The highest impurity concentration was found for zirconium and sodium, with a mean percentage ranging from 0.39% to 0.79%, while the other impurity atoms ranged from 0.03% to 0.14%. According to B. Pokroy *et al.* (2004), the concentrations observed here are not enough to lead to lattice distortions in biogenic aragonites [77]. Thus, they

**Table 4.5:** Quantitative EDX results for minor elements in the modern *Conomurex fasciatus* powdered sample S1. The atom percent values were averaged over the number of EDX taken in each sample, with the uncertainties being the SE.

| S1 sample | EDX taken | Averaged atom percentages<br>S | Zr | Si | Mg | Na |
|---|---|---|---|---|---|---|
| Unheated | 11 | 0.09±0.02 | 0.7±0.2 | 0.09±0.04 | not detected | 0.46±0.03 |
| 15 min at 500°C | 11 | 0.07±0.01 | 0.39±0.08 | 0.07±0.02 | 0.08±0.04 | 0.40±0.02 |
| 30 min at 500°C | 12 | 0.14±0.01 | 0.79±0.02 | 0.03±0.01 | not detected | 0.60±0.03 |
| 8 h at 500°C | 13 | 0.09±0.01 | 0.73±0.04 | 0.07±0.03 | not detected | 0.47± 0.01 |

could not have influenced the changes observed in the Raman quantitative parameters during the heat treatments. Additionally, these impurities also could not be used as parameters to determine whether a shell has been heated.

## 4.6 Burnt fragments

The two burnt fragments, found in layers three and ten from the KM1057 shell midden, were also characterised with RS. The fragments were identified as burnt *Conomurex fasciatus* by their visual appearance, which exhibited visible charring signals (Figure 2.2 of Chapter 2). As explained in that Chapter, the two fragments were split and analysed under three different sample preparation conditions: (i) original, (ii) cleaned and, (iii) cleaned and powdered, generating sub-fragments for each sample. The Raman quantitative parameters of these fragments were compared to the representative obtained from the heating of the modern shells. The aim was to verify if the FWHM and the peak intensity ratio $L_1/\nu_1$ could determine if these fragments had been heated, for how long and at which temperature.

Table 4.6 summarises the quantitative data obtained for the $L_1$ and $\nu_1$ peaks under all studied conditions. The peak positions, FWHM, peak intensity ratios and percentage of calcite were obtained from the average of all spectra collected for each type of sample preparation, with the uncertainties being the SE. The calcium carbonate polymorph percentage composition was again estimated using the method established by H. Edwards *et al.* (2005) [105] (Section 4.3, Equations 4.1 and 4.2). Although the archaeological shells have visual indication of heating, different percentages of calcite were estimated in the sub-fragments according to the type of sample preparation. Full conversion to calcite was observed for the powdered samples from layers three and ten and for the cleaned layer 10 sub-fragment.

Such full calcite conversion cannot be attributed to the manual sample grinding with a pestle and mortar. Studies on archaeological shells have shown that such method does not activate the aragonite to calcite transformation [171,172]; however, mechanical drilling has been observed to convert about 6% of the aragonite in otoliths [173] and up to 20% of the aragonite of archaeological shells [171]. The smaller calcite percentages found from the external surfaces were probably caused by an aragonite contamination from the shell midden since the majority of shells in the midden were not burnt and composed of aragonite. Mechanical cleaning using air-abrasive systems with aluminium oxide is an effective way of removing surficial contamination [171]. However, this method implicates in removing the shell skeleton surface. Thus, as only water and a brush were used in the cleaning process, they may not have been sufficient for removing all the external contamination, demonstrated by the same calcite percentage obtained for the original and cleaned sub-fragments from layer three (Table 4.6). It is worth highlighting that in the original and cleaned sub-fragments, the spectra were collected only from the external shell surface, comprising 60 spectra. For the powdered sub-fragments, the entire volume was sampled, comprising a total of 200 spectra. Therefore, only the results from the powdered sub-fragments were compared to the representative obtained from the heat treatments performed in the modern shells.

**Table 4.6:** Quantitative Raman parameters for the burnt *Conomurex fasciatus* shell fragments from layers three and ten in the KM1057 shell midden. Original and cleaned sample preparation conditions comprise averages of 60 spectra, while the powdered comprises 200 spectra. The uncertainties are measured by the SE.

| **Burnt fragment from Layer 3** | | | | | |
|---|---|---|---|---|---|
| **Fragment condition** | **Peak** | **Position** ($cm^{-1}$) | **FWHM** ($cm^{-1}$) | **Peak Intensity ratio** ($L_1/\nu_1$) | **Calcite** (%) |
| Original | $L_1$ | $151.4 \pm 0.2$ | $9.0 \pm 0.2$ | $0.11 \pm 0.007$ | $78 \pm 1$ |
| | $\nu_1$ | $1081.18 \pm 0.09$ | $4.1 \pm 0.1$ | | |
| Cleaned | $L_1$ | $151.3 \pm 0.1$ | $8.8 \pm 0.2$ | $0.10 \pm 0.007$ | $79 \pm 1$ |
| | $\nu_1$ | $1082.34 \pm 0.07$ | $3.92 \pm 0.09$ | | |
| Powdered | $L_1$ | $152.48 \pm 0.07$ | $10.12 \pm 0.05$ | $0.11 \pm 0.002$ | $99.9 \pm 0.1$ |
| | $\nu_1$ | $1082.74 \pm 0.06$ | $4.45 \pm 0.02$ | | |

| **Burnt fragment from Layer 10** | | | | | |
|---|---|---|---|---|---|
| **Fragment condition** | **Peak** | **Position** ($cm^{-1}$) | **FWHM** ($cm^{-1}$) | **Peak Intensity ratio** ($L_1/\nu_1$) | **Calcite** (%) |
| Original | $L_1$ | $152.2 \pm 0.1$ | $8.6 \pm 0.2$ | $0.09 \pm 0.008$ | $91 \pm 1$ |
| | $\nu_1$ | $1081.68 \pm 0.09$ | $3.80 \pm 0.07$ | | |
| Cleaned | $L_1$ | $152.8 \pm 0.1$ | $8.0 \pm 0.1$ | $0.08 \pm 0.005$ | $100 \pm 1$ |
| | $\nu_1$ | $1082.26 \pm 0.07$ | $4.2 \pm 0.1$ | | |
| Powdered | $L_1$ | $153.07 \pm 0.05$ | $9.89 \pm 0.05$ | $0.11 \pm 0.002$ | $100 \pm 1$ |
| | $\nu_1$ | $1082.84 \pm 0.05$ | $4.35 \pm 0.03$ | | |

The peak intensity ratios $L_1/\nu_1$ obtained for the powdered burnt fragments match the values found for the modern shells after the aragonite to calcite transition, thus also indicating a full polymorph conversion (Figure 4.14). Similar results were also found when these ratios were plotted against the temperature for heating times of 4h and 8h (Appendix B, Figure B.9). As the graphical trends for the modern samples show, the $L_1/\nu_1$ peak intensity ratio remains constant after this transition occurs.

When a full conversion to calcite is observed in aragonitic archaeological shells it could have been caused either by the heating process or significant diagenetic alteration, which causes the dissolution of aragonite and calcite recrystallisation. Thus, since the analysed *Conomurex fasciatus* fragments had charring signals (Figure 2.2 of Chapter 2), only the heating conversion is considered. In the modern shells, the full aragonite to calcite conversion only took place when the samples were heated for at least 2h at 400°C or 1h at 500°C (Figure 4.6), indicating these as minimal heating times and temperatures for the burnt *Conomurex fasciatus* fragments (Figure 4.14).

The FWHM values of the $L_1$ peak (~153 cm$^{-1}$) for the burnt *Conomurex fasciatus* fragments are in the range obtained for the modern shells and the results corresponding to the burnt fragments cross the values found for the modern shells at the points corresponding to a heating of 15min at 400°C (Figure 4.15a) and 7 min at 500°C (Figure 4.15a). However, as previously explained (Figure 4.6), the full aragonite to calcite transition only occurs, in a modern shell, after one 2h of heating at 400°C or 1h of heating at 500°C. Thus, as it was estimated that the powdered sub-fragments were composed only of calcite, such heating conditions (15min at 400°C or 7 min at 500°C) cannot be considered because they correspond to aragonite. From the same Figure 4.15, it can be seen that the calcite FWHM increases with heating time after the aragonite to calcite conversion. The same is observed when the FWHM of the $\nu_1$ (~1082 cm$^{-1}$) peak is plotted against the heating time for temperatures at 400°C and 500°C (Appendix B Figure B.10). Therefore, it is expected that there might be a heating time greater than 8h and/or greater than 500°C, where the modern shell results will cross the results obtained for the burnt fragments. To check the latter possibility, the FWHM of the $L_1$ (Figure 4.16) peak was plotted as function of the temperature for a heating treatment of 8h. This graph points that in a temperature greater than 500°C the burnt fragments results would coincide with the heated modern samples. Therefore, indicating that the burnt fragments could have been heated at temperatures greater than 500°C. Similar indication is also obtained from the $\nu_1$ peak (Appendix B Figure B.11). From the experiments performed with the modern shells, it was noted that as the temperature increases, the full aragonite to calcite transi-

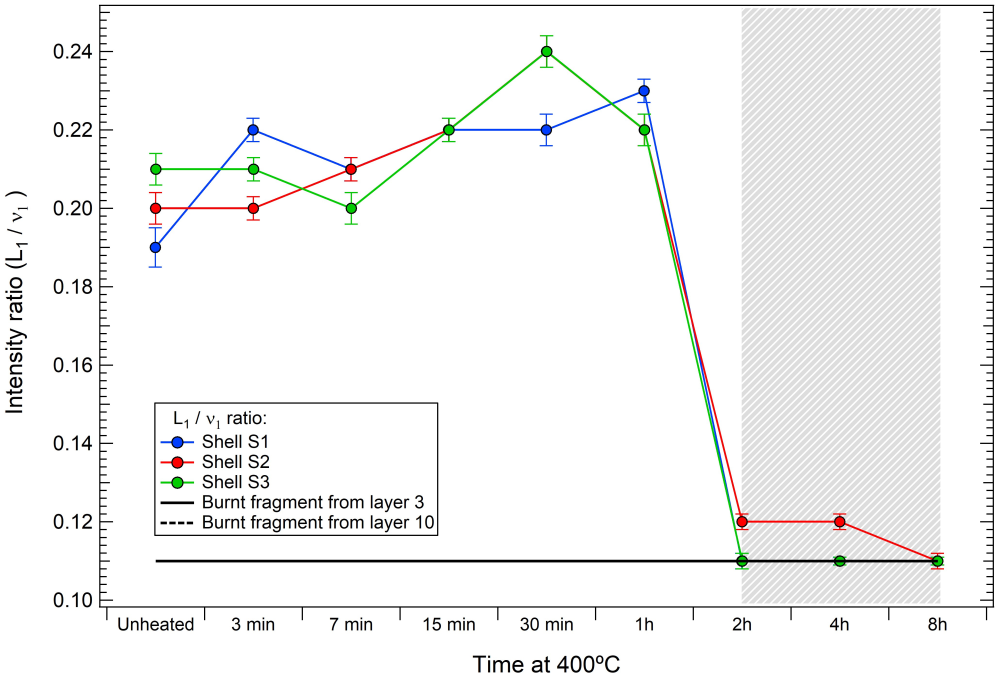

**(a)**

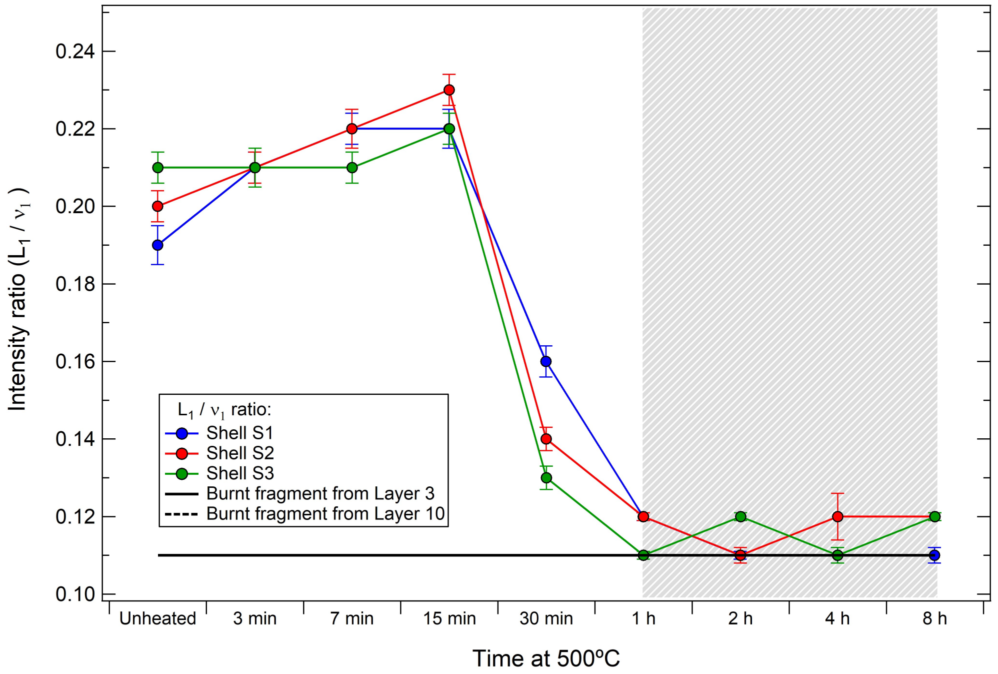

**(b)**

**Figure 4.14:** Comparison of the intensity ratio $L_1/\nu_1$ from the burnt *Conomurex fasciatus* fragments with the heated modern shells (S1, S2 and S3) as function of increasing time in the furnace for temperatures of (a) 400°C and (b) 500°C. The peak intensity ratios obtained for both burnt fragments are superposed. Full aragonite to calcite conversion is observed only after 2h heating at 400°C and 1h heating at 500°C (marked by the shaded areas), thus indicating minimal heating times and temperatures for the burnt fragments.

tion happens with shorter heating times (Figure 4.6). Thus, at temperatures greater than 500°C, the aragonite to calcite transition would happen in less than one hour of heating. The burnt fragments may not have been exposed to temperatures greater than ∼700°C to ∼800°C because this is the range for the calcite to CaO transformation in biogenic samples [84, 89, 169] and only calcite was observed in the analysed fragments. Additionally, shells treated at such elevated temperatures become brittle, as demonstrated by S. Milano *et al.* (2016) [134], and probably would not survive the shell midden environment.

Estimating the temperature to which a shell had been submitted has implications for the interpretation of a site that has burnt shell fragments. V. Aldeias *et al.* (2016) proposed that the assemblages containing shells with mixed mineralogy (calcitic and aragonitic shells of the same species) would indicate cooking, whilst completely calcite transformed assemblages indicate in burning, and therefore, should be interpreted as fire places rather than roasting hearths [142]. They studied the effect of different roasting procedures on aragonitic shellfish, testing methods consisted by constructing shallow depressions with heated rocks, placing the shells on top of hot embers and ashes, and kindling short-lived fires on top of the shells [142]. In such roasting procedures, the temperature of fire oscillated between ∼400°C and ∼900°C. Thus, temperatures greater than 500°C could be easily produced. In the shallow depression method studied by them, the shells did not come into direct contact with fire, thus not converting to calcite, and the temperature of ∼160°C produced by this method cooked the shellfish; the other two methods caused a widespread transformation of shells from aragonite to calcite and only few of the shellfish were not burnt and thus, edible [142]. The complete aragonite to calcite transformation, thus takes place when the shells are thrown into fire [142] or when they are the substrate underlying a fire [174]. The deposition of products from a hearth can indicate if it had been lit on top of a mound and later cleaned away and covered with more shells [174].

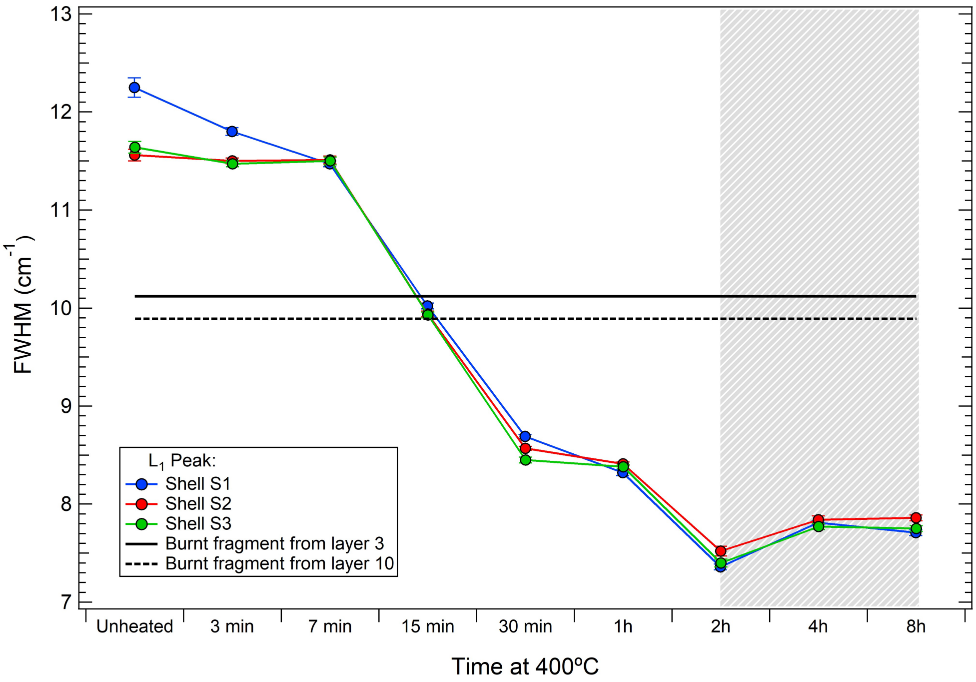

**(a)**

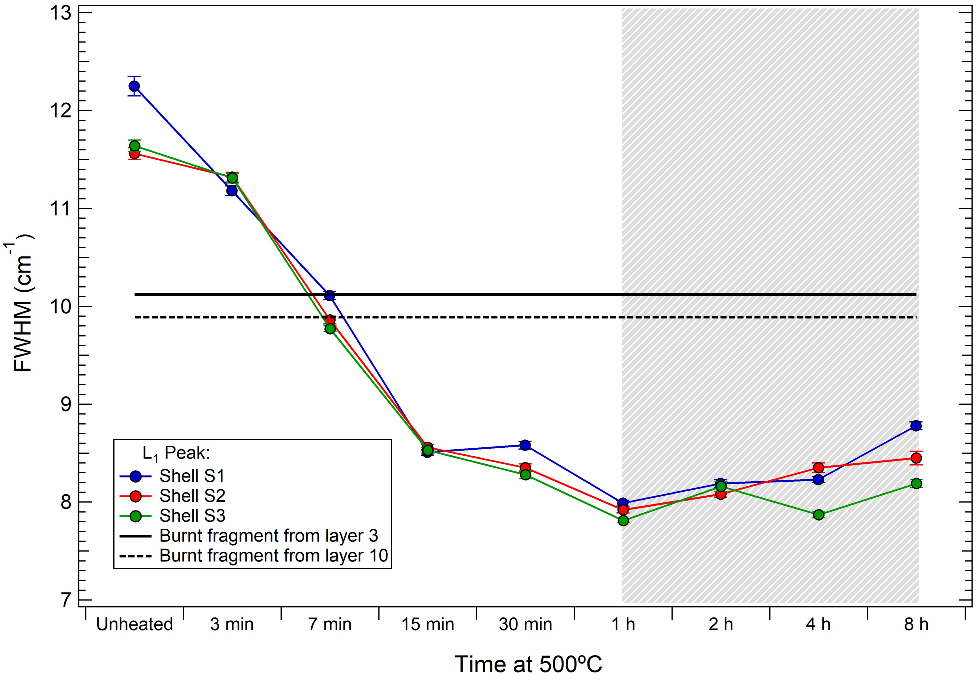

**(b)**

**Figure 4.15:** Comparison of the FWHM of the $L_1$ (∼153 cm$^{-1}$) peak of the burnt *Conomurex fasciatus* fragments with the heated modern shells (S1, S2 and S3) results as function of increasing time in the furnace at (a) 400°C and (b) 500°C. Full aragonite to calcite conversion is observed only after 2h heating at 400°C and 1h heating at 500°C (marked by the shaded areas), thus indicating minimal heating times and temperatures for the burnt fragments.

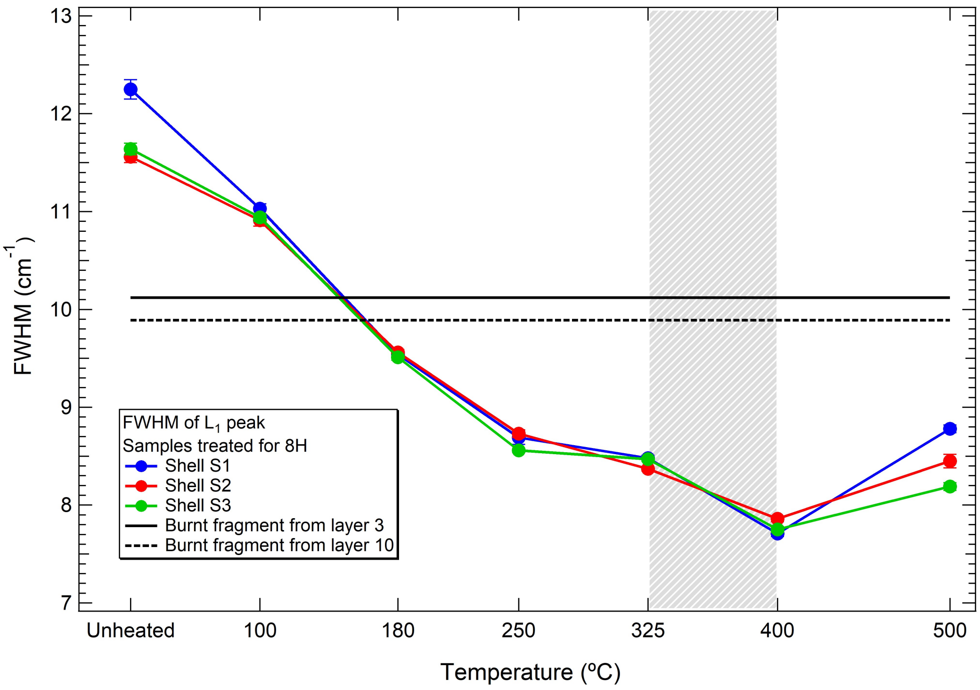

**Figure 4.16:** Comparison of the FWHM of the $L_1$ ($\sim$153 cm$^{-1}$) peak of the burnt *Conomurex fasciatus* fragments with the heated modern shells (S1, S2 and S3) as function of temperature for a heat treatment of 8h. The shaded area marks the temperature range for which the aragonite to calcite transition takes place. After the transition the $L_1$ FWHM starts to increase, indicating that the burnt fragments could have been exposed to temperatures greater than 500°C.

Therefore, following this logic, the burnt *Conomurex fasciatus* fragments could have been exposed to fire places rather than being roasted with the purpose of cooking.

A good starting point of such investigation is the analysis of the shell mineralogy. If such a shell is known to be only composed of aragonite, the presence of calcite might indicate that it could had been heated. As demonstrated by the results presented in this section, FWHM values of Raman spectra can be used to estimate temperatures to which shells had been exposed before and after the aragonite to calcite transition. Nonetheless, in order to provide more accurate results, many other temperatures and heating times have to be covered by RS. There is a lack of spectroscopic studies in this area and further research, combined with other techniques, and applied to other shell species, may unlock enough information to precisely determine temperatures and heating times.

## 4.7 Chapter conclusions

Quantitative RS allowed the detection of changes in the crystalline structure of the aragonite present in the modern *Conomurex fasciatus* powdered shells that were heat-treated for seven minutes or more at 400°C and 500°C. These observations could help find evidence of heating in archaeological shells that show no visual alterations or that have not undergone the full aragonite to calcite transition.

The $L_1/\nu_1$ peak intensity ratio was found to be a marker for the aragonite to calcite phase transition. Such as the method suggested in the literature by H. Edwards *et al.* (2005) [105], this intensity ratio could also be used for estimating the percentages of aragonite and calcite. The $L_1/\nu_1$ peak intensity ratio determined that a complete aragonite to calcite conversion happened after 2h for the modern powdered shells heated at 400°C and after 1h when heated at 500°C. The decay in the $L_1/\nu_1$ peak intensity ratio values shows when the transition to calcite occurs. However, for such a peak intensity ratio to be used for estimating the polymorphs percentages, many more time-points would need to be included in the time range for which the transition takes place. Additionally, such a method would also need to be tested and validated with the use of mixed proportions of aragonite and calcite.

Although the $L_1/\nu_1$ peak intensity ratio is sensitive to the polymorph phase, it cannot be the used to determine if a shell had been heated if the aragonite to calcite transition has not occurred. The FWHM of both the $L_1$ and $\nu_1$ peaks, from the spectra obtained from the powdered modern shells, proved to be sensitive to heat treatments. A heating of only seven minutes at 500°C was already sufficient to decrease the FWHM of both peaks. In spectroscopy, a decrease in a peak's FWHM is associated to an increase in the crystallinity of the material. For both peaks, this increase in the crystallinity was observed before the phase transition and is believed to originate from the degradation of the organic macromolecules in the shell structure. According to the literature, this degradation then leads to a mineral lattice relaxation and a size reduction of the calcium carbonate crystal blocks. The presumed degradation of the organic macromolecules could also be related to the appearance of amorphous carbon that became more evident, in the spectra of the modern heated shells, for increasing heating times at 400°C and 500°C.

A decrease in the crystallinity (or increase in the FWHM of the $L_1$ and $\nu_1$ peaks) of the modern shells was observed after the aragonite to calcite transition had occurred, with these probably related to the thermal expansion of the calcite crystal before the phase transition to calcium oxide. Such transition is observed, in the literature, to occur from ~700°C to ~800°C.

Impurities such as Fe, Zn, Pb and Mn are known to influence the crystal growth rate and to affect the crystallinity of synthetic carbonates; however, they were not found in the samples analysed with EDX. The presence of S, Zr, Si, Mg and Na was observed with atom percent values ranging from 0.03% to 0.79%. There was also no direct relation between the impurities atom percent values and the heating times.

In the literature, the lattice vibrations of geological aragonite are more affected by increasing temperatures than the internal modes of the carbonate group, thus reflecting a progressive rotational disorder that precedes the aragonite to calcite transition. Such sensitivity was also observed in the results obtained for the heated modern shells for which the FWHM of the $L_1$ peak decreased 36% and 32%, respectively for heat treatments at 400°C and 500°C, while the $\nu_1$ FWHM decreased 18% and 15% for the same temperatures.

The Raman quantitative parameters of the burnt archaeological *Conomurex fasciatus* fragments were compared to the $L_1/\nu_1$ peak intensity ratio and FWHM trends obtained from the heating of the modern shells, as a function of temperature and time. The peak intensity ratio values obtained for the burnt fragments matched the modern shells' trends, indicating a transition to calcite. A full conversion to calcite was also estimated by using the relative intensity of the $L_2$ lattice mode peaks, as established by H. Edwards *et al.* (2005) [105]. The FWHM values obtained for the burnt fragments were outside the time and temperature range covered by the modern heated shell results. However, as indicated by the increase in the FWHM of the $L_1$ and $\nu_1$ peaks, after the aragonite to calcite phase transition, the fragments could have been heated at temperatures greater than 500°C. The fragments may also not have been exposed to temperatures greater than ~700°C to ~800°C, as this is the range for the calcite to calcium oxide transformation, which makes the shells brittle and fragile. However, for the method to be more accurate, additional heating times and temperatures need to be included in quantitative RS studies of modern heat shells.

Knowing if a shell had been heated, and at which temperature, has implications in the interpretation of archaeological sites that contain burnt shell fragments, as they could be related to the action of cooking. Additionally, archaeological shells are also important for marine paleoclimatology, which is studied by correlating the temperature and salinity of the sea with isotopic ratios in shells. However, it is known that erroneous temperatures might be inferred if paleoenvironmental reconstructions are made using shells that had been heated. To date, the classification of heated shells has been made purely by visual observations or by the transition to calcite in aragonitic shells. However, this is not accurate if the heating has not caused a colour alteration or such polymorph transition. This chapter demonstrated that RS is sensitive enough to detect if a shell had been heated. The spectral bands $L_1$ and $\nu_1$ were sensitive to heat induced changes. Their FWHM can be used to predetermine if a shell underwent heating, even if the aragonite to calcite transition has not taken place. Their peak intensity ratio ($L_1/\nu_1$) is sensitive to the polymorph phase and can be used as a marker for the aragonite to calcite phase transition. To date this is the first time that the effects of heating in biogenic aragonite and aragonite to calcite transition were studied using quantitative Raman spectroscopy.

# Chapter 5

# Assessing diagenesis of shells from different layers in a shell midden with RS

This chapter describes additional experiments performed with RS on the *Conomurex fasciatus* shells where two archaeological shells obtained from layers 3, 6 and 10 from the KM1057 shell midden were compared with modern *Conomurex fasciatus* samples. As the results obtained in Chapter 3 demonstrated that RS could be used to assess diagenesis in shells, the same quantitative analyses of the calcium carbonate peaks, corresponding to the FWHM and peak intensity ratio analyses, were then applied to these additional experiments. The aim of these analyses is to explore the potential of RS in verifying the conservation state of the shells from different layers by comparing their Raman quantitative parameters.

## 5.1 Summary of the different layers of the KM1057 shell midden

The shell middens of the Farasan Islands are one of the largest concentrations of shell mounds known and only started being surveyed in 2006 [143]. They form an almost pristine distribution of material with little damage or destruction due to the inaccessibility of the islands, which were military areas until recently, as well as there being a low population density, lack of modern developments and rarity of visiting archaeologists [143].

The KM1057 shell midden is located at the Khur Maadi Bay and is 30 m in diameter and 3 m high, therefore it is considered a large mound. It is dominated by layers of *Conomurex fasciatus* shells; however, near the top section there are two layers of *Conomurex fasciatus* shells with an ash matrix (Figure 5.1a), while other shell species, as *Chama reflexa* and *Spondylus marisrubri* were observed in five thinner layers near the top and the base of the excavated section (Figure 5.1a) [143]. Due to no animal bones, fish or plant seeds being found in the KM1057 shell midden, this mound is thought to have been an intensive processing site for the *Conomurex fasciatus* shells [143]. The overlapping dates of 5515–5110 cal BP for the uppermost layer and 5461–5046 cal BP for the lowermost layer, obtained with radiocarbon dating, suggested that the shells were rapidly accumulated in the midden [143].

Aragonitic shells affected by diagenetic alterations have their mineralogy altered by the conversion of the biogenic aragonite into calcite [70, 133, 138, 140]. Such a calcium carbonate phase transition can also be triggered by heating [46,134,136,137]. The previous Chapters 3 and 4 showed that RS is a promising technique to investigate diagenesis and taphonomic alterations as demonstrated by the comparison of the FWHM of peaks from the Raman spectra of modern and archaeological *Conomurex fasciatus* shells in Section 3.3

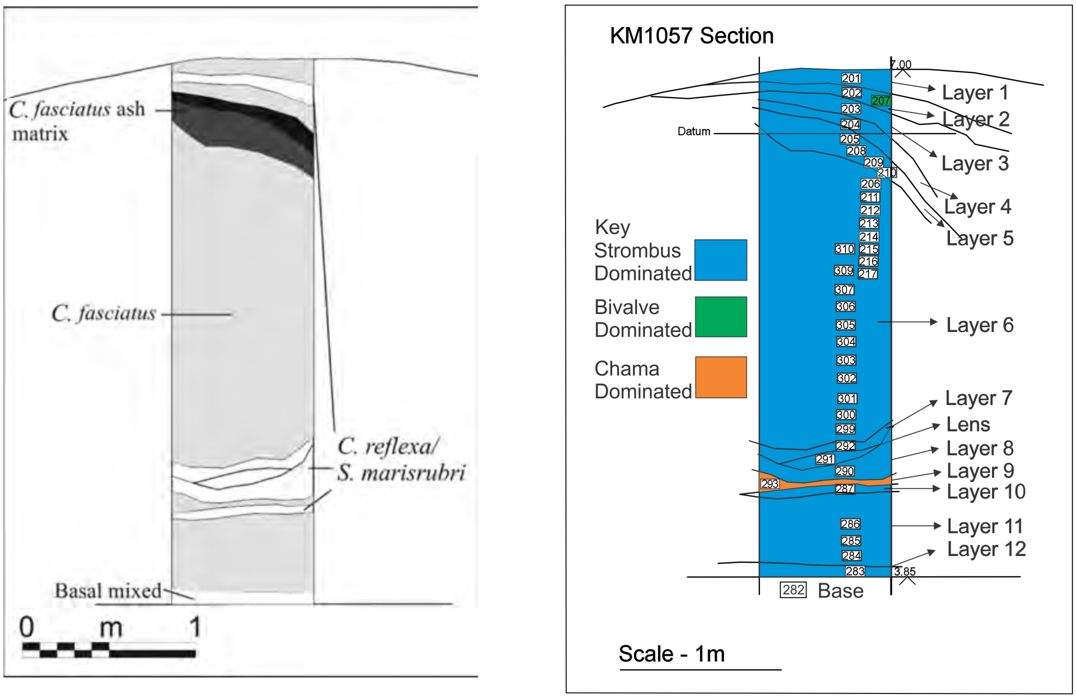

**(a)** **(b)**

**Figure 5.1:** Sections of the KM1057 shell midden, showing (a) the large prevalence of *Conomurex fasciatus* shells and the relative little occurrence of a matrix ash (grey and black areas near the top) and other shell species, such as *Chama reflexa* and *Spondylus marisrubri* (white areas near the top and the base). This image was adapted from the drawing made by Matthew Meredith-Williams [143], and (b) cross-section of the KM1057 shell midden specifying the layers and the dominant shell species in each of them. The numbers in the white boxes correspond to bags of specimens collected in spits in each layer. Drawn by Dr. Eva Laurie, University of York.

in Chapter 3 and by the results of the heating experiments performed in the *Conomurex fasciatus* shells presented in Sections 4.4 and 4.6 from Chapter 4, where both FWHM and peak intensity ratios were investigated. Therefore, since the KM1057 shell midden has been rapidly accumulated, RS was investigated as a means of verifying if shells from different layers had been differently affected by diagenetic alterations.

## 5.2 Averaged Raman spectra and peak assignments

Two archaeological *Conomurex fasciatus* shells, per layer, from layers 3 (denoted here L3S1 and L3S2), 6 (denoted L6S1 and L6S2) and 10 (named L10S1 and L10S2), from the KM1057 shell midden, were studied. Layer 6 is the largest layer in the excavated shell midden; therefore, the specimens used in this experiment came from the mid-section (specimen bag 305, Figure 5.1b). As explained in Sections 2.1 and 2.2.3 of Chapter 2, the archaeological shells from KM1057 were cleaned with fresh water and dried at room temperature. Figure 5.2 shows the six studied archaeological shells before being processed. The shells were then powdered using a pestle and mortar.

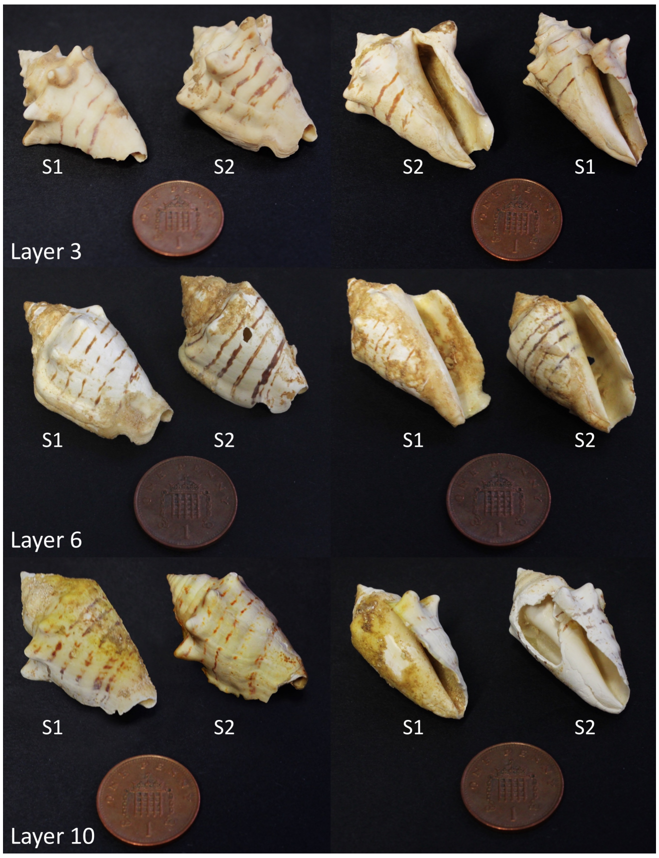

**Figure 5.2:** Images of the *Conomurex fasciatus* shells from layers 3, 6 and 10. Two different shell samples were randomly selected from each layer (S1 and S2). Before the Raman measurements, the shells were cleaned with fresh water, dried at room temperature and then powdered using a pestle and mortar. Raman spectra were randomly collected from the powdered shells.

The analyses of powdered samples allows a random sampling of the entire shell, whilst for bulk shell analyses, the data collection is restricted to the internal or external surfaces. From a sample subset of each powdered shell, 200 spectra were randomly collected as determined by the convergence test results for powdered shell analyses performed in Section 4.1 of Chapter 4. The averaged spectra of each shell are shown in Figure 5.3 and illustrate the studied peaks (marked in the figure), which were identified as corresponding to aragonite or calcite vibrations by comparison with literature references [52, 91, 92, 94, 96–99].

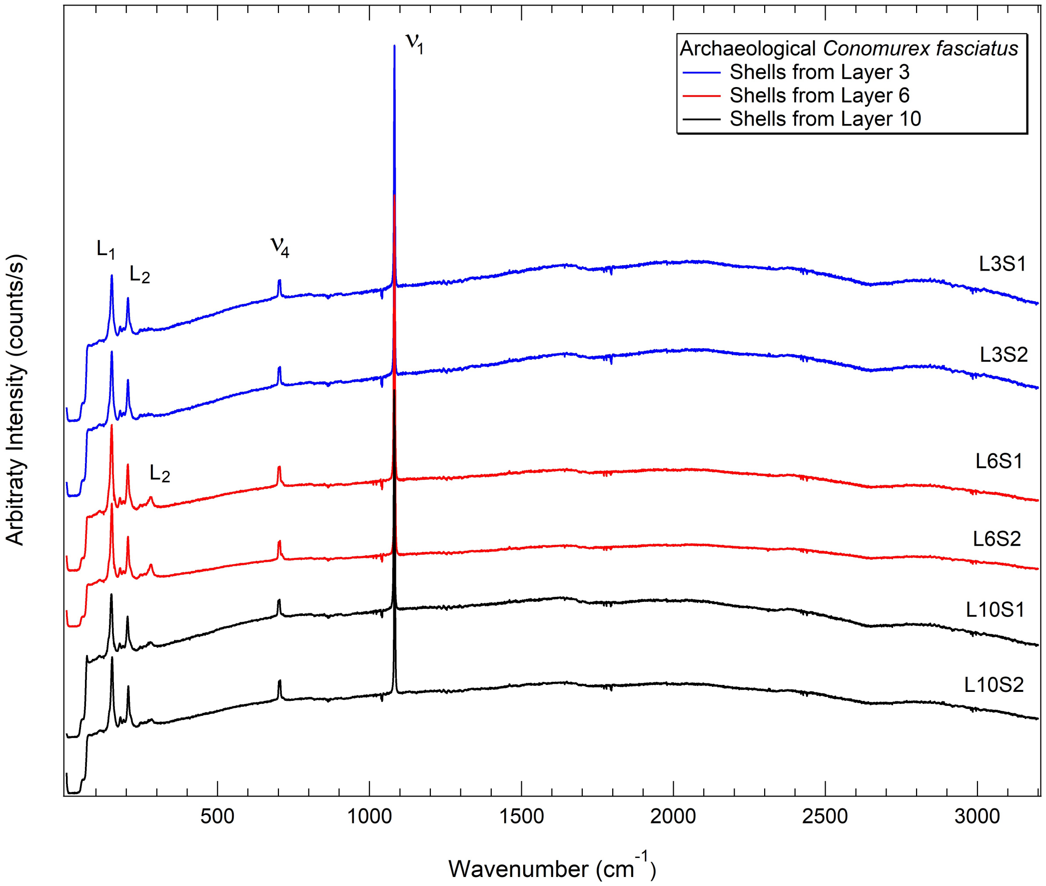

**Figure 5.3:** Averaged Raman spectra of the archaeological *Conomurex fasciatus* shells from layers 3, 6 and 10. Two specimens were analysed for each layer, with the averaged spectra comprising 200 Raman measurements obtained from each shell. Specimens from layer 3 are composed of aragonite (L3S1 and L3S2). The librational lattice mode peak ($L_2$) is observed at ~205 cm$^{-1}$ for aragonite and at ~280 cm$^{-1}$ for calcite. Such calcite peak was observed only in the samples from layers 6 and 10, indicating a recrystallisation of the biogenic aragonite into calcite. Peak assignments and corresponding literature references can be found in Table 5.1.

The obtained spectra were individually analysed, with peak fitting procedures performed on the carbonate peaks as described in Section 2.2.5 of Chapter 2. The spectra obtained from the specimens of layer 3 showed the Raman signature of aragonite, while the spectra of shells from layers 6 and 10 showed an admixture of aragonite and calcite peaks (Figure 5.3). The measured peak positions and corresponding literature references for each peak can be found in Table 5.1. These measured peak positions are the average across the 400 spectra obtained for the analysed shell samples S1 and S2 from layers 3, 6 and 10, with the standard error of the mean representing the peak position uncertainties.

**Table 5.1:** Peak positions and assignments for aragonite and calcite observed in the *Conomurex fasciatus* shells from layers 3, 6 and 10 in the KM1057 shell midden. The peak positions are the average over the 400 spectra obtained for the analysed replicate samples (S1 and S2) from the different layers. The peak position uncertainties are the standard error of the mean. Only aragonite was observed in layer 3, while an admixture of aragonite and calcite were found in both replicate samples from layers 6 and 10.

| Layer | Peak Code | Measured position ($cm^{-1}$) | Literature peak assignments |
|---|---|---|---|
| Layer 3 | $L_1$ | 152.02 ± 0.02 | Translational lattice mode [92, 94, 96–99] |
| | $L_2$ | 205.48 ± 0.02 | Librational lattice mode [92, 94, 96–99] |
| | $\nu_4$ | 701.62 ± 0.01<br>705.94 ± 0.01 | In plane antisymmetric bend [52, 92, 94, 96–99] |
| | $\nu_1$ | 1082.23 ± 0.01 | Symmetric stretch [52, 92, 94, 96–99] |
| Layer 6 | $L_1$ | 151.76 ± 0.04 | Translational lattice mode [92, 94, 96–99] |
| | $L_2$ | 205.25 ± 0.04<br>280.35 ± 0.05 | Librational lattice mode [91, 92, 94, 96, 97, 99] |
| | $\nu_4$ | 701.06 ± 0.04<br>705.36 ± 0.04 | In plane antisymmetric bend [52, 92, 94, 96–99] |
| | $\nu_1$ | 1082.59 ± 0.04 | Symmetric stretch [52, 92, 94, 96–99] |
| Layer 10 | $L_1$ | 151.87 ± 0.06 | Translational lattice mode [92, 94, 96–99] |
| | $L_2$ | 205.40 ± 0.06<br>280.2 ± 0.2 | Librational lattice mode [91, 92, 94, 96, 97, 99] |
| | $\nu_4$ | 701.06 ± 0.06<br>705.38 ± 0.06 | In plane antisymmetric bend [52, 92, 94, 96–99] |
| | $\nu_1$ | 1082.34 ± 0.05 | Symmetric stretch [52, 92, 94, 96–99] |

The $L_1$ and $\nu_1$ peaks are the bands observed in both aragonite and calcite spectra and correspond, respectively to the translational lattice mode and symmetric stretch vibrations. Their peak positions listed in Table 5.1, correspond only to aragonite for the layer 3 samples, and to the aragonite-calcite admixture for the samples from layers 6 and 10. The calcite peak measured at ~280 cm$^{-1}$, assigned to the librational lattice mode ($L_2$), was only observed in the spectra of shells from layers 6 and 10 (Figure 5.3). All the other peaks correspond only to aragonite vibrations and are the librational lattice mode peak ($L_2$) measured at ~205 cm$^{-1}$ and the internal in-plane antisymmetric bend ($\nu_4$), a characteristic doublet in the aragonite spectra, measured at ~701 cm$^{-1}$ and ~705 cm$^{-1}$ .

## 5.3 Diagenesis assessment - presence of calcite and FWHM analyses

One indication of diagenetic alteration is the presence of calcite in aragonitic shells [46, 70, 133, 138, 140]. Aragonite is an unstable calcium carbonate polymorph and, during diagenesis, the mineral stability is obtained by the dissolution and recrystallisation of this unstable phase or the appearance of new phases, such as the recrystallisation of biogenic aragonite into calcite [46, 79].

Although predominately composed of aragonite, the analysed archaeological *Conomurex fasciatus* shells presented different percentage compositions of aragonite, as demonstrated by Table 5.2. This mineral composition was estimated from the Raman spectra using the method proposed by Edwards *et al.* (2005) [105] and explained in Section 4.3 of Chapter 4. This method consists of examining the relative intensities of the $L_2$ peak of the aragonite and calcite, respectively at ~205 cm$^{-1}$ and ~280 cm$^{-1}$. The percentage mineral composition was obtained for each measured Raman spectrum and then averaged over the

**Table 5.2:** Percentage composition of aragonite in the archaeological *Conomurex fasciatus* shells from different layers in the shell midden. The composition was estimated with RS by using the method proposed by Edwards *et al.* (2005) [105] and explained in Section 4.3 of Chapter 4. The percentage values were obtained in each Raman spectrum collected and then averaged over the 200 measurements performed on each shell. The percentage aragonite composition uncertainties are the standard error of the mean.

| | Archaeological *Conomurex fasciatus* | Aragonite (%) |
|---|---|---|
| Layer 3 | Sample 1 (L3S1) | 99.5 ± 0.4 |
| | Sample 2 (L3S2) | 99.4 ± 0.4 |
| Layer 6 | Sample 1 (L6S1) | 91 ± 1 |
| | Sample 2 (L6S2) | 83 ± 2 |
| Layer 10 | Sample 1 (L10S1) | 95.5 ± 0.9 |
| | Sample 2 (L10S2) | 97.1 ± 0.8 |

200 measurements performed for each shell. The partial conversion of aragonite to calcite is confirmed by the estimated aragonite percentage values shown in Table 5.2, which were higher for the upper part of the midden (layer 3) and lower for the archaeological shell samples from layers 6 and 10. For the modern shells, the aragonite percentage was estimated in 99.2% ± 0.5%, 99.5% ± 0.3% and 100%, for the sample replicates S1, S2 and S3 respectively. The aragonite-calcite admixture spectra observed in layers 3, 6 and 10 corresponded respectively to 2, 137 and 40 spectra amongst the 400 spectra collected for both samples of each layer. The lowest values for aragonite were obtained for the two shell specimens from layer 6, for which 91 ± 1% and 83 ± 2% of aragonite were estimated, thus indicating that in these shells more of their original biogenic aragonite has recrystallised into calcite.

The shell midden depth could affect the pressure over the accumulated shells. Although the aragonite-calcite transition is not induced by pressure at room-temperature [87], aragonite is known to be more stable for increasing pressures [81], which would implicate in observing higher concentrations of calcite for layer 3. However, the results presented in Table 5.2 show no correlation between the shell midden depth and the presence of calcite. A similar conclusion was also made by Sheng *et al.* (2005), who showed that on Earth-surface conditions, pressure was not influencing the biogenic aragonite to calcite conversion in fossilised land snail shells [83].

As demonstrated in Chapter 3 (Section 3.3), the FWHM of calcium carbonate peaks, associated to the Raman spectra of shells, was a sensitive marker to assess diagenesis due to its ability to distinguish modern from archaeological *Conomurex fasciatus* shells. In that chapter, the best markers were the FWHM of the main calcium carbonate peak $\nu_1$ at $\sim$1082 cm$^{-1}$ and the FWHM of the translational lattice mode $L_1$ at $\sim$151 cm$^{-1}$. Therefore, to evaluate diagenesis, a comparison in terms of the FWHM, was performed between the archaeological *Conomurex fasciatus* shells from the different shell midden layers with the modern *Conomurex fasciatus* specimens. The spectra of the modern *Conomurex fasciatus* shells had already been collected and individually fitted, with the procedures described in Section 2.2.5 of Chapter 2, for the analyses performed in Chapter 4.

The modern versus different layer FWHM comparisons are shown from Figure 5.4 to 5.6. The investigated peaks were the $L_1$ (151 cm$^{-1}$), $L_2$ (205 cm$^{-1}$), $\nu_4$ (701 cm$^{-1}$ and 705 cm$^{-1}$) and $\nu_1$ (1082 cm$^{-1}$). It is important to remember that the $L_1$ and $\nu_1$ peaks are common in both aragonite and calcite spectra. All other peaks are present only in the aragonite spectra. The FWHM of these peaks was measured in each of the obtained Raman spectra and then averaged over the 200 spectra collected for each sample on the different layers.

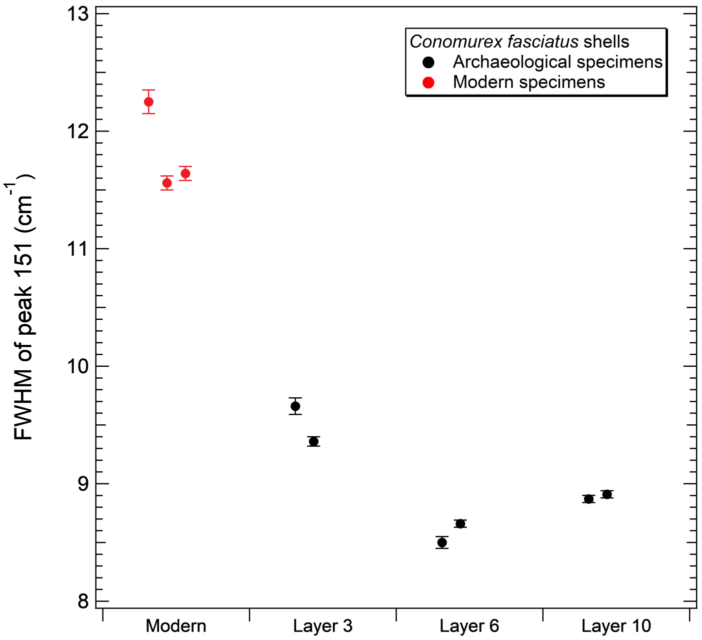

(a)

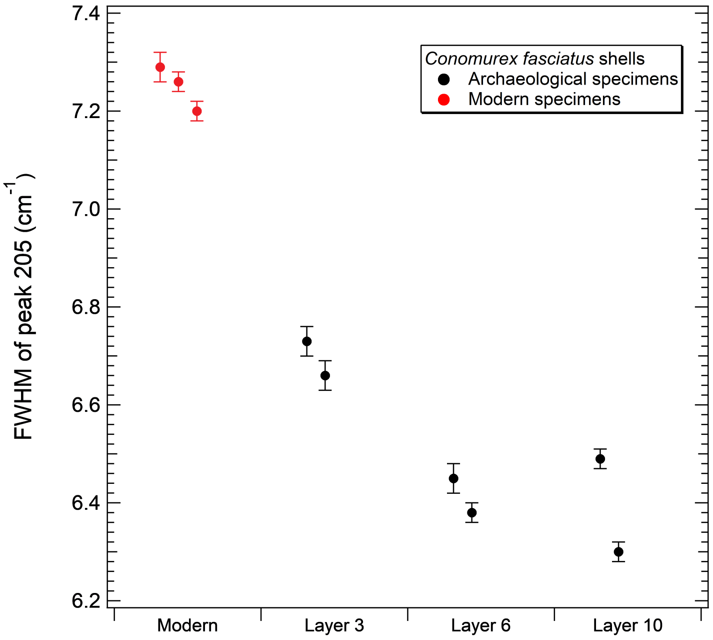

(b)

**Figure 5.4:** FWHM of the lattice mode peaks at (a) 151 cm$^{-1}$ ($L_1$) and (b) 205 cm$^{-1}$ ($L_2$) from the Raman spectra of modern *Conomurex fasciatus* shells and archaeological shell specimens from layers 3, 6 and 10 of the KM1057 shell midden. The FWHM was measured in each individual spectrum and then averaged over the 200 Raman measurements performed for each shell. The error bars represent the SE associated to the FWHM. A clear separation is observed between the FWHM of modern and archaeological shells.

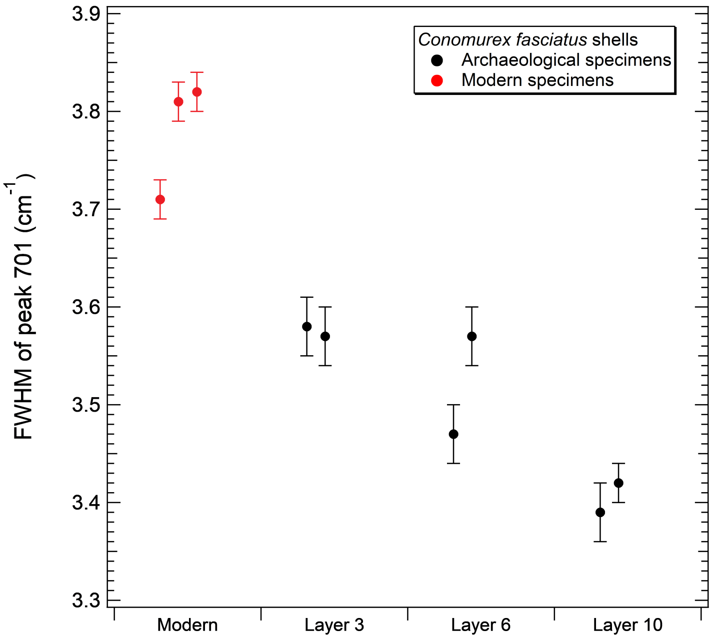

(a)

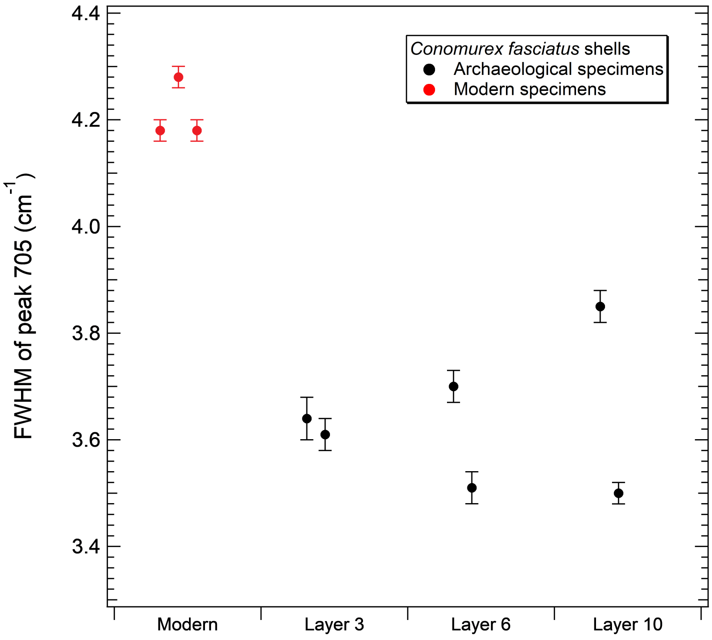

(b)

**Figure 5.5:** FWHM of the $\nu_4$ peaks at (a) 701 cm$^{-1}$ and (b) 705 cm$^{-1}$ from the Raman spectra of modern *Conomurex fasciatus* shells and archaeological shell specimens from layers 3, 6 and 10 of the KM1057 shell midden. The FWHM was measured in each individual spectrum and then averaged over the 200 Raman measurements performed for each shell. The error bars represent the SE associated to the FWHM. A clear separation is observed between the FWHM of modern and archaeological shells.

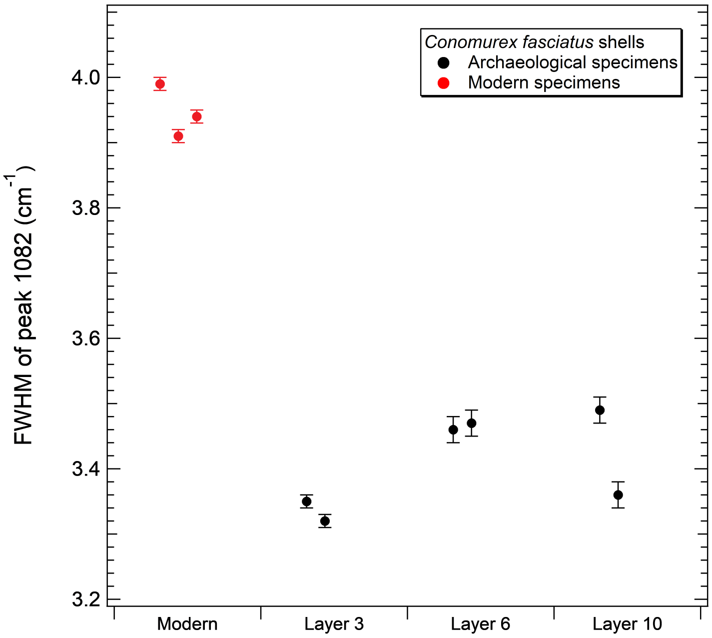

**Figure 5.6:** FWHM of the $\nu_1$ peak at 1082 cm$^{-1}$ from the Raman spectra of modern *Conomurex fasciatus* shells and archaeological shell specimens from layers 3, 6 and 10 of the KM1057 shell midden. The FWHM was measured in each individual spectrum and then averaged over the 200 Raman measurements performed for each shell. The error bars represent the SE associated to the FWHM. A clear separation is observed between the FWHM of modern and archaeological shells.

A clear separation between the FWHM of the analysed peaks from modern and ancient shells can be observed in all of these comparisons, with the FWHM of the modern samples presenting higher values than those of the archaeological specimens. When the FWHM of the archaeological shells is compared only across layers, a decreasing trend for the lattice mode peaks $L_1$ (151 cm$^{-1}$) and $L_2$ (205 cm$^{-1}$) is observed as function of the shell midden depth (Figure 5.4). The same trend is also observed for the first doublet peak corresponding to the $\nu_4$ vibration at 701 cm$^{-1}$ (Figure 5.5a). However, for the second doublet peak (705 cm$^{-1}$), the two analysed archaeological shell specimens showed contrasting features, with one of them displaying a decreasing, and the other an increasing, in the FWHM as function of the mound depth (Figure 5.5b). No decreasing, nor increasing trend, is observed for the FWHM of the main calcium carbonate peak $\nu_1$ (1082 $cm^{-1}$) as function of the mound depth (Figure 5.6).

As discussed in Chapter 3, in spectroscopy the crystallinity is associated to the FWHM, for which smaller values correspond to an increasing crystallinity of the analysed sample [50]. Thus, although there has been some variability among the results of the archaeological shells, their smaller FWHM values could indicate that they are more crystalline than the modern specimens.

An enhancement in the crystallinity has already been verified for archaeological bioapatites and linked to the loss of their organic matrices, which then caused changes to their crystal structure [39, 160–162]. The destruction of the organic components or their replacement by inorganic materials has also been observed on diagenetically altered biocarbonates [78,138,140,163]. Thus, the lower FWHM values obtained for the archaelogical shell samples when compared to the modern *Conomurex fasciatus* specimens could be due to a loss of the organic matrix. An increase in the crystallinity of biogenic calcium carbonates can be caused by a degradation of the organic macromolecules present in the shell organic matrix [73, 76, 138, 140]. Additionally, as demonstrated by Perrin and Smith (2007), the total or partial destruction of the organic matrices, in corals, is a pre-requisite for the recrystallisation of aragonite [78]. Therefore, since the archaeological shells from layers 3, 6 and 10 are mainly composed of aragonite, the loss of organic matrices, allied with the biogenic aragonite dissolution and recrystallisation, could be causing the lower FWHM values observed in the archaeological shells.

In general, the smallest difference in the FWHM values is observed between modern and layer 3 shells. The exceptions are for the FWHM values of the $\nu_4$ peak at 705 $cm^{-1}$ and for the $\nu_1$ peak at 1082 $cm^{-1}$, for which the smallest separation was between modern and layer 10 archaeological specimens (Figures 5.5b and 5.6, respectively). For each studied

**Table 5.3:** Minimum and maximum FWHM values obtained respectively for the powdered modern and archaeological *Conomurex fasciatus* shells. For each peak, the modern specimen values correspond to the smallest averaged FWHM for these shells, while the archaeological specimen values correspond to the biggest averaged FWHM across the different layers, as observed in Figures 5.4, 5.5 and 5.6. The FWHM uncertainties are the SE. The percentage difference corresponds to the smallest difference between the maximum and minimum FWHM values obtained for the analysed shell samples.

| Peak | Modern specimen | Archaeological specimen | Percentage difference (%) |
|---|---|---|---|
| 151 ($L_1$) | 11.56 ± 0.06 | 9.60 ± 0.04 | 16.9 |
| 205 ($L_2$) | 7.20 ± 0.02 | 6.73 ± 0.03 | 6.5 |
| 701 ($\nu_4$) | 3.71 ± 0.02 | 3.58 ± 0.03 | 3.5 |
| 705 ($\nu_4$) | 4.18 ± 0.02 | 3.85 ± 0.03 | 7.9 |
| 1082 ($\nu_1$) | 3.91 ± 0.01 | 3.49 ± 0.02 | 10.7 |

peak, the minimum and maximum values for the separation between the averaged FWHM of modern and archaeological *Conomurex fasciatus* shells (observed in Figures 5.4, 5.5 and 5.6) are shown in Table 5.3, which also displays the percentage difference between such FWHM values. These minimum values correspond to the smallest averaged FWHM measured for the modern shell samples, while the maximum values were obtained from the biggest averaged FWHM measurement amongst the archaeological *Conomurex fasciatus* shells. The biggest percentage differences, between the respective minimum and maximum averaged FWHM values of modern and archaeological shells, were obtained for the $L_1$ peak at 151 cm$^{-1}$, corresponding to the translational lattice mode vibration, and for the $\nu_1$ peak at 1082 cm$^{-1}$, which is the main calcium carbonate peak and is related to the symmetric stretch of the carbonate ion.

The above results are in accordance with those obtained in Chapter 3, where the modern *Conomurex fasciatus* shell was compared to an archaeological specimen, for which the better and more sensitive markers for diagenetic changes were obtained for the same peaks (Section 3.3 of Chapter 3). It has to be remembered that the analyses in Chapter 3 were done for the internal and external regions of bulk shells, while in this Chapter, the Raman measurements were performed on powdered shell samples. As previously highlighted, the $L_1$ and $\nu_1$ peaks are vibrational frequencies observed in the same Raman bands for both aragonite and calcite [92, 99]. Although aragonite and calcite also have a similar band at $\sim$704 cm$^{-1}$, corresponding to the in-plane antisymmetric bend, this band has different features depending on the carbonate polymorph, displaying a single peak for calcite or a doublet in the case of aragonite [92, 99]. In general, due to the similarities between the $L_1$ and $\nu_1$ vibrational frequencies, these peaks are not used to distinguish one calcium carbonate polymorph from another. However, it could be that because these vibrations are observed at almost the same wavenumbers for both aragonite and calcite, these two bands are favourable for the discrimination of modern and archaeological shells and, therefore, for the assessment of diagenesis. The layer 6 samples presented the lowest FWHM for the $L_1$ peak (Figure 5.4a), which could be associated with the higher presence of calcite observed in these samples (Table 5.2). However, the same correlation cannot be made for the $\nu_1$ peak, for which the lowest FWHM values were observed for the layer 3 samples (Figure 5.6), where calcite presence was the lowest (Table 5.2).

In Chapter 4, the lattice mode peak $L_1$ was more sensitive than the $\nu_1$ peak to the heat-treatments performed to the modern powdered *Conomurex fasciatus*, during which the aragonite was converted into calcite. Thus, considering these observations regarding the lattice mode peaks, the coefficient of variation of the FWHM of each studied peak was investigated. The CV values are shown in Table 5.4, along with the minimum and maximum measured FWHM values and their mean. The table shows that the lattice mode $L_1$ (151 cm$^{-1}$) and $L_2$ (205 cm$^{-1}$), when compared to the other peaks, had in general a consistently lower CV amongst all of the analysed archaeological *Conomurex fasciatus* shells, suggesting that they are more effective in measuring diagenetic alterations.

**Table 5.4:** Coefficient of variation (CV), mean and minimum and maximum FWHM values of Raman peaks for the archaeological *Conomurex fasciatus* shells from layers 3, 6 and 10. The lattice mode peaks $L_1$ (151 cm$^{-1}$) and $L_2$ (205 cm$^{-1}$) show, in general, consistently lower CV than the other measured peaks for the analysed archaeological shell specimens. The uncertainties are the standard error of the mean over the average of 200 spectra obtained for each shell sample.

| | | Statistics for the aragonite peaks analysed in the *Conomurex fasciatus* shell spectra | | | | |
|---|---|---|---|---|---|---|
| | | Peak 151 | Peak 205 | Peak 701 | Peak 705 | Peak 1082 |
| L3S1 | Mean ($cm^{-1}$) | 9.60±0.04 | 6.73±0.03 | 3.58±0.03 | 3.64±0.04 | 3.35±0.01 |
| | Min–Max ($cm^{-1}$) | 8.48–12.15 | 5.68–8.50 | 2.55–5.00 | 2.58–6.14 | 3.01–5.00 |
| | CV (%) | 5.75 | 5.92 | 11.53 | 13.83 | 6.18 |
| L3S2 | Mean ($cm^{-1}$) | 9.36±0.04 | 6.66±0.03 | 3.57±0.03 | 3.61±0.03 | 3.32±0.01 |
| | Min–Max ($cm^{-1}$) | 8.39–13.25 | 5.79–10.13 | 2.50–5.40 | 2.51–5.94 | 2.94–4.95 |
| | CV (%) | 5.99 | 7.10 | 11.11 | 12.96 | 5.95 |
| L6S1 | Mean ($cm^{-1}$) | 8.50±0.05 | 6.45±0.03 | 3.47±0.03 | 3.70±0.03 | 3.46±0.02 |
| | Min–Max ($cm^{-1}$) | 5.91–10.63 | 5.66–8.49 | 2.51–4.95 | 2.50–5.36 | 2.77–4.57 |
| | CV (%) | 7.74 | 5.63 | 10.50 | 12.08 | 9.70 |
| L6S2 | Mean ($cm^{-1}$) | 8.66±0.03 | 6.38±0.02 | 3.57±0.03 | 3.51±0.03 | 3.47±0.02 |
| | Min–Max ($cm^{-1}$) | 7.80–10.49 | 5.59–7.26 | 2.58–5.00 | 2.58–4.93 | 2.89–4.60 |
| | CV (%) | 4.25 | 3.49 | 10.35 | 11.61 | 8.44 |
| L10S1 | Mean ($cm^{-1}$) | 8.87±0.03 | 6.49±0.02 | 3.42±0.03 | 3.85±0.03 | 3.49±0.02 |
| | Min–Max ($cm^{-1}$) | 6.95–10.23 | 5.63–7.85 | 2.72–4.79 | 2.68–4.81 | 3.02–5.13 |
| | CV (%) | 4.87 | 5.19 | 11.15 | 9.95 | 9.18 |
| L10S2 | Mean ($cm^{-1}$) | 8.91±0.03 | 6.30±0.02 | 3.42±0.02 | 3.50±0.03 | 3.36±0.02 |
| | Min–Max ($cm^{-1}$) | 7.99–11.09 | 5.47–7.45 | 2.66–4.86 | 2.64–5.52 | 2.86–5.23 |
| | CV (%) | 5.39 | 4.77 | 8.65 | 10.27 | 8.94 |

The lattice mode peaks are more sensitive to the structural changes suffered by the calcium carbonate, and observed as peak position shifts and changes in the FWHM of geological calcium carbonates during heat-treatments [87,103]. Pokroy *et al.* (2006), studying 12 different types of shells with XRD noted a lattice distortion in all bio-aragonites when compared to geological aragonite [76]. They observed that heating degraded the organic molecules, thus causing a lattice relaxation that led to lattice parameters close to those of geological aragonite [76]. The reversion, upon heating, of the biogenic aragonite lattice parameters to values closer to those of geological aragonite was also observed in other studies [73, 75, 77]. Similarly to heating, diagenesis also causes the degradation of the organic shell matrix, and therefore could also lead to a lattice relaxation. Therefore, analogously to these structural changes caused by heating, the lattice modes could also be sensitive to the structural changes influenced by diagenetic alterations. Thus, taking into consideration the decrease in the FWHM observed for the lattice peaks (Figure 5.4), shells from layers 6 and 10 can be considered less preserved than the shells from layer 3. This is also consistent with the calcite percentage estimated for both samples (Table 5.2).

## 5.4 Diagenesis assessment - peak intensity ratio analyses

Peak intensity ratios of the $L_1$ (151 cm$^{-1}$), $L_2$ (205 cm$^{-1}$) and $\nu_4$ (701 cm$^{-1}$ and 705 cm$^{-1}$) peaks against the main calcium carbonate $\nu_1$ vibration (1082 cm$^{-1}$) were calculated for the archaeological *Conomurex fasciatus* shells, displayed as function of the shell midden the layers and compared to the modern specimens in Figures 5.7 and 5.8. The peak intensity ratios were calculated for each individual spectrum collected in the analysed samples. These were then averaged over the 200 Raman measurements performed in each of the shell replicates. The peak intensity ratio uncertainties correspond to the propagated SE.

As seen in Figures 5.7 and 5.8, the only peak intensity ratio that separates all the modern from all the archaeological *Conomurex fasciatus* shell replicates is the 151/1082 (Figure 5.7a). However, this separation is much smaller if compared with the separation obtained from the FWHM analyses (Section 5.3). The separation corresponds to a percent difference of 7.2%, between the maximum averaged value obtained for the modern shells and the minimum averaged value obtained for the archaeological specimens (layer 6), as seen in Figure 5.7a. Conversely to the results obtained for the FWHM (Figures 5.4), the

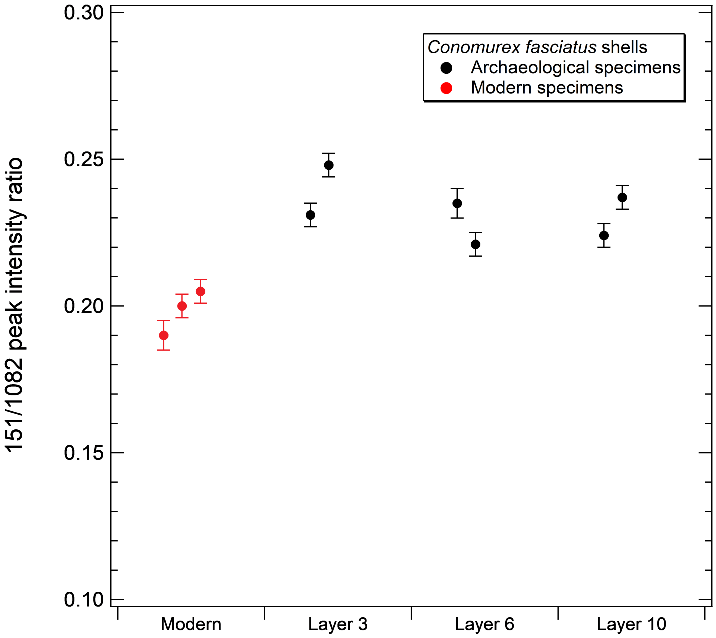

(a)

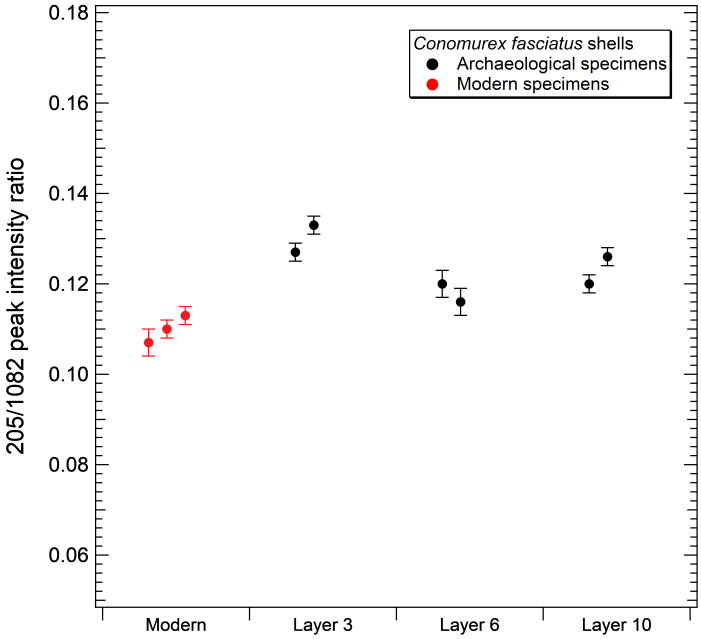

(b)

**Figure 5.7:** Peak intensity ratios of the (a) $L_1$ (151 cm$^{-1}$) and (b) $L_2$ (205 cm$^{-1}$) peaks against the $\nu_1$ (1082 cm$^{-1}$) peak from the Raman spectra of powdered modern and archaeological *Conomurex fasciatus* shells. A percent difference of 7.2% between modern and archaeological shells was obtained for the averaged values of the 151/1082 peak intensity ratio. The 205/1082 did not discriminate both shell groups. Error bars are the SE for the peak intensity ratios determined from the average of 200 spectra for each shell sample.

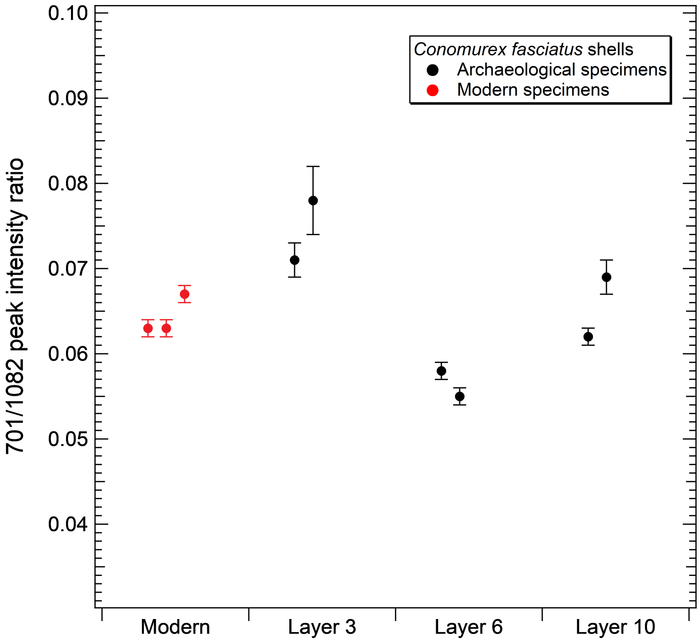

(a)

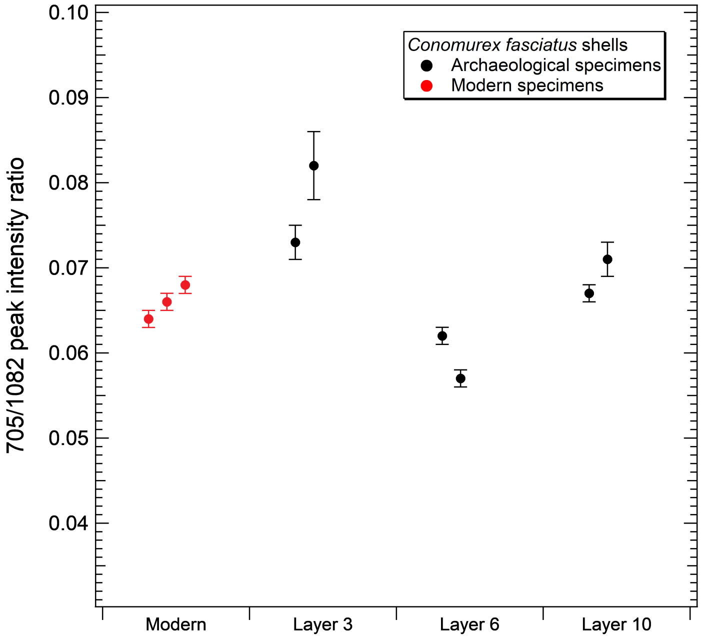

(b)

**Figure 5.8:** Peak intensity ratios of the (a) $\nu_4$ (701 cm$^{-1}$ and (b) 705 cm$^{-1}$) peaks against the $\nu_1$ (1082 cm$^{-1}$) peak from the Raman spectra of powdered modern and archaeological *Conomurex fasciatus* shells. No discrimination between modern and archaeological shell specimens is observed for both peak intensity ratios. Error bars are the SE for the peak intensity ratios determined from the average of 200 spectra for each shell sample.

peak intensity ratios of the lattice mode peaks $L_1$ (151/1082) and $L_2$ (205/1082) remained fairly constant, not showing any trend with the shell midden layers (Figure 5.7). As noted in Chapter 3, the 151/1082 and 205/1082 peak intensity ratios were able to discriminate the archaeological from the modern *Conomurex fasciatus* shell specimens analysed (Section 3.3 in Chapter 3). However, as discussed in Chapter 3, these peak intensity ratios did not display a consistent trend in separating modern from archaeological shells.

In Chapter 4, the 151/1082 ($L_1/\nu_1$) peak intensity ratio was successfully used for determining the full conversion of aragonite to calcite during the heat treatments, for which a rapid decrease of its intensity was associated with the aragonite to calcite phase transition and presence of calcite (Figure 4.7). Although the shell specimens from layers 3, 6 and 10 had different percentages of calcite and aragonite, the 151/1082 peak intensity ratio showed nearly no difference between the shell specimens from the different shell midden layers (Figure 5.7a). Shells from layer 6 had a maximum of 13% calcite composition, which was estimated by the Edwards *et al.* (2005) method [105] (Table 5.2). Thus, it might be that the 151/1082 ($L_1/\nu_1$) peak intensity ratio is not sensitive to small admixtures of aragonite and calcite. As explained in Chapter 4, for this ratio to be used more accurately to determine the calcium carbonate polymorphs percentage, and therefore indicate diagenesis, different controlled concentrations of calcite and aragonite should be tested so that the sensitivity of such ratio can be confirmed.

The incapability of separating the modern from the archaeological shells observed for the peak intensity ratios 701/1082 and 705/1082 in this section (Figure 5.8) has also been noted in Chapter 3 (Figure 3.7). Although not discriminating modern from archaeological shells, the ratios of the $\nu_4$ peaks against the $\nu_1$ peak (701/1082 and 705/1082) showed an interesting pattern, with lower ratio values obtained for the shells from layer 6 (Figure 5.8). These shells had a greater percentage of calcite, 9% and 13% for shell samples L6S1 and L6S2, respectively (Table 5.2). Modern shells were entirely composed of aragonite and specimens from layers 3 and 10 had higher aragonite percentages, in comparison to the layer 6 samples (Table 5.2).

In calcite the $\nu_4$ vibration is characterised by a single peak at ~712 $cm^{-1}$ [91, 92, 94, 96, 97, 99]. Although this single peak has not been observed in the spectra of the layer 6 shells, the relative decrease in the intensity of the aragonite $\nu_4$ doublet could be related to the presence of calcite, which was verified by the rising of the calcite $L_2$ peak at 280 $cm^{-1}$ (Figure 5.3). The $\nu_4/\nu_1$ peak intensity ratios (701/1082 and 705/1082) did not show a great distinction between modern and archaeological *Conomurex fasciatus* shells in Chapter 3 (Figure 3.7). The archaeological *Conomurex fasciatus* shell used for the experiments of Chapter 3 was also from layer 6; however, from spit 206, on the top of that layer, while the layer 6 shells used in this Chapter came from spit 305, closer to the middle of layer 6 (Figure 5.1). The difference between the results obtained in this Chapter and in Chapter 3 could be due to the archaeological shell sample used in that Chapter containing even less percentage of calcite in its composition. The proportion of aragonite estimated for the archaeological shell from Chapter 3 was 99.9% ± 0.1% for both internal and external areas of the shell. Thus, the $\nu_4/\nu_1$ peak intensity ratios could be sensitive to higher calcite concentrations, and therefore could be an additional diagenesis marker. However, to validate this assumption, this peak intensity ratio should also be tested with controlled admixtures of aragonite and calcite containing different calcite proportions.

As determined by the calcite concentration and the FWHM analyses, it can be said that the analysed *Conomurex fasciatus* shells are preserved against diagenesis. Amongst these archaeological samples, the shells from layer 6 are the least preserved from diagenetic alterations. The results presented in this section demonstrated the issues with using peak intensity ratios for the assessment of diagenesis in preserved shells. The peak intensity ratios were, in general, incapable of securely discriminating modern from archaeological shells; therefore, care should be taken if they are used as markers for the assessment of diagenesis.

## 5.5 Chapter conclusions

In this chapter, two experiments were performed, complementing the results from Chapter 3, which had established a protocol for assessing diagenesis on sea shells with RS. This protocol was based in the analyses of quantitative Raman parameters, as the FWHM and peak intensity ratios. In both experiments *Conomurex fasciatus* shells from layers 3, 6 and 10 from the KM1057 shell midden were compared to modern shell samples of the same species.

The first experiment performed compared the calcite concentration and FWHM measurements of the spectra of *Conomurex fasciatus* shells from different layers of the KM1057 shell midden, aiming to confirm if RS would be sensitive enough to detect diagenetic alterations in shells from those layers.

The FWHM analyses also showed a pronounced separation between the modern and archaeological shell specimens. Modern shells displayed higher FWHM values, while the archaeological showed lower FWHM values, thus being more crystalline. The most sensitive Raman peaks accounting for these differences were the lattice mode peak $L_1$ and the main carbonate vibration $\nu_1$, for which the FWHM respectively decreased 16.9% and 10.7% from modern to archaeological values. These results agree with the findings from Chapter 3, where the $L_1$ and $\nu_1$ peaks showed the best results with smallest dispersion. The smallest FWHM values obtained for the archaeological shells could have been caused by the loss of the organic matrix and consequent aragonite dissolution and recrystallisation.

This FWHM experiment confirmed the lattice mode peaks $L_1$ and $L_2$ as the best markers for assessing diagenesis between shells from different layers, yielding a FWHM separation over the smallest statistical dispersion, which was measured by the CV. Lattice mode peaks are sensitive to the structural changes caused in aragonite during heating, which causes the degradation of the organic matrix and, therefore a lattice relaxation. Since diagenesis also causes the loss of the organic matrix, it can be inferred that the lattice mode could also be sensitive to these structural changes caused by the diagenetic alterations. The FWHM of the lattice mode peaks classified the shell samples from layer 3 as the best preserved against diagenetic alterations, followed by those from layer 10 and 6. This is corroborated by the higher proportions of calcite estimated in the shell samples from layers 6 and 10. While shells from layer 3 were mainly composed of aragonite, shells from layer 6 had a maximum of 17% of calcite. This confirms that part of the original biogenic aragonite of the analysed shells from layer 6 had recrystallised into calcite.

The second experiment investigated the use of peak intensity ratios as diagenesis markers. For this experiment, intensity ratios were calculated between the aragonite/calcite peaks and the main calcium carbonate peak, the $\nu_1$. Similarly to what was obtained in Chapter 3, peak intensity ratios did not display consistent trends in separating such modern from archaeological specimens.

The $L_1/\nu_1$ ratio (151/1082) was able to discriminate the modern from the archaeological shells, but showed almost no difference between the shells from the different layers, although they had different proportions of aragonite and calcite. This peak was used in Chapter 4 to determine the full aragonite-calcite transition. However, it might be not sensitive to small admixtures of aragonite and calcite and further experiments with controlled concentrations of these polymorphs have to be performed to test the sensitivity of this ratio in determining the presence of calcite.

The $\nu_4/\nu_1$ peak intensity ratios did not discriminate modern from archaeological shells. However, these ratios had the lowest averaged values for the samples with the highest proportion of calcite *e.g.*, the shell samples from layer 6. The variation in the relative intensity of the $\nu_4$ aragonite doublet could be related to the presence of calcite, once this band becomes a singlet for the latter polymorph. However, for this peak intensity ratio to be used as an additional diagenesis marker, it should be further tested with controlled admixtures of calcite and aragonite to attest its sensitivity.

Despite the fact that the samples were estimated with small differences in their polymorph percentages, the peak intensity ratios obtained were not sensitive enough to completely separate the shells from different layers, or to provide a considerable separation between modern and archaeological shells.

Although the sampling performed in the KM1057 did not statistically represent the whole layers and no further conclusions can be withdraw for the whole shell midden layer, the assessment of diagenesis has to be made for each shell if they will be used for palaeoenvironmental reconstructions and isotopic analyses. This chapter confirms that quantitative RS can be used to evaluate diagenesis in shells from different layers of a shell midden and reaffirms the FWHM as one of the best markers for diagenetic alterations.

# Chapter 6

# Conclusions

Shell middens are records of human activity, their shells can be used to reconstruct the past climate and to investigate human development. However, diagenetic alterations affect analytical methods, such as isotopic analyses, which are used for palaeoenvironmental reconstructions investigating the sea temperature and salinity. The heating of shells is another factor influencing these analyses and the inappropriate assessment of a shell's integrity results in estimating the wrong temperature and salinity, thus risking the reliability of archaeological interpretations.

In general, the identification of diagenesis is made by determining if the shell's mineralogy is maintained, or in other words, if the shell has not recrystallised. This means that an aragonitic shell should be free of calcite. However, methods based on the presence of calcite are not valid for calcitic shells. Another approach is to compare the relative atom percentage of Mg and Sr with Ca, between modern and archaeological shells. However, there is no consensus, in the literature, of how these parameters should change; nonetheless, some shells may not have their Ca substituted by Mg or Sr, thus compromising this evaluation.

This research proposed to investigate if Raman spectroscopy could be used to determine and evaluate diagenesis in sea shells, as well as to identify heated or cooked shells. Usually, in the literature, when RS is applied to investigate diagenesis, this is done only qualitatively by the investigation of the shell's mineralogy. This thesis developed methods for a quantitative analysis of the Raman spectrum of shells by finding markers correlated to shell diagenesis or heating. The investigated Raman parameters resulted from peak fitting procedures were the peak position, FWHM and relative amplitude, which were then compared across samples. The studied shells were archaeological *Conomurex fasciatus* shells from the KM1057 shell midden in the Farasan Islands, Red Sea; the *Nucella* sp. from the Easington Raised Beach site, United Kingdom; and modern counterparts of these shell species. The *Conomurex fasciatus* shells are aragonitic, while the *Nucella* sp. are calcitic shells.

There is a great variability in respect to the amount of spectra considered for the analyses of shells. Therefore, initially, this work suggested a method to determine the minimum quantity of spectra necessary to statistically represent each shell sample used. This method, called a convergence test, is based in the SE associated to the FWHM of the main calcium carbonate peak, the $\nu_1$ symmetric stretching vibration. The SE decreases with an increasing amount of spectra, and the method shows how many spectra are necessary for the SE stabilisation. These tests determined that 90 to 225 spectra were necessary to statistically represent the internal and external shell areas of the bulk *Conomurex fasciatus* and *Nucella* sp. species, while 200 spectra were needed to represent the powdered *Conomurex fasciatus* shells.

From the comparison between modern and archaeological shells it was verified that the FWHM of the Raman bands were sensitive to detect diagenesis. Whether the analysed shell samples were bulk or powdered shells, the FWHM of the archaeological shells was smaller than the FWHM of the modern shells. The FWHM is correlated to the sample crystallinity; thus, the smaller FWHM values obtained for the ancient shell samples means that they had become more crystalline over time. The increase in the crystallinity can be explained by the degradation of the organic shell matrix and consequent aragonite dissolution, followed by its recrystallisation. Both, aragonite dissolution and loss of the shell organic matrix are caused by diagenesis.

For both shell sample preparations, bulk or powdered, the best FWHM markers for diagenetic alterations were for the $\nu_1$ peak at $\sim$1082 cm$^{-1}$, present in both calcite and aragonite spectra, and the lattice mode peak $L_1$ at $\sim$151 cm$^{-1}$ for aragonite and at $\sim$154 cm$^{-1}$ for calcite.

The FWHM markers were also able to assess the diagenesis in shells from different layers in a shell midden, and again the best markers were the FWHM of the the lattice mode peaks $L_1$ ($\sim$151 cm$^{-1}$) and $L_2$ ($\sim$205 cm$^{-1}$). This evaluation of the preservation state of *Conomurex fasciatus* shells from different layers in the KM1057 shell midden based on the FWHM was validated by the proportion of calcite in each shell, which was estimated from the relative intensity of the calcite and aragonite $L_2$ Raman peaks.

This research proposes that the lattice mode peaks of the Raman spectrum could also be sensitive to the structural changes caused by diagenesis. It is already known that the lattice mode peaks of the calcium carbonate are sensitive to structural changes caused by heating. It is also known that biogenic carbonates have lattice distortions when compared to geological carbonates due to the presence of large biomolecules, and that these distortions are reduced during heating because of the degradation of the organic shell matrix. Therefore, since the shell organic matrix is also degraded by diagenesis, this could explain the sensitivity of the Raman lattice mode peaks to capture such changes.

This research work also showed that peak intensity ratios between Raman bands should be carefully considered for the analysis of diagenesis due to the inconsistent results obtained between modern and ancient shells, for the different shell species analysed. Whether the studied shells were calcitic or aragonitic, the only ratios capable of discriminating modern from ancient shells were the $L_1/\nu_1$ and the $L_2/\nu_1$. Although the peak intensity ratio $\nu_4/\nu_1$ did not discriminate modern from ancient shells, it displayed the lowest ratio values for the archaeological shells that contained the highest proportion of calcite, suggesting this peak intensity ratio as another possible diagenesis marker. The decrease in this peak intensity ratio could be related to variations in the $\nu_4$ band, which is a double for aragonite and a singlet for calcite.

A heated shell can cause the deduction of erroneous temperature for palaeoenvironmental reconstructions. The identification of heated shells has been made by purely visual observations or by the transition of aragonite to calcite. Thus, the effect of heating, and therefore its identification, were also investigated in this thesis for the *Conomurex fasciatus* shells. A rapid decrease in the $L_1/\nu_1$ peak intensity ratio marked the full aragonite to calcite transition during heating, which was estimated to take place between 325°C and 400°C for this shell species. The rapid decrease observed in the $L_1/\nu_1$ suggested that this ratio is more sensitive to higher proportions of calcite, which explains its poor performance in discriminating modern from archaeological *Conomurex fasciatus* shells, once the studied ancient shells were considerably preserved against diagenesis and, therefore, presented very low calcite concentrations.

This research has shown that RS is a powerful method for identifying heated shells, providing markers that can indicate heating before the aragonite to calcite transition takes place. Quantitative RS detected changes in the crystalline structure of modern *Conomurex fasciatus* shells after being heated for only seven minutes at 400°C and 500°C. This was marked by a decrease in the FWHM of both $L_1$ and $\nu_1$ Raman peaks. This increase in the shell crystallinity originated from the degradation of the organic shell matrix during heating. Again, the $L_1$ lattice mode peak was more sensitive to these structural changes, reflecting the progressive rotational disorder preceding the aragonite to calcite transition. After the aragonite to calcite transformation, the FWHM of both $L_1$ and $\nu_1$ peaks increased, indicating a decrease in the sample crystallinity that was possibly related to the thermal expansion of the calcite crystal before the next phase transition, which is from calcite to calcium oxide.

Identifying a burnt shell and knowing at which temperature it has been heated also influences the interpretation of sites that contain burnt fragments because they can be associated to the action of cooking. Quantitative RS also provided means to estimate the temperature at which the archaeological *Conomurex fasciatus* burnt shell fragments were heated. The $L_1/\nu_1$ peak intensity ratio determined that two studied archaeological burnt fragments of the *Conomurex fasciatus* shell had fully converted to calcite, which was corroborated by the estimation of the calcite proportion using the relative intensity of the $L_2$ lattice mode peaks. The FWHM of the $L_1$ and $\nu_1$ peaks were outside both time and temperature ranges investigated by the analyses of the heated modern shells. This indicated that burnt fragments might have been heated at temperatures greater than 500°C and smaller than $\sim$700°C to $\sim$800°C, at which the conversion of calcite to calcium oxide occurs.

This thesis demonstrated that quantitative RS can be used to evaluate diagenesis and determine heating. This paragraph summarises the proxies for these assessments. The FWHM of the $L_1$ and $\nu_1$ peaks can be used as markers of diagenesis and can identify heating in shells before the aragonite to calcite transition. They are sensitive to the degradation of the organic shell matrix and, hence increase in the polymorph crystallinity, with the $L_1$ lattice mode peak being more sensitive to these structural changes. The FWHM of both $L_1$ and $\nu_1$ peaks can also be used to estimate the heating temperature of burnt archaeological shell fragments when compared to the FWHM of modern heated shells. The $L_1/\nu_1$ peak intensity ratio is sensitive to the structural transformations during heating and can be used to determine the temperature of the full aragonite-calcite transition. Finally, the $\nu_4/\nu_1$ peak intensity ratio could also be used to determine the presence of calcite in aragonitic samples; however, it needs further testing to be validated. Additionally, the ratio between the intensities of the $L_2$ peaks for aragonite and calcite, determined by Edwards *et al.* (2005) [105] can also be used to estimate the percentage of calcite in aragonitic shells, or vice-versa.

Based on the results obtained with this thesis, possible future research works are described next.

This thesis has shown that the shell crystallinity, measured with RS, is an easy and straightforward method for the evaluation of diagenesis. However, future studies should consider investigating shells from different ages, species, preservation states and geographic locations to verify how the decreasing trend in the FWHM behaves with the diversity of samples. Together with RS, the crystallinity of the archaeological shells should also be investigated with XRD, so that the relaxation of lattice parameters is investigated for diagenetically altered samples.

The $L_1/\nu_1$ peak intensity ratio was a marker of the full aragonite to calcite transition and it was used to estimate the temperature at which the transition took place. This estimation would be more accurate if more heating time-points were be included in the range for which the transition takes place. The transition temperature estimated from the Raman spectrum could also be validated by differential thermal analysis.

The $L_1/\nu_1$ peak intensity ratio could also be used to determine the polymorph concentration, similarly to the relative intensity of the $L_2$ peaks proposed by Edwards *et al.* (2005) [105]. However, this peak intensity ratio would need to be tested using controlled admixtures of calcite and aragonite to verify its sensitivity.

Expanded heating times and temperatures should be investigated in the quantitative RS analyses of the modern *Conomurex fasciatus* shells. The aim is to better estimate at which temperature the archaeological *Conomurex fasciatus* burnt shell fragments were heated. Once modern shells are heat-treated at similar temperatures to the burnt shell fragments, the effect of diagenesis on them can be assessed. The two burnt fragments used in this thesis were obtained in layers 3 and 10 of the KM1057 shell midden. However, these burnt fragments have been fully converted into calcite and therefore cannot be compared to the studied archaeological *Conomurex fasciatus* shells from the same layers, which were predominantly aragonitic.

Additionally to this expanded heating time and temperature experiments on aragonitic shells, the effect of heating on calcitic shells should also be explored so that a heating baseline is drawn for such shells, similarly to what was obtained for the aragonite in the *Conomurex fasciatus* shells.

This thesis has shown that in light of its ability for discriminating the calcium carbonate polymorphs and capacity of performing non-destructive analyses, RS is able to assess diagenesis and human intervention due to heating when combined to a quantitative data analysis.

# Appendix A

# Supplementary information for the RS comparison of modern versus ancient shells

## A.1 Convergence Tests

### A.1.1 Archaeological *Conomurex fasciatus* shell

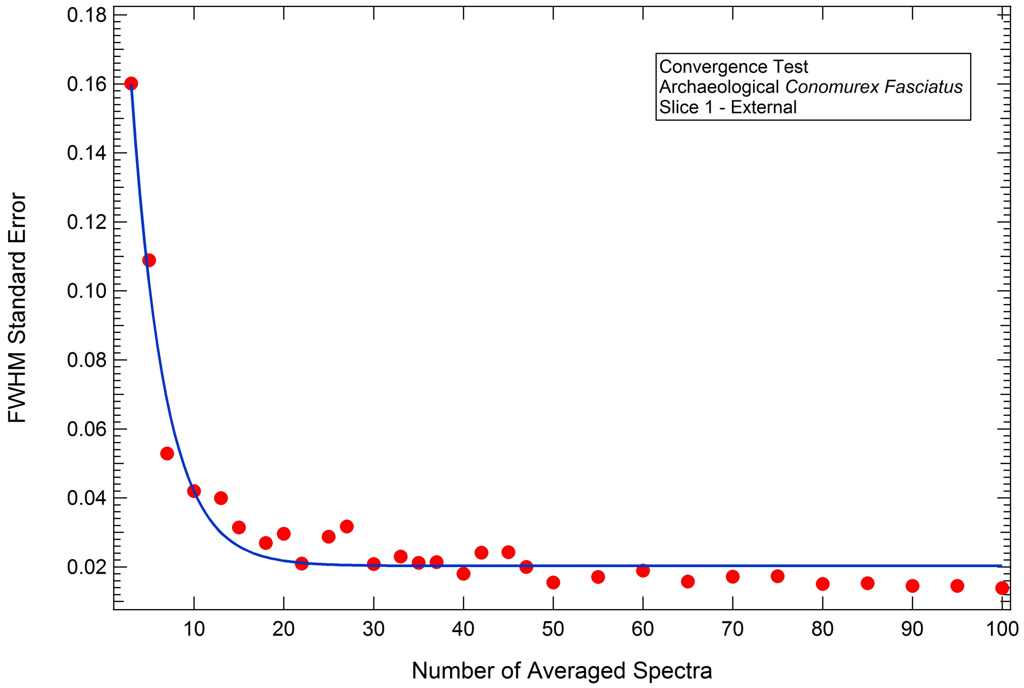

**Figure A.1:** Convergence test for the archaeological *Conomurex fasciatus* shell external region of slice 1. The blue line is the theoretical fitting and red points are the experimental data.

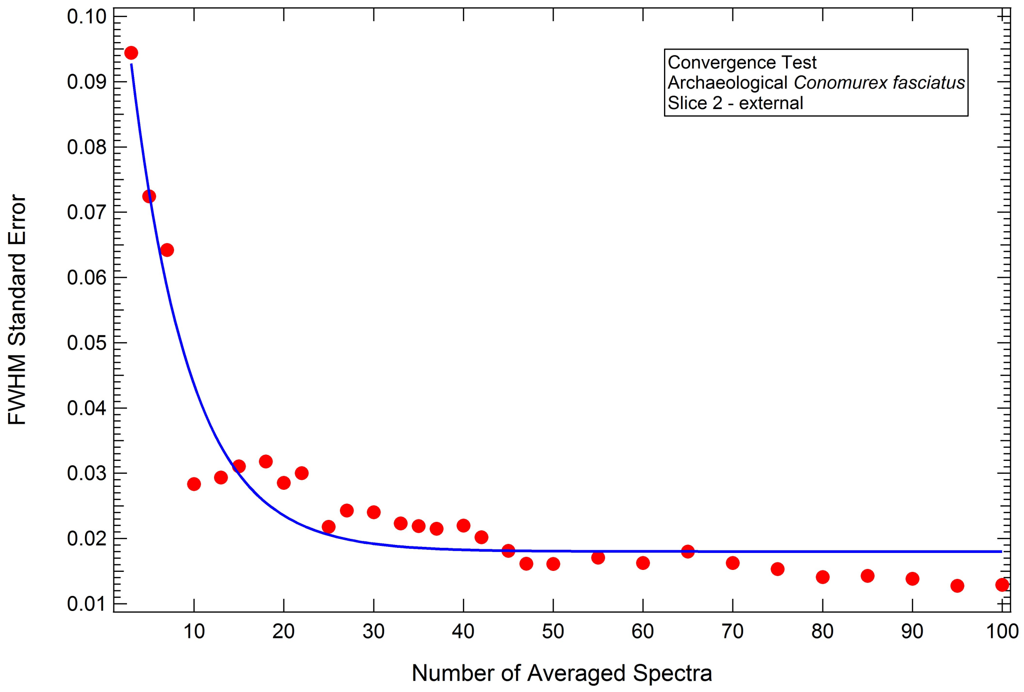

**Figure A.2:** Convergence test for the archaeological *Conomurex fasciatus* shell external region of slice 2. The blue line is the theoretical fitting and red points are the experimental data.

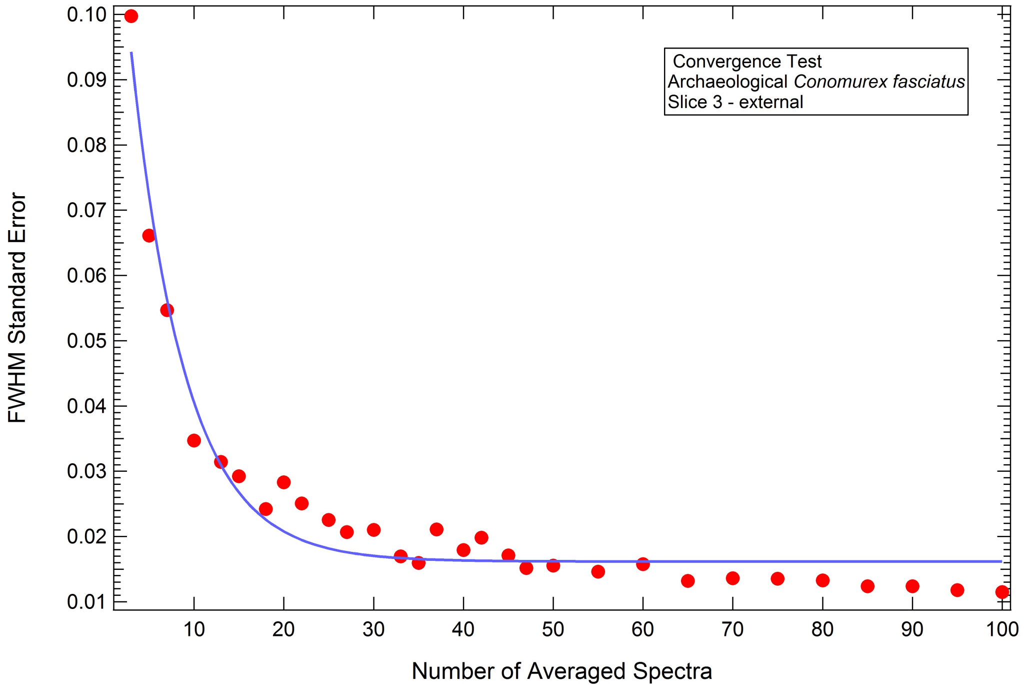

**Figure A.3:** Convergence test for the archaeological *Conomurex fasciatus* shell external region of slice 3. The blue line is the theoretical fitting and red points are the experimental data.

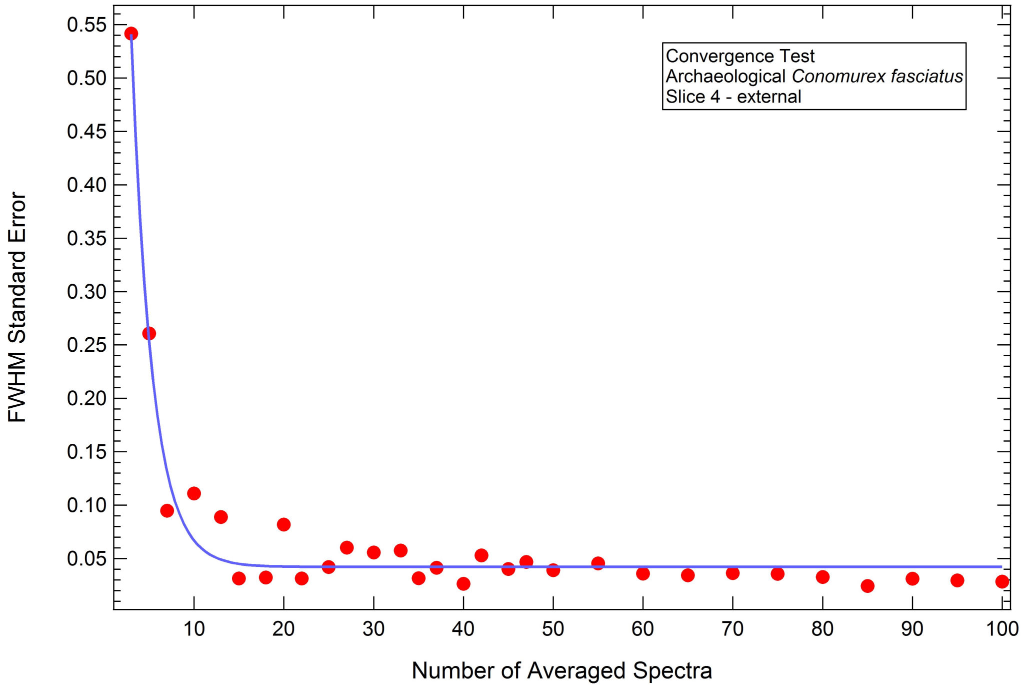

**Figure A.4:** Convergence test for the archaeological *Conomurex fasciatus* shell external region of slice 4. The blue line is the theoretical fitting and red points are the experimental data.

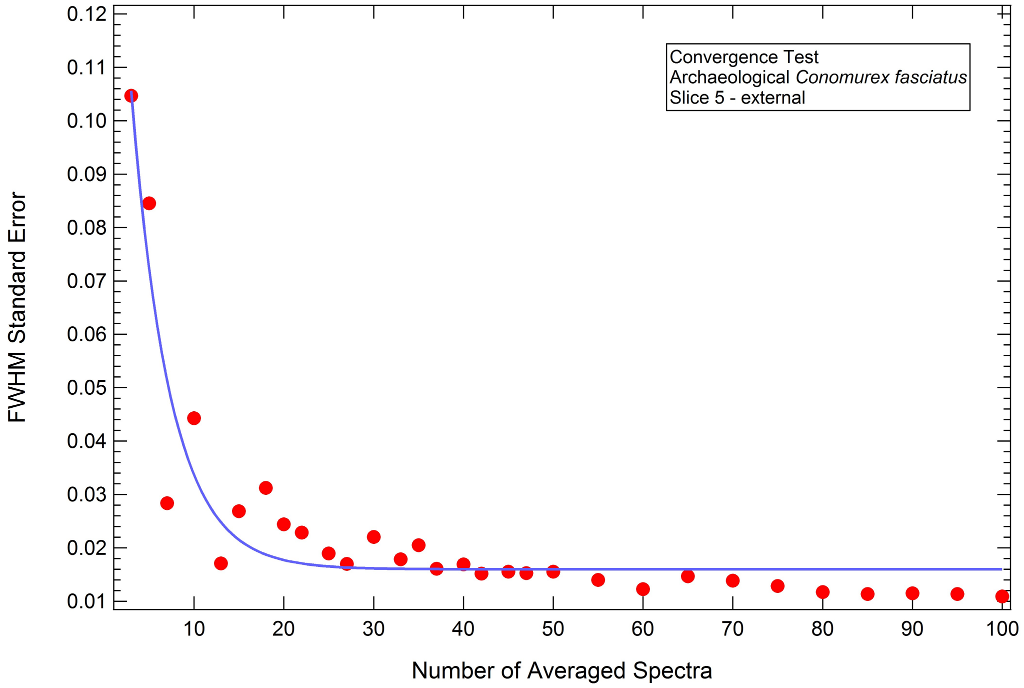

**Figure A.5:** Convergence test for the archaeological *Conomurex fasciatus* shell external region of slice 5. The blue line is the theoretical fitting and red points are the experimental data.

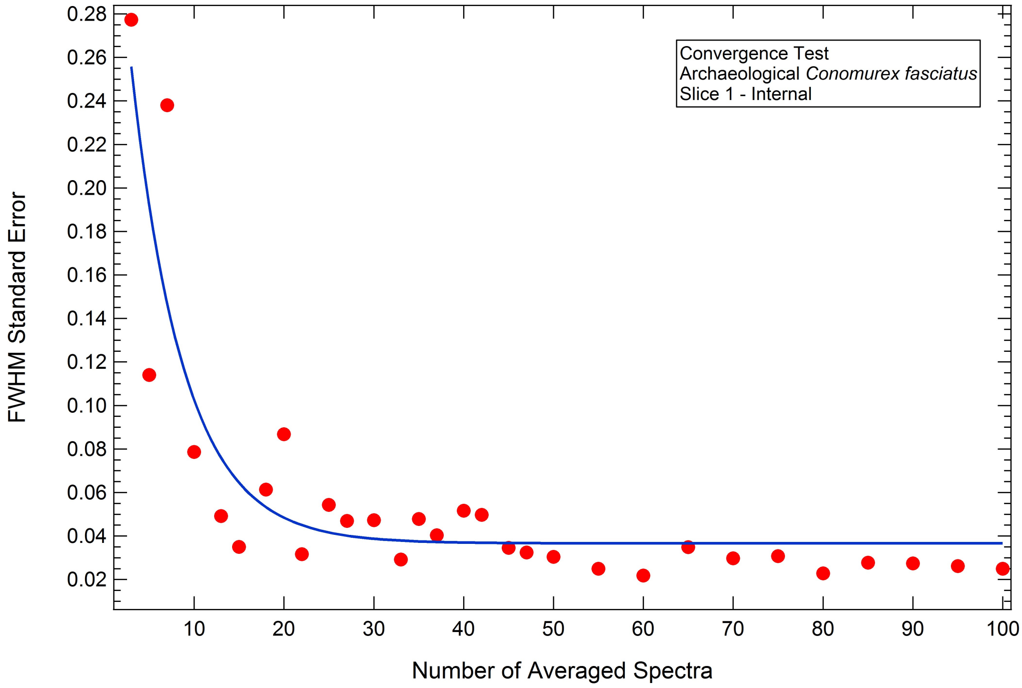

**Figure A.6:** Convergence test for the archaeological *Conomurex fasciatus* shell internal region of slice 1. The blue line is the theoretical fitting and red points are the experimental data.

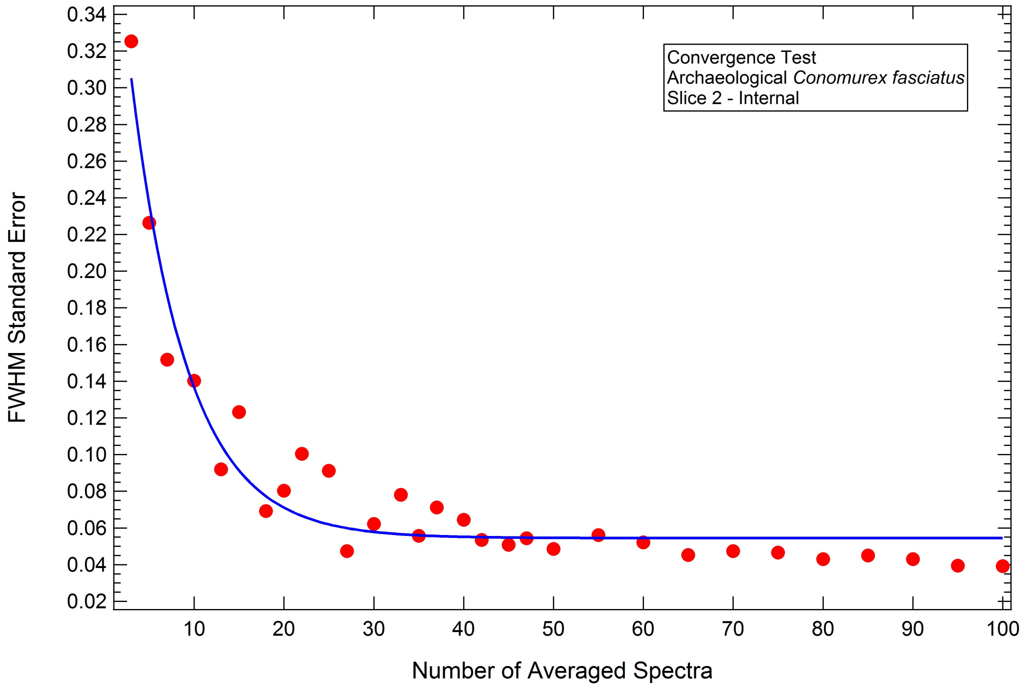

**Figure A.7:** Convergence test for the archaeological *Conomurex fasciatus* shell internal region of slice 2. The blue line is the theoretical fitting and red points are the experimental data.

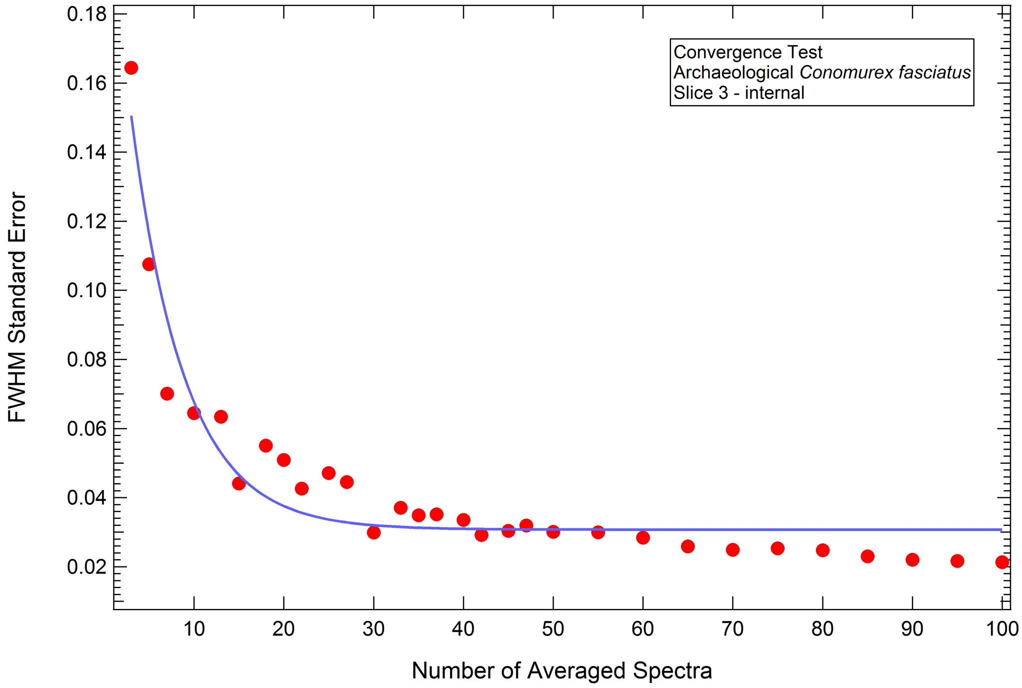

**Figure A.8:** Convergence test for the archaeological *Conomurex fasciatus* shell internal region of slice 3. The blue line is the theoretical fitting and red points are the experimental data.

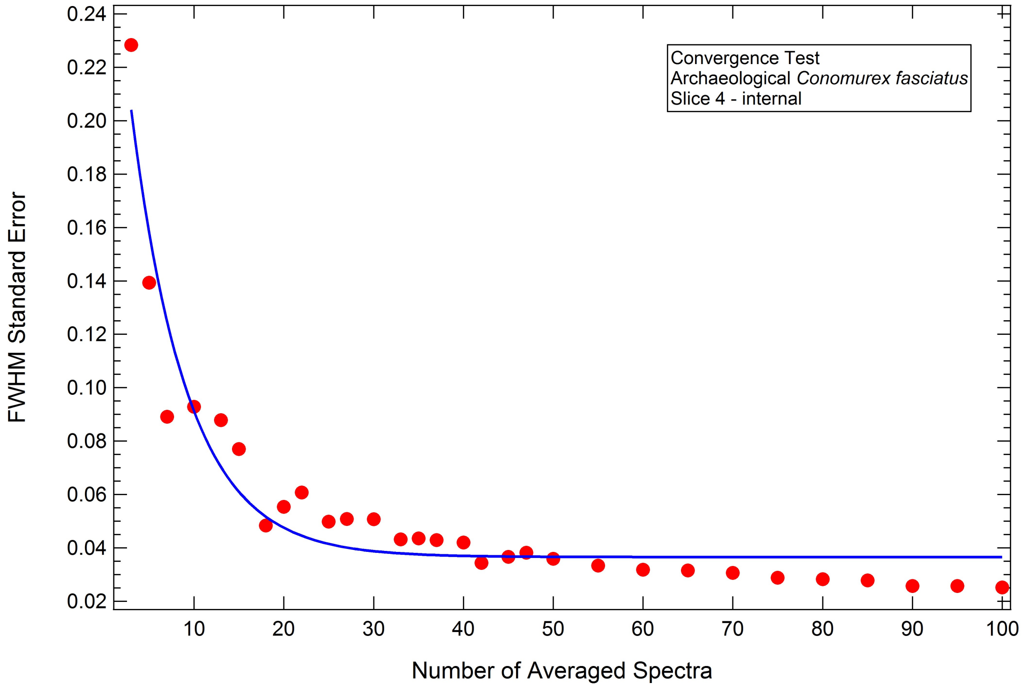

**Figure A.9:** Convergence test for the archaeological *Conomurex fasciatus* shell internal region of slice 4. The blue line is the theoretical fitting and red points are the experimental data.

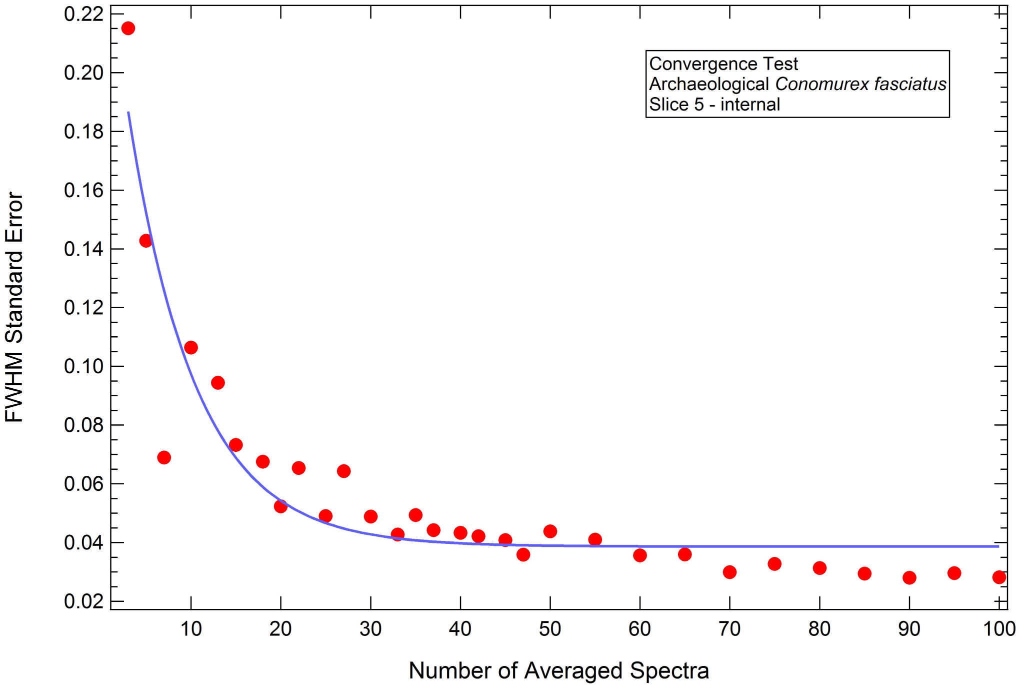

**Figure A.10:** Convergence test for the archaeological *Conomurex fasciatus* shell internal region of slice 5. The blue line is the theoretical fitting and red points are the experimental data.

### A.1.2 Modern *Conomurex fasciatus* shell

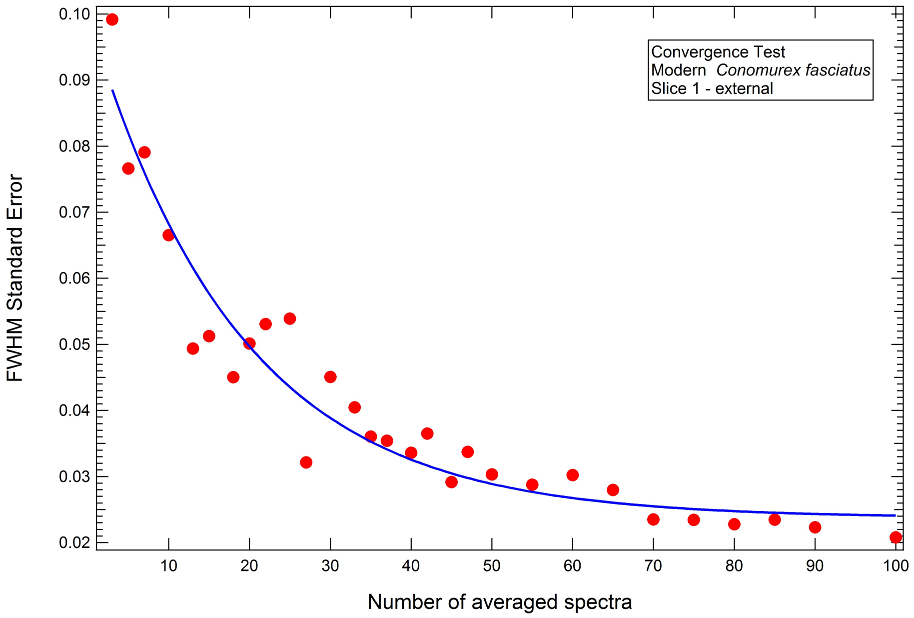

**Figure A.11:** Convergence test for the modern *Conomurex fasciatus* external region of slice 1. The blue line is the theoretical fitting and red points are the experimental data.

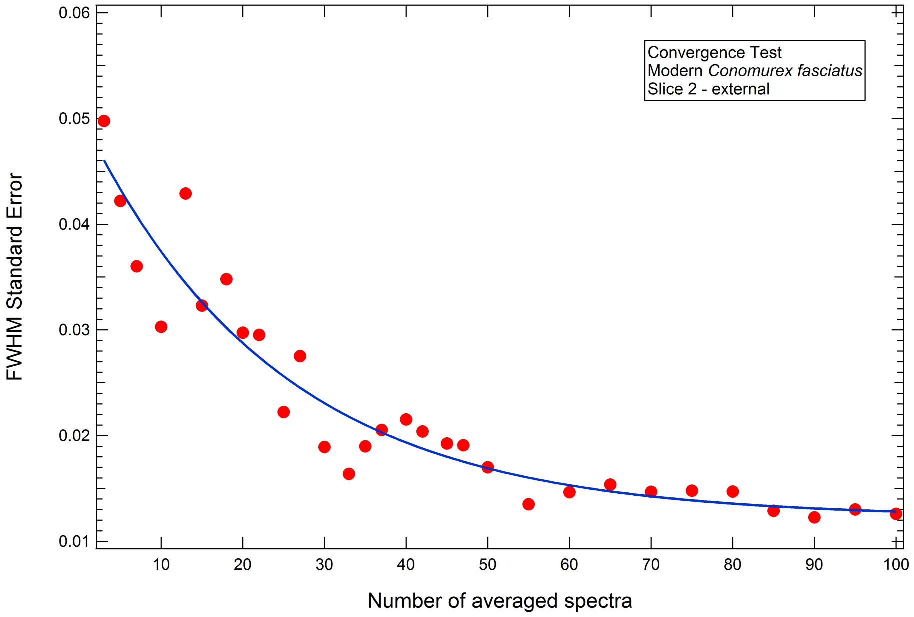

**Figure A.12:** Convergence test for the modern *Conomurex fasciatus* external region of slice 2. The blue line is the theoretical fitting and red points are the experimental data.

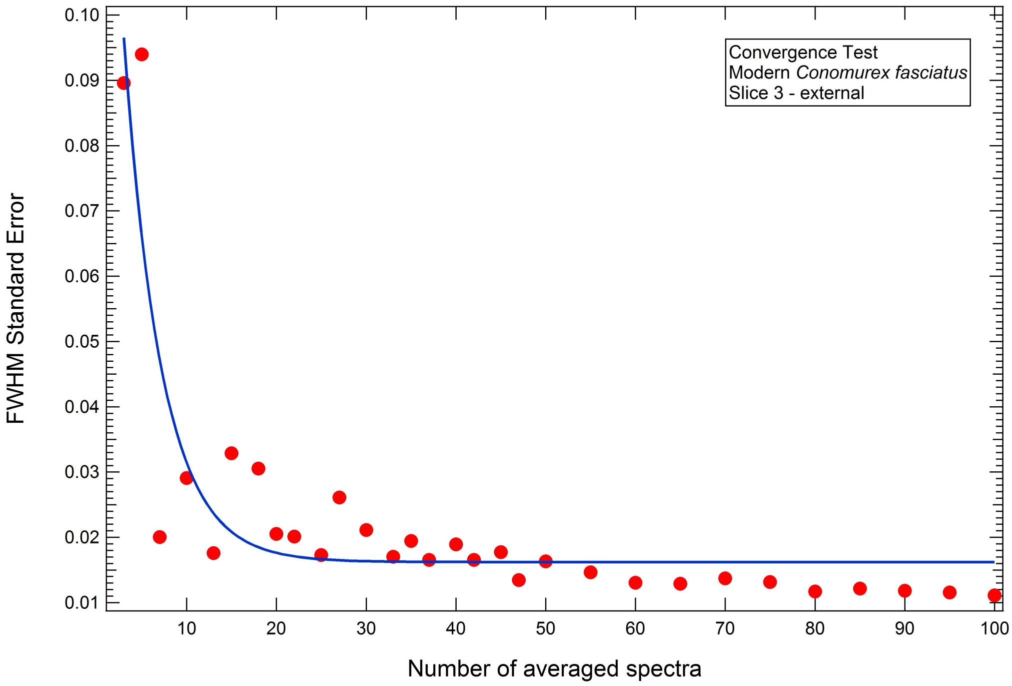

**Figure A.13:** Convergence test for the modern *Conomurex fasciatus* external region of slice 3. The blue line is the theoretical fitting and red points are the experimental data.

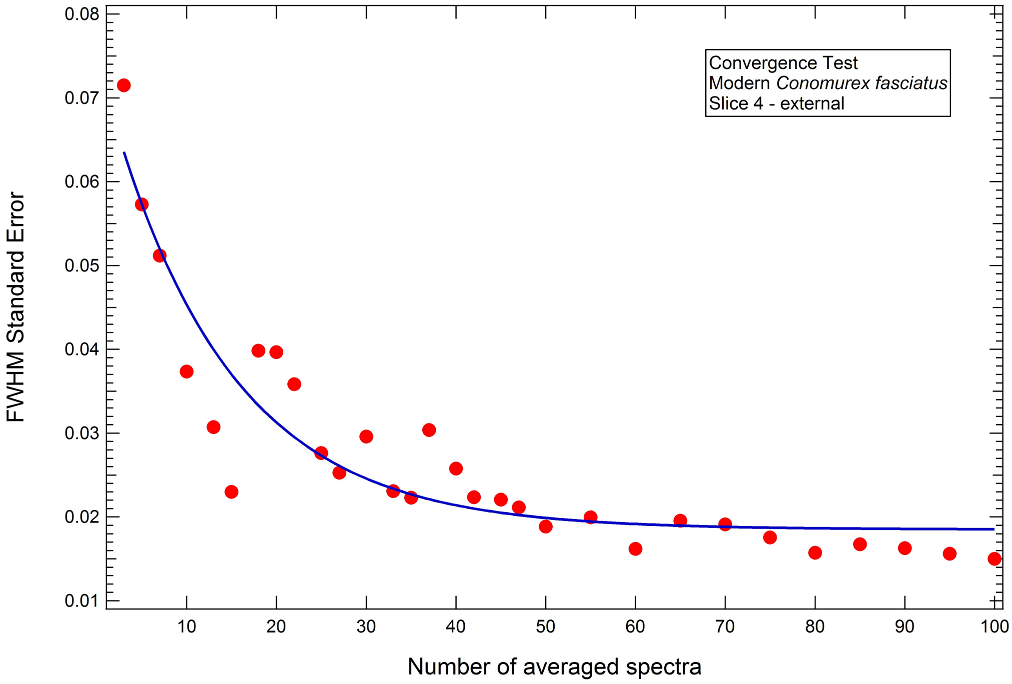

**Figure A.14:** Convergence test for the modern *Conomurex fasciatus* external region of slice 4. The blue line is the theoretical fitting and red points are the experimental data.

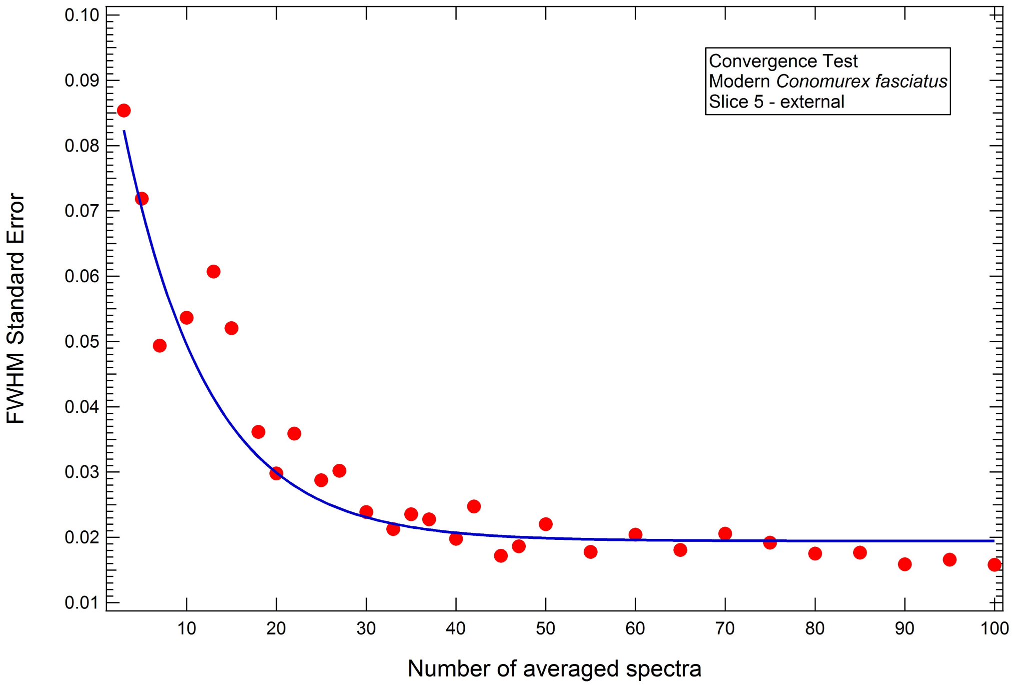

**Figure A.15:** Convergence test for the modern *Conomurex fasciatus* external region of slice 5. The blue line is the theoretical fitting and red points are the experimental data.

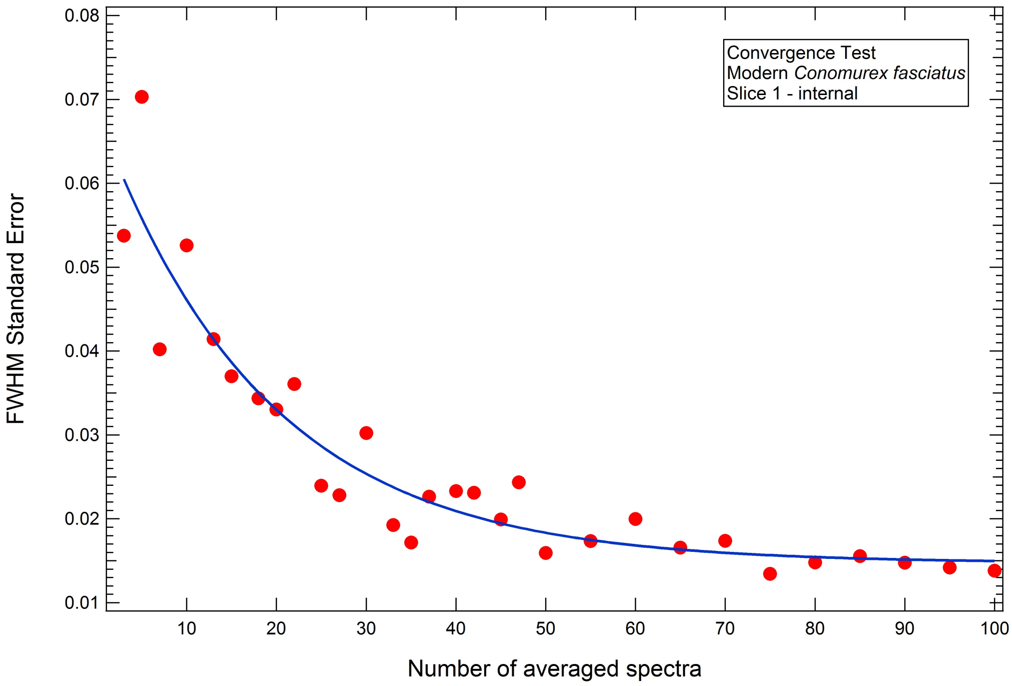

**Figure A.16:** Convergence test for the modern *Conomurex fasciatus* internal region of slice 1. The blue line is the theoretical fitting and red points are the experimental data.

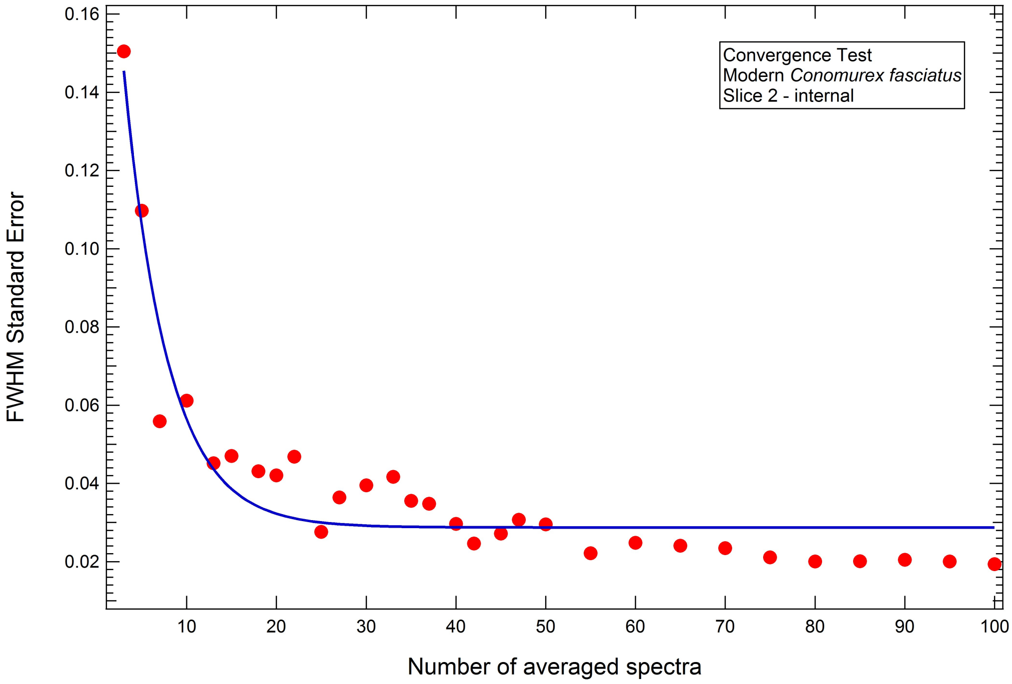

**Figure A.17:** Convergence test for the modern *Conomurex fasciatus* internal region of slice 2. The blue line is the theoretical fitting and red points are the experimental data.

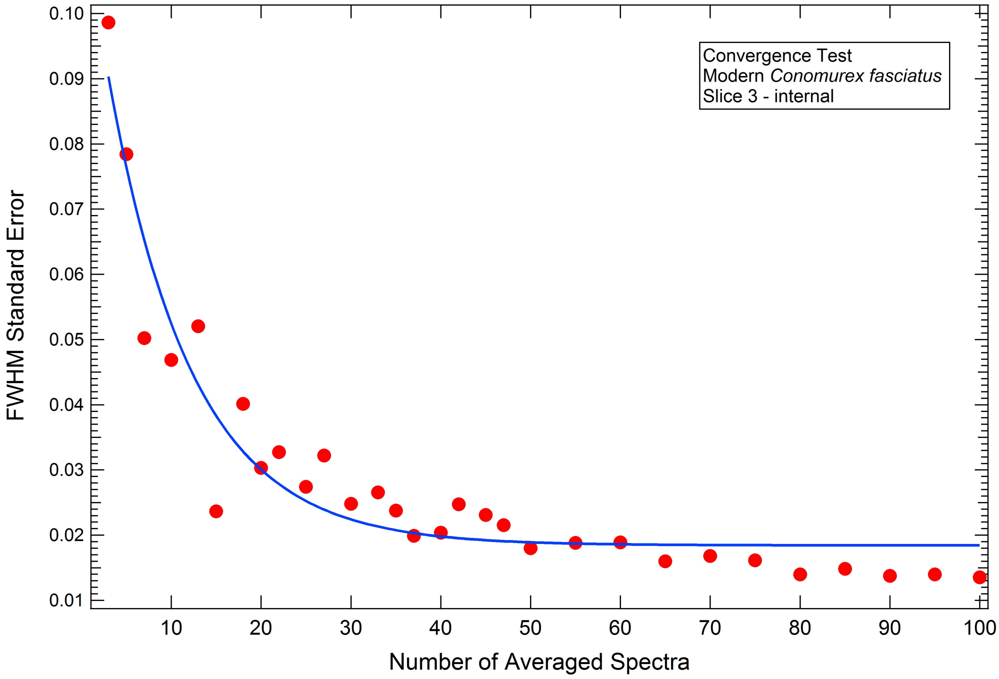

**Figure A.18:** Convergence test for the modern *Conomurex fasciatus* internal region of slice 3. The blue line is the theoretical fitting and red points are the experimental data.

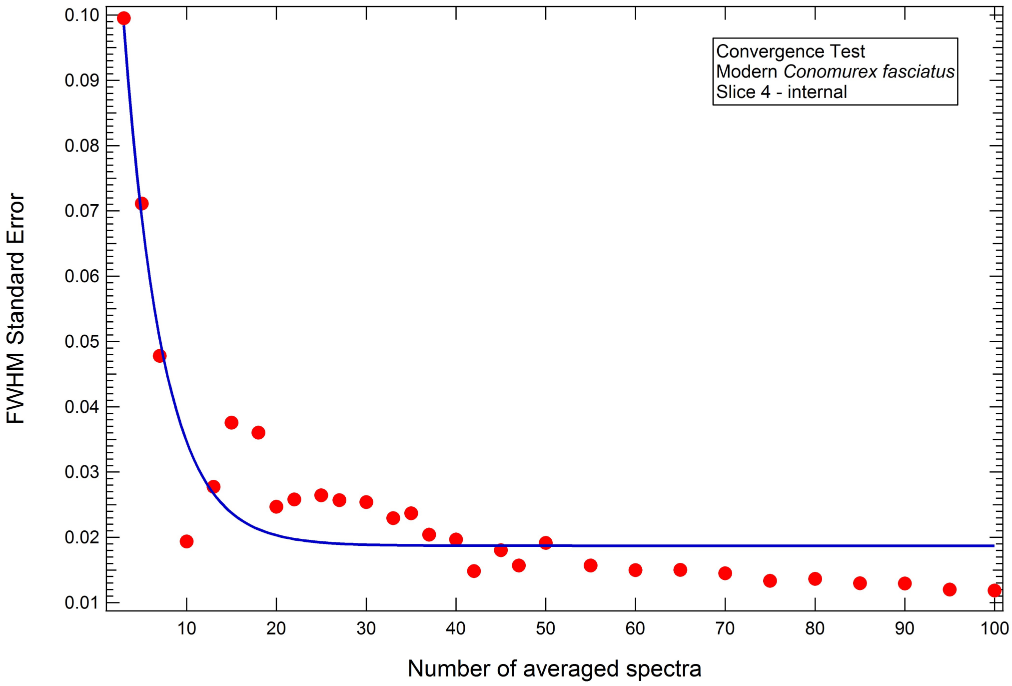

**Figure A.19:** Convergence test for the modern *Conomurex fasciatus* internal region of slice 4. The blue line is the theoretical fitting and red points are the experimental data.

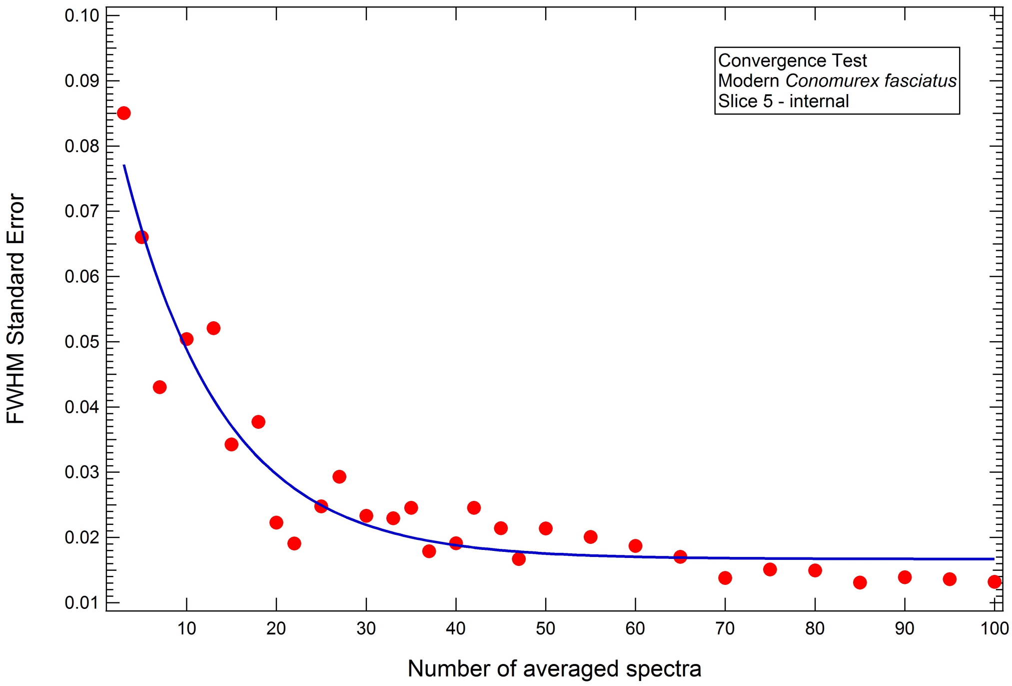

**Figure A.20:** Convergence test for the modern *Conomurex fasciatus* internal region of slice 5. The blue line is the theoretical fitting and red points are the experimental data.

### A.1.3 Fossil *Nucella* sp. shell

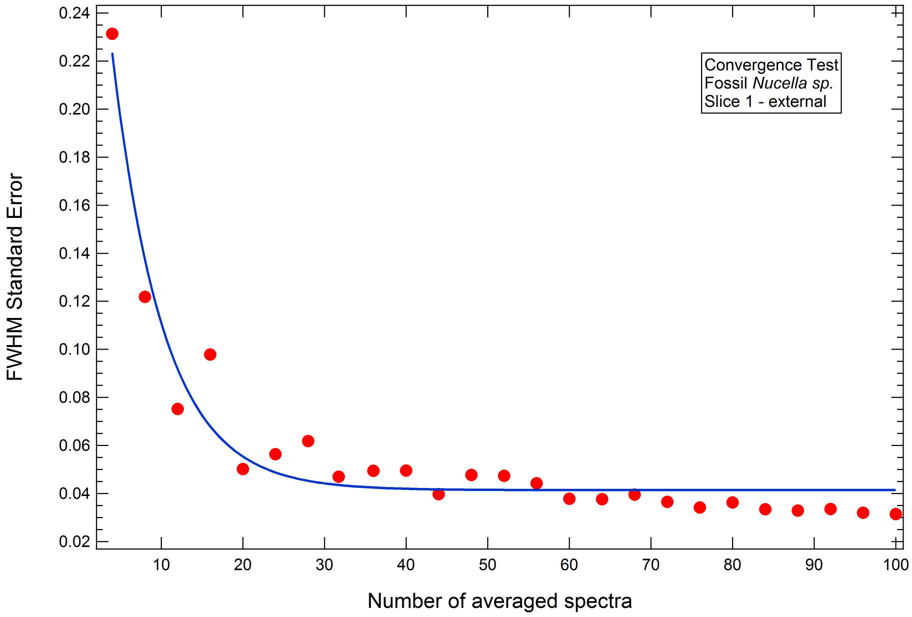

**Figure A.21:** Convergence test for the fossil *Nucella* sp. external region slice 1. The blue line is the theoretical fitting and red points are the experimental data.

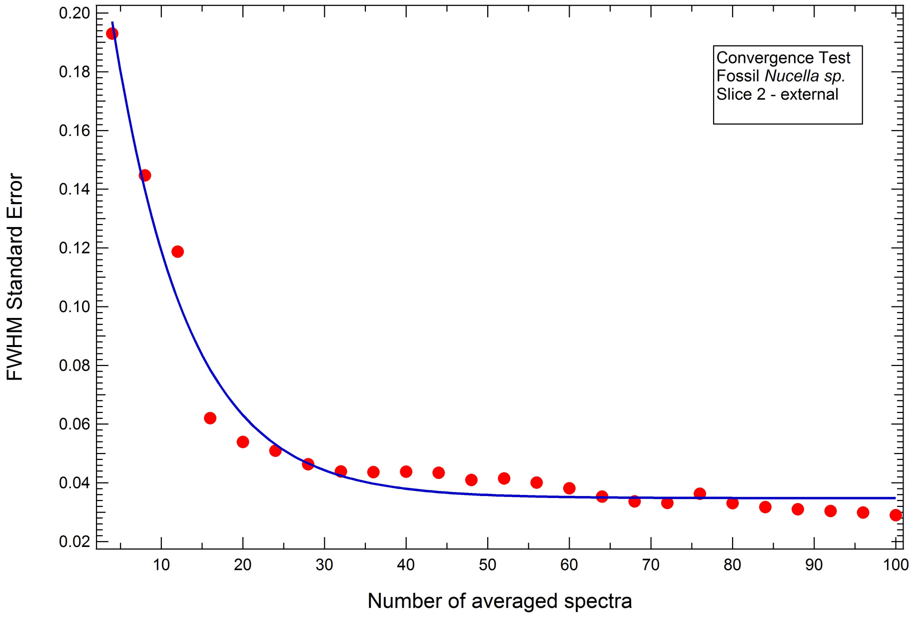

**Figure A.22:** Convergence test for the fossil *Nucella* sp. external region slice 2. The blue line is the theoretical fitting and red points are the experimental data.

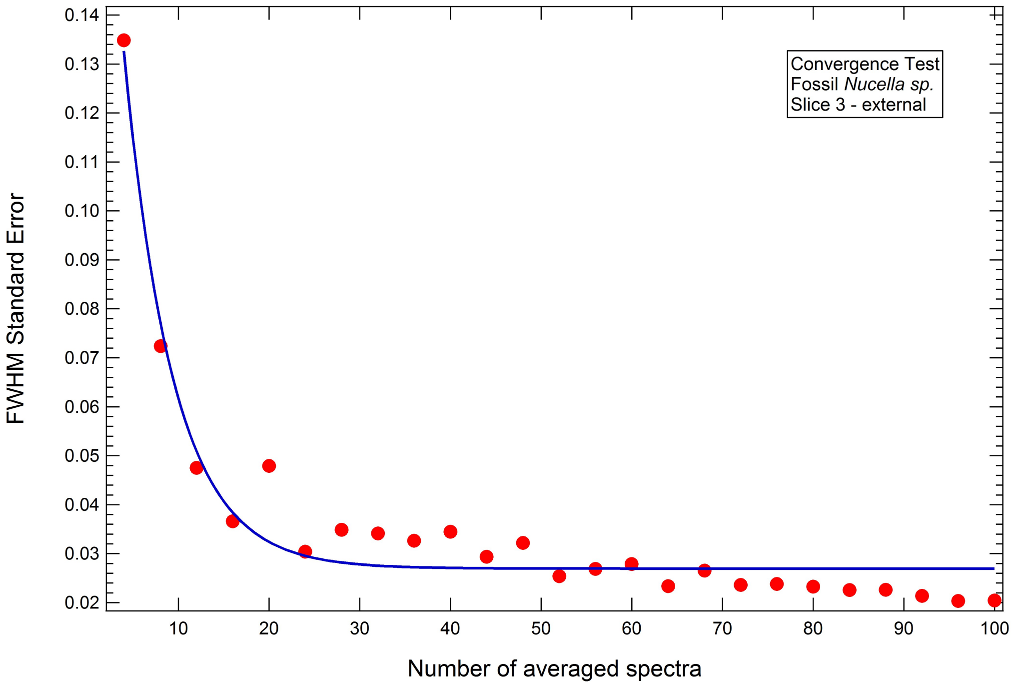

**Figure A.23:** Convergence test for the fossil *Nucella* sp. external region slice 3. The blue line is the theoretical fitting and red points are the experimental data.

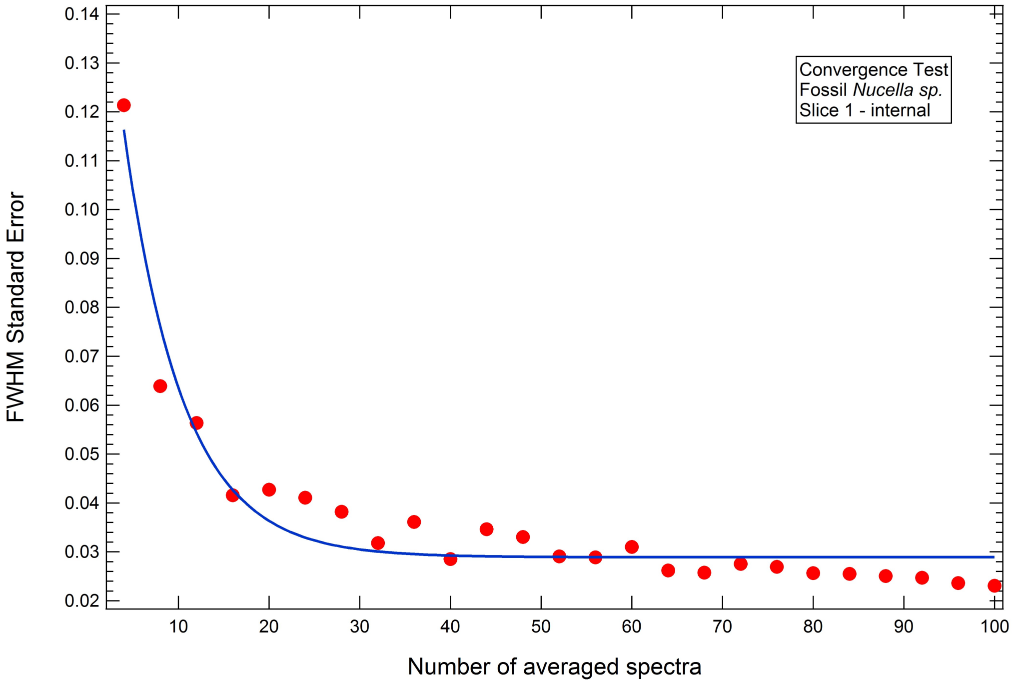

**Figure A.24:** Convergence test for the fossil *Nucella* sp. internal region slice 1. The blue line is the theoretical fitting and red points are the experimental data.

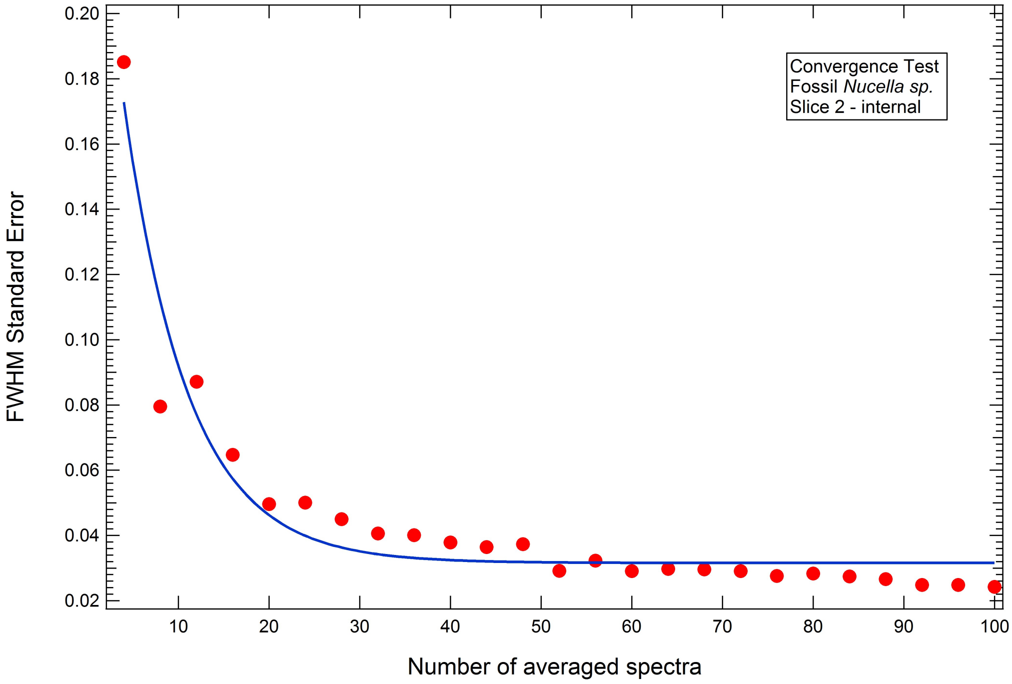

**Figure A.25:** Convergence test for the fossil *Nucella* sp. internal region slice 2. The blue line is the theoretical fitting and red points are the experimental data.

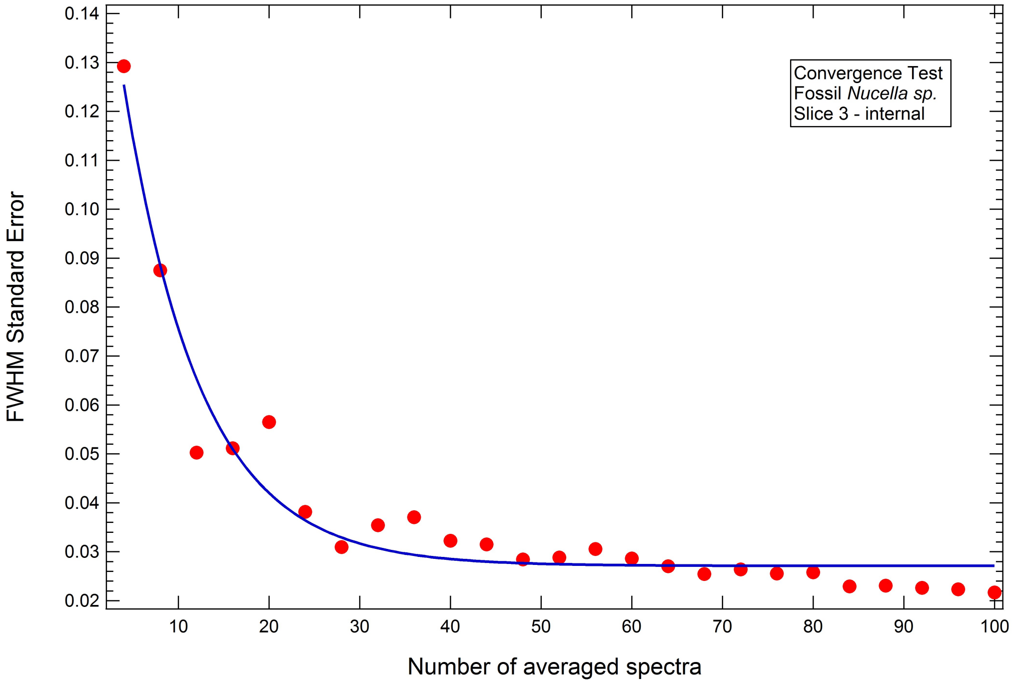

**Figure A.26:** Convergence test for the fossil *Nucella* sp. internal region slice 3. The blue line is the theoretical fitting and red points are the experimental data.

### A.1.4 Modern *Nucella lapillus* shell

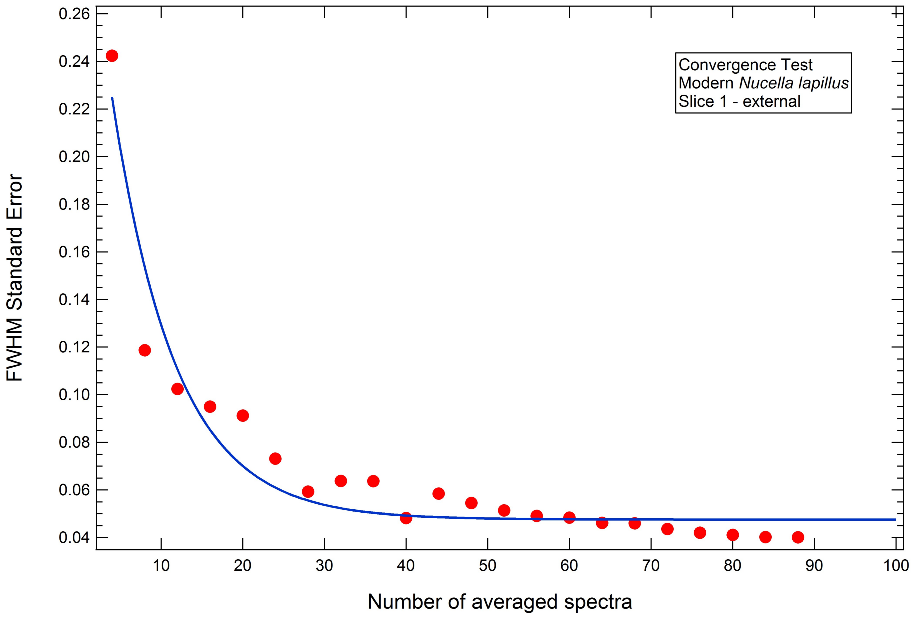

**Figure A.27:** Convergence test for the modern *Nucella lapillus* external region slice 1. The blue line is the theoretical fitting and red points are the experimental data.

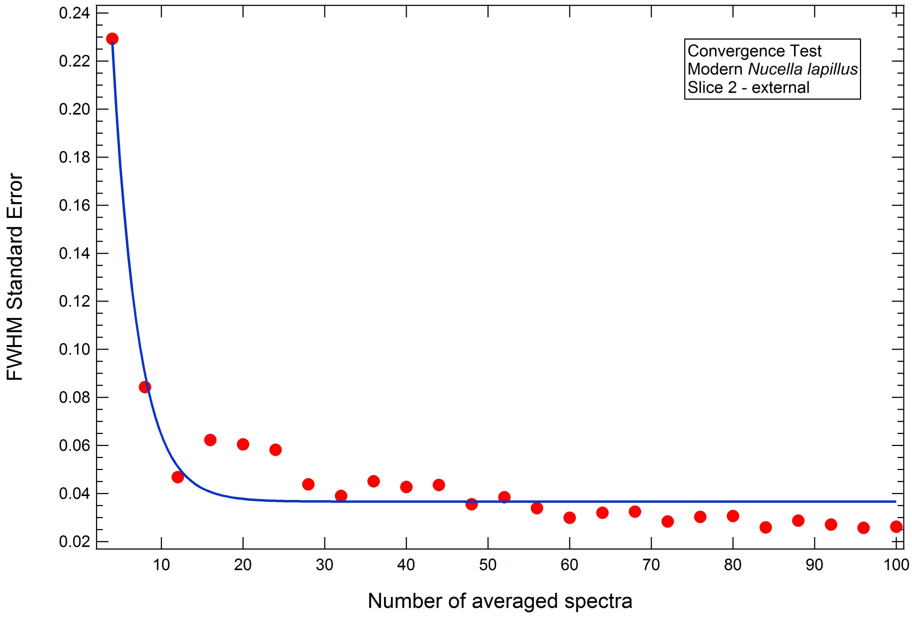

**Figure A.28:** Convergence test for the modern *Nucella lapillus* external region slice 2. The blue line is the theoretical fitting and red points are the experimental data.

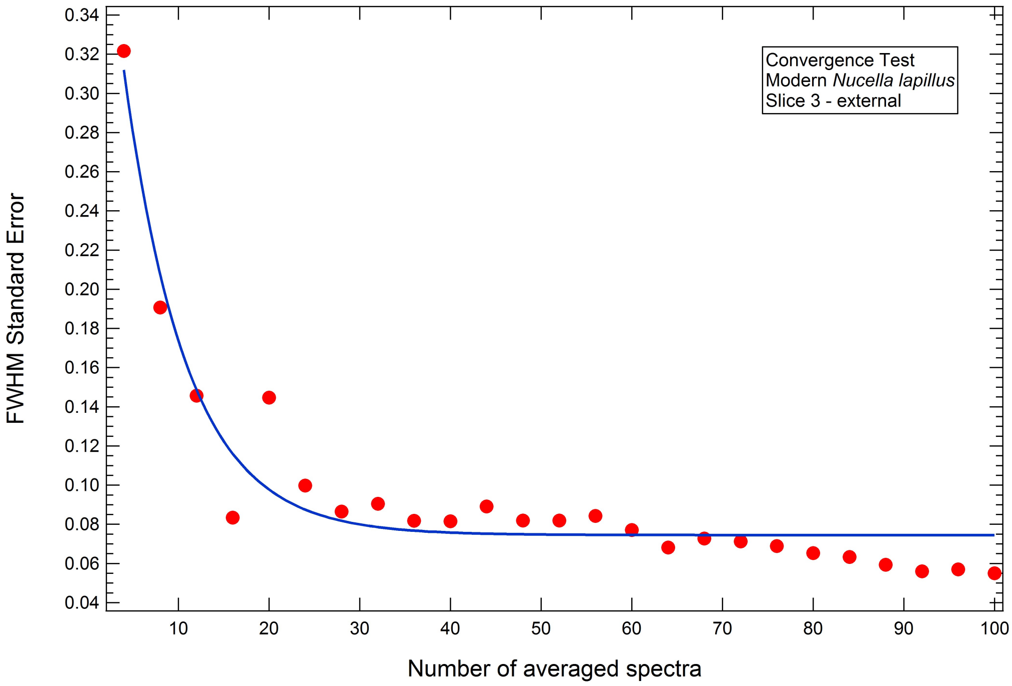

**Figure A.29:** Convergence test for the modern *Nucella lapillus* external region slice 3. The blue line is the theoretical fitting and red points are the experimental data.

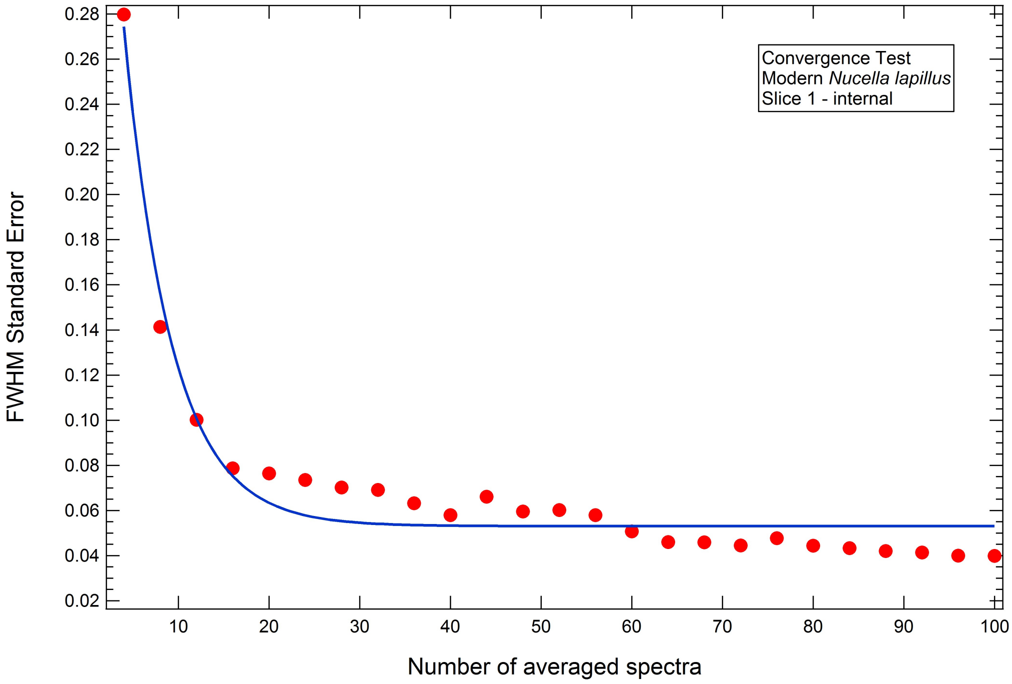

**Figure A.30:** Convergence test for the modern *Nucella lapillus* internal region slice 1. The blue line is the theoretical fitting and red points are the experimental data.

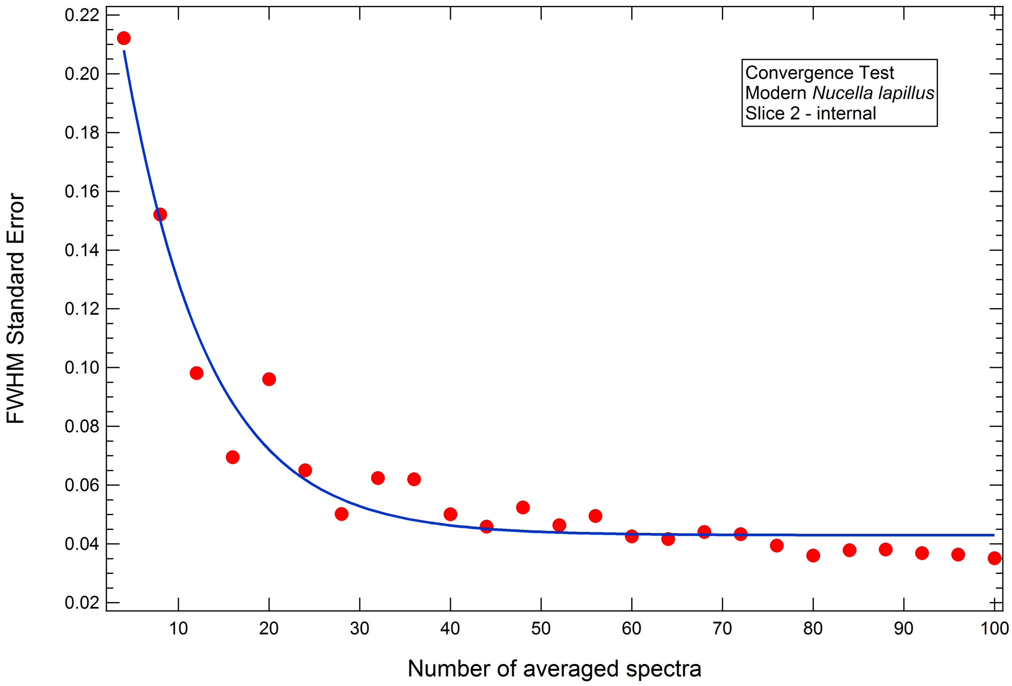

**Figure A.31:** Convergence test for the modern *Nucella lapillus* internal region slice 2. The blue line is the theoretical fitting and red points are the experimental data.

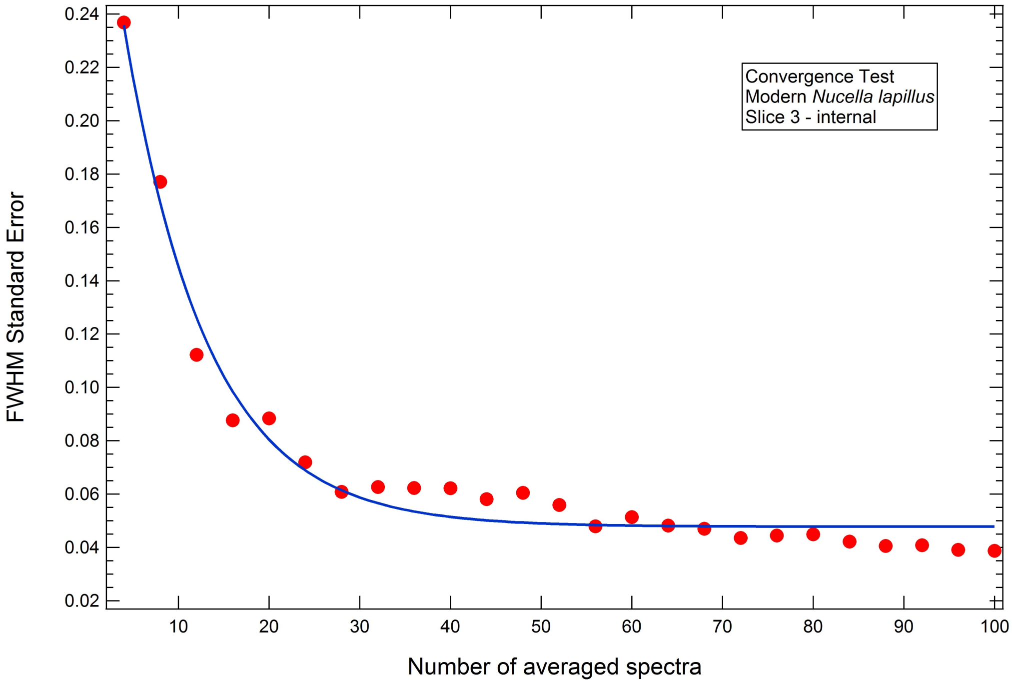

**Figure A.32:** Convergence test for the modern *Nucella lapillus* internal region slice 3. The blue line is the theoretical fitting and red points are the experimental data.

## A.2 Statistical tables

**Table A.1:** FWHM statistical table for the *Conomurex fasciatus* - external region. Apart from the coefficient of variation which is a percentage, all values are measured in $\mathrm{cm}^{-1}$.

| | | Statistics for the FWHM<br>*Conomurex fasciatus* - external results | | | | | |
|---|---|---|---|---|---|---|---|
| Spectrum region | | $L_1$ | | $L_2$ | $\nu_4$ | | $\nu_1$ |
| Peak position ($\mathrm{cm}^{-1}$) | | **141** | **151** | **205** | **701** | **705** | **1082** |
| Archaeo. | Mean | 5.10 | 9.00 | 6.10 | 3.20 | 3.70 | 3.10 |
| | SE | 0.06 | 0.04 | 0.05 | 0.02 | 0.02 | 0.01 |
| | CV (%) | 13 | 5 | 9 | 8 | 7 | 6 |
| Modern | Mean | 4.80 | 10.50 | 6.30 | 3.60 | 4.40 | 3.70 |
| | SE | 0.06 | 0.05 | 0.06 | 0.03 | 0.03 | 0.01 |
| | CV (%) | 18 | 7 | 15 | 13 | 11 | 3 |

**Table A.2:** FWHM statistical table for the *Conomurex fasciatus* - internal region. Apart from the coefficient of variation which is a percentage, all values are measured in cm$^{-1}$.

| | | Statistics for the FWHM | | | | | |
|---|---|---|---|---|---|---|---|
| | | *Conomurex fasciatus* - internal results | | | | | |
| Spectrum region | | $L_1$ | | $L_2$ | $\nu_4$ | | $\nu_1$ |
| Peak position (cm$^{-1}$) | | **141** | **151** | **205** | **701** | **705** | **1082** |
| Archaeo. | Mean | 5.50 | 9.10 | 6.50 | 3.30 | 3.90 | 3.20 |
| | SE | 0.05 | 0.07 | 0.04 | 0.02 | 0.03 | 0.02 |
| | CV (%) | 12 | 10 | 8 | 8 | 9 | 8 |
| Modern | Mean | 7.00 | 11.30 | 7.20 | 3.40 | 4.20 | 3.90 |
| | SE | 0.05 | 0.05 | 0.03 | 0.02 | 0.02 | 0.01 |
| | CV (%) | 12 | 7 | 7 | 8 | 8 | 5 |

**Table A.3:** FWHM statistical table for the *Nucella* sp. - external region. Apart from the coefficient of variation which is a percentage, all values are measured in cm$^{-1}$.

| | | Statistics for the FWHM | | | |
|---|---|---|---|---|---|
| | | *Nucella* sp. - external results | | | |
| Spectrum region | | $L_1$ | $L_2$ | $\nu_4$ | $\nu_1$ |
| Peak position (cm$^{-1}$) | | **154** | **280** | **712** | **1082** |
| Fossil | Mean | 8.80 | 11.50 | 4.90 | 4.00 |
| | SE | 0.07 | 0.04 | 0.04 | 0.02 |
| | CV (%) | 8 | 4 | 8 | 5 |
| Modern | Mean | 11.0 | 13.30 | 6.00 | 5.00 |
| | SE | 0.1 | 0.06 | 0.06 | 0.04 |
| | CV (%) | 9 | 5 | 9 | 9 |

**Table A.4:** FWHM statistical table for the *Nucella* sp. - internal region. Apart from the coefficient of variation which is a percentage, all values are measured in cm$^{-1}$.

| | | Statistics for the FWHM<br>*Nucella* sp. - internal results | | | |
|---|---|---|---|---|---|
| Spectrum region | | $L_1$ | $L_2$ | $\nu_4$ | $\nu_1$ |
| Peak position (cm$^{-1}$) | | **154** | **280** | **712** | **1082** |
| Fossil | Mean | 8.90 | 11.40 | 5.00 | 3.90 |
| | SE | 0.05 | 0.04 | 0.05 | 0.02 |
| | CV (%) | 5 | 3 | 10 | 6 |
| Modern | Mean | 11.0 | 12.80 | 5.80 | 4.80 |
| | SE | 0.1 | 0.08 | 0.08 | 0.06 |
| | CV (%) | 10 | 6 | 12 | 12 |

**Table A.5:** Peak ratio statistical table for the *Conomurex fasciatus* - external region. Apart from the coefficient of variation which is a percentage, all values are measured in cm$^{-1}$.

| | | Statistics for the peak intensity ratio<br>*Conomurex fasciatus* - external results | | | | |
|---|---|---|---|---|---|---|
| Peak ratio | | $\frac{\mathbf{141}}{\mathbf{1082}}$ | $\frac{\mathbf{151}}{\mathbf{1082}}$ | $\frac{\mathbf{205}}{\mathbf{1082}}$ | $\frac{\mathbf{701}}{\mathbf{1082}}$ | $\frac{\mathbf{705}}{\mathbf{1082}}$ |
| Archaeo. | Mean | 0.0330 | 0.130 | 0.060 | 0.0570 | 0.0630 |
| | SE | 0.0008 | 0.005 | 0.003 | 0.0005 | 0.0006 |
| | CV (%) | 30 | 52 | 60 | 11 | 11 |
| Modern | Mean | 0.0260 | 0.100 | 0.040 | 0.0640 | 0.0660 |
| | SE | 0.0005 | 0.003 | 0.002 | 0.0005 | 0.0006 |
| | CV (%) | 27 | 41 | 54 | 11 | 14 |

**Table A.6:** Peak ratio statistical table for the *Conomurex fasciatus* - internal region. Apart from the coefficient of variation which is a percentage, all values are measured in $cm^{-1}$.

| | | Statistics for the peak intensity ratio<br>*Conomurex fasciatus* - internal results | | | | |
|---|---|---|---|---|---|---|
| Peak ratio | | $\frac{\mathbf{141}}{\mathbf{1082}}$ | $\frac{\mathbf{151}}{\mathbf{1082}}$ | $\frac{\mathbf{205}}{\mathbf{1082}}$ | $\frac{\mathbf{701}}{\mathbf{1082}}$ | $\frac{\mathbf{705}}{\mathbf{1082}}$ |
| | Mean | 0.040 | 0.20 | 0.110 | 0.050 | 0.060 |
| Archaeo. | SE | 0.001 | 0.01 | 0.005 | 0.001 | 0.001 |
| | CV (%) | 31 | 59 | 61 | 28 | 25 |
| | Mean | 0.040 | 0.260 | 0.130 | 0.0450 | 0.0550 |
| Modern | SE | 0.001 | 0.008 | 0.005 | 0.0009 | 0.0009 |
| | CV (%) | 36 | 47 | 60 | 31 | 25 |

**Table A.7:** Peak ratio statistical table for the *Nucella* sp. - external region. Apart from the coefficient of variation which is a percentage, all values are measured in $cm^{-1}$.

| | | Statistics for the peak intensity ratio<br>*Nucella* sp. - external results | | |
|---|---|---|---|---|
| Peak ratio | | $\frac{\mathbf{154}}{\mathbf{1082}}$ | $\frac{\mathbf{280}}{\mathbf{1082}}$ | $\frac{\mathbf{712}}{\mathbf{1082}}$ |
| | Mean | 0.080 | 0.150 | 0.070 |
| Archaeo. | SE | 0.005 | 0.009 | 0.002 |
| | CV (%) | 62 | 56 | 21 |
| | Mean | 0.080 | 0.150 | 0.070 |
| Modern | SE | 0.004 | 0.008 | 0.001 |
| | CV (%) | 53 | 51 | 18 |

**Table A.8:** Peak ratio statistical table for the *Nucella* sp. - internal region. Apart from the coefficient of variation which is a percentage, all values are measured in cm$^{-1}$.

| | | Statistics for the peak intensity ratio *Nucella* sp. - internal results | | |
|---|---|---|---|---|
| Peak ratio | | $\mathbf{\frac{154}{1082}}$ | $\mathbf{\frac{280}{1082}}$ | $\mathbf{\frac{712}{1082}}$ |
| Archaeo. | Mean | 0.110 | 0.20 | 0.060 |
| | SE | 0.005 | 0.01 | 0.002 |
| | CV (%) | 48 | 48 | 23 |
| Modern | Mean | 0.080 | 0.150 | 0.060 |
| | SE | 0.004 | 0.007 | 0.001 |
| | CV (%) | 46 | 47 | 20 |

# Appendix B

# Supplementary information for the quantitative RS study of biogenic aragonite to calcite transition

## B.1 Raman spectra for modern *Conomurex fasciatus* powdered samples S2 and S3

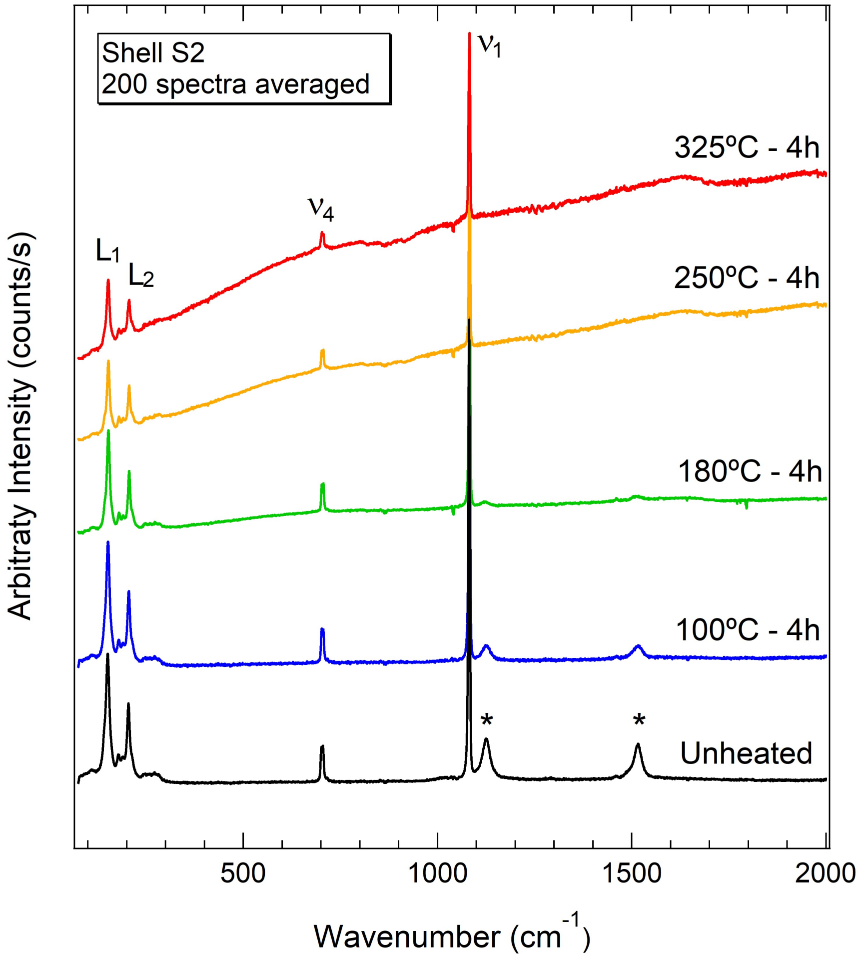

**Figure B.1:** Raman spectra for the modern *Conomurex fasciatus* powdered sample S2 heat-treated for 4h at 100°C, 180°C, 250°C and 325°C. No aragonite to calcite transition is observed. Unheated results are shown for comparison. The carotenoid peaks are marked with (*). The positions and assignments for the other peaks are shown in Table 1.1 of Chapter 4.

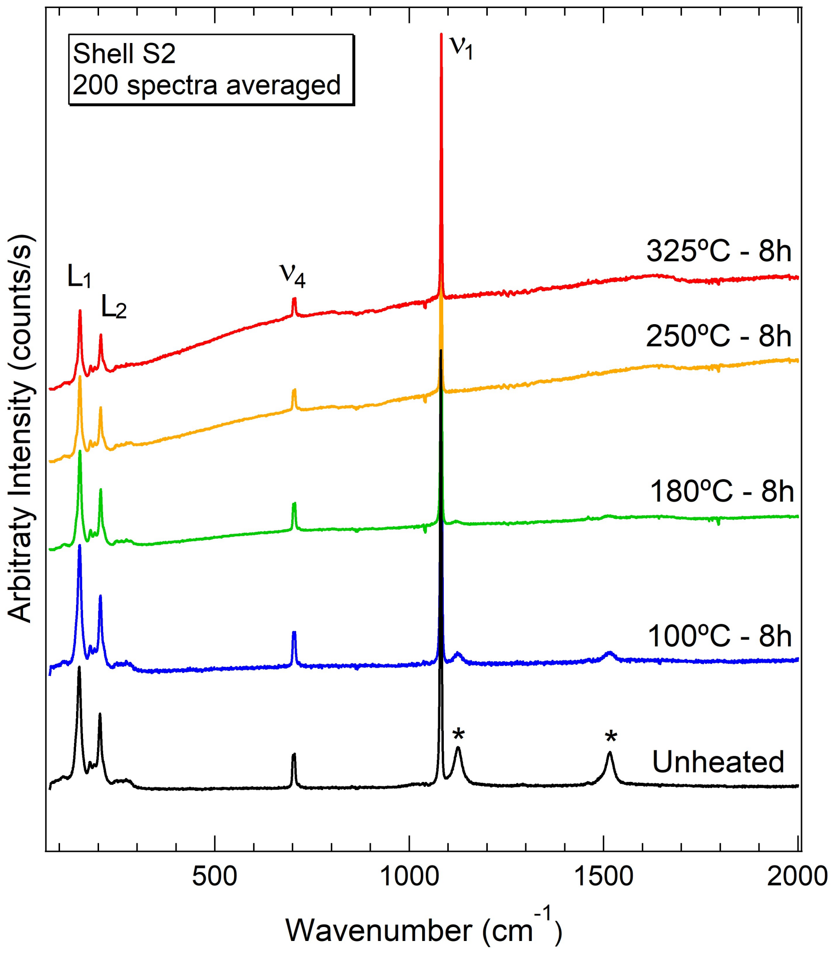

**Figure B.2:** Raman spectra for the modern *Conomurex fasciatus* powdered sample S2 heat-treated for 8h at 100°C, 180°C, 250°C and 325°C. No aragonite to calcite transition is observed. Unheated results are shown for comparison. The carotenoid peaks are marked with (*). The positions and assignments for the other peaks are shown in Table 1.1 of Chapter 4.

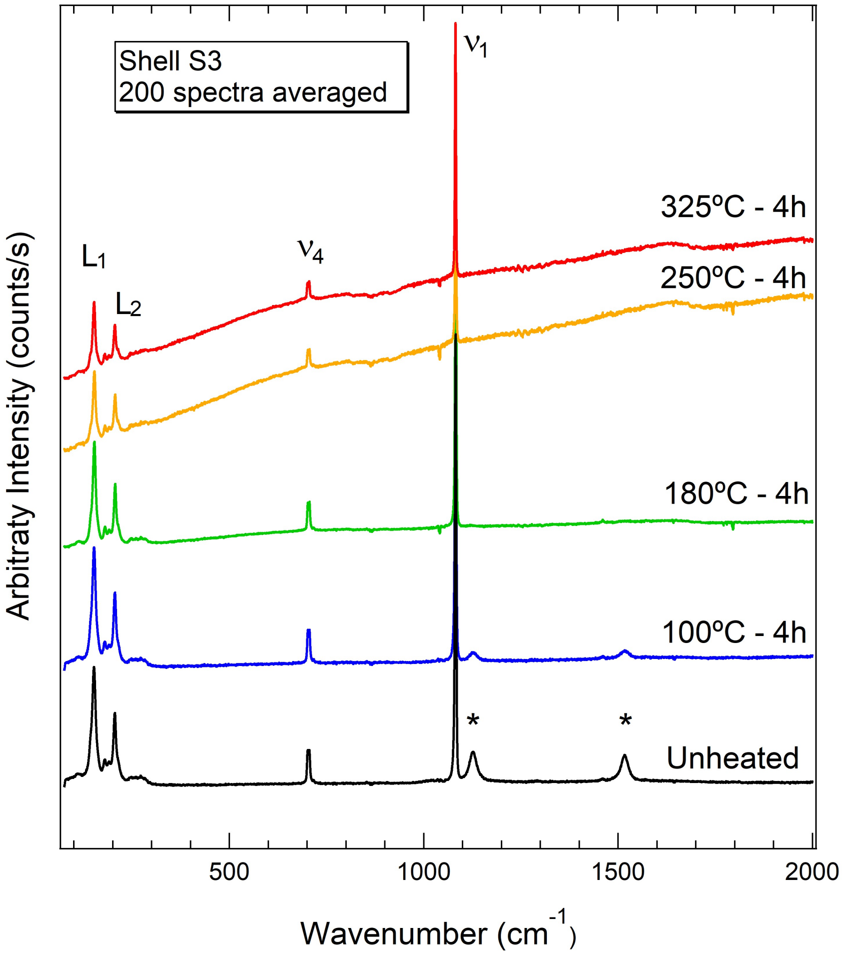

**Figure B.3:** Raman spectra for the modern *Conomurex fasciatus* powdered sample S3 heat-treated for 4h at 100°C, 180°C, 250°C and 325°C. No aragonite to calcite transition is observed. Unheated results are shown for comparison. The carotenoid peaks are marked with (*). The positions and assignments for the other peaks are shown in Table 1.1 of Chapter 4.

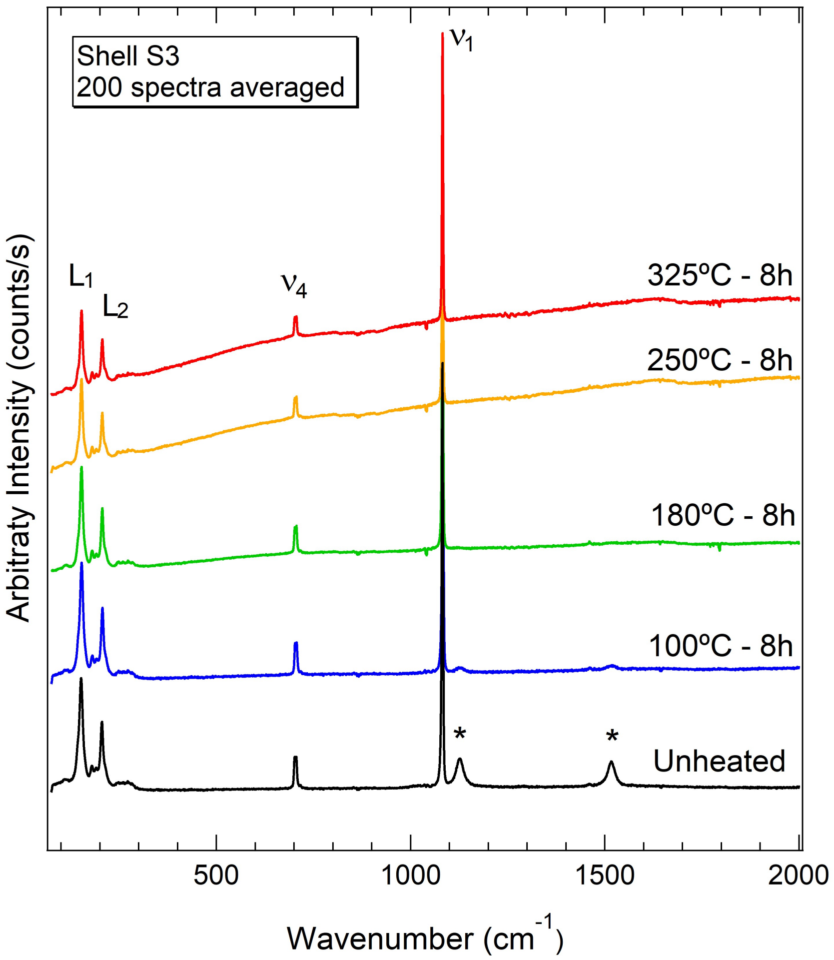

**Figure B.4:** Raman spectra for the modern *Conomurex fasciatus* powdered sample S3 heat-treated for 8h at 100°C, 180°C, 250°C and 325°C. No aragonite to calcite transition is observed. Unheated results are shown for comparison. The carotenoid peaks are marked with (*). The positions and assignments for the other peaks are shown in Table 1.1 of Chapter 4.

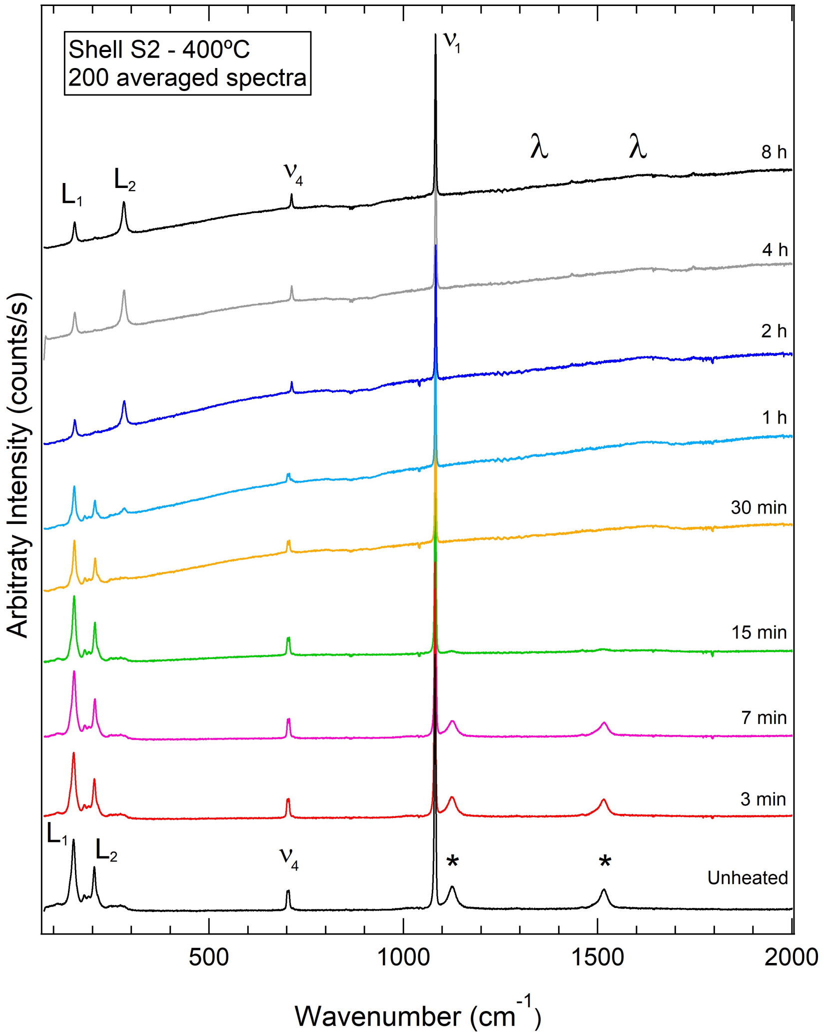

**Figure B.5:** Raman spectra of the aragonite to calcite transition at 400°C for the modern *Conomurex fasciatus* powdered sample S2. Each spectrum corresponds to the average of 200 spectra collected from each sub-sample heated for different times. The aragonite to calcite transition is noted after 1h, where initially a mixture of the spectral signatures of aragonite and calcite is observed. The unheated results are shown for comparison. The peaks associated with carotenoids and amorphous carbon are marked with (*) and ($\lambda$), respectively. The positions and assignments for the other peaks are shown in Table 1.1 of Chapter 4.

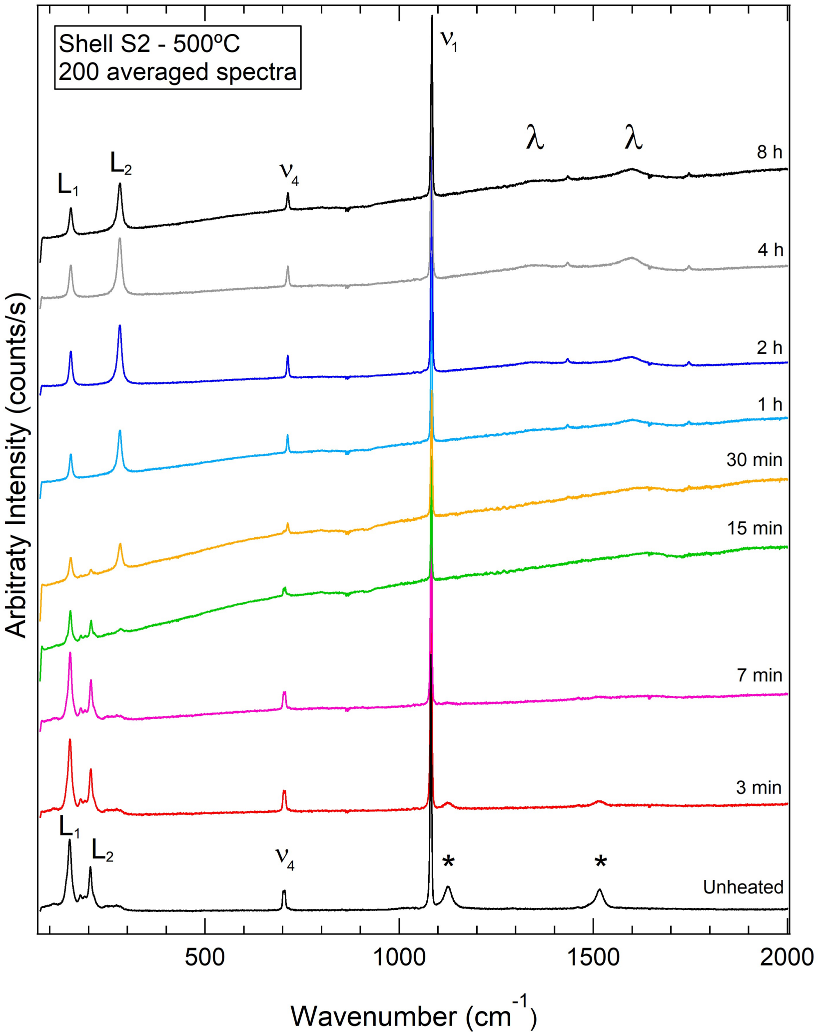

**Figure B.6:** Raman spectra of the aragonite to calcite transition at 500°C for the modern *Conomurex fasciatus* powdered sample S2. Each spectrum corresponds to the average of 200 spectra collected from each sub-sample heated for different times. The aragonite to calcite transition is noted after 15min, where initially a mixture of the spectral signatures of aragonite and calcite is observed. The unheated results are shown for comparison. The peaks associated with carotenoids and amorphous carbon are marked with (*) and ($\lambda$), respectively. The positions and assignments for the other peaks are shown in Table 1.1 of Chapter 4.

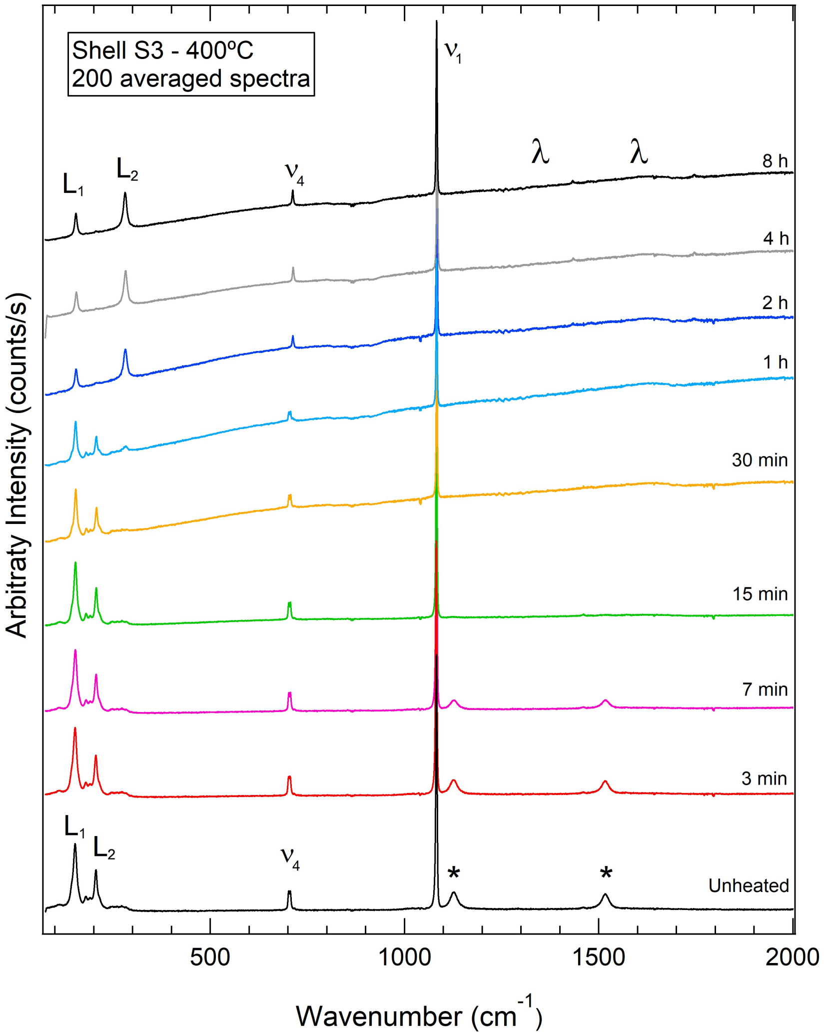

**Figure B.7:** Raman spectra of the aragonite to calcite transition at 400°C for the modern *Conomurex fasciatus* powdered sample S3. Each spectrum corresponds to the average of 200 spectra collected from each sub-sample heated for different times. The aragonite to calcite transition is noted after 1h, where initially a mixture of the spectral signatures of aragonite and calcite is observed. The unheated results are shown for comparison. The peaks associated with carotenoids and amorphous carbon are marked with (*) and ($\lambda$), respectively. The positions and assignments for the other peaks are shown in Table 1.1 of Chapter 4.

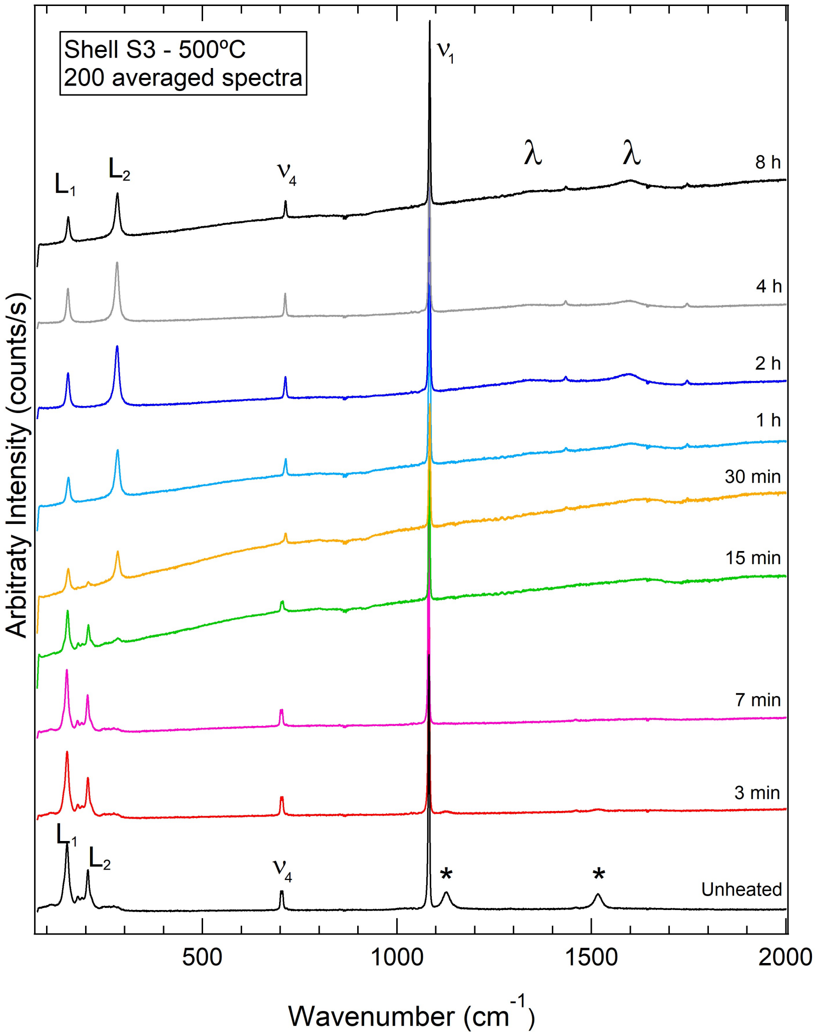

**Figure B.8:** Raman spectra of the aragonite to calcite transition at 500°C for the modern *Conomurex fasciatus* powdered sample S3. Each spectrum corresponds to the average of 200 spectra collected from each sub-sample heated for different times. The aragonite to calcite transition is noted after 15min, where initially a mixture of the spectral signatures of aragonite and calcite is observed. The unheated results are shown for comparison. The peaks associated with carotenoids and amorphous carbon are marked with (*) and (λ), respectively. The positions and assignments for the other peaks are shown in Table 1.1 of Chapter 4.

## B.2 Burnt *Conomurex fasciatus* fragments - RS quantitative properties

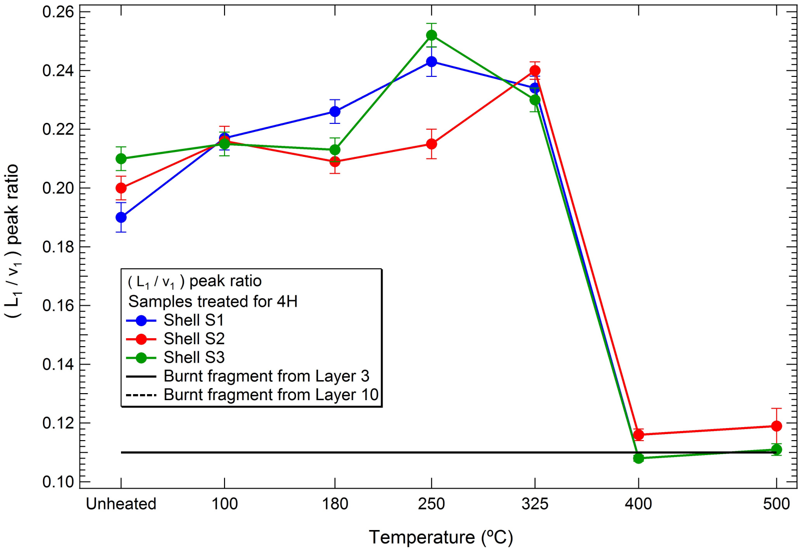

(a)

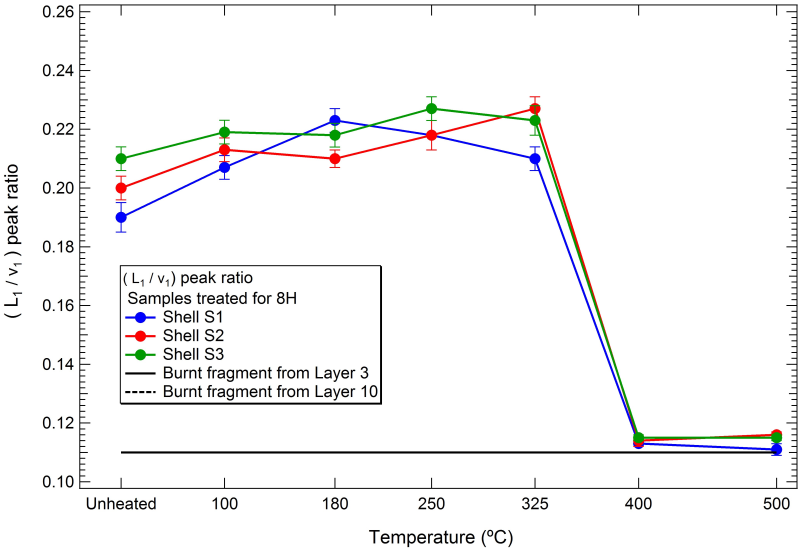

(b)

**Figure B.9:** Comparison of the intensity ratio $L_1/\nu_1$ from the burnt *Conomurex fasciatus* fragments with the heated modern shells (S1, S2 and S3) as function of temperature for heat-treatments of (a) 4h and (b) 8h. The $L_1/\nu_1$ peak intensity ratio of the modern heat shells remains constant after the aragonite to calcite transition *i.e.*, for temperatures greater than 400°C, in both heat treatments. The peak intensity ratios obtained for both burnt fragments are superposed and indicate a full aragonite to calcite conversion.

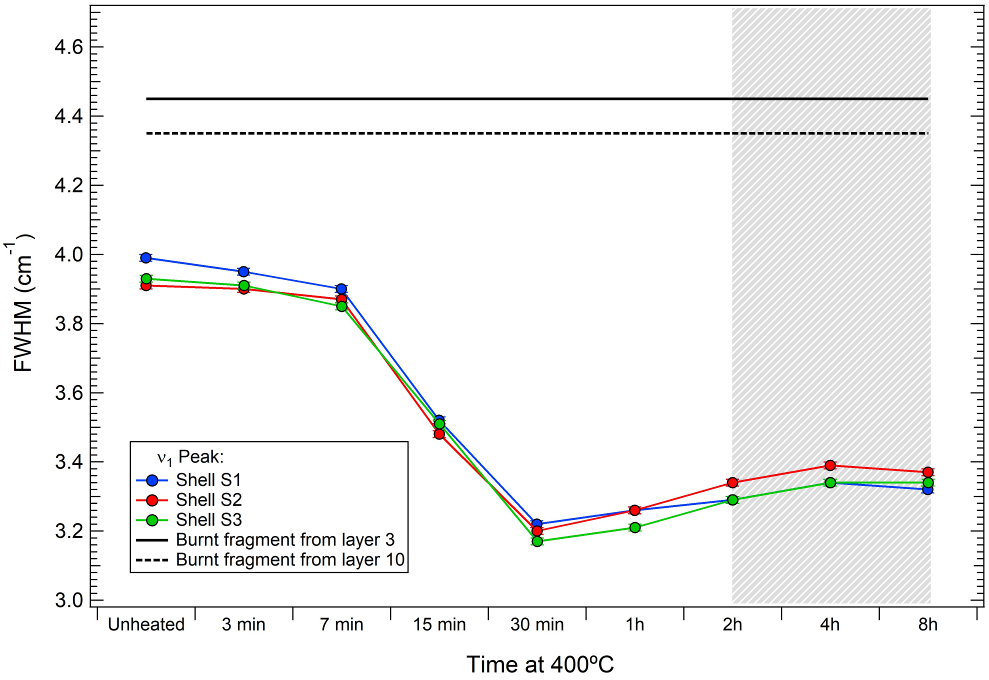

(a)

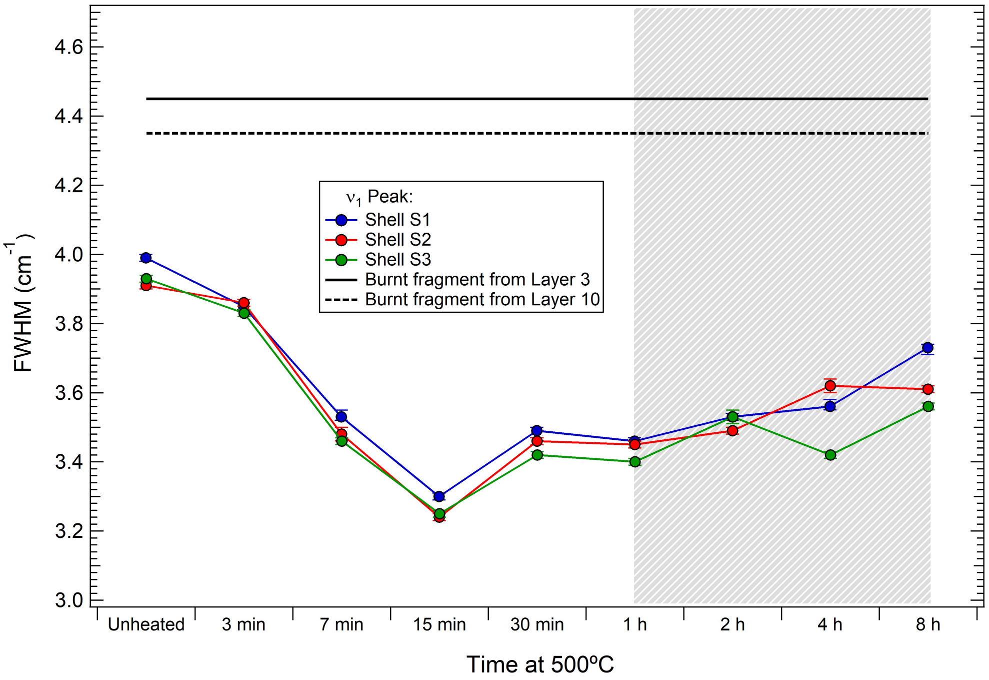

(b)

**Figure B.10:** Comparison of the FWHM of the $\nu_1$ (~1082 cm$^{-1}$) peak of the burnt *Conomurex fasciatus* fragments with the heated modern shells (S1, S2 and S3) results as function of increasing time in the furnace at (a) 400°C and (b) 500°C. Full aragonite to calcite conversion is observed only after 2h heating at 400°C and 1h heating at 500°C (marked by the shaded areas), thus indicating minimal heating times and temperatures for the burnt fragments.

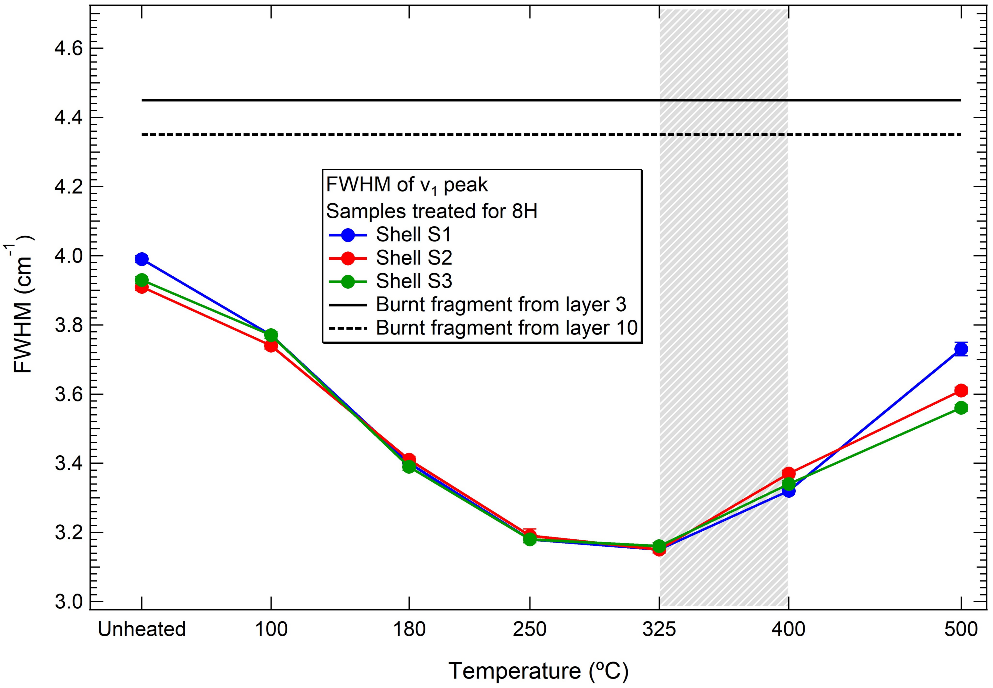

**Figure B.11:** Comparison of the FWHM of the $\nu_1$ ($\sim$1082 cm$^{-1}$) peak of the burnt *Conomurex fasciatus* fragments with the heated modern shells (S1, S2 and S3) as function of temperature for a heat treatment of 8h. The shaded area marks the temperature range for which the aragonite to calcite transition takes place. After the transition the $\nu_1$ FWHM starts to increase, indicating that the burnt fragments could have been exposed to temperatures greater than 500°C.

# Abbreviations

| | |
|---|---|
| **AAS** | Atomic absorption spectroscopy |
| **ACC** | Amorphous calcium carbonate |
| **AFM** | Atomic force microscopy |
| **CCD** | Charge-coupled device |
| **CV** | Coefficient of variation |
| **DTA** | Differential thermal analysis |
| **EDX** | Energy dispersive X-Ray |
| **FTIR** | Fourrier transformed infrared spectroscopy |
| **FWHM** | Full width at half maximum |
| **LWD** | Long working distance |
| **NA** | Numerical aperture |
| **RS** | Raman spectroscopy |
| **SDEV** | Standard deviation |

| | |
|---|---|
| **SE** | Standard error |
| **SEM** | Scanning electron microscopy |
| **TG** | Thermo gravimetric analysis |
| **XRD** | X-Ray diffraction |
| **YAG** | Yttrium aluminium garnet |

# References

[1] C. V. Raman. A new radiation. *Indian Journal of Physics*, 2:387–398, 1928.

[2] J. R. Ferraro and K. Nakamoto. *Introductory Raman Spectroscopy.* Academic Press, San Diego, USA, 1994.

[3] E. Smith and G. Dent. *Modern Raman spectroscopy - A practical approach.* Wiley, England, 1 edition, 2005.

[4] P. Larkin. *Infrared and Raman spectroscopy – principles and spectral interpretation*, chapter Basic principles, pages 7–25. Elsevier, 2011.

[5] R. L. McCreery. *Raman spectroscopy for chemical analysis.* Wiley, USA, 1 edition, 2000.

[6] B. Schrader. *Infrared and Raman spectroscopy*, volume 1st edition. VCH Publishers Inc., New York, USA, 1995.

[7] R. S. Das and Y. K. Agrawal. Raman spectroscopy: Recent advancements, techniques and applications. *Vibrational Spectroscopy*, 57:163–176, 2011.

[8] A. Ferrari and J. Robertson. Raman spectroscopy of amorphous, nanostructured, diamond-like carbon, and nanodiamond. *The Royal Society*, 362:2477–2512, 2004.

[9] A. C. Ferrari. Raman spectroscopy of graphene and graphite: disorder, electron-phonon coupling, doping and nonadiabatic effects. *Solid State Communications*, 143:47–53, 2007.

[10] A. Ferrari and J. Robertson. Interpretation of Raman spectra of disordered and amorphous carbon. *Physical Review B*, 61(20), 2000.

[11] W. Bacsa, J. Lannin, D. Pappas, and J. Cuomo. Raman scattering of laser-deposited amorphous carbon. *Physical Review B*, 47(16), 1993.

[12] A. C. Ferrari and J. Robertson. Resonant Raman spectroscopy of disordered, amorphous, and diamondlike carbon. *Physical Review B*, 64(075414), 2001.

[13] D. D. Genova, K. Hess, M. O. Chevrel, and D. B. Dingwell. Models for the estimation of $fe^{3+}/fe_{tot}$ ratio in terrestrial and extraterrestrial alkali- and iron-rich silicate glasses using Raman spectroscopy. *American Mineralogist*, 101:943–952, 2016.

[14] P. R. Bartholomew, M. D. Dyarb, and J. B. Bradyc. The role of intensity and instrument sensitivity in Raman mineral identification. *Journal of Raman Spectroscopy*, 46:889–893, 2015.

[15] L. Kiefert, H. A. Hanni, and J. Chalain. Identification of gemstone treatments with Raman spectroscopy. *Proceedings of SPIE - The international society for optical engineering*, 4098:241–251, 2000.

[16] L. Kiefert and S. Karampelas. Use of the Raman spectrometer in gemmological laboratories: Review. *Spectrochimica Acta Part A*, 80:110–124, 2011.

[17] J. Fridrichova, P. Bacik, R. Skoda, and P. Antal. The use of spectroscopic methods for determination of diamond origin and treatment. *Acta Geologica Slovaca*, 7(1):11–18, 2015.

[18] P. Buzzini and E. Suzuki. Forensic applications of Raman spectroscopy for the *in situ* analyses of pigments and dyes in ink and paint evidence. *Journal of Raman spectroscopy*, 47:16–27, 2016.

[19] C. A. F. O. Penido, M. T. T. Pacheco, I. K. Lednev, and L. Silveira Jr. Raman spectroscopy in forensic analysis: identification of cocaine and other illegal drugs of abuse. *Journal of Raman Spectroscopy*, 47:28–38, 2016.

[20] K. Virkler and I. K. Lednev. Raman spectroscopic signature of semen and its potential application to forensic body fluid identification. *Forensic Science International*, 193:52–62, 2009.

[21] J. V. Miller and E. G. Bartick. Forensic analysis of single fibers by Raman spectroscopy. *Applied Spectroscopy*, 55(12):1729–1732, 2001.

[22] A. J. Hobro, N. Pavillon, K. Fujita, M. Ozkan, C. Coban, and N. I. Smith. Label-free Raman imaging of the macrophage response to the malaria pigment hemozoin. *Analyst*, 140:2350–2359, 2015.

[23] S. Klob, B. Kampe, S. Sachse, P. Rosch, E. Straube, W. Pfister, M. Kiehntopf, and J. Popp. Culture independent Raman spectroscopy identification of urinary tract infection pathogens: a proof of principle study. *Analytical Chemistry*, 85:9610–9616, 2013.

[24] C. Matthaus, A. Kale, T. Chernenko, V. Torchilin, and M. Diem. New ways of imaging uptake and intracellular fate of liposomal drug carrier systems inside individual cells based on Raman microscopy. *Molecular Pharmaceutics*, 5:287–293, 2008.

[25] W. Huang, S. Wu, M. Chen, L. Sun, Y. Li, M. Huang, S. Huang, Z. Xu, R. Chen, and H. Zeng. Study of fingerprint and high wavenumber Raman spectroscopy of

pathological nasopharyngeal tissues. *Journal of Raman Spectroscopy*, 46:537–544, 2015.

[26] K. R. Dukor. Vibrational spectroscopy in the detection of cancer. *Handbook of vibrational spectroscopy*, 2002.

[27] Y. Chiang, S. H. Wu, I. Kuo, H. Chen, A. Chiou, and O. K. Lee. Raman spectroscopy for grading of live osteosarcoma cells. *Stem Cell Research & Therapy*, 6(1):81, 2015.

[28] C. Krafft, S. Dochow, I. Latka, B. Dietzek, and J. Popp. Diagnosis and screening of cancer tissues by fiber-optic Raman spectroscopy. *Biomedical Spectroscopy and Imaging*, 1:39–55, 2012.

[29] P. Vandenabeele, B. Wheling, L. Moens, H. Edwards, M. De Reu, and G. Van Hooydonk. Analysis with micro-Raman spectroscopy of natural organic binding media and varnishes used in art. *Spectrochimica Acta*, 407:261–274, 2000.

[30] I. M. Bell, R. J. H. Clark, and P. J. Gibbs. Raman spectroscopic library of natural and synthetic pigments. *Spectrochimica Acta Part A*, 53:2159–2179, 1997.

[31] P. Colomban, M. P. Etcheverry, M. Asquier, M. Bounichou, and A. Tournie. Raman identification of ancient stained glass and their degree of deterioration. *Journal of Raman spectroscopy*, 37:614–626, 2006.

[32] J. A. Tunon, A. Sanchez, D. J. Parras, P. Vandenabeele, and M. Montejo. Micro-Raman spectroscopy on Iberian archaeological materials. *Journal of Raman Spectroscopy*, 47:1514–1521, 2016.

[33] M. A. Legodi and D. de Waal. Raman spectroscopic study of ancient South African domestic clay pottery. *Spectrochimica Acta Part A*, 66:135–142, 2007.

[34] M. Sendova, V. Zhelyaskov, M. Scalera, and M. Ramsey. Micro-Raman spectroscopic study of pottery fragments from the Lapatsa Tomb, Cyprus, ca 2500 BC. *Journal of Raman Spectroscopy*, 36:1829–833, 2005.

[35] J. Striova, C. Lofrumento, A. Zoppi, and E. M. Castellucci. Prehistoric anasazi ceramics studied by micro-Raman spectroscopy. *Journal of Raman Spectroscopy*, 37:1139–1145, 2006.

[36] J. Zuo, C. Xu, C. Wang, and Z. Yushi. Identification of the pigment in painted pottery from the Xishan site by Raman microscopy. *Journal of Raman Spectroscopy*, 30:1053–1055, 1999.

[37] H. G. M. Edwards, R. H. Brody, N. F. N. Hassan, D. W. Farwell, and S. O'Connor. Identification of archaeological ivories using ft-Raman spectroscopy. *Analytica Chimica Acta*, 559:64–72, 2006.

[38] M. T. Kirchner, H. G. M. Edwards, D. Lucy, and A. M. Pollard. Ancient and modern specimens of human teeth: a Fourier transform Raman spectroscopic study. *Journal of Raman spectroscopy*, 28:171–178, 1997.

[39] D. B. Thomas, C. M. McGoverin, R. E. Fordyce, R. D. Frew, and K. C. Gordon. Raman spectroscopy of fossil bioapatatite - A proxy for diagenetic alteration of the oxygen isotope composition. *Paleography, Paleoclimatology and Paleoecology*, 310:62–70, 2011.

[40] H. Edwards, D. Farwell, D. Faria, A. Monteiro, M. Afonso, P. Blasis, and S. Eggers. Raman spectroscopic study of 3000-year-old human skeletal remains from a sambaqui, Santa Catarina, Brazil. *Journal of Raman Spectroscopy*, 32:17–22, 2001.

[41] A. C. Colonese, M. Collins, A. Lucquin, M. Eustace, Y. Hancock, R. A. R. Ponzoni, A. Mora, C. Smith, P. deBlasis, L. Figuti, V. Wesolowski, C. R. Plens, S. Eggers, D. S. E de Farias, A. Gledhill, and O. E. Craig. Long-term resilience of late holocene coastal subsistence system in Southeastern South America. *Plos One*, 9(4):e93854, 2014.

[42] B. Demarchi, S. O'Connor, A. L. L. Ponzoni, R. A. R. Ponzoni, A. Sheridan, K. Penkman, Y. Hancock, and J. Wilson. An integrated approach to the taxonomic identification of prehistoric shell ornaments. *Plos One*, 9(6), 2014.

[43] G. J. Vermeij. *A Natural History of Shells.* Princeton University Press, 1993.

[44] K. D. Thomas. Molluscs emergent, Part I: themes and trends in the scientific investigation of mollusc shells as resources for archaeological research. *Journal of Archaeological Sciences*, 56:133–140, 2015.

[45] F. Marin and G. Luquet. Molluscan shell proteins. *General Palaeontology*, pages 469–492, 2004.

[46] C. Claassen. *Shells.* Cambridge University Press, 1998.

[47] N. Watabe. *The Mollusca Form and Function*, volume 11, chapter Shell Structure, pages 69–77. Academic Press, 1988.

[48] L. Addadi, D. Joester, F. Nudelman, and S. Weiner. Mollusk shell formation: A source of new concepts for understanding biomineralization processes. *Chemistry A European Journal*, 12:980–987, 2006.

[49] U. Wehrmeister, A. L. Soldati, D. E. Jacob, T. Hager, and W. Hofmeister. Raman spectroscopy of synthetic, geological and biological vaterite: a Raman spectroscopic study. *Journal of Raman Spectroscopy*, 41:193–201, 2010.

[50] U. Wehrmeister, D. E. Jacob, A. L. Soldati, N. Loges, T. Hager, and W. Hofmeister. Amorphous, nanocrystalline and crystalline calcium carbonates in biological materials. *Journal of Raman Spectroscopy*, 42:926–935, 2011.

[51] H. A. Lowenstam. Minerals formed by organisms. *Science*, 211(13):1126–1131, 1981.

[52] D .E. Jacob, A. L. Soldati, R. Wirth, J. Huth, U. Wehrmeister, and W. Hofmeister. Nanostructure, composition and mechanisms of bivalve shell growth. *Geochimica et Cosmochimica Acta*, 72:5401–5415, 2008.

[53] S. M. de Paula and M. Silveira. Studies on molluscan shells: Contributions from microscopic and analytical methods. *Micron*, 40:669–690, 2009.

[54] G. Falini, S. Albeck, S. Weiner, and L. Addadi. Control of aragonite or calcite polymorphism by mollusk shell macromolecules. *American Association for the Advancement of Science*, 271:67–69, 1996.

[55] Y. Kitano, N. Kanamori, and A. Tokuyama. Effects of organic matter on solubilities and crystal form of carbonates. *American Zoologist*, 9:681–688, 1969.

[56] J. B. Ries. Review: geological and experimental evidence for secular variation in seawater Mg/Ca (calcite-aragonite seas) and its effects on marine biological calcification. *Biogeosciences*, 7:2795–2849, 2010.

[57] Y. Dauphin and A. Denis. Structure and composition of the aragonitic crossed lamellar layers in six species of Bivalvia and Gastropoda. *Comparative Biochemistry and Physiology Part A*, 126:367–377, 2000.

[58] C. Kittel. *Introduction to Solid State Physics.* John Wiley & Sons, Inc, eighth edition edition, 2005.

[59] J. P. R. Villiers. Crystal structures of aragonite, strontianite and witherite. *The American Mineralogist*, 56:758–767, 1971.

[60] B. Dickens and J. S. Bowen. Refinement of the crystal structure of the aragonite phase of $caco_3$. *Journal of Research of the National Bureau of Standards*, 75A:27–32, 1971.

[61] D. Jarosch and G. Heger. Neutron diffraction refinement of the crystal structure of aragonite. *Tschermaks Mineralogische und Petrographische Mitteilungen*, 35:127–131, 1986.

[62] S. I. Tomkeieff. The structure of aragonite. *Mineralogical Magazine*, 20:408–434, 1925.

[63] D.L. Graf. Crystallographic tables for the rhombohedral carbonates. *The American Mineralogist*, 46:1283–1316, 1961.

[64] J.R. Smyth and T.J. Ahrens. The crystal structure of calcite iii. *Geophysical Research Letters*, 24:1595–1598, 1997.

[65] A. Yamamoto, Y. Shiro, and H. Murata. Optically-active vibrations and elastic constants of calcite and aragonite. *Bulletin of the Chemical Society of Japan*, 47(2):265–273, 1974.

[66] D. J. M. Bevan, E. Rossmanith, D. K. Mylrea, S. E. Ness, M. R. Taylor, and C. Cuff. On the structure of aragonite – Lawrence Bragg revisited. *Acta Crystallographica Section B*, B58:448–456, 2002.

[67] E. N. Caspi, B. Pokroy, P. L. Lee, J. P. Kintana, and E. Zolotoyabko. On the structure of aragonite. *Acta Crystallographica Section B*, B61:129–132, 2005.

[68] H. J. Meyer. The influence of impurities on the growth rate of calcite. *Journal of Crystal Growth*, 66:639–646, 1984.

[69] Z. Z. Gobac, H. Posilovic, and V. Bermanec. Identification of biogenic calcite and aragonite using SEM. *Geologia Croatica*, 62/3:201–206, 2009.

[70] J. R. Dodd. Magnesium and Strontium in calcareous skeletons: A review. *Journal of Paleontology*, 41(6):1313–1329, 1967.

[71] E. Zolotoyabko and B. Pokroy. Biomineralization of calcium carbonate: structural aspects. *The Royal Society of Chemistry*, 9:1156–1161, 2007.

[72] C. Claassen and S. Sigmann. Sourcing *Busycon* artfacts of the eastern United States. *American Antiquity*, 58(2):333–347, 1993.

[73] B. Pokroy, J. S. Fieramosca, R. B. Von Dreele, A. N. Fitch, E. N. Caspi, and E. Zolotoyabko. Atomic structure of biogenic aragonite. *Chemistry of Materials*, 19:3244–3251, 2007.

[74] B. Pokroy, A. N. Fitch, F. Marin, M. Kapon, N. Adir, and E. Zolotoyabko. Anisotropic lattice distortions in biogenic calcite induced by intra-crystalline organic mollecules. *Journal of Structural Biology*, 155:96–130, 2006.

[75] J. Stolarski, R. Przenioslo, M. Mazur, and M. Brunelli. High-resolution synchrotron radiation studies on natural and thermally annealed scleractinian coral biominerals. *Journal of Applied Crystallography*, 40:2–9, 2007.

[76] B. Pokroy, A. N. Fitch, P. L. Lee, J. P. Quintana, E. N. Caspi, and E. Zolotoyabko. Anisotropic lattice distortions in the mollusk-made aragonite: A widespread phenomenon. *Journal of Structural Biology*, 153:145–150, 2006.

[77] B. Pokroy, J. Quintana, E. Caspi, A. Berner, and E. Zolotoyabko. Anisotropic lattice distortions in biogenic aragonite. *Nature materials*, 3:900–902, 2004.

[78] C. Perrin and D. C. Smith. Decay of skeletal organic matrices and early diagenesis in coral skeletons. *Comptes Rendus Palevol*, 6:253–260, 2007.

[79] C. Trueman. Chemical taphonomy of biomineralized tissues. *Palaeontology*, 56:475–486, 2013.

[80] Q. Shen, H. Wei, Y. Zhou, Y. Huang, H. Yang, D. Wang, and D. Xu. Properties of amorphous calcium carbonate and the templete action of vaterite spheres. *J. Phys. Chem. B*, 110:2994–3000, 2006.

[81] G. J. F. MacDonald. Experimental determination of calcite-aragonite equilibrium relations at elevated temperatures and pressures, 1956.

[82] M. Liu and R. A. Yund. Transformation kinectic of polycrystalline aragonite to calcite: New experimental data, modelling and implications. *Contributions to Mineralogy and Petrology*, 114:465–478, 1993.

[83] S. Xuefen, C. Jun, C. Yuanfeng, C. Yang, and J. Junfeng. Aragonite-calcite transformation in fossil snail shells of loess sequences in Loess Plateau, Central China. *Chinese Science Bulletin*, 50:891–895, 2005.

[84] S. Yoshioka and Y. Kitano. Transformation of aragonite to calcite through heating. *Geochemical Journal*, 19:245–249, 1985.

[85] M. Antao and I. Hassan. Temperature dependence of the structural parameters in the transformation of aragonite to calcite, as determined from in situ synchrotron powder x-ray-diffraction data. *The Canadian Mineralogist*, 48:1225–1236, 2010.

[86] D. Wardecki, R. Przenioslo, and M. Brunelli. Internal pressure in annealed biogenic aragonite. *The Royal Society of Chemistry*, 10:1450–1453, 2008.

[87] P. Gillet, C. Biellmann, B. Reynard, and P. McMillan. Raman spectroscopic studies of carbonates part 1: High-Pressure and high-temperature behaviour of calcite, magnesite, dolomite and aragonite. *Physics and Chemistry of Minerals*, 20:1–18, 1993.

[88] J. Balmain, B. Hannoyer, and E. Lopez. Fourier transform infrared spectroscopy (FTIR) and X-ray diffraction analyses of mineral and organic matrix during heating of mother pearl (nacre) from the shell of the mollusc Pinctada maxima. *J Biomed Mater Res*, 48:749–754, 1999.

[89] C. Loy, K. Matori, W. Lim, S. Schmid, N. Zainuddin, Z. Wahab, Z. Alassan, and M. Zaid. Effects of calcination on the crystallography and nonbiogenic aragonite formation of ark clam shell under ambient condition. *Advances in Materials Science and Engineering*, 2016, 2016.

[90] S. Gunasekaran and G. Anbalagan. Spectroscopic study of phase transitions in natural calcite mineral. *Spectrochimica Acta Part A*, 69:1246–1251, 2008.

[91] W. D. Bischoff, S. K. Sharma, and F. T. Mackenzie. Carbonate ion disorder in synthetic and biogenic magnesian calcites: a Raman spectral study. *American Mineralogist*, 70:581–589, 1985.

[92] J. Urmos, S. K. Sharma, and F. T. Mackenzie. Characterization of some biogenic carbonates with Raman spectroscopy. *American Mineralogist*, 76:641–646, 1991.

[93] M. Prencipe, F. Pascale, C. M. Zicovich-Wilson, V. R. Saunders, R. Orlando, and R. Dovesi. The vibrational spectrum of calcite ($CaCO_3$): an ab initio quantum-mechanical calculation. *Physics and Chemistry of Minerals*, 31:559–564, 2004.

[94] G. Nehrke and J. Nouet. Confocal Raman microscope mapping as a tool to describe different mineral and organic phases at high spatial resolution within marine biogenic carbonates: case study on *Nerita undata* (Gastropoda, Neritopsina). *Biogeosciences*, 8:3761–3769, 2011.

[95] N. Hausmann, A. Colonese, A. Ponzoni, Y. Hancock, M. Williams, M. Leng, and G. Bailey. Isotopic composition of Conomurex fasciatus shells as an environmental proxy for the Red Sea. *Quaternary International*, 427:115–127, 2017.

[96] C. Lecuyer, B. Reynard, and F. Martineau. Stable isotope fractionation between mollusc shells and marine waters from Martinique Island. *Chemical Geology*, 213:293–305, 2004.

[97] C. Lecuyer, S. Hutzler, R. Amiot, V. Daux, D. Grosheny, O. Otero, F. Martineau, F. Fourel, V. Balter, and B. Reynard. Carbon and oxygen isotope fractionations between aragonite and calcite shells from modern molluscs. *Chemical Geology*, 332–333:92–102, 2012.

[98] D. E. Jacob, R. Wirth, A. L. Soldai, U. Wehrmeister, and A. Schreiber. Amorphous calcium carbonate in the shells of adult *Unionoida*. *Journal of Structural Biology*, 173:241–249, 2011.

[99] P. L. Clode, K. Lema, and M. Saunders. Skeletal mineralogy of newly settling Acropora millepora (Scleractinia) coral recruits. *Coral Reefs*, pages 1–8, 2011.

[100] F. D. Fleischli, M. Dietiker, C. Borgia, and R. Spolenak. The influence of internal length scales on mechanical properties in natural nanocomposites: a comparative study on inner layers of seashells. *Acta Biomaterialia*, 4:1694–1706, 2008.

[101] L. Beierlein, G. Nehrke, and T. Brey. Confocal Raman microscopy in sclerochronology: A powerful tool to visualize environmental information in recent and fossil biogenic archives. *Geochem. Geophys. Geosyst.*, 16:325–335, 2015.

[102] S. A. Markgraf and R. J. Reeder. High-temperature structure refinements of calcite and magnesite. *American Minaralogist*, 70:590–600, 1985.

[103] P. K. Narayanaswamy. Influence of temperature on the Raman spectra of crystals. *Procedings of the Indian Academy of Sciences*, 26a:511–520, 1947.

[104] J. E. Parker, S. P. Thompson, A. R. Lennie, J. Potter, and C. C. Tang. A study of the aragonite-calcite transformation using Raman spectroscopy, synchrotron powder diffraction and scanning electron microscopy. *The Royal Society of Chemistry*, 12:1590–1599, 2010.

[105] H. G. M. Edwards, S. E. J. Villar, J. Jehlicka, and T. Munshi. FT-Raman spectroscopic study of calcium-rich and magnesium-rich carbonate minerals. *Spectrochimica Acta Part A*, 61:2273–2280, 2005.

[106] M Alvarez, I. B. Godino, A. Balbo, and M. Madella. Shell middens as archives of past environments, human dispersal and specialized resource management. *Quaternary International*, 239:1–7, 2011.

[107] A. Balbo, M. Madella, I. B. Godino, and M. Alvarez. Shell midden research: An interdisciplinary agenda for the Quaternary and Social Sciences. *Quaternary International*, 239:147–152, 2011.

[108] P. DeBlasis, A. Kneip, R. Scheel-Ybert, P. C. Giannini, and M. D. Gaspar. Sambaquis e paisagem: Dinamica natural e arqueologia regional no litoral sul do Brasil. *Arqueologia Sul-Americana*, 3(1):29–61, 2007.

[109] C. Fred T. Andrus. Shell midden sclerochronology. *Quaternary Science Reviews*, 30:2892–2905, 2011.

[110] I. Gutierrez-Zugasti, S. H. Andersen, A. C. Araujo, C. Dupont, N. Milner, and A. M. Monge-Soares. Shell midden research in Atlantic Europe: state of art, research problems and perspectives for the future. *Quaternary International*, 239:70–85, 2011.

[111] N. Milner, O. E. Craig, and G.N. Bailey. *Shell Middens in Atlantic Europe.* Oxbow Books, Oxford, UK, 2007.

[112] G. Bailey. World prehistory from the margins: the role of coastlines in human evolution. *Journal of Interdisciplinary Studies in History and Archaeology*, 1(1):39–50, 2004.

[113] G. Bailey, N. Flemming, G. King, K. Lambeck, G. Momber, L. Moran, A. Al-Sharekh, and C. Vita-Finzi. Coastlines, Submerged Landscapes, and Human Evolution: The Red Sea Basin and the Farasan Islands. *Journal of Island and Coastal Archaeology*, 2:127–160, 2007.

[114] A. C. Colonese, M. A. Mannino, D. E. Bar-Yosef Mayer, D. A. Fa, J. C. Finlayson, D. Lubell, and M. C. Stiner. Marine mollusc exploitation in Mediterranean prehistory: an overview. *Quaternary International*, 239:86–103, 2011.

[115] I. B. Godino, M. Alvarez, A. Balbo, D. Zurro, M. Madella, X. Villagran, and C. French. Towards high-resolution shell midden archaeology: experimental and eth-

noarchaeology in Tierra del Fuego (Argentina). *Quaternary International*, 239:125–134, 2011.

[116] A. C. Colonese, S. A. Neto, A. S. Francisco, P. DeBlasis, X. S. Villagran, R. A. R. Ponzoni, Y. Hancock, N. Hausmann, D. S. E. de Farias, A. Prendergast, B. R. Schone, F. W. da Cruz, and P. C. F. Giannini. Shell sclerochronology and stable isotopes of the bivalve *Anomalocardi flexuosa* (Linnaeus, 1767) from southern brazil: implications for environmental and archaeological studies. *Palaeogeography, Palaeoclimatology and Palaeoecology*, 2017. Article in press, http://dx.doi.org/10.1016/j.palaeo.2017.01.006.

[117] M. J. Leng and J. P. Lewis. Oxygen isotopes in Molluscan shell: applications in environmental archaeology. *Environmental Archaeology*, 21(3):295–306, 2016.

[118] K. G. Lightfoot. Long-term developments in complex hunter-gatherer societies: recent perspectives from the Pacific coast of North America. *Journal of Archaeological Research*, 1:167–201, 1993.

[119] A. Jerardino. Current methodological issues in archaeomalacological studies. *Quaternary International*, 427:1–4, 2017.

[120] N. Hausmann and M. Meredith-Willians. Exploring accumulation rates of shell deposits through seasonality data. *Journal of Archaeological Method and Theory*, pages 1–20, 2016.

[121] M. Walker. *Quaternary Dating Methods*. John Wiley & Sons, 2005.

[122] B. Demarchi, M.G. Williams, N. Milner, N. Russell, G. Bailey, and K. Penkman. Amino acid racemization dating of marine shells: A mound of possibilities. *Quaternary International*, 239:114–124, 2011.

[123] K. E. H. Penkman, D. S. Kaufman, D. Maddy, and M. J. Collins. Closed-system behaviour of the intra-crystalline fraction of amino acids in mollusc shells. *Quaternary Geochronology*, 3:2–25, 2008.

[124] B. Demarchi, E. Clements, M. Coltorti, R. van de Locht, R. Kroger, K. Penkman, and J. Rose. Testing the effect of bleaching on the bivalve *Glycymeris*: a case study of amino acid geochronology on key Mediterranean raised beach deposits. *Quaternary Geochronology*, 25:49–65, 2015.

[125] S. Epstein, R. Buchsbaum, H. A. Lowenstam, and H. C. Urey. Revised carbonate-water isotopic temperature scale. *Bulletin of the Geological Society of America*, 64:1315–1326, 1953.

[126] G. Wefer and W. H. Berger. Isotope paleontology: growth and composition of extant calcareous species. *Marine Geology*, 100:207–248, 1991.

[127] S. M. Savin. *Climate in Earth History*, chapter Stable Isotopes in Climatic Reconstructions, pages 164–171. National Academy Press, 1982.

[128] T. A. McConnaughey and D. P. Gillikin. Carbon isotopes in mollusk shell carbonates. *Geo-Marine Letters*, 28:287–299, 2008.

[129] B. R. Schone, A. D. Wanamaker Jr., J. Fiebig, J. Thebault, and K. Kreutz. Annually resolved $\delta^{13}$c chronologies of long-lived bivalve mollusks (*Arctica islandica*) reveal oceanic carbon dynamics in the temperate North Atlantic during recent centuries. *Palaeogeography, Palaeoclimatology, Palaeoecology*, 302:31–42, 2011.

[130] K. D. Thomas. Molluscs emergent, Part II: themes and trends in the scientific investigation of mollusc shells as resources for archaeological research. *Journal of Archaeological Sciences*, 56:159–167, 2015.

[131] J. S. Killingley and W. H. Berger. Stable isotopes in a mollusk shell: detection of upwelling events. *Science*, 205:186–188, 1979.

[132] G. Grupe. *Handbook of Paleoanthropology*, volume 1, chapter Taphonomic and diagenetic processes, pages 241–259. Springer, 2007.

[133] N. Guzman, Y. Dauphin, J. P. Cuif, A. Denis, and L. Ortlieb. Diagenetic changes in *Concholepas concholepas shells (Gastropoda, Muricidae) in the hyper-arid conditions of Northern Chile - implications for palaeoenvironmental reconstructions. Biogeosciences*, 6:197–207, 2009.

[134] S. Milano, A. L. Prendergast, and B. R. Schone. Effects of cooking on mollusk shell structure and chemistry: Implications for archaeology and paleoenvironmental reconstruction. *Journal of Archaeological Science: Reports*, 7:14–26, 2016.

[135] S. C. Larsen. Recrystallization of biogenic aragonite shells from archaeological contexts and implications for paleoenvironmental reconstruction. Master's thesis, Western Washington University, 2015.

[136] C. F. Andrus and D. E. Crowe. Alteration of otolith aragonite: Effects of prehistoric cooking methods on otolith chemistry. *Journal of Archaeological Science*, 29:291–299, 2002.

[137] K. Lange, C. Perles, M. Vanhaeren, and I. Reiche. Heat-induced modification of marine shells used as personal ornaments at the prehistoric site of Franchthi cave, Greece: First results of a multianalytical approach. In *Proceedings of the 9th International Conference on NDT of Art*, Jerusalem - Israel, 25–30 May 2008.

[138] B. Buchardt and S. Weiner. Diagenesis of aragonite from upper cretaceous ammonites: a geochemical case-study. *Sedimentology*, 28(423–438), 1981.

[139] P. C. Ragland, O. H. Pilkey, and B. W. Blackwelder. Diagenetic changes in the elemental composition of unrecrystallized mollusk shells. *Chemical Geology*, 25:123–134, 1979.

[140] Y. Dauphin. Structures, organo-mineral compositions and diagenetic changes in biominerals. *Current Opinion in Colloid & Interface Science*, 7:133–138, 2002.

[141] A. Perez-Huerta, M. Cusak, and J. England. Crystallography and diagenesis in fossil craniid brachiopods. *Palaeontology*, 50:757–763, 2007.

[142] V. Aldeias, S. Gur-Arieh, P. Monteiro, and P. Cura. *Shell* we cook it? An experimental approach to the microarchaeological record of shellfish roasting. *Archaeological and Anthropological Sciences*, 2016. Published online on 20 October 2016.

[143] G. Bailey, M. G. Meredith-Williams, and A. M. Alsharekh. *Shell Energy*, chapter Shell Mounds of the Farasan Islands, Saudi Arabia, pages 241–254. Oxbow Books, 2013.

[144] B. J. Davies, D. R. Bridgland, D. H. Roberts, C. O. Cofaigh, S. M. Pawley, I. Candy, B. Demarchi, K. E. H. Penkman, and W. En.N. Austin. The age and stratigraphic context of the Easington Raised Beach, county durham, uk. *Proceedings of the Geologists' Association*, 120:183–198, 2009.

[145] T. Dieing, O. Hollricher, and J. Toporski. *Confocal Raman Microscopy*, volume 158. Springer, San Diego, USA, 2011.

[146] I. R. Lewis and H. G. M. Edwards, editors. *Handbook of Raman Spectroscopy*. Marcel Dekker, 2001.

[147] H. G. M. Edwards and J. M. Chalmers. *Raman Spectroscopy in Archaeology and Art History*. The Royal Society of Chemistry, Cambridge, UK, 2005.

[148] J. M. Friedman and R. M. Hochstrasser. The use of fluorescence quenchers in resonance Raman spectroscopy. *Chemical Physics Letters*, 33(2):225–227, 1975.

[149] Horiba Scientific. *XploRA System User Manual*, 2009.

[150] HORIBA Scientific. *Labspec 5 – User Manual*, 12 2010.

[151] *http://www.bwtek.com/spectrometer-introduction.* Accessed: Feb/2017.

[152] WaveMetrics Inc. *IGOR Pro version 6.3 manual*, 2013.

[153] C. Hedegaard, J. F. Bardea, and D. Chateigner. Molluscan shell pigments: an in situ resonance Raman study. *Journal of Molluscan Studies*, 72:157–162, 2006.

[154] R. J. Weesie, J. C. Merlin, J. Lugtenburg, and G. Britton. Semiempirical and Raman spectroscopic studies of carotenoids. *Biospectroscopy*, 5:19–33, 1999.

[155] H. Okamoto, Y. Sekimoto, and M. Tasumi. Assignment and anharmonicity of overtone and combination bands observed in the resonance Raman spectra of carotenoids. *Spectrochimica Acta*, 50A:1467–1473, 1994.

[156] J. C. Merlin. Resonance Raman spectroscopy of carotenoids and carotenoid-containing systems. *Pure and Appl. Chem.*, 57(5):785–792, 1985.

[157] Y. Xie, D. Zhang, G. K. Jarori, V. J. Davisson, and D. B. Amotz. The Raman detection of peptide tyrosine phosphorylation. *Analytical Biochemistry*, 332:116–121, 2004.

[158] B. Xu and K. M. Poduska. Linking crystal structure with temperature-sensitive vibrational modes in calcium carbonate minerals. *Physical Chemestry Chemical Physics*, 16:17634–17639, 2014.

[159] R. Withnall, B. Z. Chowdhry, J. Silver, H. G. M. Edwards, and L. F. C. Oliveira. Raman spectra of carotenoids in natural products. *Spectrochimica Acta Part A*, 59:2207–2212, 2003.

[160] R. E. M. Hedges. Bone diagenesis: an overview of processes. *Archaeometry*, 44(3):319–328, 2002.

[161] C. L. King, N. Tayles, and K. C. Gordon. Re-examining the chemical evaluation of diagenesis in human bone apatite. *Journal of Archaeological Science*, 38:2222–2230, 2011.

[162] M. D. Morris and G. S Mandair. Raman assessment of bone quality. *Clinical Orthopaedics and Related Research*, 469:2160–2169, 2011.

[163] M. J. Collins, G. Muyzer, G. B. Curry, P. Sandberg, and P. Westbroek. Macromolecules in brachiopod shells: characterization and diagenesis. *Lethaia*, 24:387–397, 1991.

[164] L. S. Land. Diagenesis of skeletal carbonates. *Journal of Sedimentary Petrology*, 37:914–930, 1967.

[165] D. Chateigner, C. Hedegaard, and H.-R. Wenk. Mollusc shell microstructures and crystallographic textures. *Journal of Structural Geology*, 22:1723–1735, 2000.

[166] S. Kamat, X. Su, R. Ballarini, and A. H. Heuer. Structural basis for the fracture toughness of the shell of the conch *Strombus gigas*. *Nature*, 405:1036–1040, 2000.

[167] D. Chakrabarty and S. Mahapatra. Aragonite crystals with unconventional morphologies. *The Royal Society of Chemistry*, 9:2953–2957, 1999.

[168] C. Perles and Marian Vanhaeren. Black Cyclope neritea marine shell ornaments in the Upper Palaeolithic and Mesolithic of Franchthi Cave, Greece: Arguments for intentional heat treatment. *Journal of Field Archaeology*, 35(3), 2010.

[169] S. Lee, Y. Kim, R. Kim, and C. Choi. Nano-structured biogenic calcite: A thermal and chemical approach to folia in oyster shell. *Micron*, 39:380–386, 2008.

[170] Q. L. Feng, G. Pu, Y. Pei, F. Z. Cui, H. D. Li, and T. N. Kim. Polymorph and morphology of calcium carbonate crystals induced by proteins extracted from mollusk shell. *Journal of Crystal Growth*, 216:459–465, 2000.

[171] K. Douka, R. E. M. Hedges, and T. F. G. Higham. Improved AMS $^{14}$C dating of shell carbonates using high-precision X-ray diffraction and a novel density separation protocol (CarDS). *Radiocarbon*, 52(2–3):735–751, 2010.

[172] E. Loftus, K. Rogers, and J. Lee-Thorp. A simple method to establish calcite:aragonite ratios in archaeological mollusc shells. *Journal of Quaternary Science*, 30(8):731–735, 2015.

[173] L. C. Foster, C. Andersson, H. Hoie, N. Allison, A. A. Finch, and T. Johansen. Effects of micromilling on $\delta^{18}$O in biogenic aragonite. *Geochemistry Geophysics Geosystems*, 9(4):1–6, 2008.

[174] X. S. Villagran. A redefinition of waste: Deconstructing shell and fish mound formation among coastal groups of Southern Brazil. *Journal of Anthropological Archaeology*, 36:211–227, 2014.